COLUMNAR LIQUID-CRYSTALLINE POLYMERS CONTAINING NITROGEN AT THE BACKBONE TO BE USED TO PREPARE ION-TRANSPORT MEMBRANES

Jordi Guardià Blanch

UNIVERSITAT ROVIRA i VIRGILI

Columnar liquid-crystalline polymers containing Nitrogen at the backbone to be used to prepare ion-transport membranes

---

Jordi Guardià Blanch

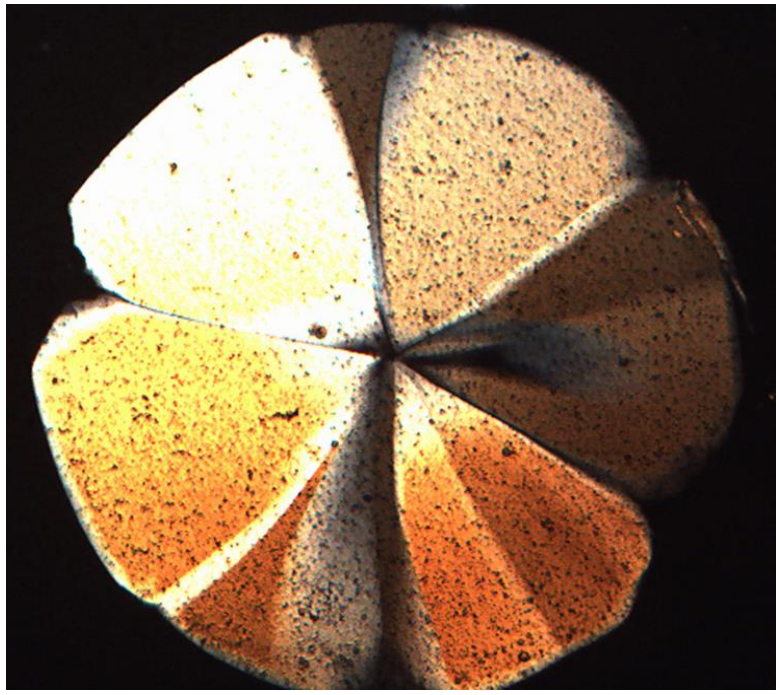

DOCTORAL THESIS

2024

UNIVERSITAT ROVIRA I VIRGILI
COLUMNAR LIQUID-CRYSTALLINE POLYMERS CONTAINING NITROGEN AT THE BACKBONE TO BE USED TO PREPARE ION-TRANSPORT MEMBRANES
Jordi Guardià Blanch

Department of Analytical Chemistry and Organic Chemistry

Columnar liquid-crystalline polymers containing Nitrogen at the backbone to be used to prepare ion-transport membranes

by

Jordi Guardià Blanch

Thesis supervisor: Dr. José Antonio Reina Lozano

Thesis co-supervisor: Dr. Xavier Montané Montané

DOCTORAL THESIS

Tarragona

2024

UNIVERSITAT ROVIRA I VIRGILI
COLUMNAR LIQUID-CRYSTALLINE POLYMERS CONTAINING NITROGEN AT THE BACKBONE TO BE USED TO PREPARE ION-TRANSPORT MEMBRANES
Jordi Guardià Blanch

UNIVERSITAT ROVIRA i VIRGILI

Department of Analytical Chemistry and Organic Chemistry

C/ Marcel·lí Domingo, s/n
Campus Sescelades, Edifici N4
43007, Tarragona
Tel: 977 559 769
Fax: 977 558 446

Doctor José Antonio Reina Lozano and Doctor Xavier Montané Montané of the Department of Analytical Chemistry and Organic Chemistry at the Universitat Rovira i Virgili,

Certify:

That the Doctoral Thesis, entitled "Columnar liquid-crystalline polymers containing Nitrogen at the backbone to be used to prepare ion-transport membranes" presented by Jordi Guardià Blanch to obtain the title of Doctor, has been carried out under our direction and that it fulfils all the requirements to be eligible for the Doctor International Mention.

Tarragona, May 24th, 2024

Doctoral Thesis Supervisors

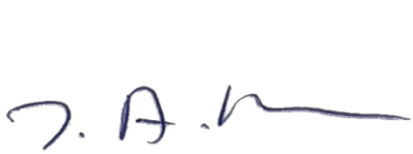

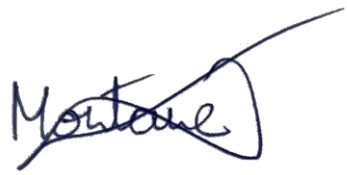

Dr. José Antonio Reina Lozano

Dr. Xavier Montané Montané

UNIVERSITAT ROVIRA I VIRGILI
COLUMNAR LIQUID-CRYSTALLINE POLYMERS CONTAINING NITROGEN AT THE BACKBONE TO BE USED TO PREPARE ION-TRANSPORT MEMBRANES
Jordi Guardià Blanch

«Las ruinas no nos dan miedo. Sabemos que no vamos a heredar más que ruinas, porque la burguesía tratará de arruinar el mundo en la última fase de su historia. Pero a nosotros no nos dan miedo las ruinas porque llevamos un mundo nuevo en nuestros corazones. Y ese mundo está creciendo en este instante.»

José Buenaventura Durruti Dumange

UNIVERSITAT ROVIRA I VIRGILI
COLUMNAR LIQUID-CRYSTALLINE POLYMERS CONTAINING NITROGEN AT THE BACKBONE TO BE USED TO PREPARE ION-TRANSPORT MEMBRANES
Jordi Guardià Blanch

Abstract

Liquid crystal materials have been used for decades in different applications, such as optoelectronics, sensors and biosensors, membranes, and energy storage applications among others. The main characteristic properties of these materials lie in their ability to exhibit some level of order like solids, while presenting certain mobility as liquids do. As a result, they rearrange in an intermediate state of matter between solid and liquid states, which are referred to as mesophase. The compounds that exhibit liquid crystal properties are called mesogens. In terms of liquid crystal molecules, they can be classified according to how the mesophase is observed or the shape of the molecule. According to the first division there are lyotropic or thermotropic liquid crystals, while according to the shape of the molecules, we can find rod-like or disc-like among other type of mesogens. Polymers can also form liquid crystal mesophases. From them, one can distinct two main groups depending on where the mesogen is located: main chain liquid crystalline polymers (MCLCPs) which present mesogenic moieties in the polymer main chain, and side chain liquid crystalline polymers (SCLCPs), in which the mesogens are attached as side chains to a given polymer backbone. This last group of liquid crystalline polymers can form supramolecular architectures that self-assemble into ordered structures spontaneously thanks to the π-π stacking of the mesogen aromatic cores. The synthesis of SCLCPs allows the formation of nanostructured membranes for proton transport in fuel cells applications.

Until now, our group has focused on the preparation of SCLCPs to be used as polymer electrolyte membrane (PEM) by chemically modifying commercially

available or other synthesized linear polymers with a tapered mesogen. These linear polymers are based on different polyamines and polyethers. Thanks to the tapered mesogen attachment to the polymer backbone, these SCLCPs can rearrange in a helical fashion allowing the formation of an inner channel. This inner channel is formed by basic heteroatoms (oxygen or nitrogen) and protected from the outer environment for the mesogen itself. Nevertheless, these membranes presented some challenges that need to be addressed, such as poor mechanical properties and brittleness. In this work, we present the synthesis and characterization of a liquid crystalline homopolymer family based on a poly(2-oxazoline), as well as its 2-oxazoline monomer precursor. This new class of liquid crystalline poly(2-oxazoline)s are used to prepare different membranes, which characterization and transport properties will be discussed. To overcome the mechanical issues presented by the previously synthetised SCLCPs in our group, new biobased supports based on delignified wood are presented. Subsequently, membranes based on dendronized poly(epichlorohydrin) (PECH), and the biobased support are prepared and characterized. Afterwards, a study of the transport properties is discussed.

Chapter 2 presents the synthesis and characterization of a 2-oxazoline tapered monomer, 2-(3,4,5-tris(4-dodecyloxybenzyloxy)phenyl)-2-oxazoline (TAPOx). For the synthesis of the tapered monomer different strategies were presented. Direct amidation of a tapered ester, or the amide formation from a tapered acid are some examples. Nevertheless, the synthesis of a tapered amide (TAPAm) intermediate from the reaction between a previously synthetised a tapered methyl ester and ethanol amine was the most successful synthetic pathway. This precursor will, lately, undergo a dehydrative cyclization to

form the desired 2-oxazoline (TAPOx), which unlike the tapered amide it is not a liquid crystal as was demonstrated by X-ray diffraction, differential scanning calorimetry and polarised optical microscopy.

Subsequently, in Chapter 3, the polymerization of TAPOx by *living* cationic ring-opening polymerization (CROP) is presented. The optimization of this synthesis was carried out by tunning several factors, such as type of initiator, solvent, and terminating agent. Additionally, temperature of the reaction, and concentration of the polymerization reaction were also investigated. The optimization of all these parameters allowed us to synthesize a 5-membered family of poly(2- (3,4,5-tris(4-dodecyloxybenzyloxy)phenyl)-2-oxazoline)s (PTOx) with controlled molecular weight as was evidenced by size exclusion chromatography (SEC). PTOx family members presented columnar mesophases in a broad range of temperatures (from around -15 to c.a. 80 °C).

Chapter 4 explains the preparation of PTOx based membranes. As we could observe in preliminary studies, PTOx membranes are not self-supported. For this reason, we used a polyester fabric to improve the mechanical performance of the membranes. Membranes were characterized by static contact angle, water uptake and optical microscopy. Transport properties of the hybrid membranes were evaluated by means of electrochemical impedance spectroscopy (EIS), permeability tests and linear sweep voltammetry (LSV). PTOx membranes revealed remarkable proton transport as was elucidated by LSV, while exhibiting an outstanding proton selectivity in front of other monovalent cations.

Finally, Chapter 5 and Chapter 6 present the preparation and use of functionalised delignified wood discs as supports for the infiltration of a

dendronized poly(epichlorohydrin) (PECH75) liquid crystalline polymer, and thus the preparation of hybrid membranes that could be used for ion transport applications. Furthermore, a comprehensive characterization of the membranes and the assessment of their ion transport was performed, respectively.

UNIVERSITAT ROVIRA I VIRGILI
COLUMNAR LIQUID-CRYSTALLINE POLYMERS CONTAINING NITROGEN AT THE BACKBONE TO BE USED TO PREPARE ION-TRANSPORT MEMBRANES
Jordi Guardià Blanch

UNIVERSITAT ROVIRA I VIRGILI
COLUMNAR LIQUID-CRYSTALLINE POLYMERS CONTAINING NITROGEN AT THE BACKBONE TO BE USED TO PREPARE ION-TRANSPORT MEMBRANES
Jordi Guardià Blanch

List of Contents

Chapter 1. General Introduction and Objectives **1**
1.1. Liquid crystals: an overview 6
1.1.1. Lyotropic liquid crystals 8
1.1.2. Thermotropic liquid crystals 11
1.1.2.1. Calamitic liquid crystals 12
1.1.2.2. Discotic liquid crystals 15
1.2. Liquid crystalline polymers 22
1.2.1. Liquid crystalline polymers-based membranes 30
1.2.1.1. Lyotropic liquid crystal based membranes 32
1.2.1.2. Thermotropic liquid crystal based membranes 33
1.3. Objectives 40
1.3.1. Goals of the thesis 40
1.4. References 42

Chapter 2. Synthesis and characterisation of dendritic compounds containing nitrogen: monomer precursors to build up biomimetic membranes **57**
2.1. Introduction 59
2.2. Experimental 62
2.2.1. Materials 62
2.2.2. Synthesis of the tapered mesogenic precursors 63
2.2.3. Synthesis of N-(2-hydroxyethyl)-3,4,5-tris(4-dodecyloxybenzyloxy) benzamide (TAPAm) 64
2.2.3.1. Direct amidation method using EDC as coupling agent 64
2.2.3.2. Direct amidation of TAPEs with ethanolamine 66
2.2.3.3. Synthesis of TAPAm using sodium methoxide. ($NaHCO_3$) as catalyst 66
2.2.4. Synthesis of 2-(3,4,5-tris(4-dodecyloxybenzyloxy)phenyl)-2-oxazoline (TAPOx) 67
2.2.4.1. Synthesis of TAPOx using a PPh_3-DDQ system 67
2.2.5. Preliminary polymerization studies 69
2.2.5.1. Bulk polymerization of TAPOx. 69
2.2.6. Characterization 69
2.3. Results and discussion 71
2.3.1. Synthesis of 2-(3,4,5-tris(4-dodecyloxybenzyloxy) phenyl)-2-oxazoline (TAPOx) 72
2.3.2. Thermal and mesomorphic characterization of TAPAm and TAPOx 88

2.3.3. Preliminary polymerization study 95
2.4. Conclusions 99
2.5. References 101
2.6. Supporting Information 108

Chapter 3. Synthesis and characterization of dendronized side chain liquid crystalline poly(2-oxazoline)s towards biomimetic ion channels 119
3.1. Introduction 121
3.2. Experimental section 123
3.2.1. Materials 123
3.2.2. Synthesis of 2-(3,4,5-tris(4-dodecyloxybenzyloxy)phenyl) -4,5-dihydro-1,3-oxazole) (TAPOx) 124
3.2.3. Synthesis of poly(2-(3,4,5-tris(4-dodecyloxybenzyloxy) phenyl)2-oxazoline)s (PTOx) 126
3.2.4. Characterization 127
3.3. Results and discussion 130
3.3.1. Chemical characterization 138
3.3.2. Thermal and mesomorphic characterization 144
3.4. Conclusions 151
3.5. References 153
3.6. Supporting Information 159

Chapter 4. Tapered hybrid poly(2-oxazoline) membranes for proton transport. New approach to PEM assembly 165
4.1. Introduction 167
4.2. Experimental Section 171
4.2.1. Materials 171
4.2.2. Polymer synthesis 171
4.2.3. Membrane Preparation 172
4.2.3.1. Surface type for membrane preparation 172
4.2.3.2. Membrane preparation 173
4.2.4. Characterization 174
4.3. Results and discussion 177
4.3.1. Membrane preparation and characterization 177
4.3.2. Transport properties 188
4.4. Conclusions 202
4.5. References 205
4.6. Supporting Information 210

Chapter 5. Development of wood-based membranes for ion transport applications. Part 1: Support preparation and membrane assembly **219**
5.1. Introduction 221
5.2. Experimental section 223
5.2.2. Synthesis of the copolymers 224
5.2.3. Wood delignification process 225
5.2.4. Wood functionalization 226
5.2.5. Preparation of the membranes 227
5.2.6. Characterization 228
5.3. Results and discussion 231
5.3.1. Wood delignification 231
5.3.2. Functionalization of delignified wood 238
5.3.3. Thermal and mesomorphic characterization 242
5.3.4. Preparation and characterization of hybrid membranes 244
5.4. Conclusions 249
5.5. References 251
5.6. Supporting Information 256

Chapter 6. Development of wood-based membranes for ion transport applications. Part 2: Membrane characterization and evaluation of ionic transport **261**
6.1. Introduction 263
6.2. Experimental Part 266
6.2.1. Materials 266
6.2.2. Synthesis of copolymers 267
6.2.3. Preparation of the membranes 267
6.2.4. Characterization 268
6.3. Results and discussion 272
6.3.1. Structural and morphological characterization 272
6.3.2. Transport properties 280
6.4. Conclusions 290
6.5. References 293
6.6. Supporting Information 299

Chapter 7. General conclusions **305**
Appendices **313**
List of figures 315
List of tables 322
Scientific contributions 325
Contributions to scientific conferences 326

UNIVERSITAT ROVIRA I VIRGILI
COLUMNAR LIQUID-CRYSTALLINE POLYMERS CONTAINING NITROGEN AT THE BACKBONE TO BE USED TO PREPARE ION-TRANSPORT MEMBRANES
Jordi Guardià Blanch

List of Abbreviations

^{13}C NMR	Carbon nuclear magnetic resonance spectroscopy
^{1}H NMR	Proton nuclear magnetic resonance spectroscopy
AAO	Anodized Aluminium oxide
ADMET	Acyclic diene metathesis
AFC	Alkaline fuel cell
BnBr	Benzyl bromide
BTF	Anhydrous benzotrifluoride
BZT	2-methyl [1,2,3] benzotriazole
C	Capacitor
CA	Contact angle
CBPHT	6-[4-(5-chloro-2-benzoxazolyl)phenoxy]-hexanethiol
CDC	Circuit description code
Col	Columnar mesophase
Col_h	Columnar hexagonal mesophase
Col_L	Columnar lamellar mesophase
Col_r	Columnar rectangular mesophase
COSY	Correlated Spectrosocpy
CPE	Constant phase element
CROP	Cationic ring opening polymerization
C-V	Current-voltage
Đ	Dispersity index
DBU	Diazobicyclo [5.4.0]undec-7-ene

DCC	N,N'-dicyclohexilcarbodiimide
DCM	Dichloromethane
DCS	Dicyanotristyrylbenzene
DCU	Dicyclohexil urea
DDQ	2,3-dichloro-5,6-dicyano-1,4-benzoquinone
DMAP	4-dimethylaminopyridine
DMF	N,N'-dimethylformamide
DMFC	Direct methanol fuel cell
DMOAP	Dimethyloctodecyl[3-(trimethoxysilyl)propyl]amonium chloride
DP	Degree of polymerization
DSC	Differential scanning calorimetry
DTGA	1st Derivative TGA
DW	Delignified Wood
DWD	Delignified wood discs
DWDM	Delignified wood discs membranes
EDC	1-Ethyl-3-(3-dimethylaminopropyl)carbodiimide
EIS	Electrochemical impedance spectroscopy
ESEM	Environmental scanning electron microscopy
FDWD	Functionalized delignified wood discs
FDWDM	Functionalized delignified wood discs membranes
FEPR	Fluorinated ethylene propylene resin
FLC	Ferroelectric liquid crystals
FT-IR	Fourier transform infrared spectroscopy

FWHM	Full width at half maximum
GHG	Green House Gases
GO	Graphene oxide
HMBC	Heteronuclear multiple-bond correlation spectroscopy
HSQC	Heteronuclear single-quantum correlation spectroscopy
I_{lim}	Limiting current
$LaTf_3$	Lanthanum triflate
LC	Liquid crystal
LCD	Liquid crystal display
LCP	Liquid crystal polymer
LOD	Limit of detection
LSV	Linear sweep voltammetry
MCFC	Molten carbonate fuel cell
MCLCP	Main chain liquid crystal polymer
MCSCLCP	Main chain/side chain liquid crystal polymers
MeOTf	Methyl trifluoromethanesulfonate
MeOTs	Methyl tosilate
M_n	Number averaged molecular weight
MS	Mild Steel
M_w	Weight averaged molecular weight
N	Nematic mesophase
NC	Nanocrystal
N_{col}	Nematic columnar

N_D	Discotic Nematic
NMR	Nuclear magnetic resonance spectroscopy
NIR	Near-infrared
NTW	Non-treated beech wood
o-DCB	*o*-dichlorobenzene
OLED	Organic light-emitting diode
PAOx	Poly(2-oxazoline)
PAZE	poly[2-aziridin-1-yl)ethanol
PBI	Perylene-bisimides
PECH	Polyepichlorohidryn
PECH75	Polyepichlorohidryn 75% modified
P(ECH-*co*-EO)	Poly(epichlorohidryn-*co*-ethylene oxide)
PEDOT:PSS	Poly(3,4-ethylenedioxythiophene)-poly(styrenesulfonate)
PEG	Polyethylene glycol
PEM	Polymer electrolyte membrane
PEMFC	Polymer electrolyte membrane fuel cell
PEO	Polyethylene oxide
PFSI	Perfluorosulfonic acid ionomer
PIFE	Photo-induced fluorescent enhancement
POM	Polarized optical microscopy
PTOx	Poly(2-(3,4,5-tris(4-dodecyloxybenzyloxy)phenyl)-2-oxazoline)
R	Resistor
RAFT	Reversible addition fragmentation chain transfer

rGO	Reduced graphene oxide
R_{ohm}	Ohmic resistance
RT	Room temperature
RTG-gel	Rotigonite-gel
SCLCP	Side chain liquid crystal polymer
SEC	Size exclusion chromatography
Sm	Smectic mesophase
Sm A	Smectic A
SmC*	Smectic C phase
SOFC	Solid oxide fuel cell
SSTF	Solid-state solar thermal fuels
TAPAc	3,4,5-tris[4-(n-dodecan-1-yloxy)benzyloxy]benzoic acid
TAPAm	N-(2-hydroxyethyl)-3,4,5-tris(4-dodecyloxybenziloxy)benzamide
TAPER	3,4,5-tris[4-(n-dodecan-1-yloxy)benzyloxy]benzoate
TAPEs	Methyl 3,4,5-tris[*p*-(n-dodecan-1-yloxy)benzyloxy]benzoate
TAPOx	2-(3,4,5-tris(4-dodecyloxybenzyloxy)phenyl)-2-oxazoline
TB	Tris-benzimidazalyl benzene
TBAB	Tetrabutylamonium bromide
T_c	Clearing temperature
TCS	Tricyanotristyrylbenzene
T_g	Glass transition temperature
TGA	Thermogravimetric analysis
THF	Tetrahydrofuran

TLC	Thin layer chromatography
TMV	Tobacco mosaic virus
T_v	Topology-freezing transition temperature
XRD	X-ray diffraction

UNIVERSITAT ROVIRA I VIRGILI
COLUMNAR LIQUID-CRYSTALLINE POLYMERS CONTAINING NITROGEN AT THE BACKBONE TO BE USED TO PREPARE ION-TRANSPORT MEMBRANES
Jordi Guardià Blanch

UNIVERSITAT ROVIRA I VIRGILI
COLUMNAR LIQUID-CRYSTALLINE POLYMERS CONTAINING NITROGEN AT THE BACKBONE TO BE USED TO PREPARE ION-TRANSPORT MEMBRANES
Jordi Guardià Blanch

Chapter 1

General Introduction and Objectives

UNIVERSITAT ROVIRA I VIRGILI
COLUMNAR LIQUID-CRYSTALLINE POLYMERS CONTAINING NITROGEN AT THE BACKBONE TO BE USED TO PREPARE ION-TRANSPORT MEMBRANES
Jordi Guardià Blanch

These days, we, as a society, are facing one of the most complex and challenging problems of our time, climate change. After the industrial revolution at the end of the XVIII century and the XIX century, the world consumption of fossil fuels has increased dramatically, especially this last century and the beginning of XXI century [1]. As consequence of this revolution, we have experimented an incredible demographic growth. Moreover, the evolution of the society has aroused an increase of demands, such as lighting, cooking, space comfort, mobility, and communication, in order to satisfy its necessities. These necessities have also produced, an increase in the exploitation of resources worldwide, which has increased the effect of the climate change [2]. The excess of fossil fuel consumption has promoted the formation in a large extend of greenhouse gasses (GHG)s, which are responsible for the global warming [3]. However, these gasses are not the only responsible of the global warming; air pollution also plays an important role in this warming, as have been highlighted in recent studies [4].

Despite the evidence of the climate change, there are still people around the globe who is sceptical about it [5]. A change on the policies [2,6], education [2] and research [6] needs to be made in order to face the climate change emergency. Furthermore, the shift of the society from a regionally conscious society to a globally conscious society is a key factor that helps the world's population gain interest in climate change awareness [7]. Another important effect of the climate change are the extreme weather events that we are living nowadays such as extreme cooling or heating. As result, an increase of the mortality and migration have been noticed in several areas of the globe [8]. This extreme weather has also a big impact on agriculture, where farmers are

vulnerable to the changes of the climate with unpredictable rainfall distribution and frequency [9–11].

With the aim to face the GHGs emissions and the climate change, the adoption of renewable energies to phase down fossil fuel energy consumption have aroused an important field to invest in, either to expand the already existing technologies or to research in new alternatives and clean energy [12]. Under this point of view, fuel cell technology has emerged as an alternative to fossil fuels, since it provides an efficient and clean energy production. One can distinct several types of fuel cells according to the used electrolyte (e.g. polymer electrolyte membrane fuel cells (PEMFC), molten carbonate fuel cells (MCFC), solid oxide fuel cells (SOFC), alkaline fuel cells (AFC), among many others) [13]. Due to their simple construction, fuel cells can be used for different applications, either stationary or portable devices. Polymer electrolyte membrane fuel cells are one of the most promising types of fuel cells. Perfluorosulfonic acid ionomer-based membranes are the most commonly used membranes for this type of fuel cells. Nafion® (a registered trademark of DuPont Co.) is the most used material for this application, since it presents several advantages, such as excellent chemical and mechanical stability, and high proton conductivity, among others. Nonetheless, it also presents some disadvantages, such as high production cost, poor chemical stability at high temperatures, methanol crossover (when operating on a direct methanol fuel cell (DMFC)), membrane swelling and a huge dependence of proton transport on presence of water. Water is required to form the conductive pathways to transport the proton across the membrane and also to transport the proton itself, since the transport mechanism is

explained by the "hopping" mechanism (also known as Grothus mechanism) and electroosmotic drag [14,15].

For this reason, alternatives to Nafion® have been proposed the last decades. Some of these alternatives include the modification of the perfluorosulfonic acid chain, which includes partially fluorinated and non-fluorinated acid ionomer-based membranes, the use of polybenzimidazole membranes (doped with phosphoric acid) or alkaline ionomer-based membranes [16]. Liquid crystals have been also emerged as alternatives to Nafion® due to their tuneability and broad range of applications [17–20]. A liquid crystal is a molecule, which, due to its chemical structure is able to form a state of matter, the liquid crystal state (also called mesophase), intermediate between a liquid and a crystalline solid. These kinds of molecules are called mesogens (or mesogenic molecules). In the liquid crystal state, these materials share some properties of a crystalline solid (ordering) and of a liquid (ability to flow), and they are characterised by a relatively rigid structure, an anisotropic shape and anisotropy of the molecular polarizability.

There exist two distinct types of liquid crystal polymers: main chain liquid crystal polymers (MCLCP)s and side chain liquid crystal polymers (SCLCP)s, depending on where the mesogen is located (at the main chain or at the side chain, respectively). Liquid crystal polymers, due to their structure are able to adopt complex organizations by self-assembling. In the last decades, our group has focused on the development of liquid crystal polymers, with the aim of synthesizing tapered side chain liquid crystal polymers (SCLCP)s to be used as membranes for fuel cells applications. For the synthesis of SCLCPs, our group has focused on the use of the tapered (or dendron) unit 3,4,5-tris[4-(n-dodecan-1-yloxy)benzyloxy]benzoate (TAPER) as mesogen, which has

been attached to polyethers, polyamines or polyoxazolines as side chain [21–36]. The presence of this dendron induces the self-assembly of the polymer structure to adopt an inner helical organization of the main chain, thus forming columnar structures, as it was established by Percec and co-workers [37–39]. Thanks to this self-assembly an inner channel is formed, which endows the ion transport as result of the presence of basic heteroatoms (oxygen or nitrogen in the main chain). The presence of the long aliphatic chains at the periphery of the structure, increase the hydrophobicity of the material and, at the same time, protects the inner channel against the environment. In this introduction we provide an explanation, classification, and up-to-date overlook of liquid crystals (LC) and liquid crystal polymers (LCPs), together with the recent advances in the field of membrane technology for different applications, focussing on membranes for fuel cell technology as alternatives to perfluorosulfonic acid-based ionomers.

1.1.Liquid crystals: an overview

Liquid crystals (LC) were first discovered by the Austrian botanist, Friedriche Reinitzer in 1888 when determining the melting point of cholesteryl benzoate. Since then, liquid crystals have been extensively studied obtaining a wide variety of molecules for different applications such as electro-optical displays [40,41], temperature sensors [42–45], solar cells [46] and biomedical applications [47–50], among many others. As everybody knows, there are three main states of matter: crystalline solid, liquid and gas. They can be distinguished according to the organization and mobility of their molecules.

In a crystalline solid state molecules are well ordered, and the substance presents a definite shape and limited volume. Liquid on the other hand, presents a more flexible shape, due to the higher mobility of its molecules. Finally, gas state, presents a chaotic mobility of the molecules and it has neither a limited volume nor definite shape. In the case of the crystalline solids, X-ray diffraction analysis reveals that their constituents (molecules, atoms, or ions) present a long-range periodic order, since they are arranged in a definite pattern, thus presenting a 3D network-crystal. As result of the described above, crystalline solids present anisotropy of their physical properties (meaning that these properties are different in different directions), meanwhile liquids and gasses are isotropic. Liquid crystals share the properties of both crystalline solids and liquids. In other words, LC present some positional and orientational ordering, meanwhile molecules diffuse through the sample. Therefore, they present anisotropic properties like a crystalline solid but with the fluidity of a liquid.

LC can be classified depending on the formation of the mesophase, that is, depending on the concentration in a given solution (lyotropic) or varying the temperature (thermotropic). From the thermotropic liquid crystals, there is also a differentiation if the liquid crystal behaviour is observed in one direction, either cooling or heating (monotropic) or in both heating and cooling (enantiotropic). In addition, they can be also classified depending on the shape of the molecule (rod-like, disc-like, etc.), and the organization at the liquid crystalline phase (smectic, columnar, nematic, etc.). Furthermore, polymers can form also liquid crystalline phases when a mesogenic moiety is attached to the main chain (namely, main chain liquid crystal polymers

(MCLCP)) or at the side chain (namely, side chain liquid crystal polymers (SCLCP)). Classification of the LCs and LCPs can be found in **Figure 1.1.**

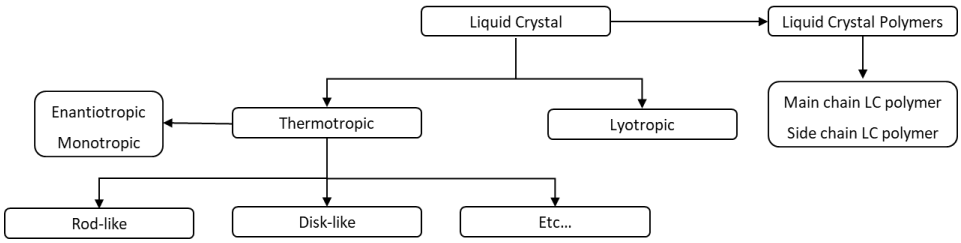

Figure 1.1. General classification of liquid crystals and liquid crystal polymers.

1.1.1. Lyotropic liquid crystals

Lyotropic liquid crystals are formed mainly by amphiphilic molecules which present a non-polar head and a polar tail. These molecules endow the liquid crystal behaviour under determinated solvents, at certain temperature and concentrations. Lyotropic LC phases can be classified in these three main groups, lamellar, columnar or cubic phases, among others, depending on the positional order [51]. Lyotropic LC can be found in the soap as surfactants, and in nature at the lipidic bilayer cell membrane [51,52] or other biomolecules such as DNA, where small fragments can be dispersed in water to present lyotropic LC phases [53]. This class of LC are used in biomedical applications, for drug delivery systems [47,48,54] and vaccine platforms [48].

In particular, non-lamellar lyotropic liquid crystals, namely, bicontinuous cubic and inverse hexagonal columnar mesophases, are the most common

systems for biomedical applications, since they can be applied either as bulk phases or as colloidal nanocarriers (cubosomes or hexosomes). Bicontinuous cubic phase is a very interesting complex structure which consists in a 3D network presenting a continuous, but not intersecting, hydrophilic sections/water channels. Inverse hexagonal columnar phase, it is a 2D phase with a hydrophilic inner channel surrounded by a lipidic bilayer. Ultimately, these columns are organised in a long-range two-dimensional hexagonal fashion.

Lyotropic liquid crystals have been proven to provide an enhancing solubility and slowing the drug release [55]. Thus, Wu and co-workers prepared a lyotropic liquid crystal gel called rotigonite-gel (RTG-gel), obtaining an inverse hexagonal phase, for the treatment of Parkinson's disease to provide a long-acting and slow-release benefits of rotigonite, which showed robust sustained release characteristics as was evidenced by in vitro and in vivo experiments, and good biocompatibility [56].

One of the problems of drug administration is the low solubility of these compounds, which affects directly to the administration and release of the same drug. As we have seen, the encapsulation of these drugs in lyotropic liquid crystals can improve this drawback for oral, injection and/or transdermal drug delivery. In the field of transdermal drug delivery, it has a great importance the study of the drug administration across the human skin. Thus, human or animal skin is used to study the diffusion of the drugs, however it entails supply and ethical issues. Lamellar lyotropic LCs, due to their structure, present some similarities with biological skin membranes since they can mimic the stratum corneum lipidic bilayers. Cen and co-workers developed a lamellar lyotropic liquid crystal as an artificial skin

membrane and studied the diffusion of four drugs with different polarities. Three artificial skin membranes were synthetised, one containing phytosterols and hydrogenated lecithin and two more, one containing sorbitan stearate and sucrose cocoate, and another containing cetearyl glucoside. Permeation tests using the synthetic artificial skins mimicked in vitro penetration test through human skin [57].

Additionally, lyotropic liquid crystals can be used also as sensors due to their stimuli response ability. For instance, Uzun Azar and co-workers have developed a cholesteric lyotropic LC based toxic gas sensor for the detection of toxic gases such as toluene, phenol and 1,2-dichloropropane, obtaining good results [58]. On the other hand, due to their fluidity, lyotropic liquid crystals can be used also as lubricants. In this sense, graphene oxide (GO) has been studied as potential material for this purpose since the aqueous dispersion of GO can form a lyotropic liquid crystal phase for concentration above 5.00 mg/mL. This lubricant is stable for several months and can reduce the friction by 37.3 % as was reported by Guo and co-workers [59]. Moreover, graphene oxide has been investigated also as scaffold for the construction of artificial muscles by Gao and co-workers [60]. In their work, they exploited the use of GO sheets in their lyotropic liquid crystal phase to prepare GO fibres combined with the conductive polymer poly(3,4-ethylenedioxythiophene)-poly(styrenesulfonate) (PEDOT:PSS), followed by the reduction of GO to reduced graphene oxide (rGO). The addition of PEDOT:PSS reported an increasing of the elasticity for the rGO fibres, which resulted in outstanding mechanical properties, such as Young's modulus, toughness, and elongation-at-break, and exceptional electrical actuation

performance. Finally, they demonstrated the potential scalability of the fibre-based artificial muscles and their integration with robotic systems.

1.1.2. Thermotropic liquid crystals

When a material presents a liquid crystal phase by varying the temperature it is called a thermotropic liquid crystal. These mesophases can be obtained by heating a crystalline solid or by cooling an isotropic liquid. The transition of a crystalline solid to a liquid crystal phase is called melting point, meanwhile, the transition of the liquid crystal phase to an isotropic liquid is called clearing point (the temperature at which this transition takes place is called clearing temperature). When a liquid crystal mesophase is obtained by both heating and cooling it is called enantiotropic. On the other hand, when the liquid crystal phase is obtained only from cooling an isotropic liquid or heating a crystalline solid it is called monotropic. However, not all molecules can lead to a thermotropic liquid crystal, they need to present some structural requirements, such as an (often) aromatic rigid core and a flexible peripheral moiety (generally long aliphatic chains). As mentioned previously, thermotropic liquid crystals can be classified in two main groups according to their shape: calamitic (rod-like) and discotic (disc-like) liquid crystals. General structures of these liquid crystals are shown in **Figure 1.2**.

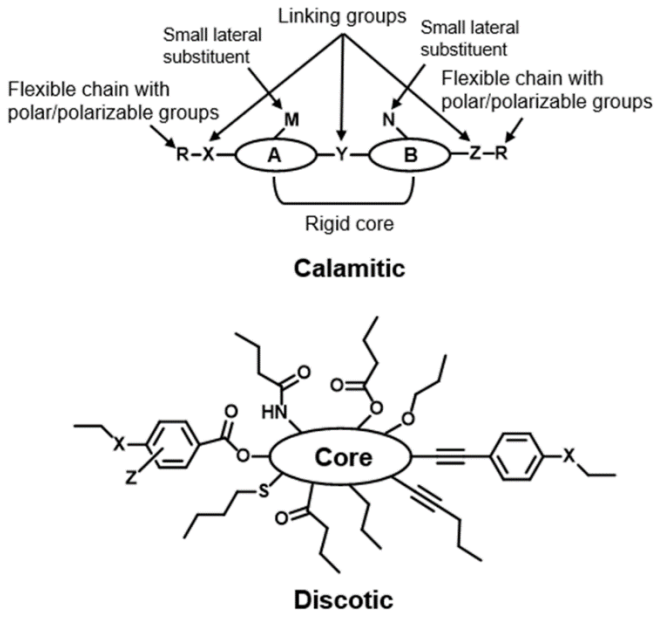

Figure 1.2. General template for thermotropic liquid crystals based on their shape.

1.1.2.1. Calamitic liquid crystals

This group of liquid crystals is the most common inside the group of thermotropic LC. They are composed of two or more rigid rings in their core (A and B, **Figure 1.2**) linked by a linking small group (Y, **Figure 1.2**); at each end there are flexible moieties (R, **Figure 1.2**), often composed of linear and/or branched aliphatic chains, bearing polar/polarizable groups. Additionally, calamitic molecules can present small lateral substituents such as -Cl, -Br, -NO_2, -CH_3, -OCH_3, etc. to reduce symmetry in a controlled manner. Due to the elevated variety of different cores, aliphatic ends, small substituents at the

core, polar/polarizable groups, and linking groups, calamitic LC can form different mesophases, namely nematic phases and smectic phases. Nematic mesophases (N) are the least-ordered mesophases (closest to the isotropic liquid) and are characterized by presenting orientational order but not positional order. Nematic mesophases are extensively used in liquid crystal devices (LCD) [61,62]. Smectic mesophases (Sm) present orientational order, same as the nematic mesophase, but with long-range positional order in one direction. Molecules in the smectic phase are arranged in layers, which present weak inter-layer interaction that allows them to flow past each other. The presence of more than one mesophase (polymorphism) for a single compound it is also possible. As matter of example, da Silva and co-workers synthetised symmetrical 2-methyl[1,2,3]benzotriazole (BZT) derivatives with elongated peripheral units linked via acetylenic triple bonds. Some of these calamitic thermotropic liquid crystals present both nematic and smectic phases upon heating or cooling at different temperatures. Moreover, the band gaps determined electrochemically for HOMO and LUMO were moderate, showing the potential use of these compounds for electro-optical applications [63].

From the nematic mesophases, there is a subclass called chiral nematic phase or cholesteric mesophase (N*). This LC mesophase is typically shown by chiral molecules. This mesophase presents a helical structure, since it can be visualized as a stack of very thin 2D nematic-like layers with the orientation of the molecules in each layer twisted slightly with respect to the layers above and below. It is also possible to induce a cholesteric mesophase for non-chiral molecules by adding chiral dopants. Hereby, the chiral dopants, which may not be LC, can induce a helical arrangement to the thermotropic liquid

crystals, whose mesophase is nematic. Smectic mesophases can also exist as a chiral phase, which is called chiral smectic C phase (SmC*). Pozhidaev and co-workers reported the synthesis of SmC* ferroelectric liquid crystals (FLCs) by mixing a nematic liquid crystal and chiral non-mesogenic dopants based on terphenyldicarboxylic acid [64]. The nematic LC was obtained by an eutectic mixture of biphenyl- and phenylpyrimidine derivatives. The FLC reported to exhibit a broad temperature range (10 °C to 63 °C). These new type of FLCs have potential for the design of different photonic devices of new generation [65].

In the field of ferroelectric liquid crystals, it also possible to induce the SmC* phase by adding inorganic dopants. In this sense, Pote and co-workers haver reported the incorporation of spinel ferrite $CoFe_2O_4$/ZnO (ZCOF) core/shell nanocrystals (NCs) in FLC. Photoluminiscent analysis revealed improved optical emission properties as direct result of the addition of ZCOF [66]. Nevertheless, the incorporation of dopants it is not the only way to obtain ferroelectric liquid crystal with SmC* phases. For instance, Węgłowska and co-workers have synthetized and characterized nine different compounds of a chiral homologous series of 4′-[ω-(2,2,3,3,4,4,4-heptafluorobutoxy) alkoxy]biphenyl-4-yl-4-(octan-2-yloxy)benzoates, containing fluorine or chlorine atoms in the lateral position of the rigid core with a chiral terminal octyloxy-chain, which exhibit chiral SmC* phases. According to their study, transductors based on these materials can form new classes of optical sensors suitable for numerous applications [67].

Moreover, thermotropic LC with cholesteric mesophases have potential uses as optical sensors for biomedical applications, since it is known that can be used to achieve the optical amplification of biological interactions [68]. Thus,

Wu and co-workers reported the preparation of a LC-based single-substrate biosensor by spin-coating of the same LC, obtaining a thin film, on a dimethyloctadecyl[3-(trimethoxysilyl)propyl]ammonium chloride (DMOAP)-decorated glass slide [69]. Thanks to the spin-coated methodology they were able to control the film thickness with precision. With this biosensor, they reported the improvement up to two orders of magnitude for the limit of detection (LOD) for bovine serum albumin (BSA) by lowering the LOD from 10^{-5} g/mL to 10^{-7} g/mL for a 4.2 μm thick film; however, when the film thickness was reduced to 3.4 μm, LOD decreased to 10^{-8} g/mL.

1.1.2.2. Discotic liquid crystals

Discotic liquid crystals are formed, as the name suggests, by disc-shaped molecules. This kind of LC, often spontaneously self-assemble into stacks thanks to the π-π interactions, which eventually will self-organize forming 2D structures (**Figure 1.3**). Discotic LC can form different mesophases: nematic, smectic, columnar and cubic. Smectic and cubic phases are very rare, meanwhile columnar mesophases, which can be easily homeotropically oriented, are the predominant structures, followed by the nematic mesophases. However, disc-like molecules are not the only ones which present columnar structures: as commented at the previous section, lyotropic liquid crystals can also form columnar structures. Moreover, dendrimers, star-shaped molecules and even rod-like molecules can exhibit thermotropic columnar phases. For instance, Carrasco and co-workers prepared red near-infrared (NIR)-emissive metal clusters compounds, with general formula

$Na_2Mo_6X_8Cl_6$ (X = Cl or Br), complexed with LC containing crown ethers [70]. The complexation was possible thanks to the well-known interaction of the sodium cations (Na^+) and the oxygens of the crown ethers. The prepared hybrid materials exhibit hexagonal columnar mesophases in broad range of temperatures. In another example, Labov and co-workers synthetised star-shaped LC molecules as nano-reservoirs for small acceptors, based on a 1,3,5-substituted benzene core and either oligo(phenylene vinylene) or oligothiophene arms [71]. The small acceptor was 2,4,7-trinitrofluorenone. X-ray scattering and solid-state NMR analysis confirmed the host-guest complexation for up to three guest molecules per LC-host. In addition, as was confirmed by differential scanning calorimetry (DSC) analysis and X-ray scattering, these materials present hexagonal columnar mesophases at high temperatures.

It is very common to confuse the terms discotic phase and disc-shaped molecules. Therefore, it is very important to remember that it is the molecule that is discotic and not the mesophase, which can be nematic, columnar, or lamellar, etc. From the mesophases shown by discotic mesogens, the discotic nematic mesophase (N_D) is the less ordered phase and least viscous, same as for the calamitic molecules. It presents translational and rotational freedom around its short axis but, on average, disk-like molecules are oriented in a preferred direction (**Figure 1.3.**). Nematic columnar (N_{col}) mesophase, on the other hand, is characterized by a columnar stacking of the discotic mesogens, which, at the same time, do not form 2D structures. Therefore, the columns lack positional order, but show orientational order. Same as happens with calamitic liquid crystals with nematic mesophases, LC materials presenting discotic nematic phases can be used for display applications.

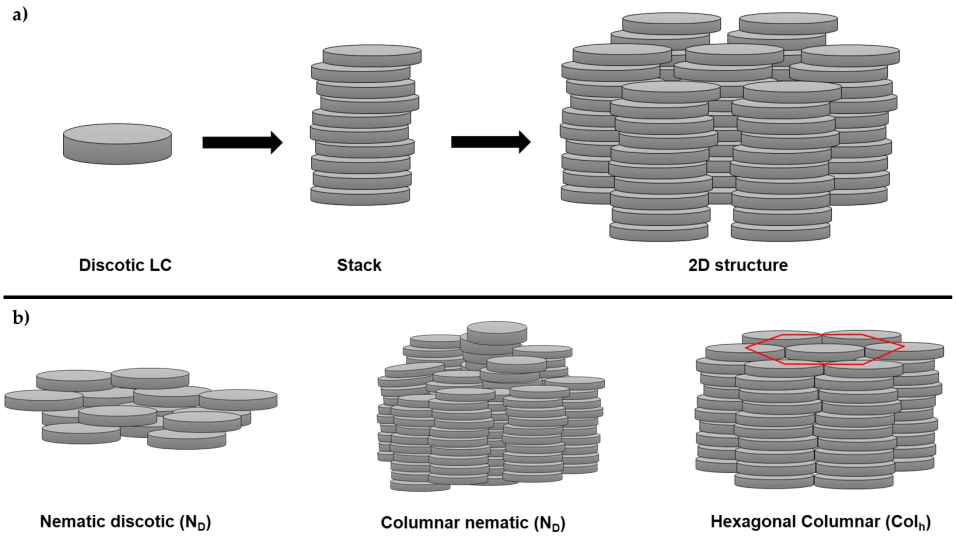

Figure 1.3. a) Example of self-assembly and self-organization of discotic liquid crystal molecules in columnar mesophases. b) Example of different mesophases presented by discotic molecules.

In this sense, Dhingra and co-workers developed a disc-like molecule based on a tri-alkynyl benzene core, which presented a nematic discotic mesophase at room temperature. The results found in this work suggest that this material proved to be advantageous as a pure deep-blue emissive component for organic light-emitting diodes (OLEDs) [72]. Moreover, disc-like molecules can be used also as solid-state solar thermal fuels (SSTF) as was demonstrated by Gupta [73]. Materials with discotic nematic mesophases were obtained through the integration of a tetra-ortho-fluoro/chloro azobenzene arm in triphenylene based LC moiety. The obtained compounds exhibited excellent photoswitching, photostability, and photocyclability for SSTF applications. The advantage of this system relies on the formation of the discotic nematic

mesophase even at sub-zero temperatures since the traditional solar panels are less efficient at sub-zero temperatures.

As commented above, discotic LC can organize in a columnar mesophase, which eventually will self-organise in various 2D lattices. 2D columnar mesophases can be classified into several classes, among which the most important are columnar hexagonal mesophase (Col_h), columnar rectangular mesophase (Col_r) and columnar lamellar mesophase (Col_L). Columnar hexagonal mesophases are characterized by a hexagonal organization of the formed columns. The planar space group for this kind of mesophase is P6/*mm*. When analysing a discotic liquid crystal compound by X-ray diffraction (XRD), at the small angle region one can easily distinct three sharp peaks whose spacings are in the ratio of 1: $1/\sqrt{3}$: 1/2, which are related to the lattice planes indexed as (1 0 0), (1 1 0) and (2 0 0), respectively, along with a broad peak in the wide-angle region [32]. Columnar rectangular mesophases are characterized by a π-π stacking of the aromatic cores of the molecules tilted with respect to the column axis and packed in a rectangular fashion. It is possible, however, to observe a crossover between a columnar rectangular mesophase to a columnar hexagonal mesophase while increasing the aliphatic side chains lengths. Finally, columnar lamellar mesophases are characterized by stacking of the discotic mesogens to form columns but, instead of presenting an organised 2D structure, the columns are arranged in layers where they can slide across the layer but do not possess translational order.

Efficient capture, transfer, and storage of solar energy represent an interesting and challenging area of research in the present day. For this purpose, in the field of discotic columnar mesophases, Mu and co-workers synthetised polymeric supramolecular columns bioinspired by the purple photosynthetic

bacteria and its natural light-harvesting [74]. Thus, a discotic molecule based on a non-planar tricyanotristyrylbenzene (TCS) was introduced to a polyacrylate backbone as pendant groups. The obtained polymeric liquid crystal exhibited a hexagonal columnar mesophase in the range of temperatures from 0 °C to 130 °C. Moreover, the columnar assembly of the material allowed some additional control over the energy transfer process. Additionally, Sharma and co-workers prepared symmetrical calix[4]pyrrole-based liquid crystals functionalized at the *para* position by urea substituents, exhibiting a hexagonal columnar mesophase at room temperature [75]. Films obtained with this material showed suitable optical energy band gap together with absorbance and extinction coefficient. The findings expressed in this work suggest the suitability of the films to implicate them as an ecofriendly optical window layer in thin films solar cells. Moreover, De and co-workers envisioned the synthesis, with a minimalistic design strategy, of a cyanovinylene-integrated pyrene-based discotic liquid crystal for solar cells applications. The obtained material exhibited a room-temperature columnar hexagonal mesophase and narrow bandgap for efficient semiconducting behaviour. Furthermore, it showed an elevated charge extraction ability from the contact electrodes at low voltage, achieving an electrical conductivity of $3.22 \cdot 10^{-4}$ S/m, which is the highest reported value for any pristine discotic LC film in a vertical charge transport device [76].

In the field of ion- conductive materials, discotic liquid crystals have aroused a great interest in the formation of electrolytes for energy storage applications due to their controllable ion channels. Notable ionic conductivity was observed for LC materials involving non-covalent two-component self-assembly interactions of salts and polar mesogenic molecules [77]. For

instance, Suwa and co-workers designed the preparation of supramolecular discotic LC with columnar mesophases driven by dipole-ion interactions [78]. In this study, they prepared self-assembled columnar structures by ion-dipole interactions between benzonitriles derivatives (N-(4-cyanophenyl)-3,4,5-tri(dodecyloxy)benzamide and 4-cyanophenyl 3,4,5-tri(dodecyloxy)benzoate) and imidazolium bromide-based ionic liquids. As it was observed during the mesomorphic characterization, benzamide-based benzonitrile did not show a liquid crystal behaviour, however when this material was combined with the imidazolium bromide-based ionic liquids it exhibited columnar mesophases as evidenced by polarized optical microscopy (POM) and X-ray diffraction (XRD). The location of the ionic liquids at the centre of the self-organized columns endows the anisotropic 1D ion-conductive properties of these materials. Ionic conductivities evaluated by electrochemical impedance spectroscopy (EIS) revealed greater conductivities for those experiments performed parallel to the column axis than to the experiments perpendicular to the column axis, which is attributed to the hindering effect of the insulating alkyl chains.

As we have seen, discotic liquid crystals can be used for a broad range of applications, from optoelectronic applications to ion-conductive materials for energy storage applications, among others. Behera and co-workers prepared a room temperature LC with columnar mesophases based on perylene-bisimides (PBIs) as a novel corrosion resistant surface film for mild steel (MS) surface [79]. The potential use of these discotic liquid crystals can be attributed to their hydrophobic nature due to the presence of aliphatic side chains and good protective coat formation on the metal surface. The obtained materials exhibited a columnar rectangular mesophase until 360 °C, including room

temperature. The elevated isotropization temperature can be correlated with the strong core-core interactions between aromatic cores. Corrosion inhibition, of the films produced with this compound, was evaluated by means of potentiodynamic and EIS at room temperature on MS in 1 M HCl. It was found to be highly effective as corrosion inhibitor, with a maximum inhibitor efficiency of 76 %.

Artificial muscles are an uprising research field in the realm of liquid crystals as we commented in the previous lyotropic liquid crystals section. Columnar materials based on discotic molecules have also aroused great interest recently in the field of artificial muscles. For example, hemiphasmidic side chain liquid crystal polymers based on a polycyclooctene as backbone and dicyanodistyrylstilbenzene (DCS) rod-like side chain mesogen linked in series to a bulky fan-like tail group, synthetized by Yang and co-workers, revealed excellent properties when evaluating its use as artificial arm [80]. These materials present a hexagonal columnar mesophase, which shows three stages, first the "frozen state", located below the glass transition temperature (T_g = 45 °C) where columnar assemblies are rigid, second the "transition zone" from T_g to 80 °C, where occurs the relaxation of the chain segment and, third the "soft state" above 80 °C where chains movements are active, and the columnar assemblies are rather supersoft. This novel hemiphasmidic side chain liquid crystal polymer with unique "breathing" motion leads to a negative thermal expansion of the columnar lattice and imitates the elongation/contraction motion of skeleton muscles. Upon heating this material to 150 °C, an elongation ratio of 118 % is observed, which is comparable to real muscle fibres (< 120%).

1.2.Liquid crystalline polymers

Liquid crystalline polymers (LCPs) gained a lot of interest after their discovery in 1923 by Vorländer [81]. Their broad range of applications, including separatory membranes, electrolytes, photoelectric conversion, and high-performance engineering plastics, among others, increases even more the already broad range of applications for non-polymeric liquid crystals. LCPs can be prepared from two different approaches; first, it is possible to attach a mesogenic moiety to a given polymer backbone as post-polymerization reaction or, second, one can directly polymerize a mesogenic monomer. Despite the used methodology to prepare these polymers, liquid crystal polymers can be classified according to the position of the mesogen. Therefore, LCPs can be classified as main-chain liquid crystal polymers (MCLCPs), when the mesogen is located at the polymer main chain, side-chain liquid crystal polymers (SCLCPs), when the mesogen is linked to the polymer backbone as a side-chain and, main-chain/side-chain liquid crystal polymers (MCSCLCPs), where the mesogens are connected as side-chain and part of the polymer main chain [82]. A schematic representation of the aforementioned types of LCP is depicted in **Figure 1.4**.

For a given SCLCP, when the mesogenic unit is rod-like, it can be linked to the main chain in two different ways, longitudinally (end-on) (**Figure 1.4. b1**)) and laterally (side-on) (**Figure 1.4. b2**)). However, it is very important for the SCLCPs to have a spacer between the polymer backbone and the mesogenic moiety. The presence of this spacer allows the interaction between mesogens leading to self-assembling structures, thus enabling the formation of

mesophases. Thanks to the flexibility introduced by the spacer, SCLCPs can form different mesophases according to the type of attached mesogen. In this way, SCLCPs with rod-like mesogens can self-assemble into nematic, smectic A (SmA), smectic C (SmC*) and cholesteric mesophases, meanwhile, thanks to the π-π interactions between the disc-like moieties SCLCPs with discotic mesogens can form columnar nematic (N_{col}), hexagonal columnar (Col_h), rectangular columnar (Col_r) and discotic nematic (N_D) mesophases.

MCSCLCPs are composed by a MCLCP with side-chain mesogens, whose side-chain mesogens can be attached directly to the mesogenic unit of the backbone or to the spacer between main-chain mesogens with or without spacers.

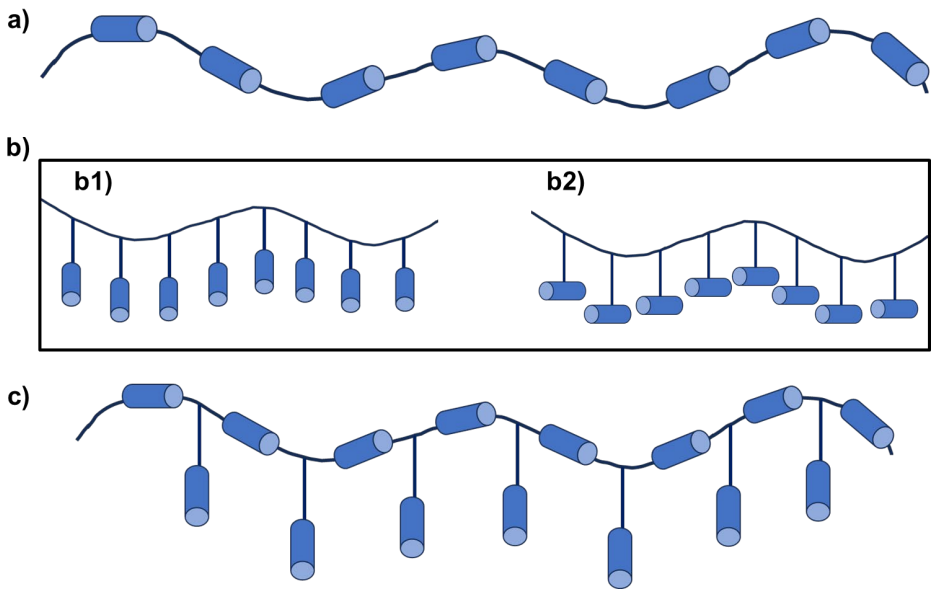

Figure 1.4. Schematic illustration of a) MCLCPs, b) SCLCPs and, c) MCSCLCPs. For the side-chain LCPs, b1) SCLCPs with longitudinally

attached rod-like mesogen and b2) SCLCPs with laterally attached rod-like mesogen. The blue cylinder is a mesogenic representative unit.

In addition to this classification, LCPs can also form LC thermosets or LC elastomers by crosslinking polymer backbones with mesogenic molecules (**Figure 1.5**). This group of LCPs can be obtained by a direct polymerization of a mesogenic monomer or by cross-linking a linear LCP via cross-linkers.

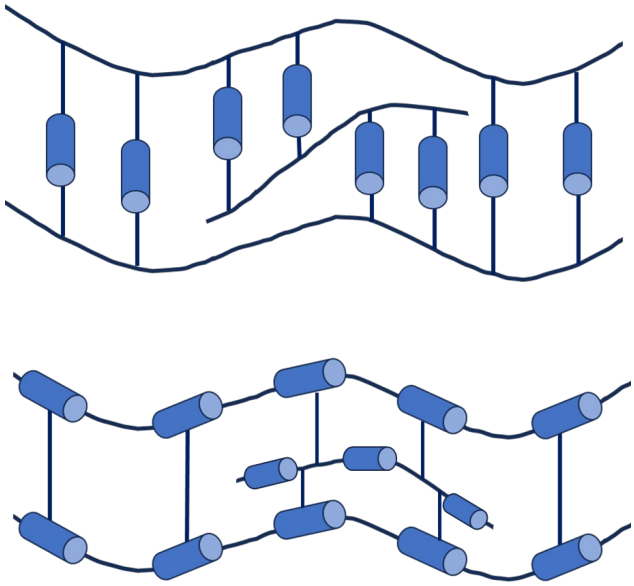

Figure 1.5. Schematic representation of a liquid crystal network.

Thus, for example, Vita and co-workers reported the evaluation of the liquid crystalline order during the curing of reactive thermotropic liquid crystal macromonomers based on phenylethynyl-terminated biphenol and naphtalenediol model units for the synthesis of LC thermosets. From their findings they suggest that curing mechanism may involve both chain extension and cross-linking, whose process do not start until 300 °C. Both

model compounds prior to the curing process exhibited nematic mesophases; however, after curing, this mesophase was no longer observed. Instead, an isotropic behaviour was observed according to polarized optical microscopy. This behaviour differs from the observed with higher molecular weight oligomeric macromonomers, where the nematic mesophase was retained upon curing. According to the authors, this fact is related to the relatively low molecular weight of the model macromonomers [83].

LC elastomers are a class of moving polymers suitable for different applications, for example, for converting external stimuli to mechanical actuations. In this sense, Pei and co-workers prepared liquid crystalline elastomers with exchangeable covalent bonds, a type of bonds used for the preparation of vitrimers. In that work they used an epoxy terminated biphenyl mesogen, and decanedioic acid as cross-linker. As result, LC elastomers can be reshaped or reprocessed at temperatures above the topology-freezing transition temperature (T_v) (below this temperature exchange reactions become extremely slow, and the material behaves as a classical covalently bonded thermoset) [84].

MCLCPs are used in several applications: for example, as fibres manufacturing, thanks to their good mechanical properties and anisotropy of the LC phases. Concerning the production of LC fibres, the most widely used MCLCP is a polyaryl amide fibre, which is also known as Kevlar (DuPont), thanks to its excellent mechanical properties. However, the LC properties of these materials are found only in solution, since they present elevated melting points, above the decomposition temperature, and a hindered mobility of the polymer chains. One strategy followed to reduce the melting temperature and improve the performance of the polymer as well as the LC properties was to

exchange the polyaryl amide core by an aromatic polyester architecture, which was further modified with the incorporation of flexible aliphatic groups at the backbone, introducing substituents to the aromatic core or changing the benzene central cores with other rigid structures (biphenylene and naphthalene groups). By doing this, a reduction of the melting point was accomplished, together with the obtention of polymers with low melt viscosity, high heat resistant temperature, high tensile strength, high modulus, and low thermal expansion [82].

More recently, following this approach, Orodepo and co-workers developed the synthesis of a series of MCLCPs carrying a biphenyl mesogen and flexible alkylene spacers in the backbone. At the same time, these polymers had attached at the polymer backbone a non-mesogenic pendant segment, such as an alkyl, polyethylene glycol (PEG) or fluoroalkyl segment. These polymers were obtained by melt polycondensation and organized in a zig-zag fashion, giving the formation of a smectic mesophase [85]. In addition, Wang and co-workers evaluated the influence of the E/Z configuration on the phase behaviour of similar biphenyl-based MCLCPs . In their work, they could conclude that Z configuration did not present a liquid crystalline mesophase, meanwhile the polymer obtained with an E configuration showed two mesophases (rectangular columnar and smectic mesophases) at different temperatures. In this particular case, MCLCPs were obtained by melt polycondensation of a biphenyl-based monomer and a tetraphenylethylene-based monomer obtaining a copolymer [86].

From side chain liquid crystal polymers, two groups of LCPs can be distinguished depending on the shape of the attached mesogenic side chain, whether rod-like or disc-like. Same as happened with low molecular weight

calamitic liquid crystal molecules, SCLCPs based on a rod-like side chain can adopt different mesophases, among which nematic and smectic (A or C) mesophases are the most common [87]. Similar to what happened with nematic phases on low molecular weight LC molecules, the addition of a chiral mesogen to a polymer main chain can induce chirality to the final LCP. As result, these LCPs can form cholesteric and smectic C mesophases [88].

Recently, with the aim to explore the research for novel smart multifunctional materials, Alaudin and co-workers proposed the synthesis of a new set of block and statistical liquid crystal copolymers based on a light-responsive mesogenic group, polar sulfonic groups, and methyl(methacrylate) (MMA) groups by using reversible addition fragmentation chain transfer (RAFT) polymerization. They performed a structural and thermal characterization as well as a study of the conductivity, revealing ionic conductivities in the range of 10^{-6} S/cm, which presents a remarkable conductivity in anhydrous conditions. The light-responsiveness and conductivity observed for these polymers opens the possibility to prepare polymer electrolytes, based on these copolymers, for energy storage and energy conversion applications [89].

Regarding the disc-like SCLCPs, self-assembling phenomena is observed same as the disc-like low molecular weight molecules commented before. A columnar organization is mostly observed for these types of polymers, thanks to the π-π interaction of the mesogenic units. The polymer main chain, the discotic mesogen, the flexible spacer and, the final aliphatic tail are key roles in the self-assembling process. Columnar organisation of SCLCPs makes them good materials to prepare membranes, where the path is only 1D governed, due to their high order and good chemical stability. Thus, for example, Bogdanowicz and co-workers, in a work carried out in our research group,

reported the synthesis of dendronized liquid crystal polymers based on a poly[2-(aziridin-1-yl)ethanol] (PAZE) modified with the dendron 3,4,5-tris[4-(n-dodecan-1-yloxy)benzyloxy]benzoate [23,29,90]. These SCLCPs were bioinspired by the tobacco mosaic virus (TMV) structure, in which its helical assembling allows the presence of an inner channel inside the tobacco mosaic virus columnar organization (**Figure 1.6**). The helix construction of the PAZE modified polymers allowed the assembling of membranes for proton transport applications, where the proton can be conducted through the membrane columnar organization thanks to the presence of basic heteroatoms (N) at the inner channel.

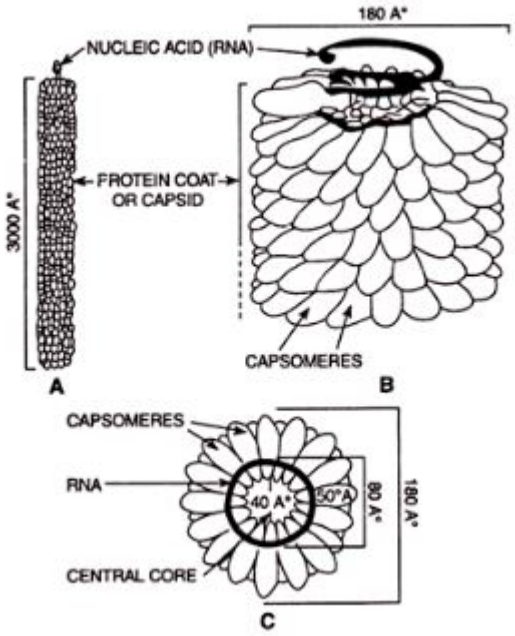

Figure 1.6. General structure of the tobacco mosaic virus.

More recently, Yang and co-workers designed the synthesis of dendritic fluorescent LCPs, with polystyrene as a main chain and tetraphenylethylene as mesogenic unit linked with different flexible alkyl spacers of 2, 4, 6, 8 or 10 methylene units. The produced LCPs exhibited columnar nematic mesophases for shorter spacers (2, 4, 6 and 8), meanwhile for longer spacers (10) showed hexagonal columnar mesophases [91]. Bi and co-workers used a similar approach when designing SCLCPs for optoelectronic applications. In this case the authors used a triphenylene mesogenic unit as monomer, in which a fluorine atom was introduced at the end of the alkoxy flexible long chain. After polymerization, the obtained LCPs exhibit hexagonal columnar mesophases [92]. This group of LC polymers and their derivatives can potentially be used as materials for optoelectronic and solar cells applications [93,94]. Thanks to its fluorescent properties, triphenylene derivatives can also be used as ink with "special" abilities. In this sense, Li and co-workers reported the preparation of a uniform colloidal dispersion based on LCP rods. In this case, the authors used triphenylene units as side chain mesogens for the preparation of different homopolymers and random copolymers with columnar structures, obtained by RAFT polymerization. The inclusion of two surfactants in this system allowed to obtain colloidal dispersions with high uniformity, regular shape, and good colloidal stability. The aforementioned "special abilities" of the ink prepared with these dispersions relies on the photo-induced fluorescent enhancement (PIFE) when irradiated with and UV lamp. As a result, a paper impregnated with this ink is not readable with the naked eye but can be read while exposed to UV light (365 nm). The finding in this work showed intriguing PIFE properties and an accompanying memory

effect, which makes these dispersions suitable for advanced colloidal inks for high-level encryption and secure delivery of paper documents [95].

1.2.1. Liquid crystalline polymer-based membranes

Since the beginning of times, biological membranes have been part of all living organisms for millennia, including the lipidic bilayer cellular membrane, the mitochondrial membrane in eukaryotic cells, liposomes and/or lysosomes, among many other examples [96]. However, the world of membranes does not end here: synthetic membranes have aroused a great interest after their large-scale industrialization since 1960s. Synthetic membranes have been extensively used in several applications such as waste-water treatment [97–101], gas separation [97,98,101,102], CO_2 capture [103], hydrogen production [104], biomedical [105–107] or polyelectrolytes[102,103,108,109], among others.

One of the challenges that have to face the research on membrane technology is the uniformity of the porous. Uniformity is a key factor for an effective separation, since the lack of uniformity endows a restriction of the molecular selectivity, thus affecting the membrane performance and its separation capability.

In order to solve this issue, nanostructured polymer membranes based on self-assembling materials are gaining a lot of interest in the recent decades; thus, liquid crystal membranes based on thermotropic liquid crystals and lyotropic liquid crystals are an emerging hot topic research field. Nevertheless, the use

of these LCPs is not unique in the formation of membranes based on liquid crystals. With this aim, it is also possible to prepare nanostructured membranes with polymerizable liquid crystals, which lately will be polymerized and cross-linked after presenting the desired organization or alignment. As a result, membranes with narrow pore sized distributions, high pore densities, control over functionality and pore sized can be prepared [110]. Thus, for instance, Suzuki and co-workers developed functional nanoporous membranes based on a photocleavable columnar LC. In this work, the authors used a taper-shaped molecule, which together with lithium triflate could adopt a column organization. Furthermore, the photocleavable moiety was composed of a *o*-nitrobenzyl ester, which was linked to the dendritic polymerizable hydrophobic part containing vinyl groups and a hydrophilic tris(oxyethylene) chain. After formation and correct alignment of the columns, the material was polymerized through acyclic diene metathesis (ADMET), thus forming a polymer membrane. Finally, the photocleavable linker was eliminated by UV irradiation resulting in the formation of ordered nanopores [111].

More recently, Lugger and co-workers prepared nanoporous films with photoswitchable absorption kinetics using a similar approach. Thus, a wedge-shaped azo derivative (4-((2,3,4-tris(undec-10-en-1-yloxy)phenyl) diazenyl) benzoic acid) formed a 3:1 columnar supramolecular complex with a tris-benzimidazolyl benzene core (TB). Upon polymerization and removal of TB, the nanoporous films is obtained. Their t*rans*-to-*cis* photoisomerization allowed the absorption of rhodamine 6G in the *cis*-enriched films. Hereby, a controlled absorption of rhodamine 6G could be modulated upon irradiation due to the isomerization of the azo moieties in the nanoporous structure [112].

1.2.1.1. Lyotropic liquid crystal polymer based-membranes

As we have seen and commented previously, lyotropic LC based materials are useful materials for the preparation of membranes for biomedical applications and drug delivery [47,48,54–56,113,114]. A significant challenge in membrane technology applications is the membrane fouling, caused mainly by proteins and other biomolecules. Lyotropic liquid crystals, have been proved to be suitable materials to address the fouling issue. For instance, Saadat and co-workers developed a thermoresponsive lyotropic liquid crystal block copolymer for potential applications such as protein purification and removal of viruses and bacteria, showing excellent anti-fouling properties [114]. Furthermore, Yue and co-workers studied the encapsulation of a dendritic antimicrobial peptide combined with gold nanoparticles into a lyotropic liquid crystal polymer for the treatment of surgical incision infections, revealing that this drug delivery system eradicated up to 99% of the bacteria in wounds while increasing significantly wound healing [113].

1.2.1.2.Thermotropic liquid crystal polymer based-membranes

Liquid crystal membranes based on thermotropic LCPs with controlled nanostructures can be formulated thanks to their self-assembling ability. Nevertheless, not all thermotropic LCPs are suitable materials to prepare LC membranes. Side chain liquid crystal polymers present unique self-

assembling characteristics that make them excellent candidates for membrane assembling. In this field, liquid crystal polymers with smectic mesophases open the possibility to use 2D conducting channels for the transport of different ionic species, since the formation of this mesophase allows the presence of 2D conducting paths. On the other hand, SCLCPs based on discotic mesogens presenting columnar mesophases endow 1D conducting paths. Both type of materials are excellent candidates to be used in ionic transport applications. For instance, SCLCPs with smectic mesophases were prepared by Zhang and co-workers, which prepared LC ionomers bearing benzoxazole-based mesogenic side chain and their membranes; these polymers presented enantiotropic smectic C mesophases [115]. In this work, the authors synthetised the heterocyclic mesogenic compound, 6-[4-(5-chloro-2-benzoxazolyl)phenoxy]-1-hexanethiol (CBPHT), as a side chain mesogen, which was grafted to commercial polyepicholorohydrin (PECH), as main chain. Membranes prepared with these materials exhibited high thermal stability, acceptable mechanical properties, and reasonably high ion conductivity. Results obtained in this work suggested the potential application of these membranes as polymer electrolyte membranes.

In a work carried out in our research group, commercial PECH was used to build up membranes with columnar structures with the aim to use them in proton transport applications such as PEMFC. Thus, PECH was modified with the dendron 3,4,5-tris[4-(n-dodecan-1-yloxy)benzyloxy] benzoate (TAPER) (**Figure 1.7a**) [22]. The obtained random copolymer exhibited a columnar hexagonal mesophase in a broad range of temperatures up to 128 °C. The main goal in this work lies in the ability of this LC polymer to self-assemble in an inner helical fashion thanks to the π-π stacking of the

neighbouring aromatic cores, thus obtaining columnar structures with an inner channel. Mimicking nature, this bioinspired construction based on the tobacco mosaic virus (**Figure 1.6**) allows the construction of channels with selectivity towards proton in front of other cations. The inner part of the columns, containing basic oxygen atoms, should be able to transport protons across the membrane thanks to the electrondonor character of oxygen, resulting in the transport of protons without the need of water. Proton transport measurements exhibited remarkable proton permeability comparable to Nafion®N117, around $2 \cdot 10^{-6}$ cm^2/s. Using a similar approach, Zare and co-workers reported the synthesis of a side-chain liquid crystal copolymer based on poly(eplichlorohydrin-*co*-ethylene oxide) (PECH-*co*-EO), as a polymer backbone, and the dendron TAPER as a side chain, obtaining degrees of modification of the epichlorohydrin unit of 20 and 40 % (**Figure 1.7b**) [24,28]. Cation transport capability of these membranes was evaluated by means of proton permeability and linear sweep voltammetry (LSV) for different monovalent cations such as H^+, Na^+, K^+ and Li^+. Proton permeability tests evaluates the transport of cationic species in both directions at the same time for a given two compartment cell (**Figure 1.8a**) in order to confirm the antiport transport mechanism. LSV evaluates the transport of a single cationic species in one direction, driven by a difference of potential (**Figure 1.8b**). Dendronized PECH-*co*-EO membranes evidenced the transport of H^+, Na^+ and Li^+ in the permeability tests, meanwhile the transport of K^+ was not noticed. The authors suggested that the size of the potassium cation was too large to permeate. LSV measurements exhibited remarkable proton transport while presenting slightly high selectivity of the proton in front of the other studied monovalent cations [28]. In order to elucidate how the polymer interacts with

the cation during ion transport using this system (dendronized PECH-*co*-EO), Bogdanowicz and co-workers used in-situ Raman spectroscopy to evaluate the transport phenomena. To carry out these experiments they used a low modified LC polyether (36 % modification degree) as model compound, using joined chronoamperometry and Raman spectroscopy. For the transport experiments the authors used proton and sodium cations as model cationic species. In case of proton transport, it was found that the polyether backbone was mainly involved in the cation conductivity, since a change in the intensity of the band at 2870 cm^{-1} was noticed. Nevertheless, an additional coordination site was also observed, coming from the lateral oxygen of the carbonyl linker group. This extra coordination site was evidenced thanks to a change of the intensity of the band centred at 1250 cm^{-1}. Furthermore, the presence of water inside the system was proved not to influence the cation transport across the membrane [116].

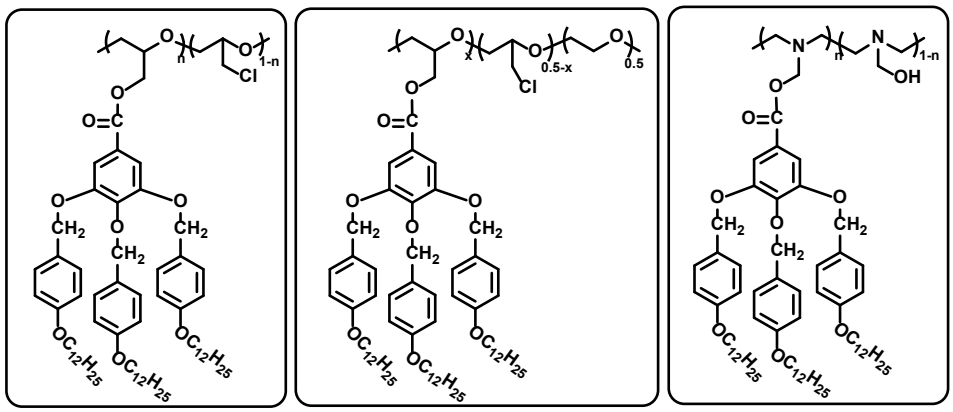

Figure 1.7. Chemical structure of SCLCPs modified with the dendron 3,4,5-tris[4-(n-dodecan-1-yloxy)benzyloxy]benzoate. According to the backbone: a) PECH, b) PECH-co-EO and c) PAZE

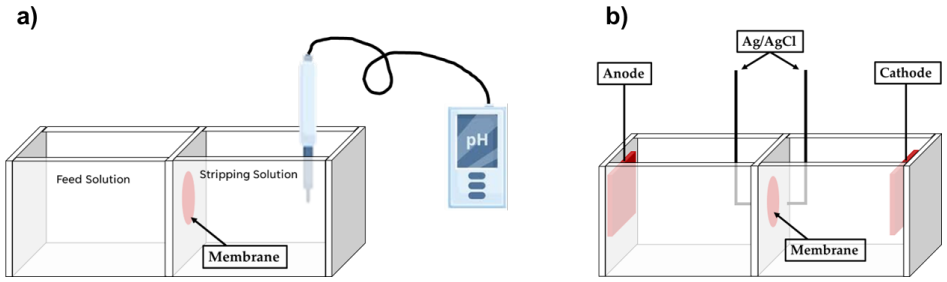

Figure 1.8. Experimental set-up of a) permeability tests and b) linear sweep voltammetry.

On the other hand, Ŝakalytė and co-workers prepared a family of polyamines, based on poly[2-(aziridin-1-yl)ethanol] (PAZE) (**Figure 1.7c**), modified with the same dendron, with the aim to improve the proton conductivity due to the higher basic character of nitrogen atoms on the main chain [21,30]. A family with different degrees of modification was prepared, from 16 to 100 % (all of them presenting columnar mesophases). Bogdanowicz and co-workers used these polyamines to try to prepare ion-conducting membranes [23,29]. Nevertheless, the assembling of self-standing membranes was nearly impossible, since they presented brittleness, resulting in poor mechanical properties. In order to solve this drawback, an anodized aluminium oxide (AAO) support was used to improve the mechanical resistance of the membrane.

As aforementioned, an advantage of these materials is their ability to build up columnar structures, however this organization is not always well oriented. In other words, these columnar structures are often randomly oriented. One of the goals of this work was to homeotropically orient the polymer columns in order to obtain 1D parallel channels perpendicular to the membrane surface, thus obtaining effective conductive paths. The use of a natural

oriented support like AAO, that presents a natural honeycomb like structure, should help the orientation of the polymer columns and also the mechanical resistance, as mentioned. The hybrid membranes prepared with this support showed columnar mesophases, and some of them hexagonal columnar mesophases as was evidenced by X-ray diffraction [23]. Transport properties evaluated with LSV revealed remarkable proton transport when compared to Nafion®117, and outstanding selectivity of the proton in front of other monovalent cations (Na^+, K^+ and Li^+). Permeability tests evidenced the same behaviour observed for the dendronized PECH-*co*-EO membranes: antiport transport mechanism was confirmed for H^+, Na^+ and Li^+, meanwhile no conductivity was denoted for K^+ [29].

PAZE-based copolymers exhibit a strong tendency to crystallize, mostly due to the tendency to stablish hydrogen bonding. This trend is independent on the degree of modification: it was observed from a low degree of modification to 100% modified polymers. This makes the polymers difficult to be oriented and confers them brittleness. To overcome these drawbacks, Montané and co-workers explored the preparation of PAZE modified copolymers with both benzoyl groups and TAPER, since this was expected to inhibit the crystallization tendency of the LCP [26]. It was found that the presence of the benzoyl group reduces the clearing temperature of the system, nonetheless, hexagonal columnar mesophases were observed. Homeotropically oriented membranes were prepared as was evidenced by X-ray diffraction. LSV data revealed worse selectivity capability of these membranes than the previously reported PAZE-based membranes. Nevertheless, those membranes were reported to be easier to prepare, cheaper, to posses' high thermal stability and were not brittle [27].

As we have seen, all these TAPER-containing SCLCPs were obtained from a post-polymerization procedure involving the modification of commercial polyethers (PECH and PECH-*co*-EO) or synthetised polyamines (PAZE) with the dendronized mesogen TAPER. As a result, SCLCPs with different modification degree were obtained, achieving degrees of modification up to 100 % for PAZE and 72 % for PECH modified polymers. With this methodology copolymers were always obtained, except for 100 % modified PAZE, where a homopolymer was obtained; however, this polymer revealed a strong tendency to crystallize (probably due to its high symmetry) and low ability to form films.

With the aim to obtain dendronized side-chain LC homopolymers, Ŝakalytė and co-workers synthetized an aziridine dendronized monomer [30]. Polymerization of this tapered monomer, however, resulted unsuccessful since the cleavage of the benzyl ether linkage took place while an effective polymerisation did not occur.

1.3.Objectives

1.3.1. Goals of the thesis

The overall purpose of this doctoral thesis is the design and development of ion conductive membranes based on liquid crystalline poly(2-oxazoline)s, together with the development of hybrid membranes based on a dendronized polyether and bio-based supports for fuel cell applications. Specific objectives can be summarized as follows:

- Synthesis and characterization of a dendritic 2-oxazoline monomer (2-(3,4,5-tris(4-dodecyloxybenzyloxy)phenyl)-2-oxazoline, TAPOx) and its tapered amide precursor (N-(2-hydroxyethyl)-3,4,5-tris(4-dodecyloxybenzyloxy)benzamide, TAPAm).
- Synthesis and characterization of a family of poly(2-oxazoline)s: poly(2-(3,4,5-tris(4-dodecyloxybenzyloxy)phenyl)-2-oxazoline)s (PTOx). These syntheses will be carried out by cationic ring opening polymerization of the previously synthesized TAPOx monomer.
- Preparation and characterization of novel ion conducting membranes derived from the previously synthetised poly(2-oxazoline)s and assessment of their transport properties.
- Design and assembly of hybrid membranes based on dendronized poly(epichlorhydrin) using bio-based wood supports for ion transport applications.

- Characterization of the previously assembled membranes and evaluation of their transport properties.

The main hypothesis which reinforces the objectives are:

- The preparation of side-chain liquid crystalline poly(2-oxazoline)s with tapered side dendrons should induce the formation of columnar mesophases thanks to the supramolecular interactions between the aromatic cores.
- The formation of columnar mesophases would favour the formation of inner channels as ion-conductive pathways. The presence of electron-donor atoms like nitrogen or oxygen should favours the interaction with proton or other cations.
- The natural hierarchical organization of the wood pores in beech wood discs should influence the orientation of the polymer columns to achieve a homeotropical orientation of the dendronized polymer once it has been introduced into the wooden discs.
- Hydroxyl groups of hemicellulose and cellulose that constitute wood should hinder the correct infiltration of the polymer into the wood support. The functionalization of wood to obtain highly hydrophobic wood supports should favour the diffusion of the polymer inside the support.

1.4.References

[1] M. Höök, J. Li, K. Johansson, S. Snowden, Growth Rates of Global Energy Systems and Future Outlooks, Natural Resources Research 21 (2012) 23–41. https://doi.org/10.1007/s11053-011-9162-0.

[2] V. Wittmann, D. Meissner, The nexus of global challenges and global studies: a trans-disciplinary global sustainability science curriculum, Discover Sustainability 5 (2024) 43. https://doi.org/10.1007/s43621-024-00220-7.

[3] D. Kweku, O. Bismark, A. Maxwell, K. Desmond, K. Danso, E. Oti-Mensah, A. Quachie, B. Adormaa, Greenhouse Effect: Greenhouse Gases and Their Impact on Global Warming, J Sci Res Rep 17 (2018) 1–9. https://doi.org/10.9734/jsrr/2017/39630.

[4] V. Ramanathan, Y. Feng, Air pollution, greenhouse gases and climate change: Global and regional perspectives, Atmos Environ 43 (2009) 37–50. https://doi.org/10.1016/j.atmosenv.2008.09.063.

[5] B. Tranter, K. Booth, Scepticism in a changing climate: A cross-national study, Global Environmental Change 33 (2015) 154–164. https://doi.org/10.1016/j.gloenvcha.2015.05.003.

[6] Y.-L. Hsieh, S.-C. Yeh, The trends of major issues connecting climate change and the sustainable development goals, Discover Sustainability 5 (2024) 31. https://doi.org/10.1007/s43621-024-00183-9.

[7] K. Running, World Citizenship and Concern for Global Warming: Building the Case for a Strong International Civil Society, Social Forces 92 (2013) 377–399. https://doi.org/10.1093/sf/sot077.

[8] O. Deschênes, E. Moretti, Extreme Weather Events, Mortality, and Migration, Review of Economics and Statistics 91 (2009) 659–681. https://doi.org/10.1162/rest.91.4.659.

[9] S.S. Jatav, Farmers' perception of climate change and livelihood vulnerability: a comparative study of Bundelkhand and Central regions of Uttar Pradesh, India, Discover Sustainability 5 (2024) 11. https://doi.org/10.1007/s43621-024-00193-7.

[10] H.N. Chuong, T.T. Loc, T.L.T. Tuyen, B.H. Ngoc, Livelihood transitions in rural Vietnam under climate change effects in the period of 2008–2018, Discover Sustainability 5 (2024). https://doi.org/10.1007/s43621-023-00178-y.

[11] I. Idawati, N.A. Sasongko, A.D. Santoso, M. Septiani, T. Handayani, A.Y.N. Sakti, B.D. Purnamasari, Cocoa farmers' characteristics on climate variability and its effects on climate change adaptation strategy, Global Journal of Environmental Science and Management 10 (2024) 337–354. https://doi.org/10.22034/gjesm.2024.01.21.

[12] N.N. Dalei, A. Gupta, Adoption of renewable energy to phase down fossil fuel energy consumption and mitigate territorial emissions: evidence from BRICS group countries using panel FGLS and panel GEE models, Discover Sustainability 5 (2024) 52. https://doi.org/10.1007/s43621-024-00237-y.

[13] O.Z. Sharaf, M.F. Orhan, An overview of fuel cell technology: Fundamentals and applications, Renewable and Sustainable Energy Reviews 32 (2014) 810–853. https://doi.org/10.1016/j.rser.2014.01.012.

[14] N.W. Deluca, Y.A. Elabd, Polymer electrolyte membranes for the direct methanol fuel cell: A review, J Polym Sci B Polym Phys 44 (2006) 2201–2225. https://doi.org/10.1002/polb.20861.

[15] M.A. Aminudin, S.K. Kamarudin, B.H. Lim, E.H. Majilan, M.S. Masdar, N. Shaari, An overview: Current progress on hydrogen fuel cell vehicles, Int J Hydrogen Energy 48 (2023) 4371–4388. https://doi.org/10.1016/j.ijhydene.2022.10.156.

[16] H. Zhang, P.K. Shen, Recent development of polymer electrolyte membranes for fuel cells, Chem Rev 112 (2012) 2780–2832. https://doi.org/10.1021/cr200035s.

[17] T. Kato, M. Yoshio, T. Ichikawa, B. Soberats, H. Ohno, M. Funahashi, Transport of ions and electrons in nanostructured liquid crystals, Nat Rev Mater 2 (2017). https://doi.org/10.1038/natrevmats.2017.1.

[18] Z.Z. Nie, B. Zuo, L. Liu, M. Wang, S. Huang, X.M. Chen, H. Yang, Nanoporous Supramolecular Liquid Crystal Polymeric Material for Specific and Selective Uptake of Melamine, Macromolecules 53 (2020) 4204–4213. https://doi.org/10.1021/acs.macromol.0c00322.

[19] R.J. Carlton, J.T. Hunter, D.S. Miller, R. Abbasi, P.C. Mushenheim, L.N. Tan, N.L. Abbott, Chemical and biological sensing using liquid crystals, Liq Cryst Rev 1 (2013) 29–51. https://doi.org/10.1080/21680396.2013.769310.

[20] B.R. Kaafarani, Discotic liquid crystals for opto-electronic applications, Chemistry of Materials 23 (2011) 378–396. https://doi.org/10.1021/cm102117c.

[21] A. Šakalyte, J.A. Reina, M. Giamberini, Liquid crystalline polyamines containing side dendrons: Toward the building of ion channels based on polyamines, Polymer (Guildf) 54 (2013) 5133–5140. https://doi.org/10.1016/j.polymer.2013.07.027.

[22] B. Tylkowski, N. Castelao, M. Giamberini, R. Garcia-Valls, J.A. Reina, T. Gumí, The importance of orientation in proton transport of a polymer film based on an oriented self-organized columnar liquid-crystalline polyether, Materials Science and Engineering C 32 (2012) 105–111. https://doi.org/10.1016/j.msec.2011.10.003.

[23] K.A. Bogdanowicz, G.A. Rapsilber, J.A. Reina, M. Giamberini, Liquid crystalline polymeric wires for selective proton transport, part 1: Wires preparation, Polymer (Guildf) 92 (2016) 50–57. https://doi.org/10.1016/j.polymer.2016.03.073.

[24] A. Zare, B. Pascual-Jose, S. De la Flor, A. Ribes-Greus, X. Montané, J.A. Reina, M. Giamberini, Membranes for cation transport based on dendronized poly(Epichlorohydrin-co-ethylene oxide). part 1: The effect of dendron amount and column orientation on copolymer mobility, Polymers (Basel) 13 (2021). https://doi.org/10.3390/polym13203532.

[25] K.A. Bogdanowicz, S. V. Bhosale, Y. Li, I.F.J. Vankelecom, R. Garcia-Valls, J.A. Reina, M. Giamberini, Mimicking nature: Biomimetic ionic channels, J Memb Sci 509 (2016) 10–18. https://doi.org/10.1016/j.memsci.2016.02.038.

[26] X. Montané, K.A. Bogdanowicz, G. Colace, J.A. Reina, P. Cerruti, A. Lederer, M. Giamberini, Advances in the design of self-supported ion-conducting membranes-new family of columnar liquid crystalline polyamines. Part 1: Copolymer synthesis and membrane preparation, Polymer (Guildf) 105 (2016) 298–309. https://doi.org/10.1016/j.polymer.2016.10.047.

[27] X. Montané, K.A. Bogdanowicz, J. Prats-Reig, G. Colace, J.A. Reina, M. Giamberini, Advances in the design of self-supported ion-conducting membranes – New family of columnar liquid crystalline polyamines. Part 2: Ion transport characterisation and comparison to hybrid membranes, Polymer (Guildf) 105 (2016) 234–242. https://doi.org/10.1016/j.polymer.2016.10.046.

[28] A. Zare, X. Montané, J.A. Reina, M. Giamberini, Membranes for cation transport based on dendronized poly(Epichlorohydrin-co-ethylene oxide). part 2: Membrane characterization and transport properties, Polymers (Basel) 13 (2021). https://doi.org/10.3390/polym13223915.

[29] K.A. Bogdanowicz, P. Sistat, J.A. Reina, M. Giamberini, Liquid crystalline polymeric wires for selective proton transport, part 2: Ion transport in solid-state, Polymer (Guildf) 92 (2016) 58–65. https://doi.org/10.1016/j.polymer.2016.03.080.

[30] A. Šakalyte, M. Giamberini, J.A. Reina, Synthesis and characterisation of a monotropic dendritic liquid crystalline aziridine monomer, Liq Cryst 41 (2014) 153–162. https://doi.org/10.1080/02678292.2013.845309.

[31] J. Guardià, A. Zare, J. Eleeza, M. Giamberini, J.A. Reina, X. Montané, Synthesis and characterization of dendritic compounds containing nitrogen: monomer precursors in the construction of biomimetic membranes, Sci Rep 12 (2022). https://doi.org/10.1038/s41598-022-05747-1.

[32] J. Guardià, M. Giamberini, J.A. Reina, X. Montané, Synthesis and Characterization of Dendronized Side Chain Liquid Crystalline Poly(2-oxazoline)s towards Biomimetic Ion Channels, Eur Polym J (2023) 112273. https://doi.org/10.1016/j.eurpolymj.2023.112273.

[33] X. Montané, S.V. Bhosale, J.A. Reina, M. Giamberini, Columnar liquid crystalline polyglycidol derivatives: A novel alternative for proton-conducting membranes, Polymer (Guildf) 66 (2015) 100–109. https://doi.org/10.1016/j.polymer.2015.03.071.

[34] M. Giamberini, J.C. Ronda, J.A. Reina, Poly(epichlorohydrin) modified with 3,4,5-tris(dodecyloxy)benzoate: The structure and dynamics of the aliphatic side chains in the columnar mesophase, J Polym Sci A Polym Chem 43 (2005) 2099–2111. https://doi.org/10.1002/pola.20680.

[35] S.V. Bhosale, M.A. Rasool, J.A. Reina, M. Giamberini, New liquid crystalline columnar poly(epichlorohydrin-co-ethylene oxide) derivatives

leading to biomimetic ion channels, Polym Eng Sci 53 (2013) 159–167. https://doi.org/10.1002/pen.23240.

[36] M. Giamberini, J.A. Reina, J.C. Ronda, Influence of the side group shape on the arrangement of liquid-crystalline polyethers obtained by ring opening polymerization of oxiranes, J Polym Sci A Polym Chem 44 (2006) 1722–1733. https://doi.org/10.1002/pola.21280.

[37] V. Percec, M.N. Holerca, S.N. Magonov, D.J.P. Yeardley, G. Ungar, H. Duan, S.D. Hudson, Poly(oxazolines)s with tapered minidendritic side groups. The simplest cylindrical models to investigate the formation of two-dimensional and three-dimensional order by direct visualization, Biomacromolecules 2 (2001) 706–728. https://doi.org/10.1021/bm015550j.

[38] A. Rapp, I. Schnell, D. Sebastiani, S.P. Brown, V. Percec, H.W. Spiess, Supramolecular Assembly of Dendritic Polymers Elucidated by 1 H and 13 C Solid-State MAS NMR Spectroscopy, J Am Chem Soc 125 (2003) 13284–13297. https://doi.org/10.1021/ja035127d.

[39] V. Percec, M. Glodde, T.K. Bera, Y. Miura, I. Shiyanovskaya, K.D. Singer, V.S.K. Balagurusamy, P.A. Heiney, I. Schnell, A. Rapp, H.W. Spiess, S.D. Hudsonk, H. Duan, Self-organization of supramolecular helical dendrimers into complex electronic materials, Nature 417 (2002) 384–387. https://doi.org/10.1038/nature01072.

[40] R. Zhang, Z. Zhang, J. Han, L. Yang, J. li, Z. Song, T. Wang, J. Zhu, Advanced liquid crystal-based switchable optical devices for light protection applications: principles and strategies, Light Sci Appl 12 (2023). https://doi.org/10.1038/s41377-022-01032-y.

[41] A. Surampudi, G. Zhang, R. Singh, G. Faulkner, D.C. O'Brien, M.J. Booth, S.M. Morris, Liquid Crystals for Luminescent Concentrators: A Review, Crystals (Basel) 13 (2023). https://doi.org/10.3390/cryst13121615.

[42] Y. Choi, D. Choi, J.K. Choi, K.S. Oh, E. Cho, J.H. Im, D.P. Singh, Y.K. Kim, Stimuli-Responsive Materials from Liquid Crystals, ACS Applied Optical Materials 1 (2023) 1879–1897. https://doi.org/10.1021/acsaom.3c00282.

[43] M. Tsuei, M. Shivrayan, Y.K. Kim, S. Thayumanavan, N.L. Abbott, Optical "blinking" Triggered by Collisions of Single Supramolecular Assemblies of Amphiphilic Molecules with Interfaces of Liquid Crystals, J Am Chem Soc 142 (2020) 6139–6148. https://doi.org/10.1021/jacs.9b13360.

[44] Y.K. Kim, Y. Huang, M. Tsuei, X. Wang, N.C. Gianneschi, N.L. Abbott, Multi-Scale Responses of Liquid Crystals Triggered by Interfacial Assemblies of Cleavable Homopolymers, ChemPhysChem 19 (2018) 2037–2045. https://doi.org/10.1002/cphc.201800106.

[45] H. Shi, Y. Deng, Y. Shi, Cellulose-Based Stimuli-Responsive Anisotropic Hydrogel for Sensor Applications, ACS Appl Nano Mater 6 (2023) 11524–11530. https://doi.org/10.1021/acsanm.3c01551.

[46] D. Devadiga, A. Tantri Nagaraja, D. Devadiga, M. Selvakumar, Minireview and Perspectives of Liquid Crystals in Perovskite Solar Cells, Energy and Fuels 38 (2024) 854–868. https://doi.org/10.1021/acs.energyfuels.3c04050.

[47] V.P. Chavda, S. Dyawanapelly, S. Dawre, I. Ferreira-Faria, R. Bezbaruah, N. Rani Gogoi, P. Kolimi, D.J. Dave, A.C. Paiva-Santos, L.K. Vora, Lyotropic liquid crystalline phases: Drug delivery and biomedical applications, Int J Pharm 647 (2023). https://doi.org/10.1016/j.ijpharm.2023.123546.

[48] M. Chountoulesi, S. Pispas, I.K. Tseti, C. Demetzos, Lyotropic Liquid Crystalline Nanostructures as Drug Delivery Systems and Vaccine Platforms, Pharmaceuticals 15 (2022). https://doi.org/10.3390/ph15040429.

[49] M. Zatloukalova, L. Poltorak, R. Bilewicz, J. Vacek, Lipid-based liquid crystalline materials in electrochemical sensing and nanocarrier technology, Microchimica Acta 190 (2023). https://doi.org/10.1007/s00604-023-05727-w.

[50] A. Akram, T.G. Shahzady, S. Hussain, N.A. Saad, M.T. Islam, M. Ikram, Liquid Crystal Polymers: Overview of Characteristics and Applications in Communication and Biomedical Technologies, Russian Journal of Applied Chemistry 94 (2021) 1585–1593. https://doi.org/10.1134/S107042722112003X.

[51] D.L. Gin, C.S. Pecinovsky, J.E. Bara, R.L. Kerr, Functional lyotropic liquid crystal materials, Struct Bond 128 (2007) 181–222. https://doi.org/10.1007/430_2007_064.

[52] R. Mezzenga, J.M. Seddon, C.J. Drummond, B.J. Boyd, G.E. Schröder-Turk, L. Sagalowicz, Nature-Inspired Design and Application of Lipidic Lyotropic Liquid Crystals, Advanced Materials 31 (2019). https://doi.org/10.1002/adma.201900818.

[53] I. Dierking, A.M.F. Neto, Novel trends in lyotropic liquid crystals, Crystals (Basel) 10 (2020) 1–24. https://doi.org/10.3390/cryst10070604.

[54] A. Stepulane, K. Ahlgren, A. Rodriguez-Palomo, A.K. Rajasekharan, M. Andersson, Lyotropic liquid crystal elastomers for drug delivery, Colloids Surf B Biointerfaces 226 (2023). https://doi.org/10.1016/j.colsurfb.2023.113304.

[55] V.P. Chavda, G. Jogi, A.C. Paiva-Santos, A. Kaushik, Biodegradable and removable implants for controlled drug delivery and release application, Expert Opin Drug Deliv 19 (2022) 1177–1181. https://doi.org/10.1080/17425247.2022.2110065.

[56] X. Wu, D. Cheng, Y. Lu, R. Rong, Y. Kong, X. Wang, B. Niu, A liquid crystal in situ gel based on rotigotine for the treatment of Parkinson's disease, Drug Deliv Transl Res 14 (2024) 1048–1062. https://doi.org/10.1007/s13346-023-01449-x.

[57] Y. Cen, H. Wang, P. Wen, G. Xu, F. Tian, F. Bian, X. Zeng, The development of an artificial skin membrane mimicking the lipid bilayer structure for in vitro permeation study, Colloids Surf A Physicochem Eng Asp 642 (2022). https://doi.org/10.1016/j.colsurfa.2022.128609.

[58] O.U. Araz, E. Kemiklioglu, B. Gurboga, Modeling of the lyotropic cholesteric liquid crystal based toxic gas sensor using adaptive neuro-fuzzy inference systems, Expert Syst Appl 240 (2024). https://doi.org/10.1016/j.eswa.2023.122326.

[59] Y. Guo, H. Li, J. Li, X. Zeng, Stable graphene oxide-based lyotropic liquid crystals for interfacial lubrication, Friction 12 (2024) 954–967. https://doi.org/10.1007/s40544-023-0813-z.

[60] Y. Gao, J. Liu, S. Yang, Liquid crystalline reduced graphene oxide composite fibers as artificial muscles, Materials Today 69 (2023) 19–30. https://doi.org/10.1016/j.mattod.2023.08.003.

[61] X. Wu, C. Xu, Z. Zhang, Preparation and optimization of Si3N4 ceramic slurry for low-cost LCD mask stereolithography, Ceram Int 47 (2021) 9400–9408. https://doi.org/10.1016/j.ceramint.2020.12.072.

[62] X. Gong, G.Q. Lv, J.J. Li, Z.A. Hu, Z. Wang, Q. Bin Feng, Analyzing the effect of temperature on optical performance of dual-layer liquid crystal displays, J Soc Inf Disp 29 (2021) 537–546. https://doi.org/10.1002/jsid.996.

[63] E.R. da Silva, A.R.C. Hinojosa, J. Eccher, M.D. Tonet, D. Brondani, E. Zapp, S.F. Curcio, B.B. Postacchini, T. Cazati, A.A. Vieira, Strongly luminescent and liquid-crystalline π-conjugated 2-methyl[1,2,3]benzotriazoles with a linear donor-acceptor-donor structure, J Mol Liq 314 (2020). https://doi.org/10.1016/j.molliq.2020.113616.

[64] E.P. Pozhidaev, S.I. Torgova, E.M. Budynina, T.P. Tkachenko, A. V. Kuznetsov, V.A. Barbashov, Ferroelectric Smectic c* Phase with Sub-Wavelength Helix Pitch Induced in a Nematic Liquid Crystal by Chiral Non-Mesogenic Dopants, Zhidkie Kristally i Ikh Prakticheskoe Ispol'zovanie 20 (2020) 26–33. https://doi.org/10.18083/LCAppl.2020.3.26.

[65] E.P. Pozhidaev, E.M. Budynina, A. V. Kuznetsov, S.I. Torgova, T.P. Tkachenko, V.A. Barbashov, Short helix pitch ferroelectric liquid crystals induced in nematic matrix by chiral non-mesogenic dopants, J Mol Liq 391 (2023). https://doi.org/10.1016/j.molliq.2023.123351.

[66] N. Pote, S. Hinge, P. Ganguly, A. Banpurkar, Improvement of optical properties and memory effect in ferroelectric liquid crystal by incorporating core/shell CoFe2O4/ZnO nanocrystals, Journal of Materials Science: Materials in Electronics 35 (2024). https://doi.org/10.1007/s10854-024-12039-z.

[67] D. Węgłowska, Y. Chen, F. Ladouceur, L. Silvestri, R. Węgłowski, M. Czerwiński, Single ferroelectric liquid crystal compounds targeted for optical voltage sensing, J Mol Liq 399 (2024). https://doi.org/10.1016/j.molliq.2024.124454.

[68] J. Tang, Z. Li, M. Xie, Y. Luo, J. Yu, G. Chen, Z. Chen, Liquid Crystal Based Label-Free Optical Sensors for Biochemical Application, Photonic Sensors 14 (2024). https://doi.org/10.1007/s13320-024-0707-3.

[69] P.C. Wu, C.P. Pai, M.J. Lee, W. Lee, A single-substrate biosensor with spin-coated liquid crystal film for simple, sensitive and label-free protein detection, Biosensors (Basel) 11 (2021). https://doi.org/10.3390/bios11100374.

[70] I. Carrasco, P. Ehni, M. Ebert, N. Dumait, G. Taupier, M. Amela-Cortes, C. Roiland, S. Cordier, J.A. Knöller, E. Jacques, S. Laschat, Y. Molard, Game of Crowns: Na+ Is Coming! Red NIR-Emissive Hybrid Liquid Crystals Containing Discotic Crown Ethers and Na2Mo6X8iCl6 (Xi = Cl or Br), ACS Appl Mater Interfaces 15 (2023) 39752–39764. https://doi.org/10.1021/acsami.3c08441.

[71] M. Lambov, N. Hensiek, A.C. Pöppler, M. Lehmann, Columnar Liquid Crystals from Star-Shaped Conjugated Mesogens as Nano-Reservoirs for Small Acceptors, Chempluschem 85 (2020) 2219–2229. https://doi.org/10.1002/cplu.202000341.

[72] S. Dhingra, F.R. Chen, I. Siddiqui, S.P. Gupta, C.W. Wang, J.H. Jou, S.K. Pal, Room temperature tri-alkynyl benzene based discotic nematic mesophase enabling high-efficiency deep blue OLEDs, J Mol Liq 390 (2023). https://doi.org/10.1016/j.molliq.2023.122984.

[73] M. Gupta, Ashy, Solar Thermal Energy Storage Systems Based on Discotic Nematic Liquid Crystals That Can Efficiently Charge and Discharge below 0 °C, Adv Energy Mater (2024). https://doi.org/10.1002/aenm.202303845.

[74] B. Mu, X. Hao, X. Luo, Z. Yang, H. Lu, W. Tian, Bioinspired polymeric supramolecular columns as efficient yet controllable artificial light-harvesting platform, Nat Commun 15 (2024). https://doi.org/10.1038/s41467-024-45252-9.

[75] V.S. Sharma, A.S. Sharma, S.L. Rathod, H.A. Mali, D. Suthar, M.S. Dhaka, P.S. Shrivastav, A New Conformationally Symmetrical Calix[4]pyrrole Based Supramolecular System for Liquid Crystalline and Window Layer Solar Cell Applications, ChemPhysChem 24 (2023). https://doi.org/10.1002/cphc.202200760.

[76] R. De, M. Maity, A. Joseph, S.P. Gupta, Y. Nailwal, M.A.G. Namboothiry, S.K. Pal, High Electrical Conductivity and Hole Transport in an Insightfully Engineered Columnar Liquid Crystal for Solution-Processable Nanoelectronics, Small (2024). https://doi.org/10.1002/smll.202308983.

[77] C. Liu, S. Cao, M. Yoshio, Ion-Conducting Non-Flammable Liquid Crystal–Polymer Composites for High-Frequency Soft Actuators, Adv Funct Mater 33 (2023). https://doi.org/10.1002/adfm.202300538.

[78] S. Suwa, C. Liu, M. Yoshio, Anisotropic ion-conductive supramolecular columnar liquid crystals composed of a benzonitrile derivative and ionic liquids, Mater Today Chem 34 (2023). https://doi.org/10.1016/j.mtchem.2023.101829.

[79] P.K. Behera, S. Rao, L.T. Popoola, S.A. Swamirayachar, M.G.K. AlFalah, F. Kandemirli, S. Kodange, G.K. Prashanth, A.S. Achalkumar, Room Temperature Columnar Liquid Crystalline Perylene Bisimide as a Novel

Corrosion Resistant Surface Film for Mild Steel Surface, J Bio Tribocorros 9 (2023). https://doi.org/10.1007/s40735-022-00735-4.

[80] Z. Yang, J. Li, X. Chen, Y. Fan, J. Huang, H. Yu, S. Yang, E.Q. Chen, Precisely Controllable Artificial Muscle with Continuous Morphing based on "Breathing" of Supramolecular Columns, Advanced Materials 35 (2023). https://doi.org/10.1002/adma.202211648.

[81] D. Demus, One century liquid crystal chemistry: From Vorländer's rods to disks, stars and dendrites, Molecular Crystals and Liquid Crystals Science and Technology Section A: Molecular Crystals and Liquid Crystals 364 (2001) 25–91. https://doi.org/10.1080/10587250108024978.

[82] X. Lyu, A. Xiao, D. Shi, Y. Li, Z. Shen, E.Q. Chen, S. Zheng, X.H. Fan, Q.F. Zhou, Liquid crystalline polymers: Discovery, development, and the future, Polymer (Guildf) 202 (2020). https://doi.org/10.1016/j.polymer.2020.122740.

[83] F. Vita, F.C. Adamo, M. Pisani, L.M. Heist, M. Li, M. Hegde, T.J. Dingemans, E.T. Samulski, O. Francescangeli, Liquid crystal thermosets. A new class of high-performance materials, Liq Cryst 47 (2020) 2016–2026. https://doi.org/10.1080/02678292.2019.1641233.

[84] Z. Pei, Y. Yang, Q. Chen, E.M. Terentjev, Y. Wei, Y. Ji, Mouldable liquid-crystalline elastomer actuators with exchangeable covalent bonds, Nat Mater 13 (2014) 36–41. https://doi.org/10.1038/nmat3812.

[85] G.O. Orodepo, E.B. Gowd, S. Ramakrishnan, Main-chain liquid crystalline polymers bearing periodically grafted folding elements, Polym Chem 12 (2021) 1050–1059. https://doi.org/10.1039/d0py01661f.

[86] J. Wang, Q. Jiang, S. Cao, C. Sun, Y. Zhang, Y. Qiu, H. Wang, G. Yin, Y. Liao, X. Xie, Z/E Effect on Phase Behavior of Main-Chain Liquid Crystalline Polymers Bearing AIEgens, Macromolecules 54 (2021) 10740–10749. https://doi.org/10.1021/acs.macromol.1c02051.

[87] R. Imanishi, Y. Nagashima, K. Takishima, M. Hara, S. Nagano, T. Seki, Induction of Highly Ordered Smectic Phases in Side Chain Liquid Crystalline Polymers by Means of Random Copolymerization, Macromolecules 53 (2020) 1942–1949. https://doi.org/10.1021/acs.macromol.9b02649.

[88] Y. Chen, P. Lu, Z. Li, Y. Yuan, H. Zhang, Side-chain chiral fluorescent liquid crystal polymers with highly efficient circularly polarized

luminescence emission in a glassy-state SmC∗ film, Polym Chem 12 (2021) 2572–2579. https://doi.org/10.1039/d1py00199j.

[89] S.M. Alauddin, N.F.K. Aripin, T.S. Velayutham, A. Martinez-Felipe, Liquid crystalline copolymers containing sulfonic and light-responsive groups: From molecular design to conductivity, Molecules 25 (2020). https://doi.org/10.3390/molecules25112579.

[90] R. Teruel-Juanes, K.A. Bogdanowicz, J.D. Badia, V.S. de Juano-Arbona, R. Graf, J.A. Reina, M. Giamberini, A. Ribes-Greus, Molecular mobility in oriented and unoriented membranes based on poly[2-(Aziridin-1-yl)ethanol], Polymers (Basel) 13 (2021). https://doi.org/10.3390/polym13071060.

[91] M. Yang, L. Huang, P. Guo, B. Zhou, Y. Tao, C. Yang, Design, synthesis and performance control of dendritic fluorescent liquid crystal polymers with aggregation-induced emission properties, Eur Polym J 186 (2023). https://doi.org/10.1016/j.eurpolymj.2023.111855.

[92] W. Bi, Z. Zheng, Y. Wang, Z. Shi, K. Wang, Y. Liu, S. Xu, S. Cao, Design, synthesis and properties of mesogen jacketed liquid crystalline polymers with fluorinated triphenylene pendants, J Mol Liq 391 (2023). https://doi.org/10.1016/j.molliq.2023.123225.

[93] A. Hinokimoto, T. Ono, M. Fujiwara, H. Mori, R. Akiyoshi, S. Nakamura, O. Tsutsumi, A. Saeki, Y. Kitagawa, S. Horike, D. Tanaka, Synthesis and Strong π–π Interaction of Hexaazatriphenylene Derivatives with Alternating Electron-Withdrawing and -Donating Groups, Chem Asian J 17 (2022). https://doi.org/10.1002/asia.202200225.

[94] X.P. Xiong, Q. Yang, R.J. Wang, L.Y. Zeng, W.H. Yu, H.M. Chen, H.L. Ni, C. Feng, K.Q. Zhao, P. Hu, Fast thermally-responsive azatriphenylene ionic discotic liquid crystalline polymers with shape-memory properties, Polym Chem 14 (2023) 4521–4529. https://doi.org/10.1039/d3py00656e.

[95] M. Li, J. Guo, C. Zhang, Y. Che, Y. Yi, B. Liu, Uniform Colloidal Polymer Rods by Stabilizer-Assisted Liquid-Crystallization-Driven Self-Assembly, Angewandte Chemie - International Edition 62 (2023). https://doi.org/10.1002/anie.202309914.

[96] J. Lombard, Once upon a time the cell membranes: 175 years of cell boundary research, Biol Direct 9 (2014). https://doi.org/10.1186/s13062-014-0032-7.

[97] A. Naeem, B. Saeed, H. AlMohamadi, M. Lee, M.A. Gilani, R. Nawaz, A.L. Khan, M. Yasin, Sustainable and green membranes for chemical separations: A review, Sep Purif Technol 336 (2024). https://doi.org/10.1016/j.seppur.2024.126271.

[98] Y. Wen, J. Wang, F. Wang, H. Wu, J. Zhou, Z. Dai, H. Guo, Recent advances in membranes modified with plant polyphenols in wastewater treatment: A review, Sep Purif Technol 334 (2024). https://doi.org/10.1016/j.seppur.2023.125861.

[99] W. Yu, L. Xiong, J. Teng, C. Chen, B. Li, L. Zhao, H. Lin, L. Shen, Advances in synthesis and application of amphoteric polymer-based water treatment agents, Desalination 574 (2024). https://doi.org/10.1016/j.desal.2023.117280.

[100] M. Zubair, M. Yasir, D. Ponnamma, H. Mazhar, V. Sedlarik, A.H. Hawari, M.A. Al-Harthi, M. Al-Ejji, Recent advances in nanocellulose-based two-dimensional nanostructured membranes for sustainable water purification: A review, Carbohydr Polym 329 (2024). https://doi.org/10.1016/j.carbpol.2024.121775.

[101] S. Karki, G. Hazarika, D. Yadav, P.G. Ingole, Polymeric membranes for industrial applications: Recent progress, challenges and perspectives, Desalination 573 (2024). https://doi.org/10.1016/j.desal.2023.117200.

[102] Y. Sun, J. Wu, X. Zhu, Poly(ionic liquids) membranes preparation and its application, J Mol Struct 1304 (2024). https://doi.org/10.1016/j.molstruc.2024.137683.

[103] J. Kang, N. Deng, B. Cheng, W. Kang, Progress in the application of polymer fibers in solid electrolytes for lithium metal batteries, Journal of Energy Chemistry 92 (2024) 26–42. https://doi.org/10.1016/j.jechem.2023.12.035.

[104] A. Mishra, H. Park, F. El-Mellouhi, D. Suk Han, Seawater electrolysis for hydrogen production: Technological advancements and future perspectives, Fuel 361 (2024) 130636. https://doi.org/10.1016/j.fuel.2023.130636.

[105] X. Wei, V.S. Reddy, S. Gao, X. Zhai, Z. Li, J. Shi, L. Niu, D. Zhang, S. Ramakrishna, X. Zou, Recent advances in electrochemical cell-based biosensors for food analysis: Strategies for sensor construction, Biosens Bioelectron 248 (2024). https://doi.org/10.1016/j.bios.2023.115947.

[106] M. Borràs-Brull, P. Blondeau, J. Riu, Characterization and Validation of a Platinum Paper-based Potentiometric Sensor for Glucose Detection in Saliva, Electroanalysis 33 (2021) 181–187. https://doi.org/10.1002/elan.202060221.

[107] R. Cánovas, M. Parrilla, P. Blondeau, F.J. Andrade, A novel wireless paper-based potentiometric platform for monitoring glucose in blood, Lab Chip 17 (2017) 2500–2507. https://doi.org/10.1039/c7lc00339k.

[108] E.Y. Safronova, A.A. Lysova, D.Y. Voropaeva, A.B. Yaroslavtsev, Approaches to the Modification of Perfluorosulfonic Acid Membranes, Membranes (Basel) 13 (2023). https://doi.org/10.3390/membranes13080721.

[109] Y. Deng, A. Hussain, W. Raza, X. Cai, D. Liu, J. Shen, Review on current development of polybenzimidazole membrane for lithium battery, Journal of Energy Chemistry 91 (2024) 579–608. https://doi.org/10.1016/j.jechem.2023.12.044.

[110] J. Kloos, N. Joosten, A. Schenning, K. Nijmeijer, Self-assembling liquid crystals as building blocks to design nanoporous membranes suitable for molecular separations, J Memb Sci 620 (2021). https://doi.org/10.1016/j.memsci.2020.118849.

[111] Y. Suzuki, T. Sakamoto, M. Yoshio, T. Kato, Development of functional nanoporous membranes based on photocleavable columnar liquid crystals – Selective adsorption of ionic dyes, Eur Polym J 134 (2020). https://doi.org/10.1016/j.eurpolymj.2020.109859.

[112] J.A.M. Lugger, P.P. Marín San Román, C.C.E. Kroonen, R.P. Sijbesma, Nanoporous Films with Photoswitchable Absorption Kinetics Based on Polymerizable Columnar Discotic Liquid Crystals, ACS Appl Mater Interfaces 13 (2021) 4385–4392. https://doi.org/10.1021/acsami.0c19180.

[113] X. Yue, Z. Zhong, C. Wang, Z. Zhao, X. Zhang, G. Wang, W. Wang, X. Xia, Z. Zhou, Y. Cui, Y. Huang, C. Wu, X. Pan, Antimicrobial peptide dendrimers assisted Nanocomposite-Loaded lyotropic liquid crystalline for multimodal surgical site infection management, Chemical Engineering Journal 479 (2024). https://doi.org/10.1016/j.cej.2023.147812.

[114] Y. Saadat, S.M. Tabatabaei, K. Kim, R. Foudazi, Thermoresponsive antifouling ultrafiltration membranes from mesophase templating, J Memb Sci 684 (2023). https://doi.org/10.1016/j.memsci.2023.121861.

[115] M. Zhang, G. Liu, S. Du, R. Chen, P. Chen, Q. Weng, A. Gao, X. Chen, Z. An, Preparation and properties of novel liquid crystal ionomers bearing benzoxazole-based mesogenic side-chains and their membranes, J Mol Liq 394 (2024). https://doi.org/10.1016/j.molliq.2023.123677.

[116] K.A. Bogdanowicz, D. Pirone, J. Prats-Reig, V. Ambrogi, J.A. Reina, M. Giamberini, In situ raman spectroscopy as a tool for structural insight into cation non-ionomeric polymer interactions during ion transport, Polymers (Basel) 10 (2018). https://doi.org/10.3390/polym10040416.

UNIVERSITAT ROVIRA I VIRGILI
COLUMNAR LIQUID-CRYSTALLINE POLYMERS CONTAINING NITROGEN AT THE BACKBONE TO BE USED TO PREPARE ION-TRANSPORT MEMBRANES
Jordi Guardià Blanch

UNIVERSITAT ROVIRA I VIRGILI
COLUMNAR LIQUID-CRYSTALLINE POLYMERS CONTAINING NITROGEN AT THE BACKBONE TO BE USED TO PREPARE ION-TRANSPORT MEMBRANES
Jordi Guardià Blanch

Chapter 2

Synthesis and characterisation of dendritic compounds containing nitrogen: monomer precursors to build up biomimetic membranes

(Sci. Rep. 12, (2022),1725)

UNIVERSITAT ROVIRA I VIRGILI
COLUMNAR LIQUID-CRYSTALLINE POLYMERS CONTAINING NITROGEN AT THE BACKBONE TO BE USED TO PREPARE ION-TRANSPORT MEMBRANES
Jordi Guardià Blanch

CHAPTER 2

2.1.Introduction

4,5-Dihydro-1,3-oxazoles, more commonly known as 2-oxazolines or Δ^2-1,3-oxazolines, are five-membered cyclic imino ethers which were synthesised for the first time in 1884 [1], although their structure was not clearly elucidated until 5 years later by Gabriel [2]. Since then, distinct synthetic routes have been described for the synthesis of these heterocyclic organic compounds, being direct synthesis from carboxylic acids or their derivatives (esters or acid halides) and the cyclisation of β-hydroxyamides with different dehydrating agents the most typically reported pathways [3,4].

Different applications have been reported for 2-oxazolines: they have been utilised as ligands in asymmetric catalysis [5,6], as synthetic intermediates[7], as structural components of natural products or as protecting groups for carboxylic acid functionalities [8]. Furthermore, these cyclic organic compounds are principally employed to build-up substituted poly(2-oxazoline)s (PAOx) with a well-defined structure by *living* cationic ring-opening polymerization (CROP) [3,9-11]. In these cases, the substituent of the 2-oxazoline cycle determines the properties of the obtained poly(2-oxazoline)s. Precisely, the similar chemical structure of the resulting poly(2-oxazoline)s to natural polypeptides confers to these polymers an excellent biocompatibility, which together with their low viscosity and high stability make this kind of polymeric materials an ideal candidate in biomedical applications. As proof of these exceptional properties, Moreadith and co-workers reported recently a drug loaded PAOx that has been tested as a therapeutic agent in the Phase 1 clinical trials of Parkinson's disease [12].

CHAPTER 2

Side-chain liquid-crystalline polymers (SCLCPs) have aroused a great interest due to its self-assembling ability, which gives them unique optical, electrical and mechanical properties [13]. Therefore, the well-ordered SCLCPs have been used in a vast range of applications in many fields such as optical data storage [14], non-linear optics [15], optical compensators [16], separation membranes [17,18], solid polymer electrolytes [19,20] or electronic devices [21,22].

According to that, the synthesis of the first liquid-crystalline poly(2-oxazoline)s via CROP of 2-substituted 2-oxazolines, which contain a side-chain mesogenic group, was presented by the research group of Virgil Percec in 1987 [23]. Since then, this group conducted a wide investigation on the self-assembly of several minidendritic 2-oxazolines and the subsequent self-organisation of the dendronized poly(ethyleneimine)s into LC phases via self-assembly process [24-27].

Furthermore, Kim and co-workers reported the synthesis of a family of side-chain liquid-crystalline poly(2-oxazoline)s with different contents of cyanobiphenyl-based mesogenic groups [28]. Moreover, they grafted distinct mesogens that differ in the methylene units of the spacer length (2, 4, 6 and 10 methylene units, respectively) to a partially hydrolysed poly(2-methyl-2-oxazoline) via Steglich esterification. They proved that at least a modification degree equal to 27% of cyanobiphenyl mesogenic group is required in the resulting poly(2-oxazoline)s to detect a liquid-crystalline mesophase by DSC (differential scanning calorimetry) or POM (polarized optical microscopy). Furthermore, the LC phase range of the poly(2-oxazoline)s, which exhibit smectic or nematic LC textures, is correlated with the length of the spacer moiety of the mesogen.

CHAPTER 2

In the last decades, our research group has focused on the design and synthesis of dendronized liquid-crystalline polyethers and polyamines by grafting dendritic side groups into these polymers, which induce their self-assembly into columnar structures, thus resulting in the formation of an inner channel, which contains polar ether or amine linkages, which allow it to work as an ion channel [29-31]. Membranes prepared using the previously synthesized low molecular weight side-chain liquid-crystalline polyamines exhibited a remarkable proton transport, despite their poor mechanical properties and brittleness [32,33]. To minimize these drawbacks, in this paper the synthesis of higher molecular weight side-chain liquid crystalline polyamines was tackled by the polymerization of dendritic monomers. It must be mentioned that the synthesis and characterization of a dendritic liquid-crystalline aziridine was reported by us [34], which exhibited a monotropic columnar LC phase on cooling. Even so, attempts to polymerize it did not provide satisfactory results [34].

Thus, in this work, we describe the synthesis and characterization of a novel dendritic 2-oxazoline monomer 2-(3,4,5-tris(4-dodecyloxybenzyloxy)phenyl)-4,5-dihydro-1,3-oxazole) (TAPOx) and its amide precursor *N*-(2-hydroxyethyl)-3,4,5-tris(4-dodecyloxybenzyloxy)benzamide (TAPAm). The 2-oxazoline monomer can be subsequently polymerized in a controlled manner taking advantage of the "living" character of CROP of this type of monomers to obtain side-chain liquid-crystalline acyl-substituted poly(ethyleneimine)s, that can be a promising candidate in the preparation of membranes that allow the transport of cations thanks to the presence of nitrogen atoms in their inner channel. Moreover, the nature of the CROP would let us to obtain high molecular weight SCLCPs, which will enable the preparation of membranes

that should exhibit improved mechanical properties than the cation exchanges membranes tested in polymer electrolyte fuel cells with the previously synthesized side-chain liquid-crystalline polyethers and polyamines.

2.2.Experimental

2.2.1. Materials

1-Ethyl-3-(3-dimethylaminopropyl)carbodiimide (EDC, > 97 %), 4-dimethylaminopyridine (DMAP, ≥ 99 %), ethanolamine (≥ 99 %), sodium methoxide (NaOMe, solution 0.5 M in methanol), n-butyllithium (n-BuLi, solution 2.5 M in hexanes), thionyl chloride ($SOCl_2$, ≥ 99 %), anhydrous lanthanum triflate ($LaTf_3$, 99.999 %), anhydrous lanthanum chloride ($LaCl_3$, 99.9 %), methyl tosylate (MeOTs, 98%), anhydrous benzotrifluoride (≥ 99 %) and dodecylamine (98 %) were purchased from Sigma Aldrich. 1,8-Diazabicyclo[5.4.0]undec-7-ene (DBU, 99%) and 2,3-dichloro-5,6-dicyano-1,4-benzoquinone (DDQ, 98%) were supplied by Alfa Aesar. *N,N'*-Dicyclohexylcarbodiimide (DCC, ≥ 99%) was purchased from Fluka and triphenylphosphine (PPh_3, 99%) was supplied by Acros Organics. The other solvents were supplied by Scharlab. Furthermore, toluene, dichloromethane (DCM), dimethylformamide (DMF) and ethanolamine were dried before use according to literature [35].

2.2.2. Synthesis of the tapered mesogenic precursors

The synthesis of methyl 3,4,5-tris[*p*-(n-dodecan-1-yloxy)benzyloxy]benzoate (TAPEs) was performed following a slight modification of a reported procedure that involved easier workup and higher yield [36]:

p-(n-dodecan-1-yloxy)benzyl chloride (36.1 g, 0.12 mol), methyl 3,4,5-trihydroxybenzoate (7.1 g, 0.04 mol), powdered potassium carbonate (48.1 g, 0.35 mol) and dry DMF (400 mL) were added into a twin-neck round bottom flask. The mixture was stirred and heated at 60 °C during 4 h under argon atmosphere. The reaction was monitored by thin layer chromatography (TLC) using toluene as an eluent. After complete conversion of *p*-(n-dodecan-1-yloxy)benzyl chloride, the reaction was poured to 1.5 L of ice water, filtered, and recrystalized twice in acetone. Finally, the product was dried under vacuum at room temperature to yield 30.1 g (77 %) of a white solid.

The synthesis of 3,4,5-tris-[4-(n-dodecan-1-yloxy)benzyloxy]benzoic acid (TAPAc) was carried out as described elsewhere [31].

2.2.3. Synthesis of *N*-(2-hydroxyethyl)-3,4,5-tris(4-dodecyloxybenzyloxy)benzamide (TAPAm)

2.2.3.1. Direct amidation method using EDC as coupling agent

In a round-bottomed flask, 0.50 g of TAPAc (0.50 mmol) were dissolved into 10 mL of chloroform. The solution was stirred at 0 °C in an ice-water bath for 15 min. Then, DMAP (49.2 mg, 0.40 mmol) was added, and the solution was kept under stirring at 0 °C during 15 min more. After that, EDC (97.3 mg, 0.50 mmol) was added, leaving the magnetic stirring for additionally 15 min at the same temperature. At this moment, ethanolamine (0.09 mL, 1.49 mmol) was added dropwise. When the addition of ethanolamine was completed, the reaction mixture was warmed to room temperature and kept under stirring. The conversion of TAPAc was monitored by TLC using n-hexane/ethyl acetate as mixture of eluents (1:2). After complete conversion of TAPAc was observed by TLC (27 h), the crude mixture was first extracted twice with water and then once with brine. The organic layer was dried over anhydrous $MgSO_4$ and vacuum evaporated. Finally, the obtained solid was purified by flash column chromatography (gradient of n-hexane/ethyl acetate as mixture of eluents; starting proportion = 2:1), obtaining pure TAPAm as a white powder (212.5 mg, 42 %).

^{1}H NMR [$CDCl_3$, δ, ppm]: 7.23 (d, 4H, -O-**Ar-H**-CH_2-O-Ar-CONH- from 2 and 6 positions of the lateral benzylic units), 7.16 (d, 2H, -O-**Ar-H**-CH_2-O-Ar-CONH- from 2 and 6 positions of the central benzylic unit), 6.98 (s, 2H, **ArH**-

CONH-), 6.80 (d, 4H, -O-**Ar-H**-CH_2-O-Ar-CONH- from 3 and 5 positions of the lateral benzylic units), 6.67 (d, 2H, -O-**Ar-H**-CH_2-O-Ar-CONH- from 3 and 5 positions of the central benzylic unit), 6.47 (t, 1H, -N**H**-), 4.93 (s, 4H, -**CH_2**-O-Ar-CONH- in lateral benzylic units), 4.90 (s, 2H, -**CH_2**-O-Ar-CONH- in central benzylic units), 3.86 (m, 4H, -Ar-O-**CH_2**-$(CH_2)_{10}$-CH_3 in lateral benzylic units), 3.83 (t, 2H, Ar-O-**CH_2**-$(CH_2)_{10}$-CH_3 in central benzylic units), 3.73 (t, 2H, -NH-CH_2-**CH_2**-OH), 3.50 (dt, 2H, -NH-CH_2-CH_2-OH), 1.70 (m, 6H, -Ar-O-CH_2-**CH_2**-$(CH_2)_9$-CH_3), 1.37 (m, 6H, -Ar-O-CH_2-CH_2-**CH_2**-$(CH_2)_8$-CH_3), 1.20 (m, 48H, -Ar-O-CH_2-CH_2-CH_2-**$(CH_2)_8$**-CH_3), 0.81 (t, 9H, -Ar-O-CH_2-$(CH_2)_{10}$-**CH_3**).

^{13}C NMR [$CDCl_3$, δ, ppm]: 168.4 (-**C**ONH-), 159.2 (**ArC**-O-$(CH_2)_{11}$-CH_3 in lateral and central benzylic units), 153.0 (**ArC** meta to -CONH-), 141.5 (**ArC** para to -CONH-), 130.4 (**ArC** meta to -O-$(CH_2)_{11}$-CH_3 in central benzylic unit), 129.5 (**ArC**-CONH-), 129.4 (**ArC** meta to -O-$(CH_2)_{11}$-CH_3 in lateral benzylic units), 128.6 (**ArC**-CH_2-O-Ar-CONH-), 114.6 (**ArC** ortho to -O-$(CH_2)_{11}$-CH_3 in lateral benzylic units), 114.2 (**ArC** ortho to -O-$(CH_2)_{11}$-CH_3 in central benzylic unit), 107.3 (**ArC** ortho to -CONH-), 74.9 (-**CH_2**-O-Ar-CONH- in central benzylic unit), 71.4 (-**CH_2**-O-Ar-CONH- in lateral benzylic units), 68.2 (-**CH_2**-$(CH_2)_{10}$-CH_3 in central and lateral benzylic units), 62.5 (-NH-CH_2-**CH_2**-OH), 43.1 (-NH-**CH_2**-CH_2-OH), 32.1 (-**CH_2**-CH_2-CH_3), 29.8 -29.4 (**-$(CH_2)_6$**-CH_2-CH_3) and (-**CH_2**-$(CH_2)_9$-CH_3), 26.2 (-**CH_2**-$(CH_2)_8$-CH_3), 22.8 (-**CH_2**-CH_3), 14.2 (-**CH_3**).

IR (cm^{-1}): 3295 (ν (O-H)); 2950 (ν (C-H) in -CH_3 (asymmetric)); 2917 – 2850 (ν (C-H) in -CH_3 (symmetric) and -CH_2- (asymmetric and symmetric)); 1614 (ν (C = O)); 1514 (ν (C=C-C aromatic)); 1333 (δ (O-H) in plane bend); 1243 (ν (=C-O-C) asymmetric); 1121 (ν (-C-O-H)); 817 (δ (C-H) *p*-disubstitution).

2.2.3.2. Direct amidation of TAPEs with ethanolamine

In a pear-shaped flask, 1.00 g of TAPEs (0.99 mmol) was dissolved in ethanolamine (1.98 g, 33.07 mmol). The crude of the reaction, which was monitored by TLC (n-hexane/ethyl acetate (1:2) as mixture of eluents), was vigorously stirred under reflux at 140 °C. After total conversion of TAPEs (15 h), the black solution was cooled to RT and 10 mL of $CHCl_3$ were added. The organic solution was extracted three times with water and then once more with brine. After that, the organic layer was dried over anhydrous $MgSO_4$ and vacuum evaporated. Finally, the product was recrystallized twice with ethanol, obtaining 456.6 mg of TAPAm (43 %).

2.2.3.3. Synthesis of TAPAm using sodium methoxide. ($NaHCO_3$) as catalyst

In a round bottomed flask, a mixture of sodium methoxide (0.64 mL, 0.31 mmol), methyl 3,4,5-tris[*p*-(n-dodecan-1-yloxy)benzyloxy]benzoate (3.17 g, 3.14 mmol), ethanolamine (0.31 mL, 5.03 mmol) and dry toluene (6 mL) was heated at 50 °C for 22 h under argon atmosphere. The reaction was monitored by TLC using n-hexane/ethyl acetate (1:2) as mixture of eluents. When the reaction was completed, the resulting mixture was quenched with an aqueous saturated NH_4Cl solution (40 mL). After the extraction with ethyl acetate (x 3), the organic layer was separated, dried over anhydrous $MgSO_4$ and the solvent vacuum evaporated. Finally, the obtained solid was purified by recrystallization in ethanol to obtain 2.98 g of TAPAm (92 %).

2.2.4. Synthesis of 2-(3,4,5-tris(4-dodecyloxybenzyloxy) phenyl)-2-oxazoline (TAPOx)

2.2.4.1. Synthesis of TAPOx using a PPh_3-DDQ system.

In a previously dried Schlenk tube, 258.3 mg of PPh_3 (0.98 mmol) and 223.6 mg of DDQ (0.98 mmol) were dissolved in 5 mL of dry DCM under argon atmosphere. Then, the mixture was stirred for 3 min at room temperature. At this point, 680.2 mg of TAPAm (0.66 mmol) was then added. The reaction was monitored by TLC using n-hexane/ethyl acetate (1:2) as mixture of eluents. After 20 min, when a complete conversion of TAPAm was reached, the crude mixture was washed with an aqueous NaOH solution (5 %, 40 mL). After that, the separated water layer was back-extracted with DCM (15 mL x 4). The two organic layers were combined and washed together with brine solution, dried over anhydrous $MgSO_4$ and the solvent was vacuum evaporated. Finally, the brown solid was purified by flash column chromatography using n-hexane/ethyl acetate (2:1) as mixture of eluents, giving the corresponding product as white solid (570.6 mg, 85 %).

^{1}H NMR [$CDCl_3$, δ, ppm]: 7.25 (d, 4H, , -O-**Ar-H**-CH_2-O-Ar-C=N- from 2 and 6 positions of the lateral benzylic units), 7.21 (s, 2H, **Ar-H**-C=N-), 7.17 (d, 2H, -O-**Ar-H**-CH_2-O-Ar-C=N- from 2 and 6 positions of the central benzylic unit), 6.83 (d, 4H, -O-**Ar-H**-CH_2-O-Ar-C=N- from 3 and 5 positions of the lateral benzylic units), 6.67 (d, 2H, -O-**Ar-H**-CH_2-O-Ar-C=N- from 3 and 5 positions of the central benzylic unit), 4.96 (s, 4H, -**CH_2**-O-Ar-C=N- in lateral benzylic units), 4.91 (s, 2H, -**CH_2**-O-Ar-C=N- in central benzylic unit), 4.34 (t, 2H, -C=N-

CH_2-**CH_2**-O-), 3.97 (t, 2H, -C=N-**CH_2**-CH_2-O-), 3.89 (t, 4H, -Ar-O-**CH_2**-$(CH_2)_{10}$-CH_3 in lateral benzylic units), 3.84 (t, 2H, Ar-O-**CH_2**-$(CH_2)_{10}$-CH_3 in central benzylic units), 1.70 (m, 6H, -Ar-O-CH_2-**CH_2**-$(CH_2)_9$-CH_3), 1.38 (m, 6H, -Ar-O-CH_2-CH_2-**CH_2**-$(CH_2)_8$-CH_3), 1.20 (m, 48H, -Ar-O-CH_2-CH_2-CH_2-(**CH_2**)$_8$-CH_3), 0.81 (t, 9H, -Ar-O-CH_2-$(CH_2)_{10}$-**CH_3**).

^{13}C NMR [$CDCl_3$, δ, ppm]: 164.7 (-**C**=N-), 159.1 (**ArC**-O-$(CH_2)_{11}$-CH_3 in lateral and central benzylic units), 152.9 (**ArC** meta to -C=N-), 141.2 (**ArC** para to -C=N-), 130.4 (**ArC** meta to -O-$(CH_2)_{11}$-CH_3 in central benzylic unit), 129.7 (**ArC**-CH_2-O-Ar-C=N- in central benzylic unit), 129.4 (**ArC** meta to -O-$(CH_2)_{11}$-CH_3 in lateral benzylic units), 128.9 (**ArC**-CH_2-O-Ar-C=N- in lateral benzylic units), 122.9 (**ArC**-C=N-), 114.6 (**ArC** ortho to -O-$(CH_2)_{11}$-CH_3 in lateral benzylic units), 114.2 (**ArC** ortho to -O-$(CH_2)_{11}$-CH_3 in central benzylic units), 107.9 (**ArC** ortho to -C=N-), 74.8 (-**CH_2**-O-Ar-C=N- in central benzylic unit) 71.2 (-**CH_2**-O-Ar-C=N- in lateral benzylic units), 68.2 (-**CH_2**-$(CH_2)_{10}$-CH_3 in central and lateral benzylic units), 67.9 (-C=N-CH_2-**CH_2**-O-), 55.0 (-C=N-**CH_2**-CH_2-O-), 32.1 (-**CH_2**-CH_2-CH_3), 29.8-29.5 (-**$(CH_2)_6$**-CH_2-CH_3) and (-**CH_2**-$(CH_2)_9$-CH_3), 26.2 (-**CH_2**-$(CH_2)_8$-CH_3), 22.8 (-**CH_2**-CH_3), 14.3 (-**CH_3**).

IR (cm^{-1}): 2950 (ν (C-H) in -CH_3 (asymmetric)); 2917 – 2848 (ν (C-H) in -CH_3 (symmetric) and -CH_2- (asymmetric and symmetric)); 1643 (ν (C = N)); 1588 (ν (C=C-C aromatic)); 1514 (ν (C=C-C aromatic)); 1245 (ν (=C-O-C) asymmetric); 818 (δ (C-H) *p*-disubstitution).

2.2.5. Preliminary polymerization studies

2.2.5.1. Bulk polymerization of TAPOx.

In a previously flame-dried Schlenk tube, 505.0 mg of TAPOx monomer (0.49 mmol) were added. Then, the tube was immersed into a preheated oil bath at 130 °C, where TAPOx was stirred during 15 min under argon flow conditions. After that, 1 % mol of methyl tosylate (0.91 mg, $4.9 \cdot 10^{-3}$ mmol) were added and the reaction mixture was kept under argon until a complete conversion of TAPOx was detected by ^{1}H NMR. At this point, an excess of dodecylamine (0.50 mL, 2.17 mmol) was added as terminating agent, maintaining the same temperature for 24 h, when the crude mixture was cooled to room temperature. Finally, the resulting mixture was dissolved in THF and the polyoxazoline was isolated by precipitation twice into cold methanol, obtaining 312.0 mg of a beige solid (62 %).

2.2.6. Characterization

Thermogravimetric analysis (TGA). Thermal stability studies were carried out in ALU OXIDE crucibles of 70 μL (ME-24123) with a Mettler Toledo TGA2 thermobalance. All samples, weighing around 6 – 8 mg, were heated between 30 and 600 °C at a heating rate of 10 °C/min in N_2 atmosphere with a flow rate of 50 cm^3/min. The equipment was previously calibrated with indium (156.6 °C) and aluminium (660.3 °C) pearls.

Differential scanning calorimetry (DSC). Calorimetric analyses were carried out on a Mettler DSC-821 instruments calibrated using indium (156.6 °C) and zinc (419.6 °C) pearls. Samples were placed in an aluminum standard crucible of 40 μL with pierced lids (between 4 – 6 mg of sample), which were analysed in N_2 atmosphere (gas flow rate of 50 cm^3/min). Heating and cooling rate of 10 °C/min has been always employed.

Polarized optical microscopy (POM). LC mesophases were investigated by polarised optical microscopy (POM). The textures of the samples were observed with an Anxiolab Zeiss optical microscope equipped with a Linkam TP92 hot stage.

Nuclear magnetic resonance (NMR) spectroscopy. All synthesized compounds were characterized by ^1H NMR and ^{13}C NMR spectra, which were recorded in deuterated chloroform ($CDCl_3$) with a Bruker Avance Neo 400 MHz spectrometer (^1H – 400 MHz; ^{13}C – 100.4 MHz) at room temperature. The chemical shifts were given in parts per million (ppm) from TMS (Tetramethylsilane) in ^1H NMR spectra, while the central peak of the solvent was taken as reference in the case of ^{13}C NMR spectra.

Fourier transform infrared (FT-IR) spectroscopy. FT-IR spectra were recorded on an FT/IR-6700 spectrophotometer from JASCO in the wavelength range of 4000 – 400 cm^{-1} with a resolution of 4 cm^{-1} in the absorbance mode. This device is equipped with an attenuated total reflection accessory (ATR)

with thermal control and a diamond crystal (Golden Gate heated single reflection diamond ATR from Specac-Teknokroma). The spectra were recorded at room temperature from the solid-state pure compounds.

X-ray diffraction (XRD). X-ray diffraction measurements (XRD) were made using a Bruker-AXS D8-Advance diffractometer with vertical θ-θ goniometer, incident- and diffracted-beam Soller slits of 2.5 °, a fixed 0.5 ° receiving slit and an air-scattering knife on the sample surface. The angular 2θ range was between 2 and 40°. The data were collected with an angular step of 0.02 ° at a step/time of 0.5 s. Cukα radiation was obtained from a copper X-ray tube operated at 40 kV and 40 mA. Diffracted X-rays were detected with a PSD detector LynxEye-XE-T with an opening angle of 2.9 °. The sample was placed inside an MTC-LOWTEMP chamber for in-situ temperature analysis.

2.3.Results and discussion

The main goal of this work was the synthesis of a dendronized 2-oxazoline monomer bearing the tapered 3,4,5-tris[4-(n-dodecan-1-yloxy)benzyloxy)benzoate group, which will allow us to prepare LC poly(2-oxazoline)s by *living* CROP. Moreover, the thermal and mesomorphic characterization of the new mesogenic compounds was performed to determine their LC mesophases.

2.3.1. Synthesis of 2-(3,4,5-tris(4-dodecyloxybenzyloxy) phenyl)-2-oxazoline (TAPOx)

Different synthetic routes have been explored in this work to synthesize 2-(3,4,5-tris(4-dodecyloxybenzyloxy)phenyl)-2-oxazoline (TAPOx), considering the number of involved stages. Besides, the following dendrons were used as starting materials:

- Methyl 3,4,5-tris[*p*-(n-dodecan-1-yloxy)benzyloxy]benzoate (TAPEs).
- 3,4,5-tris[*p*-(n-dodecan-1-yloxy)benzyloxy]benzoic acid (TAPAc).

The synthetic pathway of both dendrons was described in previous studies [31] and in the experimental section of this paper. Their chemical structure is depicted in **Figure 2.1**.

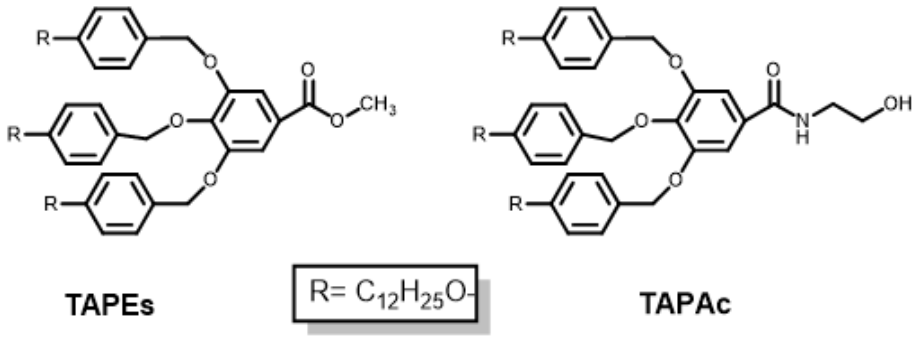

Figure 2.1. Chemical structure of: Methyl 3,4,5-tris[*p*-(n-dodecan-1-yloxy) benzyloxy] benzoate (TAPEs) and 3,4,5-tris[*p*-(n-dodecan-1-yloxy) benzyloxy] benzoic acid (TAPAc).

In this way, the first synthetic method selected comprised of two steps starting from TAPAc:

- The first step consisted of TAPAc amidation by means of DCC as coupling agent to obtain *N*-(2-hydroxyethyl)-3,4,5–tris(4-dodecyloxybenzyloxy)benzamide (TAPAm).
- The second step involve the cyclisation of TAPAm with thionyl chloride ($SOCl_2$) to isolate the desired product (TAPOx).

Regarding the first step, the esterification of carboxylic acids using a carbodiimide as a promoter along with dimethylaminopyridine (DMAP) to activate an acid and favour the ester formation is one of the most common esterification methods employed due to the high number of advantages that this reaction shows: high versatility, mild conditions are usually required for the reaction to proceed (room temperature), which also facilitates its use with different types of substrates [37]. Moreover, it allows the obtention of esters from tertiary alcohols because the steric impediments do not affect this type of esterification. It was mentioned before that our group reported the chemical modification of polyethers and polyamines with the dendron 3,4,5-tris[*p*-(n-dodecan-1-yloxy)benzyloxy]benzoic acid (TAPAc) by means of Steglich esterification, obtaining side-chain liquid crystalline polyethers and polyamines [30-32]. The promoter that we used in all these studies was *N*,*N*′-dicyclohexylcarbodiimide (DCC) [31].

Despite the advantages of Steglich esterification, this reaction presents some drawbacks: stoichiometric amounts or more of the carbodiimide are required,

the yields are not always high and undesired *N*-acylureas are occasionally formed. These disadvantages may be minimized by the addition of strong acids like *p*-toluenesulfonic acid [38], *N*-hydroxy derivatives [39] or tertiary amines [40], which suppress the formation of *N*-acylurea and favour the formation of the corresponding ester.

In this direction, the amidation of amines instead of alcohols to the corresponding amides took place with DCC as coupling agent following the same mechanism because amines present a more nucleophilic character. Therefore, the amidation of TAPAc with ethanolamine using the same conditions reported previously was carried out (**Figure 2.S1**) Although ethanolamine also contains a hydroxyl group, the amidation reaction will be favoured due to the chemoselectivity of the amine group present in ethanolamine versus the hydroxyl group. The dendronized amide was obtained in our case, even though a large amount of the *N*-acylurea side product was found mixed with TAPAm. Nonetheless, the complete removal of the dicyclohexylurea (DCU) was not possible by the purification methods employed in the work-up process of the crude mixture: filtration or flash column chromatography; obtaining always a highly impurified product.

To avoid this problem, DCC was replaced by a water soluble carbodiimide, 1-ethyl-3-(3-dimethylaminopropyl)carbodiimide (EDC). Despite EDC is an expensive reagent, the formed *N*-acylurea can be easily removed by aqueous extraction [39,41,42]. Besides, it was observed that the formation of the amide took place faster when EDC was used as coupling agent compared with the reaction using DCC (27 h *vs.* 4 days, respectively). Nonetheless, it was still necessary to purify the crude mixture by flash column chromatography.

Although amides can be obtained from carboxylic acids, we can take advantage of the greater reactivity of the ester group present in TAPEs to synthesize TAPAm [43,44]. In this way, Percec and co-workers reported a simple method for the amidation of dendronized esters into the corresponding amides by using a large excess of ethanolamine with yields higher than 80 % [26, 45]. So, the direct amidation of TAPEs with ethanolamine was also explored following the conditions reported by Percec group to increase the yield in the synthesis of TAPAm. Nevertheless, lower yields were obtained in our case (43 %).

On the other hand, the addition of a catalyst facilitates the formation of amides from the corresponding esters under mild conditions with excellent yields. Different types of catalyst have been reported in literature, which exhibited an improved efficiency in the formation of amides: inorganic catalysts such as $Sb(OEt)_3$ [46] or $Zr(O^tBu)_4$-HOAt) [47]; or organic catalysts, including *N*-heterocyclic carbine [48], DBU [49] and triazabicyclo[4.4.0]dec-5-ene [50]. Furthermore, Yang and co-workers showed that the combination of different catalysts (1,2,4-triazole and DBU) accelerates the ester conversion to generate the corresponding amides at room temperature in high yields [51]. However, the preparation of many of these catalysts is quite complex, which implies that the catalytic activity of simpler and cheaper compounds is investigated. In this sense, sodium methoxide (NaOMe) is a well-known commercial compound that is widely used as catalyst in the production of biodiesel by transesterification of triglycerides with methanol [52]. When Ohshima et al. used catalytic amounts of sodium methoxide (≤ 10 %) in the direct amidation of esters, they observed that the addition of this non-toxic catalyst results in the obtention of the corresponding amides under mild conditions, although

this reaction requires the use of inert atmosphere to suppress the saponification of the starting esters [53].

According to that, this procedure was followed in the amidation of TAPEs (**Figure 2.2**). In our case, the addition of 10 % mol of NaOMe not only simplified the work-up process of TAPAm, since flash column chromatography was replaced by a recrystallization in EtOH, but also caused an increase of more than double of the yield of the reaction with respect to the attempts reported before (92 %).

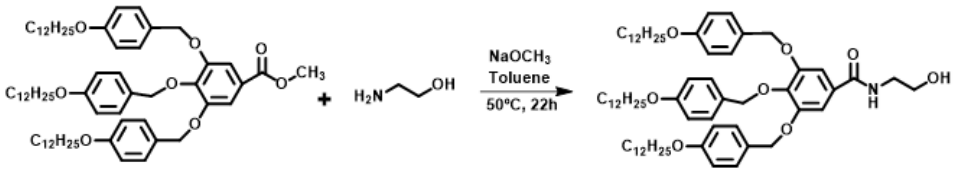

Figure 2.2. Synthesis of *N*-(2-hydroxyethyl)-3,4,5–tris(4-dodecyloxy benzyloxy) benzamide (TAPAm).

Table 2.1 shows the different precursors, the solvent and the reaction conditions used in the chemical reactions tested in the synthesis of TAPAm, together with the obtained results.

Table 2.1. Starting materials, solvent, reaction conditions and results of the distinct chemical reactions carried out to obtain TAPAm.

Starting materials (mmols)	Solvent	Temperature (°C)	Time (h)	Yield (%) / Comments
TAPAc (1.01) Ethanolamine (2.98) DCC (1.02) DMAP (0.83)	$CHCl_3$	RT [a]	96	A mixture of TAPAm with *N,N'*-dicyclohexylurea was always isolated (TAPAm cannot be isolated alone from the final mixture).
TAPAc (0.50) Ethanolamine (1.49) EDC (0.50) DMAP (0.40)	$CHCl_3$	RT [a]	27	42 / The use of EDC allows the separation of TAPAm from water soluble *N,N'*-dicyclohexylureas. However, a flash column chromatography is required to obtain pure TAPAm.
TAPEs (0.99) Ethanolamine (33.07)	Ethanolamine	140	15	43 / TAPAm was obtained after recrystallization with ethanol (x2). Easy to scale-up.
TAPEs (3.14) Ethanolamine (5.03) $NaOCH_3$ (0.31)	Anhydrous Toluene	50	22	92 / TAPAm was obtained after recrystallization with ethanol (x2) with a high yield. Easy to scale-up.

[a] RT, room temperature = 20 ± 3 °C.

To confirm its chemical structure, dendronized TAPAm precursor was characterized by NMR and FT-IR spectroscopy.

Figure 2.3 shows its ^{1}H NMR spectrum, which was performed using $CDCl_3$ as solvent. The aromatic region shows five signals at 7.23, 7.16, 6.98, 6.80 and 6.67 ppm. In comparison with previously reported characterization of methyl 3,4,5-tris[*p*-(n-dodecan-1-yloxy) benzyloxy] benzoate [54], the signals at 7.23 and 7.16 ppm (6 H) can be assigned to the protons in *ortho* position to -CH_2O- of lateral and central benzylic units, respectively. The signal at 6.98 ppm (2 H) corresponds to the protons of the benzoate group linked to the amide, whose multiplicity appears as a singlet. The other two signals at 6.80 and 6.67 ppm correspond to the protons in *metha* position to -CH_2O- of the lateral and central benzylic units, respectively. Furthermore, a triplet at 6.47 ppm corresponds to the proton of the amide group (-N<u>H</u>-), which is coupled to the neighbouring methylene as observed in the recorded 2D NMR spectra (COSY and HSQC NMR spectra; **Figures 2.S2 and 2.S3**). The two signals centred at 4.93 and 4.90 ppm are assigned to the benzylic methylenes of the dodecyloxybenzyloxy substituents. Moving upfield in the spectrum, two triplets centred at 3.86 and 3.83 ppm are attributed to methylene attached to the oxygen in the long alkyl chains in lateral and central benzylic units, respectively. As we move to lower chemical shifts, the presence of two characteristic signals at 3.73 and 3.50 ppm confirm that the amidation reaction took place because they are assigned to the *N*-(hydroxyethyl) moiety. Particularly, the triplet at 3.73 is assigned to the methylenic protons next to the hydroxylic group, while the signal at 3.50 ppm corresponds to the methylene unit contiguous to the amide group, since these protons are coupled to neighbouring methylene group and -NH proton as confirmed by 2D NMR experiments (COSY and HSQC; **Figures 2.S2 and**

2.S3). Finally, the signals at 1.70, 1.37, 1.20 and 0.81 ppm of the high-field region can be assigned to the protons of the alkyl long chains of the dendron.

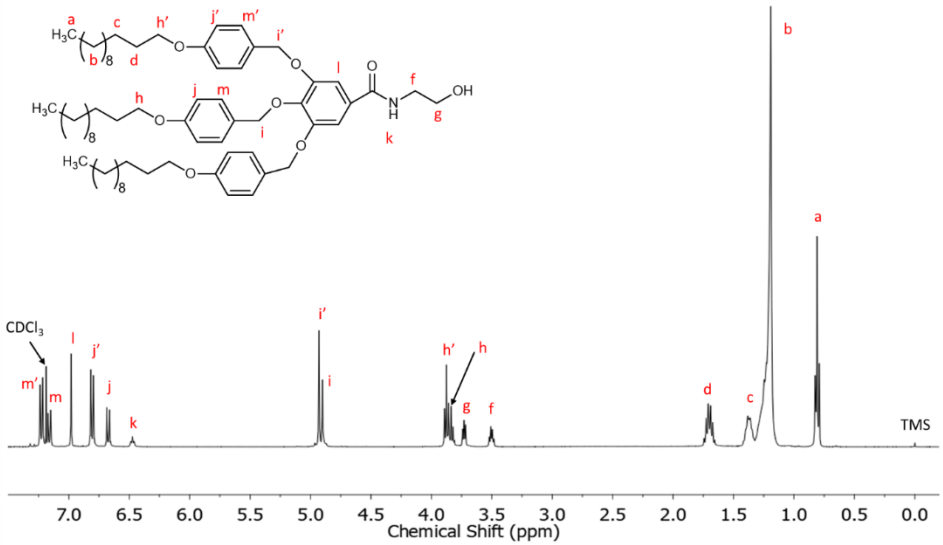

Figure 2.3. ^{1}H NMR spectrum in $CDCl_3$ of TAPAm.

Figure 2.4 shows the ^{13}C NMR of TAPAm with the corresponding assignments, taking the central peak of the solvent ($CDCl_3$) as reference. The carbonyl carbon appears at 168.4 ppm, while the aromatic carbons appear between 159.2 and 107.3 ppm. The carbons that belong to the long aliphatic chain of the dendron (indexed with letters a – e) appear upfield in the spectrum (region between 32.1 and 14.2 ppm). The carbon of the long alkyl chains indexed with the letter *h* appears at 68.2 ppm. Besides, the signals at 62.5 and 43.1 ppm correspond to the *N*-(hydroxyethyl) moiety, the carbons of which were assigned as follows: the signal at 62.5 ppm is assigned to the

methylene contiguous to the hydroxylic group (-OH), while the shielded signal at 43.1 ppm is attributed to the methylene contiguous to the amide group. Both signals were confirmed by HSQC NMR spectra (**Figure 2.S3**) and agreed with the characterization of similar 2-oxazoline derived dendrons previously described by Percec *et al*. [26,45]. The chemical shift (δ) of the benzylic methylenes depends on their relative position in the aromatic ring: Those in positions 3 and 5 appear at 71.4 ppm and corresponds to the lateral units (assigned with the letter *i'*), while the signal for the central unit appears downfield at 74.9 ppm (assigned with the letter *i*).

Furthermore, TAPAm structure was also characterized by means of FT-IR spectroscopy. Thus, the FT-IR spectrum of TAPAm shows a broad band at 3295 cm^{-1}, which is attributed to the O-H stretching. Furthermore, a strong and thin band at 1614 cm^{-1} is attributed to the stretching of the carbonyl group of the amide. There are two more bands in the fingerprint region of the FT-IR that are associated to the O-H bond: the band at 1333 cm^{-1}, which corresponds to the in-plane bending of the O-H bond, while the band at 1121 cm^{-1} can be assigned to the –(**C-O)**– stretching of the amide. The presence of all these bands corroborates that the amidation of TAPAm was successfully accomplished.

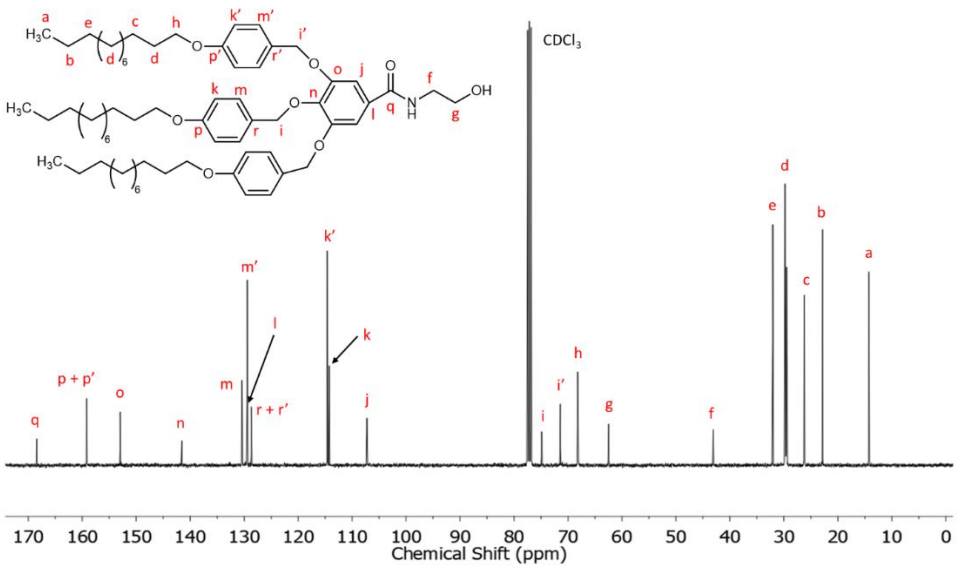

Figure 2.4. ^{13}C NMR spectrum in $CDCl_3$ of TAPAm.

Due to the versatility of the oxazoline functional group, considerable efforts have been made to develop a broad scope of synthetic routes starting from esters [55,56], nitriles [57], carboxylic acids [58,59] and *N*-(hydroxyethyl)amides [3,60,61]. From all of them, one of the most simple and well-known process is to convert the hydroxyl group of the *N*-(2-hydroxyethyl)amides into a good leaving group using thionyl chloride ($SOCl_2$), followed by a basic treatment with $NaHCO_3$ to isolate the 2-oxazoline derived ring [62]. Unfortunately, from what was observed when this reaction was carried out with TAPAm, the generated HCl in the reaction medium induced the cleavage of the ether benzylic moieties present in TAPAm. To suppress this side reaction, an excess of a non-nucleophilic base (DBU) was added before the addition of thionyl chloride to act as scavenger of the in-situ generated hydrochloric acid during the reaction as Šakalytė and co-workers

did [31]. Nonetheless, the formation of TAPOx was not detected in the crude mixture while TAPAm was being consumed.

Thus, alternative reagents that favour the dehydrative cyclisation of amides should be considered. We selected the methodology reported by Xu and co-workers, who described a facile and rapid procedure for the synthesis of 2-oxazolines using PPh_3-DDQ as oxidizing agent [63]. Among the advantages of this reaction, the authors highlighted its versatility (because it works well with distinct solvents such as DCM, 1,4-dioxane, THF, toluene), the mild reaction conditions (it takes place at room temperature) combined with the high yields of 2-oxazoline. Therefore, the synthesis of TAPOx was attempted using the PPh_3-DDQ system (**Figure 2.5**) and DCM as solvent. As Xu and co-workers previously demonstrated with various esters, we detected a complete conversion of the amide (TAPAm) by TLC after 20 min and TAPOx was isolated from the crude mixture by flash column chromatography with a high yield (85 %).

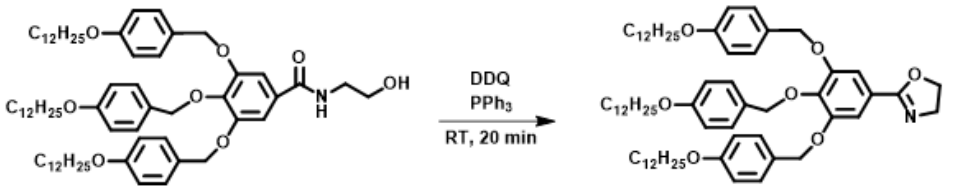

Figure 2.5. Synthesis of 2-(3,4,5-tris(4-dodecyloxybenzyloxy)phenyl)-2-oxazoline (TAPOx).

To validate the chemical structure of TAPOx, the obtained product was characterized by NMR and FT-IR spectroscopy. **Figures 2.6** and **2.7** show the ^{1}H NMR and ^{13}C NMR spectra of TAPOx respectively, which were recorded using deuterated chloroform as solvent.

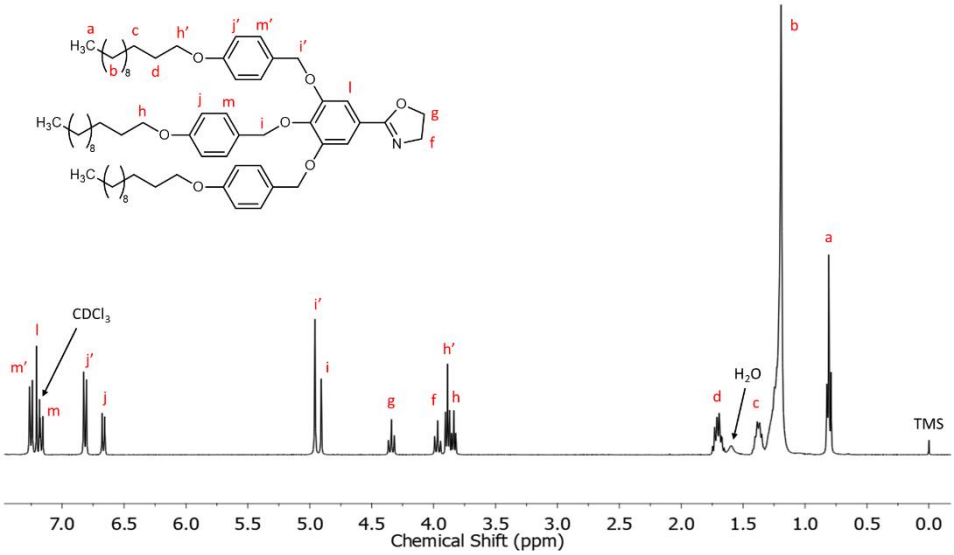

Figure 2.6. ^{1}H NMR spectrum in $CDCl_3$ of TAPOx.

Starting with the downfield region in ^{1}H NMR spectrum, the peaks between 7.25 – 6.67 ppm are assigned to the aromatic protons of the molecule. The two singlets that appear between 4.96 and 4.91 ppm are assigned to the benzylic methylenes of the dodecyloxybenzyloxy substituents. Furthermore, the two new triplets at 4.34 and 3.97 ppm are assigned to the methylenes of the formed oxazoline cycle: The triplet at 4.34 ppm is attributed to the methylene next to the oxygen, while the triplet centred at 3.97 ppm corresponds to the methylene

contiguous to the nitrogen atom of the oxazoline ring as confirmed by COSY, HSQC and HMBC NMR spectra (**Figure 2.S4, 2.S5** and **2.S6,** respectively). Moreover, these assignments are in agreement with the characterization of 2-oxazoline monomers previously described by Percec and co-workers [26,45]. Furthermore, the two triplets centred at 3.89 and 3.84 ppm are attributed to methylene attached to the oxygen in long alkyl chains in lateral and central benzylic units, respectively. In the same manner than in the precursor TAPAm, signals between 1.70 – 0.81 ppm are attributed to the alkyl long chains of the dendron.

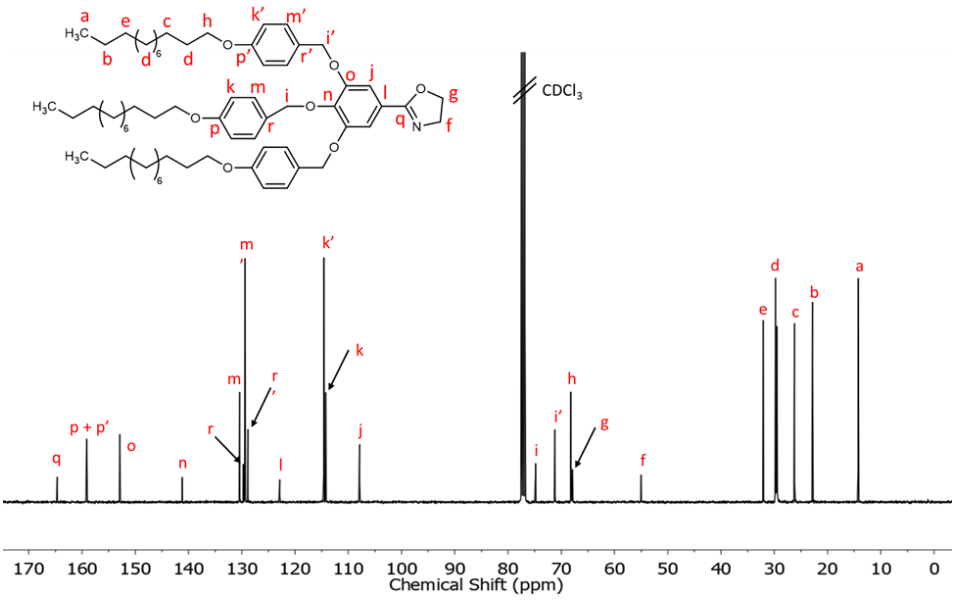

Figure 2.7. ^{13}C NMR spectrum in $CDCl_3$ of TAPOx.

Related to ^{13}C NMR, the carbon signal attributed to the -C=N- of the oxazoline ring appears at 164.7 ppm. The signals between 159.1 and 107.9 ppm are attributed to the aromatic carbons of the dendronized 2-oxazoline monomer. Is remarkable that the carbon of the aromatic ring linked to the oxazoline cycle appears slightly upfield in the spectrum compared to TAPAm precursor (122.9 ppm in front of the 129.5 ppm value observed in TAPAm). Same as TAPAm, the signals of the carbons that constitute the long alkyl chains appear at the expected region between 32.1 and 14.3 ppm (carbons labelled as a – e). The signals at 67.9 and 55.0 ppm are assigned to both methylene units of the 2-oxazoline ring, being the signal that appears at 67.9 ppm the one that corresponds to the methylene next to the oxygen, while the signal at 55.0 ppm is attributed to the methylene unit bonded to the nitrogen of the cycle. HSQC and HMBC NMR spectra allowed us to confirm the assignment of the characteristic signals of the 2-oxazoline ring (**Figure 2.S5 and 2.S6**). Besides, the assignment agrees with the elucidation described in previous studies by Percec and co-workers [26,45].

Moreover, the characteristic functional groups found in the chemical structure of TAPOx were characterized by FT-IR spectroscopy. In its FT-IR spectrum, no bands were observed above 3000 cm^{-1} and a new band attributed to the C=N stretching appears at 1643 cm^{-1}, which is characteristic of the 2-oxazoline ring and confirms that the dehydrative cyclisation of *N*-(2-hydroxyethyl)-3,4,5–tris(4-dodecyloxybenzyloxy)benzamide was achieved [64].

Finally, the direct synthesis of TAPOx from methyl 3,4,5-tris[*p*-(n-dodecan-1-yloxy)benzyloxy]benzoate (TAPEs) using lanthanide salts as catalyst was explored. The main advantage of this synthetic route is that only involves a single-step reaction as demonstrated by Zhou *et al*. [55]. In their work, the

authors developed a simple and efficient method for the amidation of different carboxylic esters taking advantage of distinct inorganic catalyst ($LaCl_3$, $LaTf_3$ and $SmCl_3$) obtaining 2-oxazolines in good yield when the reaction was performed under reflux of toluene. According to that, we carried out the one-pot synthesis of TAPOx from the starting ester dendron (TAPEs) using the conditions reported by Zhou and co-workers. In our case, different catalytic amounts of $LaCl_3$ (5, 10, 20 % mol respect to TAPEs) and $LaTf_3$ (10 % mol respect to TAPEs) were tested as catalyst. Nevertheless, the formation of 2-oxazoline compound was never detected in the reaction medium even though the formation of the amide (TAPAm) was observed when lanthanum triflate was employed. These observations agree with the results presented by Morimoto and co-workers, in which they reported the amidation of esters using 5 % mol of $LaTf_3$ in mild conditions with good yields (≥ 80 %) [65]. However, we could not isolate the TAPAm fraction from the crude mixture even by flash column chromatography due to its complexity and the low amount of TAPAm that it presented.

To summarize the reactions that were carried out in the synthesis of TAPOx, **Table 2.2** presents the starting materials, the solvent and the reaction conditions employed in all the reactions performed. Furthermore, the obtained yield and general remarks have been also shown.

At the end, **Figure 2.8** outlined all the synthetic routes that we had explored to obtain TAPOx monomer.

Table 2.2. Starting materials, solvent, reaction conditions and results obtained in the chemical reactions performed in the synthesis of TAPOx.

Starting materials (mmols)	Solvent	Temperature (°C)	Time (h)	Yield (%) / Comments
TAPAm (0.38); $SOCl_2$ (1.15); DBU (2.31)	DCM	RT [a]	2	No TAPOx was detected in the crude mixture after the complete consumption of TAPAm.
TAPAm (0.66); PPh_3 (0.98); DDQ (0.98)	Anhydrous DCM	RT [a]	0.33	85 / TAPOx was obtained with high yield. Nevertheless, a flash column chromatography is required to obtain pure TAPOx.
TAPEs (0.99); Ethanolamine (2.48); n-BuLi (2.25); Anhydrous $LaCl_3$ (0.05)	Anhydrous Toluene	100	27	No TAPOx was detected in the crude mixture after complete consumption of TAPEs despite the formation of TAPAm was detected.
TAPEs (0.99); Ethanolamine (2.48); n-BuLi (2.25); Anhydrous $LaCl_3$ (0.10)	Anhydrous Toluene	100	24	No TAPOx was detected in the crude mixture after complete consumption of TAPEs despite the formation of TAPAm was detected.
TAPEs (1.00); Ethanolamine (2.50); n-BuLi (2.25); Anhydrous $LaCl_3$ (0.20)	Anhydrous Toluene	100	22	No TAPOx was detected in the crude mixture after complete consumption of TAPEs despite the formation of TAPAm was detected.
TAPEs (0.99); Ethanolamine (2.48); n-BuLi (2.25); Anhydrous $LaTf_3$ (0.10)	Anhydrous Toluene	100	22	No TAPOx was detected in the crude mixture after complete consumption of TAPEs despite the formation of TAPAm was detected.

[a] RT, room temperature = 20 ± 3 °C.

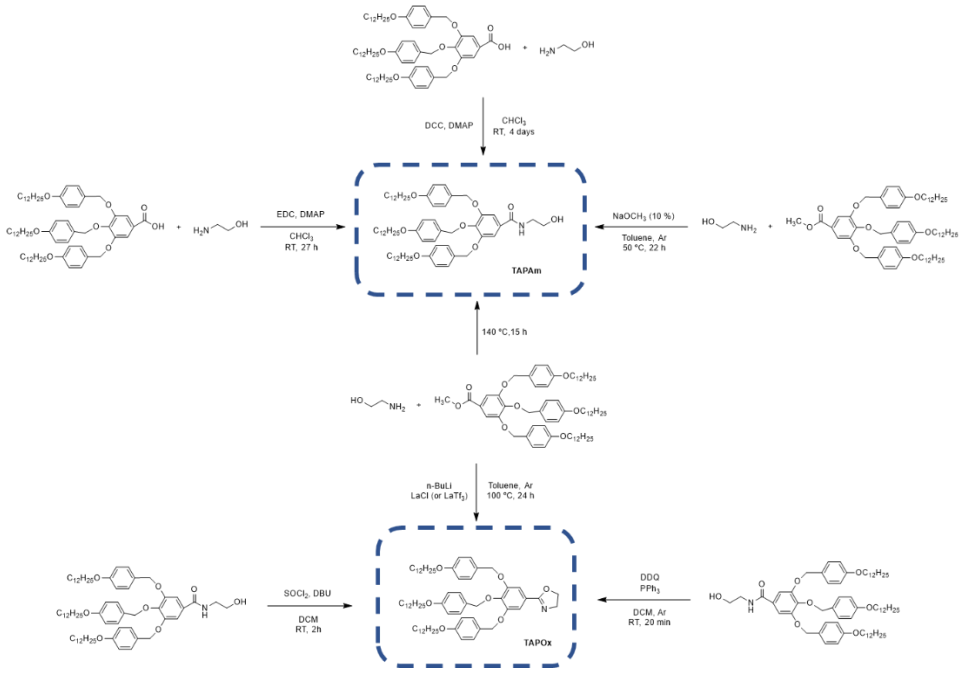

Figure 2.8. General scheme of the synthetic routes addressed in the synthesis of dendronized TAPOx monomer.

2.3.2. Thermal and mesomorphic characterization of TAPAm and TAPOx

Thermal and mesomorphic characterization of TAPAm and TAPOx was performed by DSC, TGA, POM and XRD experiments. DSC study of TAPAm is depicted in **Figure 2.9**. First and second heating scans are shown as well as the first cooling scan. The first heating scan shows a broad endotherm at 84 °C, followed by a second sharper endotherm at 101 °C; finally, a small endotherm is shown at 118 °C. On cooling scan, we only observe an exotherm

centred at about 83 °C. At second heating scan, we are able only to see two endotherms, the first one centred at 101 °C and the second one at 118 °C. As we could observe, after the clearing of the substrate the first endotherm was no longer observed, showing only these two peaks which are compatible with the occurrence of a mesophase in the range of temperatures from 101°C to 118°C. **Table 2.3** shows the associated enthalpies for each phase transition and clearing temperature for TAPAm on first and second heating scans.

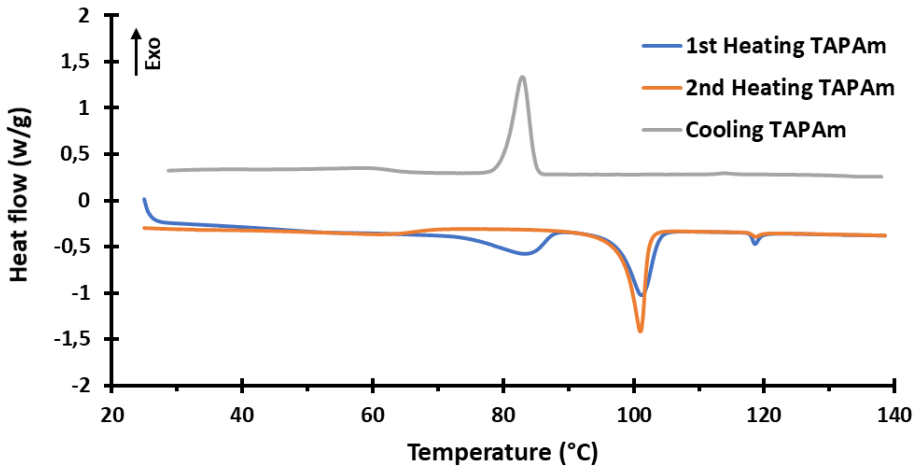

Figure 2.9. Calorimetric analysis of TAPAm; (blue) first heating, (orange) second heating, and (grey) cooling. Scan rate: 10 °C/min.

Table 2.3. Enthalpies of phase transitions detected in the case of TAPAm.

	1st Heating		2nd Heating	
	T (°C)	**ΔH (kJ/mol)**	**T (°C)**	**ΔH (kJ/mol)**
1st Endotherm	84	11.0	-	-
2nd Endotherm	101	19.0	101	21.8
T_c	118	0.8	118	0.3

Based on DSC and XRD experiments (**Figure 2.10**), we observed a metastable crystalline phase below first endotherm on first heating, since this phase was not observed at the second heating. On the other hand, we envisioned a highly ordered columnar phase between 84 °C and 101 °C at first heating. POM observation, in this range of temperatures, put into evidence a pseudo-focal conic fan-shaped texture (**Figure 2.11**). XRD pattern recorded at 90 °C (**Figure 2.10b**) shows three main peaks centred at 2θ = 2.4° (d = 36 Å), 4.6° (d = 19 Å), 6.2° (d = 14 Å) and an unsymmetrical broad halo at 2θ = 20° (d = 4 Å approximately) showing shoulders. The lower spacing observed in the XRD pattern should correspond to the planar distance between dendrons and the higher spacing might correspond to the lateral distance between columns. It is noteworthy that for the second heating only this phase was observed below the endotherm centred at 101 °C.

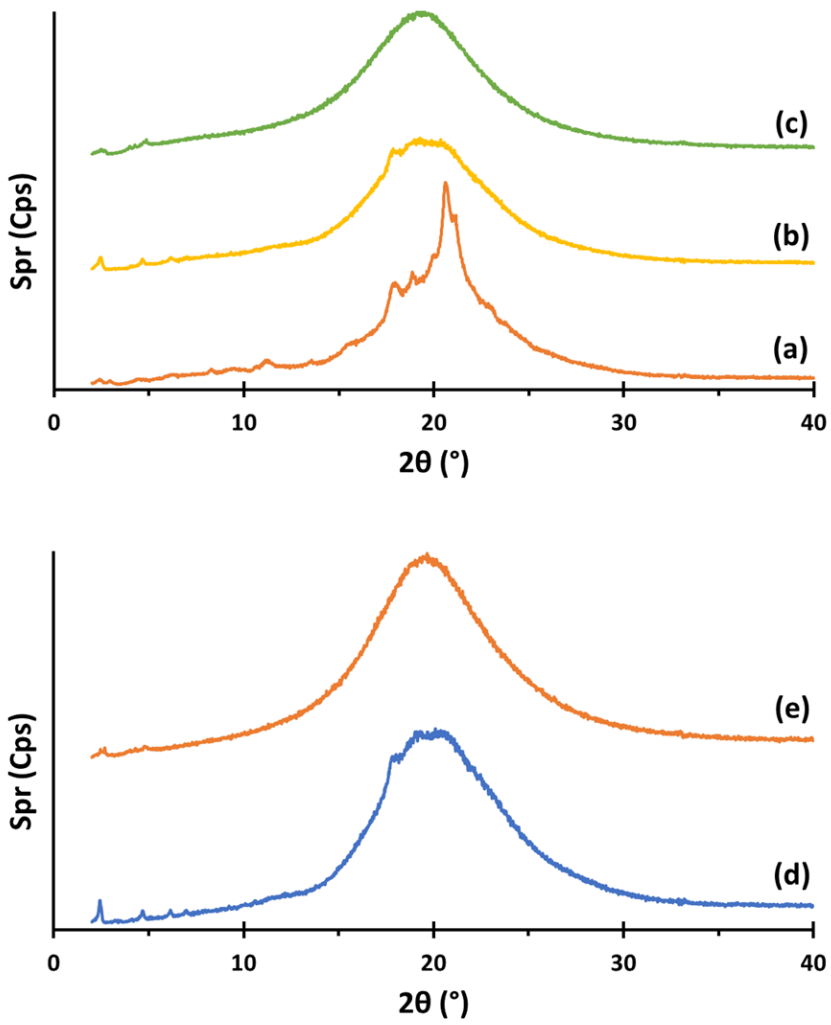

Figure 2.10. XRD patterns of TAPAm recorded on heating at: (a) 70 °C, (b) 90 °C and (c) 110 °C on first heating; and (d) 80 °C and (e) 110 °C on second heating.

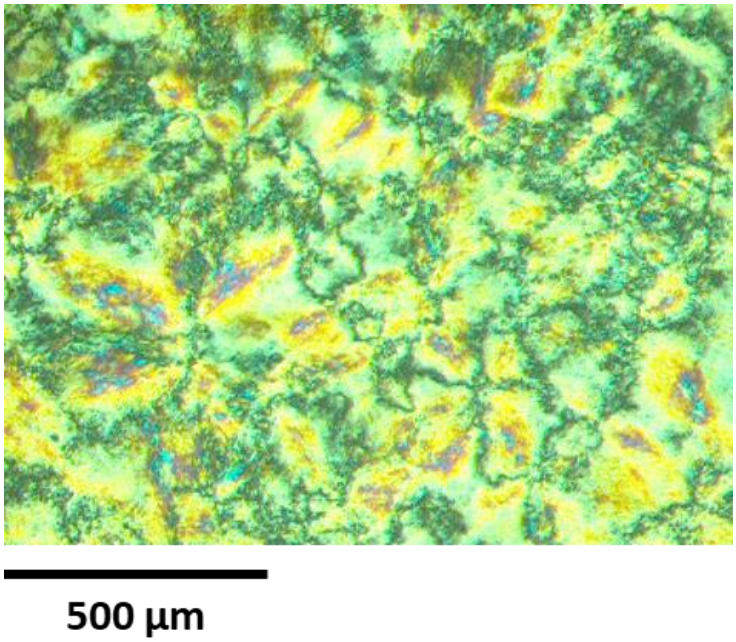

Figure 2.11. Optical micrographs between crossed polars of TAPAm recorded during the first heating at 90 °C.

For the range of temperature between 101 °C and 118 °C, we observed the presence of a mesophase. This was confirmed by XRD experiments, with a pattern recorded at 110 °C (**Figure 2.10c and 2.10e**); we saw four main peaks centred at 2θ = 2.6° (d = 34 Å), 3.9° (d = 22 Å), 4.3° (d = 20 Å), 4.9° (d = 18 Å) and a symmetrical broad halo at 2θ = 20° (d = 4 Å approximately). Same as before, the lower spacing can be attributed to the distance between dendrons and the higher one to the lateral distance between columns. In this case, the phase observed is quite disordered, as we could inferred by DSC, where the enthalpy of the endotherm was only 0.8 kJ/mol (**Table 2.3**). Furthermore, on second heating we observed the same behaviour as first heating in the range of temperatures from 101 °C to 118 °C. It is remarkable that on cooling from

the melt state we did not observe the formation of this phase by DSC nor POM. Therefore, it is suggested that TAPAm should present a monotropic columnar mesophase in the range of temperature from 101 °C to 118 °C.

Calorimetric study by DSC of TAPOx is depicted in **Figure 2.12**, showing first and second heating and cooling scans. On heating we observe one endotherm centred at 89 °C for the first heating and 86 °C for the second heating, which can be attributed to the melting of TAPOx, meanwhile on cooling we observe a peak centred at 73 °C, which can be assigned to the crystallization of TAPOx. According to POM experiments, on heating we did not observe a mesophase below melting point and an isotropic liquid was observed above the endotherm. Moreover, on cooling we did not notice the presence of a mesophase from the melt state. This behaviour was also confirmed by XRD experiments, showing a crystalline phase below the melting point and an isotropic liquid above the endotherm (**Figure 2.S7**). Therefore, TAPOx shows no mesomorphic behaviour. Thus, it seems that the stiffness of the oxazoline ring strongly difficults the packing of tapered groups, avoiding the formation of columnar phases.

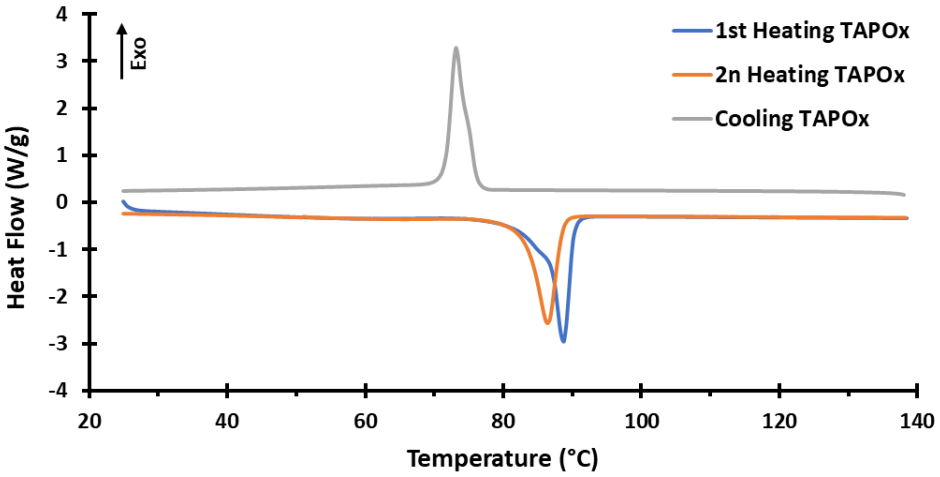

Figure 2.12. Calorimetric analysis of TAPOx; (blue) first heating, (orange) second heating, and (grey) cooling. Scan rate: 10 °C/min.

Thermal stability of TAPAm and TAPOx was studied by TGA (**Figure 2.13**). Onset of thermal weight loss (determined as the temperature corresponding to 5 % mass loss) was 271 °C for TAPAm with 14 % of remaining char yield at 600 °C. TAPOx is slightly more stable, with an onset of the thermal weight loss of 285 °C and a similar char yield at 600 °C (15 %) compared with its amide precursor. In the case of TAPEs, it presents the higher onset of thermal weight loss of the 3 dendronized compounds: 291 °C, but the smallest remaining char yield (12 %). Besides, the thermal degradation of these three dendronized compounds showed a two-step weight loss, as confirmed by DGTA curves (Figure S8). The presence of a hydroxyl group in TAPAm chemical structure can lead to an easy dehydration that could induce the thermal degradation of TAPAm at a lower temperature than TAPOx and TAPEs, which DTGA curve showed the same trend.

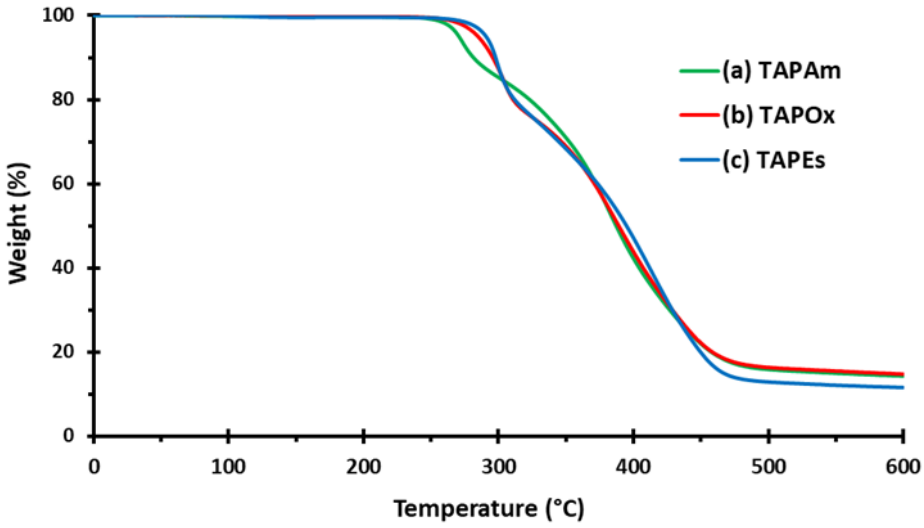

Figure 2.13. TGA thermogram of (a) TAPAm, (b) TAPOx and (c) TAPEs recorded at a heating rate of 10 °C/min in nitrogen atmosphere.

2.3.3. Preliminary polymerization study

As aforementioned, it is described that 2-substituted-2-oxazolines polymerize by *living* cationic ring opening polymerization (CROP). Many procedures to polymerize these compounds can be founded in literature, i.e. Percec and co-workers described the polymerization of 2-[3,4-bis(*n*-alkan-1-yloxy)phenyl]-2-oxazolines using *o*-dichlorobenzene as a solvent at 110 °C and bulk polymerization at 160 °C, with methyl triflate (MeOTf) as an initiator [26]. Apart from MeOTf, a wide variety of initiators have been used, such as sulfonate esters, Lewis acids and alkyl halides among others [10].

Furthermore, several terminating agents have been employed in this type of polymerizations, such as primary, secondary and aromatic amines, hydroxide salts and alcohols, among others [3].

Herein, we describe a preliminary study of polymerization of TAPOx. All the conditions tested in each polymerization of TAPOx are summarized in **Table 2.4**. On our first attempt, we try to synthetize our polymer using methyl tosylate (MeOTs) as an initiator and toluene as a solvent under reflux conditions. We monitored the reaction by ^{1}H NMR; nevertheless, after 12 days of reaction the product was not noticed, and only unreacted monomer was observed at the reaction medium. On a second attempt, we follow the procedure described by Pásztói et al. [66], where benzotrifluoride was used as an environmentally less harmful solvent to polymerize 2-ethyl-2-oxazoline at 100 °C using MeOTs as an initiator. Unfortunately, following the same trend as the first attempt, the polymer was not detected after 10 days of reaction and only unreacted TAPOx was present at the reaction medium.

Therefore, we decided to carry out a bulk polymerization of TAPOx at 130 °C using MeOTs as an initiator. In this case, we could confirm the total conversion of the monomer through ^{1}H NMR analysis (**Figure 2.14a**) and ^{13}C NMR (**Figure 2.14b**) experiments. Regarding ^{1}H NMR analysis, the characteristic signals corresponding to both methylenes in the oxazoline ring at 4.34 and 3.97 ppm (see **Figure 2.6**) disappear and a broad signal corresponding to the main chain of polyoxazoline appears centred at 3.67 ppm. Furthermore, according to ^{13}C NMR experiments, full conversion of TAPOx was also confirmed, since the signal corresponding to the methylene contiguous to nitrogen inside the oxazoline ring, at 55.0 ppm (see **Figure 2.7**), also disappeared. Despite the full conversion of the monomer was confirmed by

NMR, the yield of the polymerization after work-up was only 62 %. This fact indicates us that we must optimize the purification process. Besides, based on the relationship between the signals of the terminating agent added (dodecylamine) and the polymer in ^{1}H NMR, we found that only oligomers were synthetized; in fact, pentamers were obtained.

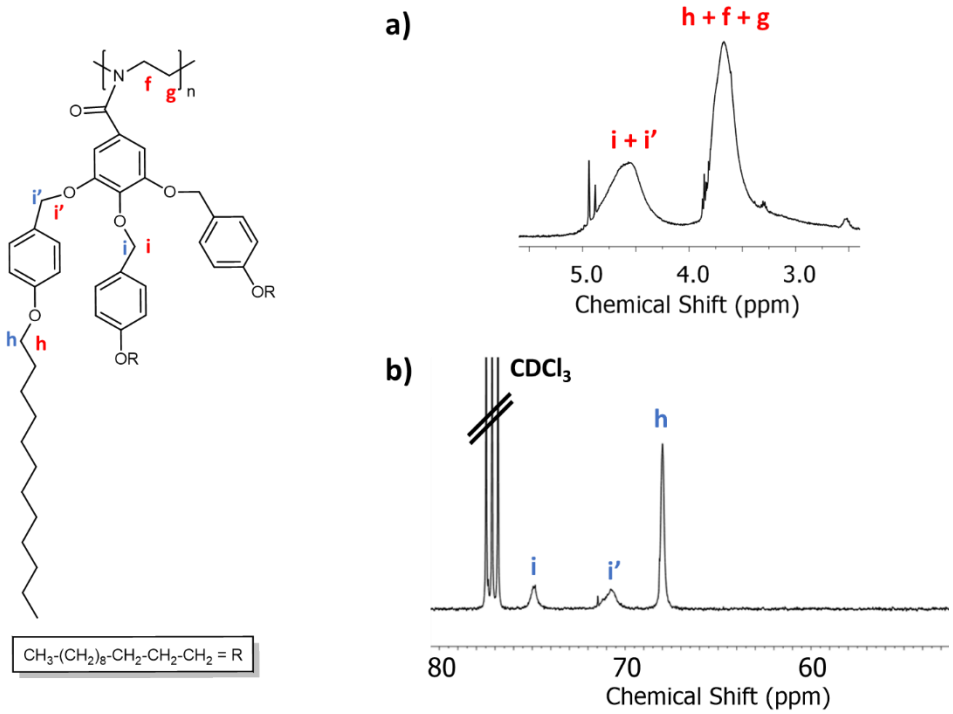

Figure 2.14. Zooms of the NMR spectra of the polyoxazoline derived from TAPOx: a) ^{1}H NMR spectrum between 2.5 - 5.5 ppm (signals labelled in red); and b) ^{13}C NMR spectrum between 50-80 ppm (signals labelled in blue).

Table 2.4. Polymerization reaction conditions of TAPOx monomer (initiator, terminating agent, solvent, and reaction conditions) and the obtained results.

Entry	Initiator (% mol) / Terminating Agent	Solvent	Reaction Conditions	Comments / Yield (%)
1	MeOTs (1) / -	Anhydrous toluene	130 °C; 12 days	Virgin monomer was recovered
2	MeOTs (1) / -	Anhydrous benzotrifluoride	90 °C; 10 days	Virgin monomer was recovered
3	MeOTs (1) / Dodecylamine	-	130°C; 2 h	62

As a complementary analysis, we decided to observe the synthesized oligomers by polarized optical microscopy in order to see whether it presents a mesophase. We found that, on heating, a mesophase was noticed, actually, an homeotropic texture was observed.

It is clear that, the polymerization of TAPOx deserves a deeper study, in order to find the conditions to get a columnar polyoxazolines of quite high molecular weight. This study is in progress and will be the subject of a forthcoming paper.

2.4.Conclusions

A novel mesogenic oxazoline, 2-(3,4,5-tris(4-dodecyloxybenzyloxy)phenyl)-2-oxazoline (TAPOx), was successfully synthetized in 2 steps. Firstly, the amidation in mild conditions of methyl 3,4,5-tris[*p*-(n-dodecan-1-yloxy)benzyloxy]benzoate (TAPEs) using 10 % mol of sodium methoxide as catalyst, since a high yield of the resulting amide (TAPAm) is obtained due to its easy purification by recrystallization (92 %). The second step involves a dehydrative cyclisation of the amide using PPh_3-DDQ system as oxidizing agent. Although the corresponding 2-oxazoline derived monomer was purified by flash column chromatography, TAPOx was also obtained with a good yield (85 %).

Thermal and mesomorphic studies showed that a monotropic columnar mesophase was observed on heating for TAPAm in the range of temperatures

from 101 to 118°C, meanwhile any liquid crystalline texture was detected in the case of TAPOx.

Furthermore, a preliminary research of the cationic ring opening polymerization of TAPOx was carried out, from which it was deduced that a profound investigation should be addressed to find the optimal conditions to get columnar polyoxazolines with high molecular weight.

2.5.References

[1] Andreasch, R. Zur Kenntniss des Allylharnstoffs. Monats. Chem. 5, (1884), 33–46.

[2] Gabriel, S. Zur Kenntniss des Bromäthylamins. Ber. Dtsch. Chem. Ges. 22, (1889), 2220–2223.

[3] Glassner, M., Vergaelen, M. & Hoogenboom, R. Poly(2-oxazoline)s: A comprehensive overview of polymer structures and their physical properties. Polym. Int. 67, (2018), 32–45. https://doi.org/10.1002/pi.5457.

[4] Varanaraja, Z., Kim, J. & Becer, C. R. Poly(2-oxazine)s: A comprehensive overview of the polymer structures, physical properties and applications. Eur. Polym. J. 147, (2021), 110299. https://doi.org/10.1016/j.eurpolymj.2021.110299.

[5] Nishiyama, H. et al. Chiral and C2-Symmetrical Bis(oxazolinylpyridine)rhodium(III) Complexes: Effective Catalysts for Asymmetric Hydrosilylation of Ketones. Organometallics 8, (1989), 846–848. https://doi.org/10.1021/om00105a047.

[6] Do, H. Q., Chandrashekar, E. R. R. & Fu, G. C. Nickel/bis(oxazoline)-catalyzed asymmetric negishi arylations of racemic secondary benzylic electrophiles to generate enantioenriched 1,1-diarylalkanes. J. Am. Chem. Soc. 135, (2013), 16288–16291. https://doi.org/10.1021/ja408561b.

[7] Saravanan, P. & Corey, E. J. A short, stereocontrolled, and practical synthesis of α-methylomuralide, a potent inhibitor of proteasome function. J. Org. Chem. 68, (2003), 2760–2764. https://doi.org/10.1021/jo0268916.

[8] Meyers, A. I., Temple, D. L., Nolen, R. L. & Mihelich, E. D. Oxazolines. IX. Synthesis of homologated acetic acids and esters. J. Org. Chem. 39, (1974), 2778–2783. https://doi.org/10.1021/jo00932a022.

[9] Kobayashi, S. Ethylenimine polymers. Prog. Polym. Sci. 15, (1990), 751–823. https://doi.org/10.1016/0079-6700(90)90011-O.

[10] Aoi, K. & Okada, M. Polymerization of oxazolines. Prog. Polym. Sci. 21, (1996), 151–208. https://doi.org/10.1016/0079-6700(95)00020-8.

[11] Verbraeken, B., Monnery, B. D., Lava, K. & Hoogenboom, R. The chemistry of poly(2-oxazoline)s. Eur. Polym. J. 88, (2017), 451–469. https://doi.org/10.1016/j.eurpolymj.2016.11.016.

[12] Moreadith, R. W. et al. Clinical development of a poly(2-oxazoline) (POZ) polymer therapeutic for the treatment of Parkinson's disease – Proof of concept of POZ as a versatile polymer platform for drug development in multiple therapeutic indications. Eur. Polym. J. 88, (2017), 524–552. https://doi.org/10.1016/j.eurpolymj.2016.09.052.

[13] Li, X. & Yu, H. Side Chain Liquid Crystalline Polymers: Advances and Applications. in Liquid Crystalline Polymers, Volume 2 - Processing and Applications (Eds. Thakur, V. K.; Kessler, M. R.) Vol. 2, pp. 369–386 (Springer Science+Business Media, 2015)

[14] Vicari, L. Optical applications of liquid crystals (Taylor & Francis, 2010).

[15] Bustamante, E. A. S. & Haase, W. Synthesis and characterization of new liquid crystalline monomers for non-linear optics. X-ray study of re-entrant nematic behaviour with smectic-like fluctuations of C-type. Liq. Cryst. 23, (1997), 603–612. https://doi.org/10.1080/026782997208217.

[16] Shih, H. F., Wu, D. Y., Tien, C. L. & Dai, C. L. Optical compensator with switchable modes using polymer stabilized liquid crystals. Opt. Rev. 20, (2013), 218–223. https://doi.org/10.1007/s10043-013-0039-9.

[17] Gin, D. L. & Noble, R. D. Designing the next generation of chemical separation membranes. Science 332, (2011), 674–676. https://doi.org/10.1126/science.1203771.

[18] Zhou, M. et al. New type of membrane material for water desalination based on a cross-linked bicontinuous cubic lyotropic liquid crystal assembly. J. Am. Chem. Soc. 129, (2007), 9574–9575. https://doi.org/10.1021/ja073067w.

[19] Cho, B. K. Nanostructured organic electrolytes. RSC Adv. 4, (2014), 395–405. https://doi.org/10.1039/c3ra45044a.

[20] Sakuda, J. et al. Liquid-crystalline electrolytes for lithium-ion batteries: Ordered assemblies of a mesogen-containing carbonate and a lithium salt. Adv. Funct. Mater. 25, (2015), 1206–1212. https://doi.org/10.1002/adfm.201402509.

[21] Sergeyev, S., Pisula, W. & Geerts, Y. H. Discotic liquid crystals: A new generation of organic semiconductors. Chem. Soc. Rev. 36, (2007), 1902–1929. https://doi.org/10.1039/b417320c.

[22] Funahashi, M. Development of liquid-crystalline semiconductors with high carrier mobilities and their application to thin-film transistors. Polym. J. 41, (2009), 459–469. https://doi.org/10.1295/polymj.PJ2008324.

[23] Rodríguez-Parada, J. M. & Percec, V. Synthesis and characterization of liquid crystalline poly(N-acylethyleneimine)s. J. Polym. Sci. Part A Polym. Chem. 25, (1987), 2269–2279. https://doi.org/10.1002/pola.1987.080250823.

[24] Percec, V., Johansson, G., Schlueter, D., Ronda, J. C. & Ungar, G. Molecular recognition directed self-assembly of tubular supramolecular architectures from building blocks containing monodendrons as exo-receptors and crown- or pseudo-crown-ethers as endo-receptors. Macromol. Symp. 101, (1996), 43–60. https://doi.org/10.1002/masy.19961010107.

[25] Yeardley, D. J. P., Ungar, G., Percec, V., Holerca, M. N. & Johansson, G. Spherical supramolecular minidendrimers self-organized in an 'inverse micellar'-like thermotropic body-centered cubicliquid crystalline phase. J. Am. Chem. Soc. 122, (2000), 1684–1689. https://doi.org/10.1021/ja993915q.

[26] Percec, V. et al. Poly(oxazolines)s with tapered minidendritic side groups. The simplest cylindrical models to investigate the formation of two-dimensional and three-dimensional order by directvisualization. Biomacromolecules 2, (2001), 706–728. https://doi.org/10.1021/bm015550j.

[27] Percec, V., Holerca, M. N., Uchida, S., Yeardley, D. J. P. & Ungar, G. Poly(oxazoline)s with tapered minidendritic side groups as models for the design of synthetic macromolecules with tertiary structure. A demonstration of the limitations of living polymerization in the design of 3-D structures based on single polymer chain. Biomacromolecules 2, (2001), 729–740. https://doi.org/10.1021/bm015559l.

[28] Kim, K. M., Imai, Y., Naka, K. & Chujo, Y. Synthesis and characterization of new side-chain liquid crystalline polyoxazolines. Polym. J. 32, (2000), 657–664. https://doi.org/10.1295/polymj.32.657.

[29] Bhosale, S., Rasool, M., Reina, J. & Giamberini, M. New Liquid Crystalline Columnar Poly(epichlorohydrin-co-ethylene oxide) Derivatives Leading to Biomimetic Ion Channels. Polym. Eng. Sci. 53, (2013), 159–167. https://doi.org/10.1002/pen.23240.

[30] Montané, X., Bhosale, S. V., Reina, J. A. & Giamberini, M. Columnar liquid crystalline polyglycidol derivatives: A novel alternative for proton-conducting membranes. Polymer 66, (2015), 100–109. https://doi.org/10.1016/j.polymer.2015.03.071.

[31] Šakalytė, A., Reina, J. A. & Giamberini, M. Liquid crystalline polyamines containing side dendrons: Toward the building of ion channels based on polyamines. Polymer 54, (2013), 5133–5140. https://doi.org/10.1016/j.polymer.2013.07.027.

[32] Montané, X. et al. Advances in the design of self-supported ion-conducting membranes-new family of columnar liquid crystalline polyamines. Part 1: Copolymer synthesis and membrane preparation. Polymer 105, (2016), 298–309. https://doi.org/10.1016/j.polymer.2016.10.047.

[33] Montané, X. et al. Advances in the design of self-supported ion-conducting membranes – New family of columnar liquid crystalline polyamines. Part 2: Ion transport characterisation and comparison to hybrid membranes. Polymer 105, (2016), 234–242. https://doi.org/10.1016/j.polymer.2016.10.046.

[34] Šakalytė, A., Giamberini, M. & Reina, J. A. Synthesis and characterisation of a monotropic dendritic liquid crystalline aziridine monomer. Liq. Cryst. 41, (2014), 153–162. http://dx.doi.org/10.1080/02678292.2013.845309.

[35] Perrin, D. D. & Armarego, W. L. F. Purification of Laboratory Chemicals. (Pergamon Press, 2009).

[36] Ronda, J. C., Reina, J. A. & Giamberini, M. Self-organized liquid-crystalline polyethers obtained by grafting tapered mesogenic groups onto poly(epichlorohydrin): Toward biomimetic ion channels 2. J. Polym. Sci. Part A Polym. Chem. 41, (2003), 2918–2929. https://doi.org/10.1002/pola.11016.

[37] Bernhard, N. & Wolfgang, S. Simple Method for the Esterification of Carboxylic Acids. Angew. Chemie Int. Edit. 17, (1978), 522–524. https://doi.org/10.1246/bcsj.54.1267.

[38] Holmberg, K. & Hansen, B. Ester Synthesis with Dicyclohexylcarbodiimide Improved by Acid Catalysts. Acta Chem. Scand. B 33, (1979), 410–412. https://doi.org/10.3891/acta.chem.scand.33b-0410.

[39] El-Faham, A. & Albericio, F. Peptide coupling reagents, more than a letter soup. Chem. Rev. 111, (2011), 6557–6602. https://doi.org/10.1021/cr100048w.

[40] Carpino, L. A. & El-Faham, A. The Diisopropylcarbodiimide/1-Hydroxy-7-azabenzotriazole System: Segment Coupling and Stepwise Peptide Assembly. Tetrahedron 55, (1999), 6813–6830. https://doi.org/10.1016/S0040-4020(99)00344-0.

[41] Sheehan, J., Cruickshank, P. & Boshart, G. Notes- A Convenient Synthesis of Water-Soluble Carbodiimides. J. Org. Chem. 26, (1961), 2525–2528. https://doi.org/10.1021/jo01351a600.

[42] Wigman, L. et al. Byproducts of commonly used coupling reagents: Origin, toxicological evaluation and methods for determination. Am. Pharm. Rev. 17, (2014), 1–16.

[43] Klausner, Y. S. & Bodansky, M. Coupling Reagents in Peptide Synthesis. Synthesis-Stuttgart. 1972, (1972), 453–463.

[44] Smith, M. B. Advanced Organic Chemistry: Reactions, mechanisms, and structure. (John Wiley & Sons, Inc., 2020).

[45] Holerca, M. N. et al. Dendronized Poly(2-oxazoline) Displays within only Five Monomer Repeat Units Liquid Quasicrystal, A15 and σ Frank-Kasper Phases. J. Am. Chem. Soc. 140, (2018), 16941–16947. https://doi.org/10.1021/jacs.8b11103.

[46] Ishihara, K., Kuroki, Y., Hanaki, N., Ohara, S. & Yamamoto, H. Antimony-templated macrolactamization of tetraamino esters. Facile synthesis of macrocyclic spermine alkaloids, (±)-buchnerine, (±)-verbacine, (±)-verbaskine, and (±)-verbascenine. J. Am. Chem. Soc. 118, (1996), 1569–1570 (1996). https://doi.org/10.1021/ja953541a.

[47] Han, C., Lee, J. P., Lobkovsky, E. & Porco, J. A. Catalytic ester-amide exchange using group (IV) metal alkoxide-activator complexes. J. Am. Chem. Soc. 127, (2005), 10039–10044. https://doi.org/10.1021/ja0527976.

[48] Movassaghi, M. & Schmidt, M. A. N-heterocyclic carbene-catalyzed amidation of unactivated esters with amino alcohols. Org. Lett. 7, (2005), 2453–2456. https://doi.org/10.1021/ol050773y.

[49] Price, K. E. et al. Mild and efficient DBU-catalyzed amidation of cyanoacetates. Org. Lett. 11, (2009), 2003–2006. https://doi.org/10.1021/ol900435t.

[50] Sabot, C., Kumar, K. A., Meunier, S. & Mioskowski, C. A convenient aminolysis of esters catalysed by 1,5,7-triazabicyclo[4.4.0]dec-5-ene (TBD) under solvent free conditions. Tetrahedron Lett. 48, (2007), 3863–3866. https://doi.org/10.1016/j.tetlet.2007.03.146.

[51] Yang, X. & Birman, V. B. Acyl transfer catalysis with 1,2,4-Triazole anion. Org. Lett. 11, (2009), 1499–1502. https://doi.org/10.1021/ol900098q.

[52] Meher, L. C., Vidya Sagar, D. & Naik, S. N. Technical aspects of biodiesel production by transesterification - A review. Renew. Sustain. Energy Rev. 10, (2006), 248–268 (2006). https://doi.org/10.1016/j.rser.2004.09.002.

[53] Ohshima, T. et al. Sodium methoxide: A simple but highly efficient catalyst for the direct amidation of esters. Chem. Commun. 48, (2012), 5434–5436. https://doi.org/10.1039/c2cc32153j.

[54] Johansson, G., Percec, V., Ungar, G. & Abramic, D. Molecular Recognition Directed Self-Assembly of Tubular Liquid Crystalline Supramolecular Architectures from Taper Shaped (15-Crown-5)methyl 3,4,5-Tris(p-alkoxybenzyloxy)benzoates and (15-Crown-5)methyl 3,4,5-Tris(p-dodecyloxy)benzoate. J. Chem. Soc. Perkin Trans. 1 1994, (1994), 447–459. https://doi.org/10.1039/p19940000447.

[55] Zhou, P., Blubaum, J. E., Bums, C. T. & Natale, N. R. The Direct Synthesis of 2-Oxazolines from Carboxyfic Esters Using Lanthanide Chloride as Catalyst. Tetrahedron Lett. 38, (1997), 7019–7020. https://doi.org/10.1016/S0040-4039(97)01641-9.

[56] Ilkgul, B., Gunes, D., Sirkecioglu, O. & Bicak, N. Synthesis of 2-oxazolines via boron esters of N-(2-hydroxyethyl) amides. Tetrahedron Lett. 51, (2010), 5313–5315. https://doi.org/10.1016/j.tetlet.2010.07.167.

[57] Mohammadpoor-Baltork, I., Moghadam, M., Tangestaninejad, S., Mirkhani, V. & Hojati, S. F. Environmental-friendly synthesis of oxazolines, imidazolines and thiazolines catalyzed by tungstophosphoric acid. Catal. Commun. 9, (2008), 1153–1161. https://doi.org/ 10.1016/j.catcom.2007.10.026.

[58] Bandgar, B. P. & Pandit, S. S. Direct synthesis of 2-oxazolines from carboxylic acids using 2-chloro-4,6-dimethoxy-1,3,5-triazine under mild conditions. Tetrahedron Lett. 44, (2003), 2331–2333. https://doi.org/10.1016/S0040-4039(03)00251-X.

[59] Kangani, C. O. & Day, B. W. A novel and direct synthesis of 1,3,4-oxadiazoles or oxazolines from carboxylic acids using cyanuric chloride/indium. Tetrahedron Lett. 50, (2009), 5332–5335. https://doi.org/10.1016/j.tetlet.2009.07.032.

[60] Verbraeken, B., Lava, K. & Hoogenboom, R. Poly(2-oxazoline)s. in Encyclopedia of Polymer Science and Technology (John Wiley & Sons, Inc., 2002).

[61] Huang, H., Yang, W., Chen, Z., Lai, Z. & Sun, J. A mild catalytic synthesis of 2-oxazolines: Via oxetane ring-opening: Rapid access to a diverse family of natural products. Chem. Sci. 10, (2019), 9586–9590. https://doi.org/10.1039/c9sc03843d.

[62] Holerca, M. N. & Percec, V. 1H NMR Spectroscopic Investigation of the Mechanism of 2- Substituted-2-Oxazoline Ring Formation and of the Hydrolysis of the Corresponding Oxazolinium Salts. European J. Org. Chem. 2000, (2000), 2257–2263.

[63] Xu, Q. & Li, Z. A facile synthesis of 2-oxazolines using a PPh3-DDQ system. Tetrahedron Lett. 50, (2009), 6838–6840. https://doi.org/10.1016/j.tetlet.2009.09.127.

[64] Kagiya, T. & Matsuda, T. Selective Polymerization of 2-Isopropenyl-2-oxazoline and Cross-linking Reaction of the Polymers. Polym. J. 3, (1972), 307–314. https://doi.org/10.1295/polymj.3.307.

[65] Morimoto, H., Fujiwara, R., Shimizu, Y., Morisaki, K. & Ohshima, T. Lanthanum(III) triflate catalyzed direct amidation of esters. Org. Lett. 16, (2014), 2018–2021. https://doi.org/10.1021/ol500593v.

[66] Pásztói, B. et al. Quasiliving cationic ring-opening polymerization of 2-ethyl-2-oxazoline in benzotrifluoride, as an alternative reaction medium. Polymer 212, (2021), 123165. https://doi.org/10.1016/j.polymer.2020.123165.

2.6.Supporting Information

Synthesis of *N*-(2-hydroxyethyl)-3,4,5-tris(4-dodecyloxybenzyloxy) benzamide (TAPAm)

Direct amidation method using DCC as coupling agent. In a round-bottomed flask, 1.01 g of TAPAc (1.01 mmol) was dissolved into 10 mL of chloroform. The solution was stirred at 0 °C in an ice-water bath for 15 min. Then, DMAP (102.2 mg, 0.83 mmol) was added, and the solution was kept under stirring at 0 °C during 15 min more. After that, DCC (210.9 mg, 1.02 mmol) was added, leaving the magnetic stirring for additionally 15 min at the same temperature. At this point, ethanolamine (0.18 mL, 2.98 mmol) was added dropwise. When the addition of ethanolamine was completed, the reaction mixture was warmed to room temperature and kept under stirring for 4 days, during which it was monitored by TLC using n-hexane/ethyl acetate (1:2) as mixture of eluents (A complete conversion of TAPAc was detected after 4 days of reaction). At this time, the crude of the reaction was filtered to eliminate the undesirable N, N'-dicyclohexylurea and the solvent was eliminated under vacuum at the rotavapor. The resulting orange solid was purified by flash column chromatography using a gradient of n-hexane/ethyl acetate (starting proportion = 2:1) as mixture of eluents. Nevertheless, a mixture of TAPAm and N,N'-dicyclohexylurea was always isolated.

CHAPTER 2

Synthesis of 2-(3,4,5-tris(4-dodecyloxybenzyloxy)phenyl)-2-oxazoline (TAPOx)

Direct synthesis of TAPOx from TAPAm using thionyl chloride ($SOCl_2$) and DBU. In a round bottomed flask, 400.5 mg of TAPAm (0.38 mmol) were dissolved in 5 mL of DCM at room temperature. After that, DBU (346.3 mg, 2.31 mmol) was added, which was followed by the dropwise addition of thionyl chloride (147.4 mg, 1.15 mmol). The reaction was monitored by TLC using n-hexane/ethyl acetate (1:2) as mixture of eluents. After complete conversion of TAPAm (2 h), the formation of TAPOx was not detected by ^1H NMR in the crude mixture.

Direct synthesis of TAPOx from TAPEs using Lanthanum (III) salts as catalyst. Anhydrous Lanthanum (III) chloride ($LaCl_3$) (5, 10, 20 % mol respect to TAPEs) or anhydrous Lanthanum (III) triflate ($LaTf_3$) (10 % mol regarding TAPEs) and ethanolamine (0.15 mL, 2.48 mmol) were dissolved in 10 mL of dry toluene inside a two neck round bottom flask under argon flow conditions. Subsequently, n-BuLi (0.90 mL, 2.25 mmol) was added dropwise at 0 °C, keeping the mixture under stirring for 15 min. Then, the reaction mixture was warmed to reflux at 100 °C, when TAPEs (1.01 g, 0.99 mmol) was added carefully. The reaction was monitored by TLC using n-hexane/ethyl acetate (1:2) as mixture of eluents. When a total conversion of TAPEs was achieved (24 h), the crude mixture was cooled to RT and washed several times with water. Finally, the organic layer was dried over anhydrous $MgSO_4$, and the solvent was vacuum evaporated. After that, the obtained solid was

purified by flash column chromatography using n-hexane/ethyl acetate (2:1) as mixture of eluents. Nonetheless, TAPOx was not isolated in any of the collected fractions.

Preliminary polymerization studies

Polymerization of TAPOx with toluene as solvent. In a previously flame-dried Schlenk tube, 500.0 mg of TAPOx monomer (0.49 mmol) were dissolved in 5.0 mL of dry toluene. Then, 1 % of methyl tosylate were added at room temperature. After that, the tube was immersed into a preheated oil bath at 130 °C and kept under stirring in an argon flow conditions for 12 days. The reaction was monitored by ^{1}H NMR. However, only unreacted TAPOx monomer was detected.

Polymerization of TAPOx with benzotrifluoride as solvent. In a previously flame-dried Schlenk tube, 503.0 mg of TAPOx monomer (0.49 mmol) were dissolved in 2.5 mL of anhydrous benzotrifluoride. Then, 1 % of methyl tosylate were added at room temperature. After that, the tube was immersed into a preheated oil bath at 90 °C and kept under stirring in an argon flow conditions for 10 days. The reaction was monitored by ^{1}H NMR. Nevertheless, only unreacted TAPOx monomer was detected after 10 days of reaction.

CHAPTER 2

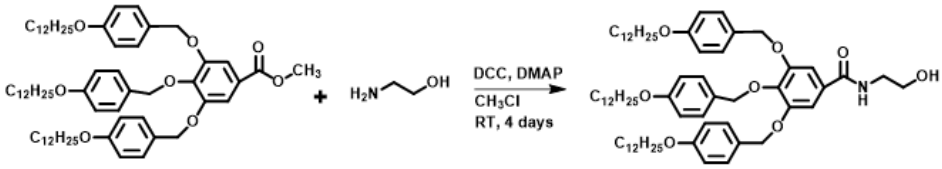

Figure 2.S1. Amidation of TAPAc with ethanolamine.

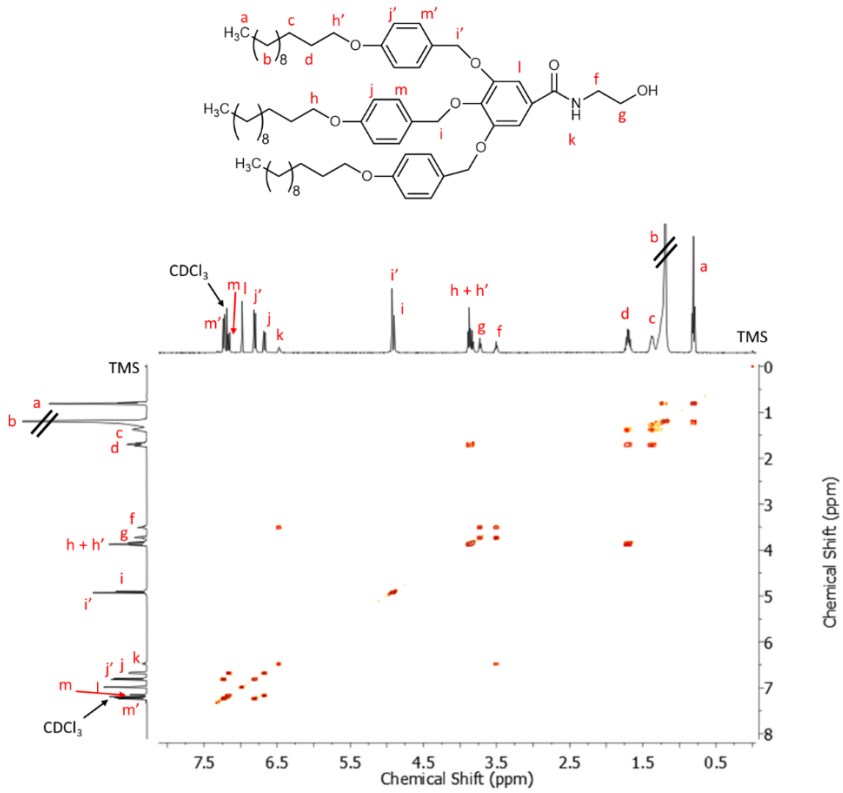

Figure 2.S2. COSY NMR spectra of TAPAm.

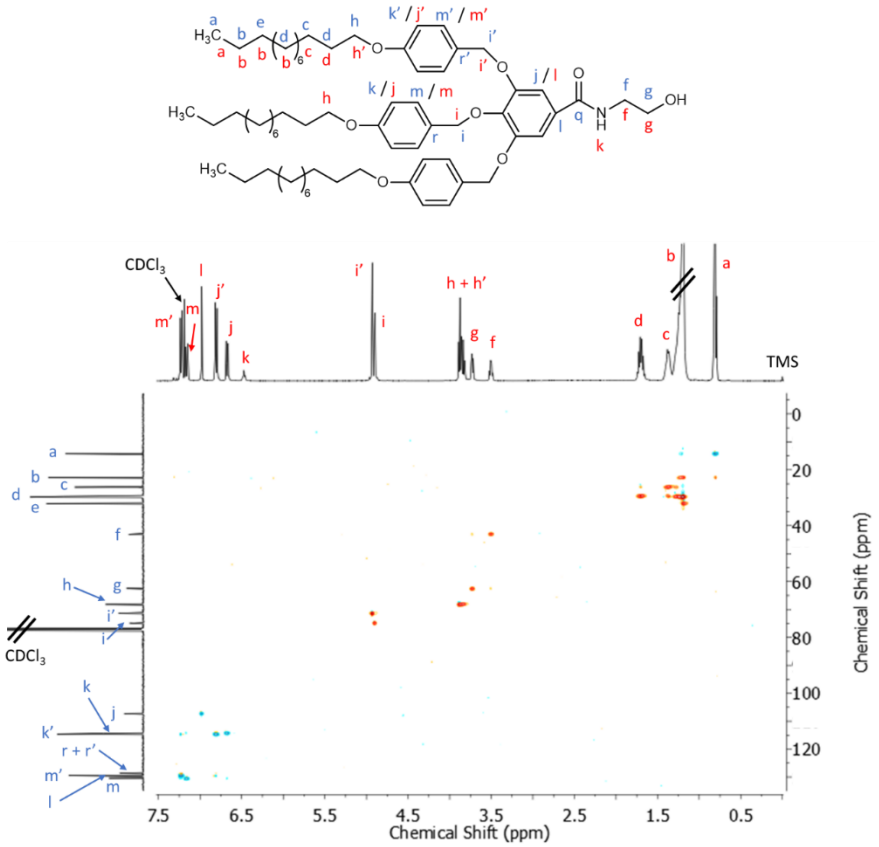

Figure 2.S3. HSQC spectra of TAPAm. In the spectra, the blue signals correspond to -CH- and -CH_3 signals, while the red ones correspond to -CH_2- signals.

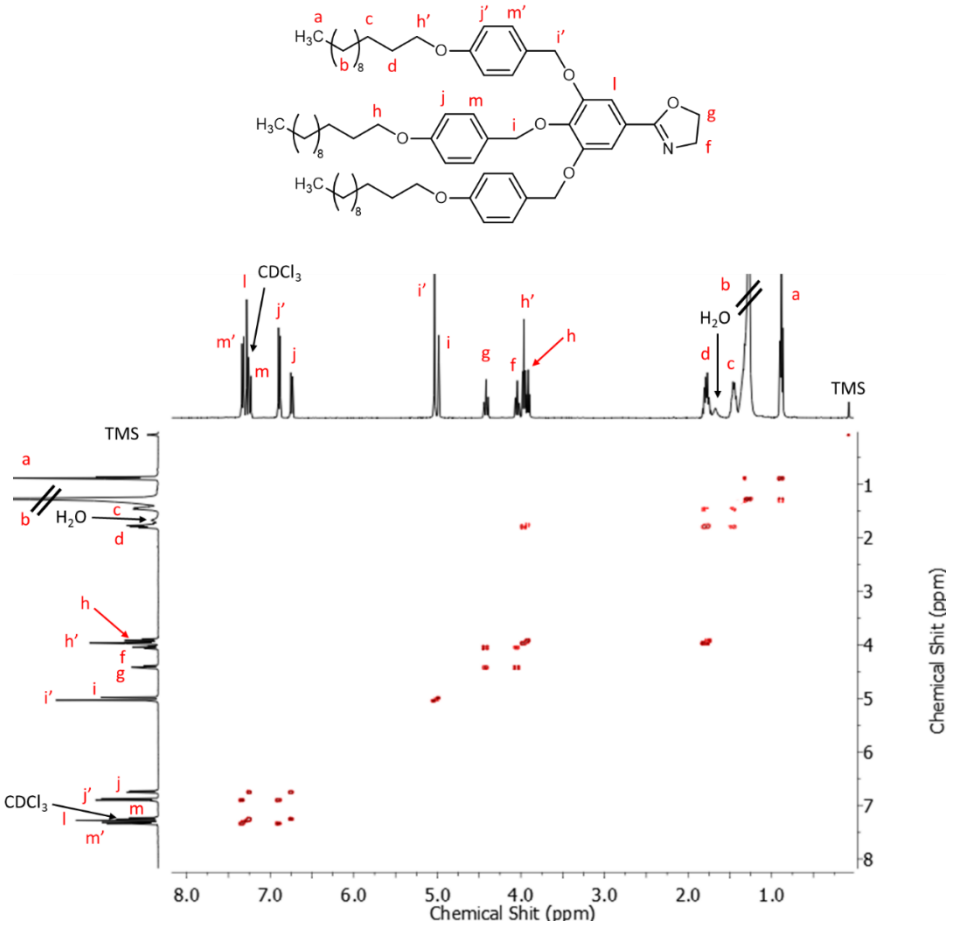

Figure 2.S4. COSY spectra of TAPOx.

CHAPTER 2

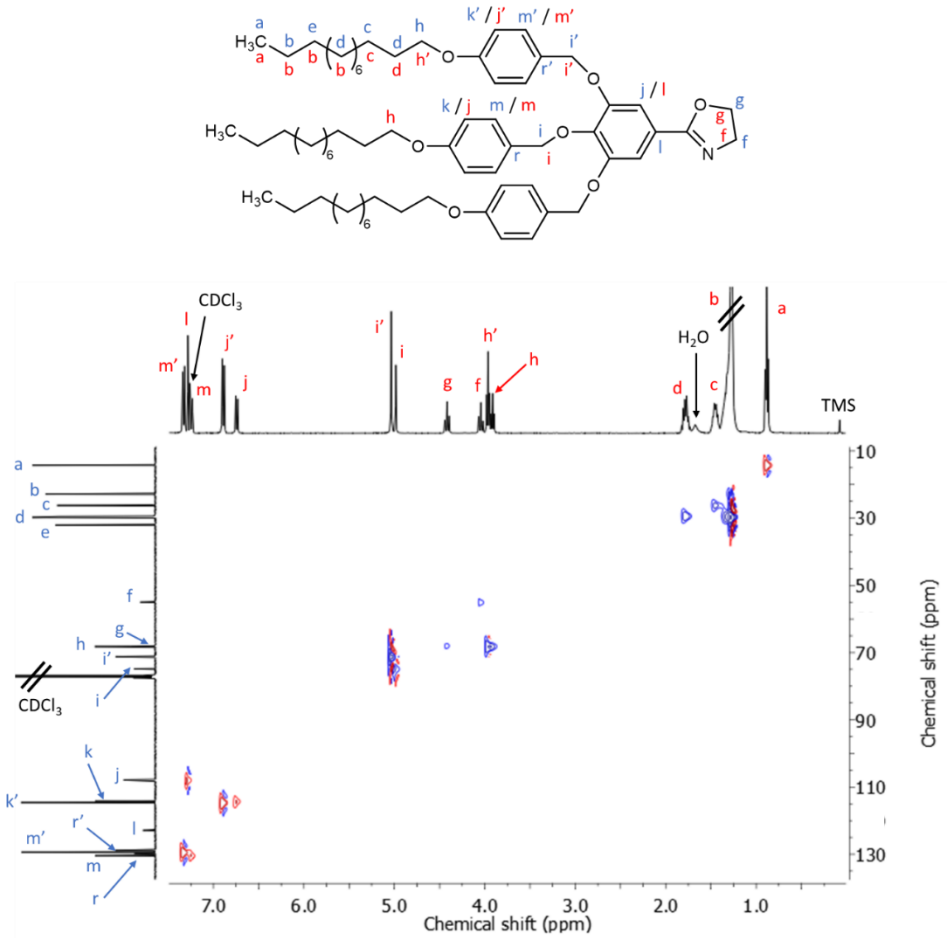

Figure 2.S5. HSQC spectra of TAPOx. In the spectra, the blue signals correspond to -CH- and -CH_3 signals, while the red ones correspond to -CH_2- signals.

CHAPTER 2

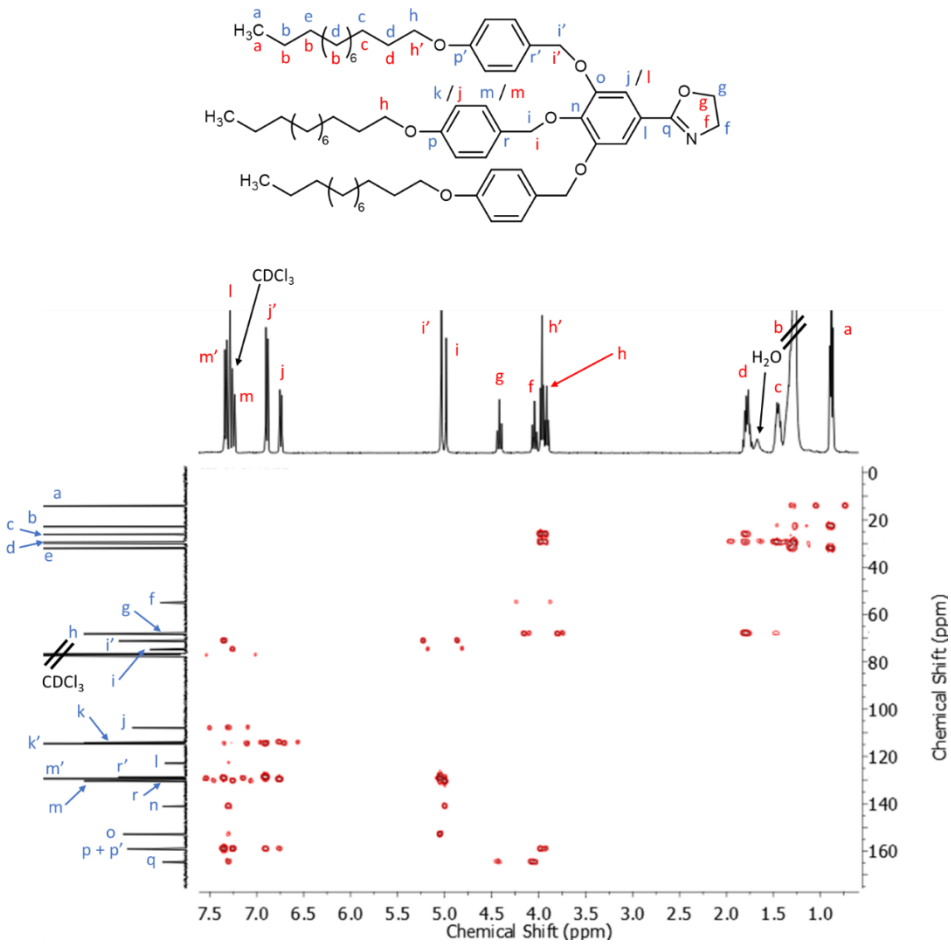

Figure 2.S6. HMBC spectra of TAPOx.

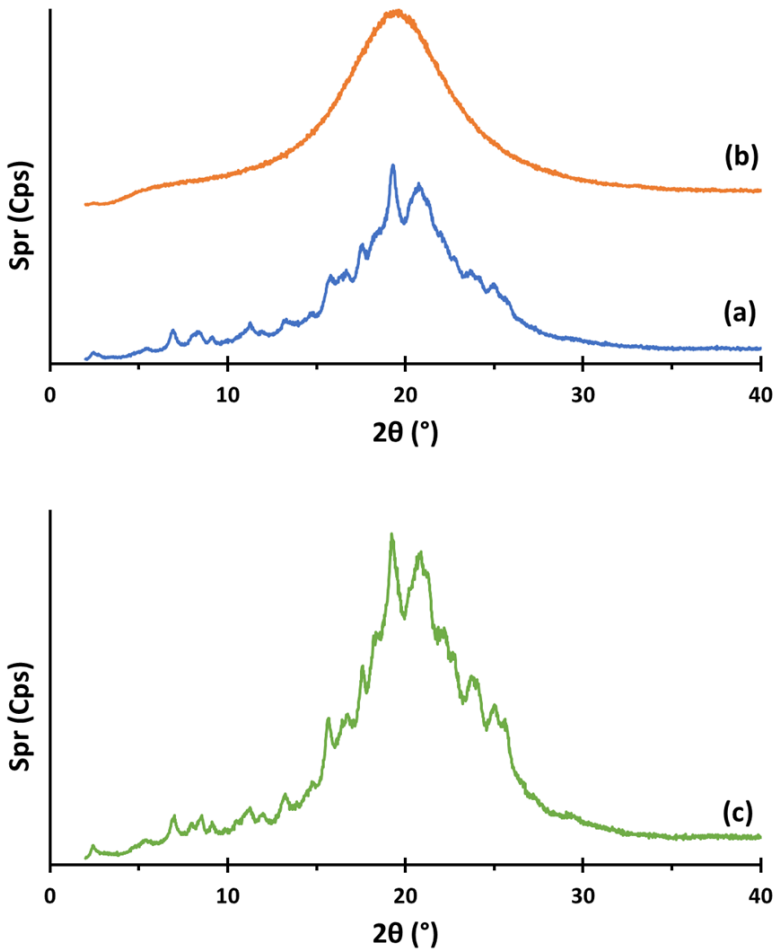

Figure 2.S7. XRD patterns of TAPOx recorded on heating at: (a) 70 °C and (b) 100 °C on first heating; and (c) 70 °C on second heating.

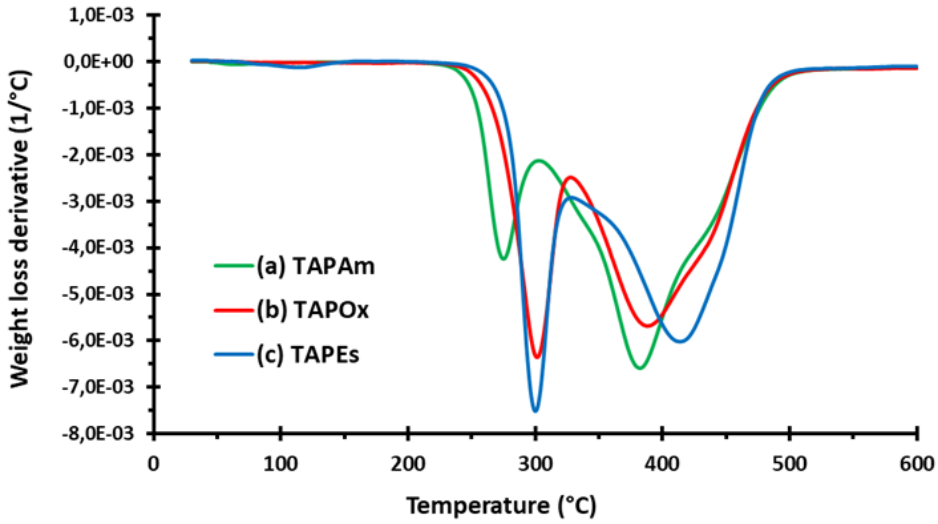

Figure 2.S8. DTGA curves of (a) TAPAm, (b) TAPOx and (c) TAPEs recorded at a heating rate of 10 °C/min in nitrogen atmosphere.

UNIVERSITAT ROVIRA I VIRGILI
COLUMNAR LIQUID-CRYSTALLINE POLYMERS CONTAINING NITROGEN AT THE BACKBONE TO BE USED TO PREPARE ION-TRANSPORT MEMBRANES
Jordi Guardià Blanch

Chapter 3

Synthesis and Characterization of Dendronized Side Chain Liquid Crystalline Poly(2-oxazoline)s towards Biomimetic Ion Channels

(Eur. Poly. J. 196, (2023), 112273)

UNIVERSITAT ROVIRA I VIRGILI
COLUMNAR LIQUID-CRYSTALLINE POLYMERS CONTAINING NITROGEN AT THE BACKBONE TO BE USED TO PREPARE ION-TRANSPORT MEMBRANES
Jordi Guardià Blanch

CHAPTER 3

3.1.Introduction

Nowadays, most of polymer proton exchange membranes are based on perfluorosulfonic acid ionomer (PFSI). Among them, Nafion® (a registered trademark of DuPont Co.) based membranes are the most used due to their excellent electrochemical stabilities, as well as proton conductivities. However, Nafion® presents some drawbacks: (I) an elevated cost due to its complicated manufacturing process, (II) insufficient resistance to methanol crossover and (III) poor mechanical and chemical stability at high temperatures [1]. In order to overcome these drawbacks, other types of polymers have been investigated in recent years [2,3].

Side chain liquid crystalline polymers (SCLCPs) have raised a great interest due to their self-assembly ability, which provides them unique mechanical, optical and electrical properties. For this reason, SCLCPs have been used in a wide range of applications such as optical devices [4], membrane separation [5,6] and solid polymer electrolytes [7,8], among others.

In the second half of 1960's, four independent research groups reported the synthesis of different poly(2-oxazoline)s [9–12]. These groups proposed their synthesis by thermally induced cationic ring-opening polymerization (CROP). Poly(2-alkyl/aryl-2-oxazoline)s (PAOx) are a family of polymers that has raised a great interest, since their properties can be easily modified by end-group modification, initiator modification, as well as by modifying the pendant group of the 2-substituted-2-oxazoline monomer [13].

In recent years, PAOx received on-going research interest in the biomedical field, due to their biocompatibility [14–17], low toxicity, protein adsorption

and stealth behaviour; all these features are similar to those of poly(ethylene glycol) (PEG) (also known as poly(ethylene oxide) (PEO)). Actually, PAOx are an emerging class of polymers who could substitute, even outperform PEG, regarding its increased antifouling behaviour [18–20]. Sedlacek and co-workers developed a method for the synthesis of superhydrophilic PAOx, obtaining poly(2-methoxymethyl-2-oxazoline) which is the most hydrophilic PAOx reported to date [19]. Furthermore, Percec and co-workers reported the first liquid crystalline poly(2-oxazoline) synthesized by CROP, which contains a side chain mesogenic group, describing the synthesis of a SCLC poly(2-oxazoline) [21,22].

During the last two decades, our group has mainly focused on the synthesis of dendronized liquid crystalline polyethers [23,24] and polyamines [25–27] by grafting a tapered group on these polymers as a post polymerization procedure. This tapered group induces the self-assembly of the polymer into columnar structures, which contain an inner channel formed by the polyether or the polyamine main chain, respectively, that work as an ion transport channel. However, in the case of the polyamines synthetized by us, they exhibit a strong tendency to crystallize, which results in poor mechanical properties and brittleness. This can be due either to the low molecular weight of the polyamine and the presence of free hydroxyl groups contained in the pendant group of the polymer main chain. However, supported membranes based on these SCLC polyamines showed a remarkable proton transport [26,27].

Hence, in this article we describe the synthesis and characterization of novel liquid crystalline dendronized poly(2-oxazoline)s, poly(2-(3,4,5-tris(4-dodecyloxybenzyloxy)phenyl)-2-oxazoline)s (PTOx). PTOx has been

successfully synthetized by *living* CROP, using methyl trifluoromethanesulfonate (MeOTf) as an initiator and morpholine as a terminating agent, after testing several initiators and terminating agents. Besides, the "living" character of this cationic ring-opening polymerization allowed us to precisely control the final molecular weight of the synthesized poly(2-oxazoline)s, obtaining a family of acyl-substituted poly(ethyleneimine)s in a range between 20 and 60 kDa. Due to the presence of nitrogen in the polymer backbone, PTOx can be a promising candidate material to prepare membranes able to transport different ions. This new type of polymer should present improved mechanical properties, in comparison with previously reported polyamines, due to the absence of free hydroxyl groups, and higher and controlled molecular weight.

3.2.Experimental section

3.2.1. Materials

Methyl trifluoromethanesulfonate (MeOTf, ≥98 %), 1-dodecylamine (98 %), piperidine (99 %), anhydrous benzotrifluoride (BTF, ≥99 %), methyl *p*-toluenesulfonate (MeOTs, 98 %), 2-(isopropylamino)ethanol (70 %) and chlorobenzene were supplied by Sigma Aldrich. 2,3-dichloro-5,6-dicyano-1,4-benzoquinone (DDQ, 98 %) and morpholine (99 %) were purchased from Alfa Aesar. Triphenylphosphine (PPh_3, 99 %) and benzyl bromide (98 %) were supplied by Across Organics, while dichloromethane (DCM), toluene and *o*-dichlorobenzene (*o*-DCB) were purchased from Scharlab. Furthermore,

toluene, chlorobenzene, *o*-DCB, morpholine and 2-(isopropylamino)ethanol were dried prior to use according to literature [28].

3.2.2. Synthesis of 2-(3,4,5-tris(4-dodecyloxybenzyloxy) phenyl)-4,5-dihydro-1,3-oxazole) (TAPOx)

2-(3,4,5-tris(4-dodecyloxybenzyloxy)phenyl)-4,5-dihydro-1,3-oxazole) (TAPOx) monomer was synthetized following a slight modification of a reported procedure that involved easier workup and higher yield [29]:

In a previously dried Schlenk tube, 2.61 g of PPh_3 (9.95 mmol) and 2.30 g of DDQ (10.14 mmol) were dissolved in 80 mL of dry DCM under argon atmosphere. Then, the mixture was stirred for 3 min at room temperature (RT = 25 ± 5 °C). At once, 7.04 g of *N*-(2-hydroxyethyl)-3,4,5-tris(4-dodecyloxybenzyloxy)benzamide (TAPAm) (6.80 mmol) was then added. The reaction was monitored by TLC using n-hexane/ethyl acetate (1:2) as mixture of eluents. After 20 min, when a complete conversion of TAPAm was reached, the crude mixture was washed with an aqueous NaOH solution (5 wt. %, 80 mL). After that, the separated water layer was back-extracted with DCM (50 mL x 4). The two organic layers were combined and washed together with brine solution, dried over anhydrous $MgSO_4$ and the solvent was vacuum evaporated. At this point, the brown solid was purified by recrystallization twice with ethanol. Finally, the product was dried under vacuum at 40 °C overnight to yield 6.16 g of a white solid (89 %).

^{1}H NMR [$CDCl_3$, δ, ppm]: 7.25 (d, 4H, -O-**Ar-H**-CH_2-O-Ar-C=N- from 2 and 6 positions of the lateral benzylic units), 7.21 (s, 2H, **Ar-H**-C=N-), 7.17 (d, 2H, -O-**Ar-H**-CH_2-O-Ar-C=N- from 2 and 6 positions of the central benzylic unit), 6.83 (d, 4H, -O-**Ar-H**-CH_2-O-Ar-C=N- from 3 and 5 positions of the lateral benzylic units), 6.67 (d, 2H, -O-**Ar-H**-CH_2-O-Ar-C=N- from 3 and 5 positions of the central benzylic unit), 4.96 (s, 4H, -**CH_2**-O-Ar-C=N- in lateral benzylic units), 4.91 (s, 2H, -**CH_2**-O-Ar-C=N- in central benzylic unit), 4.34 (t, 2H, -C=N-CH_2-**CH_2**-O-), 3.97 (t, 2H, -C=N-**CH_2**-CH_2-O-), 3.89 (t, 4H, -Ar-O-**CH_2**-$(CH_2)_{10}$-CH_3 in lateral benzylic units), 3.84 (t, 2H, -Ar-O-**CH_2**-$(CH_2)_{10}$-CH_3 in central benzylic unit), 1.70 (m, 6H, -Ar-O-CH_2-**CH_2**-$(CH_2)_9$-CH_3), 1.38 (m, 6H, -Ar-O-CH_2-CH_2-**CH_2**-$(CH_2)_8$-CH_3), 1.20 (m, 48H, -Ar-O-CH_2-CH_2-CH_2-(**$(CH_2)_8$**-CH_3), 0.81 (t, 9H, -Ar-O-CH_2-$(CH_2)_{10}$-**CH_3**).

^{13}C NMR [$CDCl_3$, δ, ppm]: 164.7 (-**C**=N-), 159.1 (**ArC**-O-$(CH_2)_{11}$-CH_3 in lateral and central benzylic units), 152.9 (**ArC** meta to -C=N-), 141.2 (**ArC** para to -C=N-), 130.4 (**ArC** meta to -O-$(CH_2)_{11}$-CH_3 in central benzylic unit), 129.7 (**ArC**-CH_2-O-Ar-C=N- in central benzylic unit), 129.4 (**ArC** meta to -O-$(CH_2)_{11}$-CH_3 in lateral benzylic units), 128.9 (**ArC**-CH_2-O-Ar-C=N- in lateral benzylic units), 122.9 (**ArC**-C=N-), 114.6 (**ArC** ortho to -O-$(CH_2)_{11}$-CH_3 in lateral benzylic units), 114.2 (**ArC** ortho to -O-$(CH_2)_{11}$-CH_3 in central benzylic unit), 107.9 (**ArC** ortho to -C=N-), 74.8 (-**CH_2**-O-Ar-C=N- in central benzylic unit) 71.2 (-**CH_2**-O-Ar-C=N- in lateral benzylic units), 68.2 (-**CH_2**-$(CH_2)_{10}$-CH_3 in central and lateral benzylic units), 67.9 (-C=N-CH_2-**CH_2**-O-), 55.0 (-C=N-**CH_2**-CH_2-O-), 32.1 (-**CH_2**-CH_2-CH_3), 29.8-29.5 (-**$(CH_2)_6$**-CH_2-CH_3 and -**CH_2**-$(CH_2)_9$-CH_3), 26.2 (-**CH_2**-$(CH_2)_8$-CH_3), 22.8 (-**CH_2**-CH_3), 14.3 (-**CH_3**).

FT-IR (cm^{-1}): 2950 (ν (C-H) in -CH_3 (asymmetric)); 2917 – 2848 (ν (C-H) in -CH_3 (symmetric) and -CH_2- (asymmetric and symmetric)); 1643 (ν (C=N));

1588 (ν (C=C-C aromatic)); 1514 (ν (C=C-C aromatic)); 1245 (ν (=C-O-C) asymmetric); 818 (δ (C-H) *p*-disubstitution).

3.2.3. Synthesis of poly(2-(3,4,5-tris(4-dodecyloxybenzyloxy) phenyl)2-oxazoline)s (PTOx) (Scheme 1)

From all the attempts, the best conditions for the polymerization of TAPOx monomer to achieve "living" behaviour are summarized as follows:

A previously flame dried Schlenk tube was filled with TAPOx (0.5 g, 0.5 mmol) and kept under vacuum for 30 min. After that, the tube was immersed in a previously heated oil bath at 105 °C. When TAPOx was melted, the appropriate amount of dry chlorobenzene was added to reach 1.0 M concentration inside the Schlenk tube (considering the amount of chlorobenzene that is already added with the initiator). Then, the initiator (MeOTf) was added via syringe according to the desired degree of polymerization (DP) from a freshly prepared solution of the initiator in dry chlorobenzene ([MeOTf] = 0.135 M). The mixture was stirred until ^{1}H NMR spectrum indicated almost complete conversion of the monomer (≥93 %). Then, a large excess of morpholine (200 μL) was added to the reaction mixture, acting as a terminating agent. After 30 min, the crude mixture was precipitated twice in a cold KOH solution (0.1 M). Finally, the product was dried under vacuum at 50 °C until constant weight to obtain a beige solid. Monomer conversion was estimated by ^{1}H NMR, comparing the integration of the signal attributed to the methylene contiguous to the nitrogen atom of the monomer oxazoline ring (3.97 ppm) with the integration of the signal

attributed to the methyl groups of the long aliphatic chain of the tapered side dendron. The number of each member of the family indicates the expected quantity of repeating units it contains. NMR and FT-IR data of PTOx40 is shown below:

^{1}H NMR [**Figure 3.1**, $CDCl_3$, δ, ppm]: 7.34 – 6.25 (Ar), 5.23 – 4.20 (i, i'), 4.03 – 3.42 (f, g, s, y, 1), 2.35 (x) 1.62 (2), 1.19 (3-11), 0.81 (12).

^{13}C NMR [**Figure 3.3**, $CDCl_3$, δ, ppm]: 171.8 (q), 158.9 (VIII), 152.9 (III), 138.9 (IV), 129.9 (VI), 129.5 (I, VI'), 128.7 (V), 114.2 (VII), 106.7 (II), 74.9 (i), 70.8 (i'), 68.2 (1, y), 53.0 (x), 46.1 (f, g), 32.1 (10), 29.8 (2, 4 – 9), 26.3 (3), 22.8 (11), 14.3 (12).

FT-IR [**Figure 3.S1**, cm^{-1}]: 2951 (ν (C-H) in $-CH_3$ (asymmetric)); 2920 – 2851 (ν (C-H) in $-CH_3$ (symmetric) and $-CH_2-$ (asymmetric and symmetric)); 1613 (ν (C = O)); 1584 (ν (C=C-C aromatic)); 1512 (ν (C=C-C aromatic)); 1242 (ν (=C-O-C) asymmetric); 822 (δ (C-H) *p*-disubstitution).

3.2.4. Characterization

Thermogravimetric analysis (TGA). Thermal stability studies were carried out in ALU OXIDE crucibles of 70 μL (ME-24123) with a Mettler Toledo TGA2 thermobalance. All samples, weighing around 6 – 8 mg, were heated between 30 and 600 °C at a heating rate of 10 °C/min in N2 atmosphere with a flow rate of 50 cm3/min. The equipment was previously calibrated with indium (156.6 °C) and aluminum (660.3 °C) pearls.

Differential scanning calorimetry (DSC). Calorimetric analyses were carried out on a Mettler DSC-821 instruments calibrated using indium (156.6 °C) and zinc (419.6 °C) pearls. Samples were placed in an aluminum standard crucible of 40 μL with pierced lids (between 4 – 6 mg of sample), which were analysed in N_2 atmosphere (gas flow rate of 50 cm^3/min). Heating and cooling rate of 10 °C/min was always employed.

Polarized optical microscopy (POM). LC mesophases were investigated by polarized optical microscopy (POM). The textures of the samples were observed with an Axiolab Zeiss optical microscope equipped with a Linkam TP92 hot stage and a Moticam S6 digital camera.

Nuclear magnetic resonance (NMR) spectroscopy. All synthesized compounds were characterized by ^1H NMR and ^{13}C NMR spectra, which were recorded in deuterated chloroform ($CDCl_3$) with a Bruker Avance Neo 400 MHz spectrometer (^1H – 400 MHz; ^{13}C – 100.4 MHz) at RT (25 ± 5 °C). The chemical shifts were given in parts per million (ppm) from TMS (Tetramethylsilane) in ^1H NMR spectra, while the central peak of the solvent was taken as a reference in the case of ^{13}C NMR spectra.

Fourier transform infrared (FT-IR) spectroscopy. FT-IR spectra were recorded on an FT/IR-6700 spectrophotometer from JASCO in the wavelength range of 4000 – 400 cm^{-1} with a resolution of 4 cm^{-1} in the absorbance mode. This device is equipped with an attenuated total reflection accessory (ATR)

with thermal control and a diamond crystal (Golden Gate heated single reflection diamond ATR from Specac-Teknokroma). The spectra were recorded at RT (25 ± 5 °C) from the solid-state pure compounds.

X-ray diffraction (XRD). X-ray diffraction measurements (XRD) were made using a Bruker-AXS D8-Advance diffractometer with vertical θ-θ goniometer, incident- and diffracted-beam Soller slits of 2.5 °, a fixed 0.5 ° receiving slit and an air-scattering knife on the sample surface. The angular 2θ range was between 2 and 40 °. The data were collected with an angular step of 0.02 ° at a step/time of 0.5 s. Cukα radiation was obtained from a copper X-ray tube operated at 40 kV and 40 mA. Diffracted X-rays were detected with a PSD detector LynxEye-XE-T with an opening angle of 2.9 °. The sample was placed inside an MTC-LOWTEMP chamber for in-situ temperature analysis.

Size exclusion chromatography (SEC). Molecular weight analysis was performed via size exclusion chromatography (SEC) using an Agilent 1200 series system equipped with three serial columns (PLgel 3 μm MIXED-E, 5 μm PLgel MIXED-D and PLgel 20 μm MIXED-A from Polymer Laboratories) and an Agilent 1100 series refractive index detector working at 35 °C at a nominal flow rate of 1.0 mL/min with a sample concentration of 0.1 % w/w in tetrahydrofuran (THF) as solvent. The SEC system was calibrated using narrow polystyrene standards from Polymer Laboratories with molecular weights ranging from 500 to 400.000 Da.

3.3.Results and discussion

As mentioned in the introduction, the primary aim of this work was to synthetize a family of poly(2-(3,4,5-tris(4-dodecyloxybenzyloxy)phenyl)-2-oxazoline)s (PTOx) with different molecular weights from its monomer precursor TAPOx, through *living* cationic ring-opening polymerization (CROP) (**Scheme 3.1**). With this purpose, several conditions, such as solvent, concentration, temperature, initiator and terminating agent were tested (**Table 3.1**). The progress of the reaction (reaction time) was monitored by ^{1}H NMR.

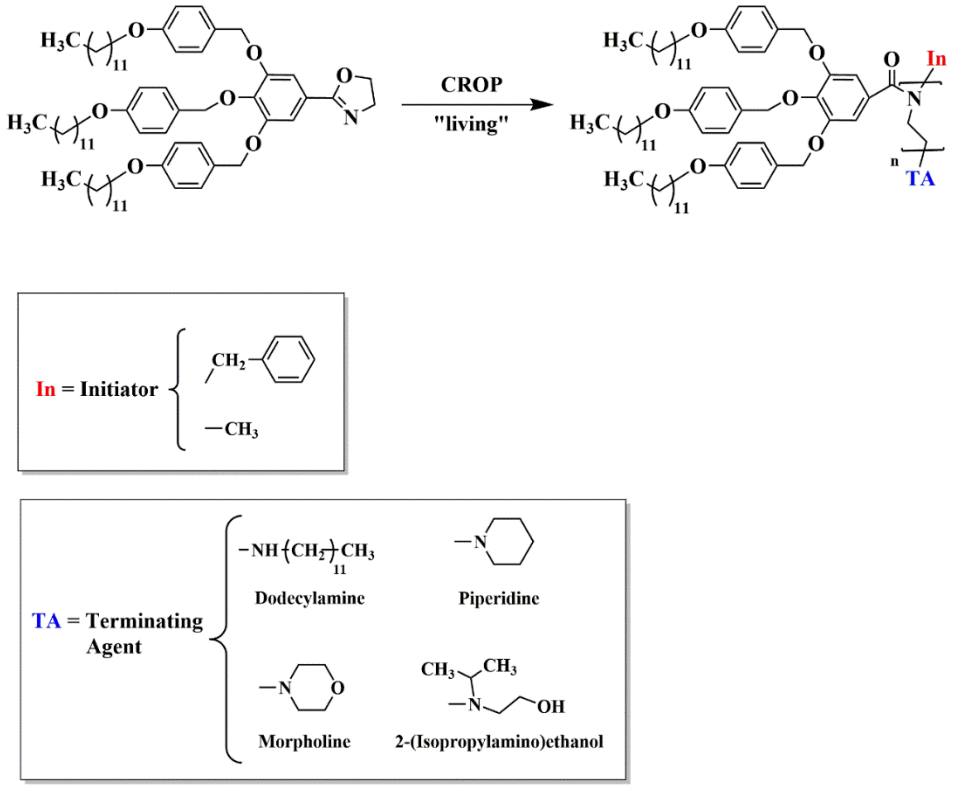

Scheme 3.1. Scheme of the *living* CROP of TAPOx.

CHAPTER 3

In a typical polyoxazoline synthesis by CROP, we can differentiate three main steps: 1) initiation, which takes place by nucleophilic attack of the cyclic imino ether to the electrophilic initiator, forming the oxazolinium cation and triggering the polymerization; 2) propagation, in which the monomer is added to the on growing polyoxazoline backbone, and finally, 3) termination, which occurs via nucleophilic attack of an added terminating agent on the *living* cationic chain-end (**Scheme 3.2**) [30].

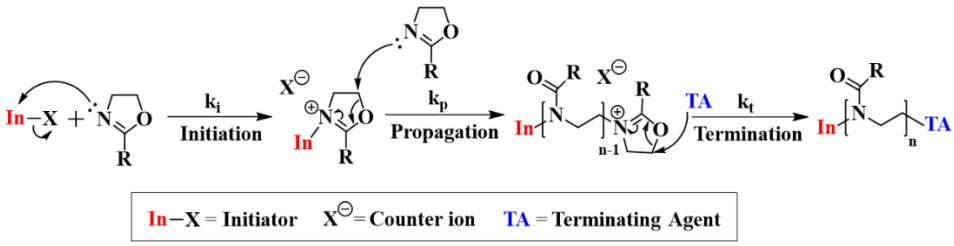

Scheme 3.2. General simplified mechanism of the CROP of 2-oxazolines.

Since the first reported synthesis of a polyoxazoline by CROP, a broad number of initiators has been employed, including methyl, benzyl and acetyl halides, alkyl sulfonates, such as trifluoromethanesulfonates (triflates), *p*-toluenesulfonates (tosylates) and *p*-nitrobenzenesulfonates (nosylates), Lewis's acids, and oxazolinium salts [30,31]. More recently, other initiators have been explored: for instance, Klikovits and co-workers have reported the use of a photoacid generator as an initiator for the cationic photopolymerization of different 2-oxazolines [32].

In our case, we decided to first test benzyl bromide (BnBr) as an initiator (**Entry 1**). Unfortunately, the reaction did not take place and no polymer was observed by ^{1}H NMR within 10 days of reaction, showing that this initiator is

not active enough to trigger the polymerization [33]. Therefore, we decided to change it to a more active initiator, an alkyl sulfonate-based initiator [34]. In this case, anhydrous benzotrifluoride (BTF) was chosen as a solvent (**Entries 2-3**), which is reported as environmentally less harmful than various conventional solvents, such as halogenated solvents and aromatic solvents [35]. In these reactions, we used MeOTs as an initiator, while two different monomer concentrations were employed in each of them. It was observed that the polymerization of TAPOx did not take place in the less concentrated Schlenk tube (**Entry 2**), although the polymerization reaction was successfully performed within 7 days when the monomer concentration was increased up to 0.5 M (**Entry 3**). Afterwards, we decided to carry out a reaction in bulk (**Entry 4**), inspired by a previously reported work by Percec and co-workers [36]. Nevertheless, the cleavage of the benzylic positions of the dendritic side group after 2 h was detected by NMR.

According to Hoogenboom and co-workers, the most appropriate temperature to polymerize 2-phenyl-2-oxazolines with MeOTs as an initiator was established at 130 °C [33,37]. In order to perform these experiments, we decided to change the solvent of the reaction to a higher boiling point one, since BTF has a boiling point of 102 °C. Therefore, we used *o*-dichlorobenzene (*o*-DCB), which has a boiling point of 180 °C. Hence, we decided to set up the reaction temperature at 130 °C with different monomer concentrations (0.5, 1.0 and 3.0 M). Unfortunately, in these attempts (**Entries 5-7)**, the cleavage of the benzylic methylene of the dodecyloxybenzyloxy substituents of the side dendron was observed again. For this reason, we considered not to vary the monomer concentration, keeping it at 1.0 M from now on.

Concerning the reaction temperature, we explored the polymerization of PTOx at temperatures lower than 130 °C to avoid the cleavage of the benzylic positions. At the same time, we also used a more active initiator, methyl triflate [34,38], in order to obtain shorter reaction times. These reactions (**Entries 8-10**) were carried out at 110, 95 and 105 °C, respectively. Regarding the reaction that was carried out at 110 °C, the cleavage of the benzylic positions of the side dendron after 20 h of reaction was still detected. In contrast, the polymerization reaction at 95 °C proceeded successfully within 65 h; unfortunately, the terminating agent (dodecylamine) also provoked the cleavage of the benzylic methylene of the dodecyloxybenzyloxy substituents, when kept in the crude mixture for longer times (up to 16 h).

Consequently, we decided to change the terminating agent, from a primary amine to a more hindered secondary amine. Furthermore, the reaction was accelerated by increasing the temperature up to 105 °C as can be seen in **Entry 10**: in this way, it was successfully accomplished in 44 h, obtaining a pallid orange solution. In this case, morpholine was added as a terminating agent; and a polymer with a degree of polymerization equal to 17 (versus an expected one of 20) was obtained with a yield of 43 %. At this point, we decided to change the solvent, *o*-DCB, to a less polar one, i.e. chlorobenzene [39]. Using chlorobenzene, we noticed that reaction time was reduced from 44 h to 30 h, which agreed with the results previously reported by Monnery and co-workers [38]. Finally, other amine-based terminating agents were explored, piperidine and 2-(isopropylamino)ethanol. Unfortunately, they did not react as expected and, in addition, an increase of the side reactions was detected by ^{1}H NMR. Thus, the final degree of polymerization could not be estimated in these experiments.

Table 3.1 . Chemical reaction conditions and degrees of polymerization in the optimisation of the polymerization reaction of PTOx.

Entry	Initiator (mol %)	Solvent	T (°C)	Monomer concentration	Time	Terminating agent	Monomer conversion [a] (%)	Yield [b] (%)	EDP [c] (DP [d])
1	BnBr (1)	Toluene	90	0.1 M	10 days	-	-	-	100 (-)
2	MeOTs (1)	BTF [e]	95	0.2 M	10 days	-	-	-	100 (-)
3	MeOTs (5)	BTF	95	0.5 M	7 days	Dodecylamine	92	34	20 (7)
4	MeOTs (1)	Bulk	160	-	2 h	-	-	-	100 (-)
5	MeOTs (5)	*o*-DCB [f]	130	3.0 M	3 h	-	-	-	20 (-)
6	MeOTs (5)	*o*-DCB	130	1.0 M	5 h	-	-	-	20 (-)
7	MeOTs (5)	*o*-DCB	130	0.5 M	16 h	-	-	-	20 (-)
8	MeOTf (5)	*o*-DCB	110	1.0 M	20 h	-	-	-	20 (-)
9	MeOTf (5)	*o*-DCB	95	1.0 M	65 h	Dodecylamine	92	-	20 (-)
10	MeOTf (5)	*o*-DCB	105	1.0 M	44 h	Morpholine	93	43	20 (17)
11	MeOTf (5)	Chlorobenzene	105	1.0 M	30 h	Morpholine	96	64	20 (23)
12	MeOTf (5)	Chlorobenzene	105	1.0 M	29 h	Piperidine	93	-	20 (-)
13	MeOTf (5)	Chlorobenzene	105	1.0 M	30 h	2-(Isopropylamino)ethanol	94	-	20 (-)

[a] Estimated by ^{1}H NMR. [b] % of polymer isolated after purification. [c] EDP: Expected degree of polymerization. [d] DP: Degree of polymerization estimated by ^{1}H NMR. [e] BTF: Benzotrifluoride. [f] *o*-DCB*: o*–Dichlorobenzene.

In view of these results, we decided to choose the best reaction conditions as follows: 1.0 M concentration of TAPOx monomer, reaction temperature of 105 °C, MeOTf as an initiator, chlorobenzene as a solvent and morpholine as a terminating agent. In such conditions (**Entry 11**), a conversion of 96 % was obtained and the expected DP roughly coincides with the one estimated by ^{1}H NMR, which is in agreement with the expected "living" character of this polymerization. The degree of polymerization can be estimated from ^{1}H NMR spectra, by taking the signals of either initiator or terminating agent (or both) as a reference, and then compare their integrations with the integration of some signals assigned to the repeating units of the polymer. In our case, we decided to use only the terminating agent signals as a reference, since the signal of the initiator appeared overlapped with the polymer main chain signal in ^{1}H NMR spectra (3.42 – 4.03 ppm, **Figure 3.1**). In fact, only the methylene adjacent to the nitrogen of the morpholine terminating agent, located at 2.35 ppm (**Figure 3.1**), was used, since the methylene contiguous to the oxygen appeared also overlapped with the polymer main chain signal. The integration of this signal was compared with the integration of the signal that appears between 4.20 – 5.23 ppm, which is assigned to the benzylic methylene of the dodecyloxybenzyloxy substituents, and additionally with the integration of the signal that appear centred at 0.80, which correspond to the terminal methyl groups of the long aliphatic chain of the tapered side group (**Figure 3.1**). The estimated DP from both comparisons was the same, in addition to agreeing with the expected DP as shown in **Table 3.1**. A more detailed explanation of NMR characterization of PTOx is reported in section 3.3.1.

After optimising all the parameters of the polymerization reaction, we decided to modify the percentage of initiator used in order to increase in a controlled manner the molecular weight of the polymers. To do so, the amount of initiator has to be reduced since we kept the amount of TAPOx constant (**Table 3.2**). The first noteworthy fact is that the reaction time slowly increased on reducing the initiator until 2.0 % (**Entries 11, 14-16)**. With amounts of initiator less than 2.0 %, the reaction time increased dramatically, as can be seen in **Entry 17**, in which 84 h were needed to reach a monomer conversion equal to 93 %. The variation of the viscosity of the reaction crude over time could delay the progress of the polymerization reaction.

Table 3.2 shows the monomer conversion and the obtained yields of the performed reactions. As estimated by ^{1}H NMR, monomer conversion was higher than 93 % in **Entries 11** and **14-17**, which makes the experimental DPs of the synthesized poly(2-oxazoline)s practically identical to the expected DPs (obtained from the monomer/initiator molar ratio). The narrow molecular weight distributions, estimated by SEC (**Table 3.2**), corroborated the expected "living" character exhibited by this polymerization, since dispersity values between 1.16 and 1.35 were obtained. When we tried to increase the expected DP beyond 80 units (**Entries 18-19**), the complete conversion of the monomer was not reached. In fact, we observed that there was about 25 – 28 % of TAPOx remaining unreacted, even after 5 – 6 days of reaction, which could not be separated from the formed poly(2-oxazoline)s during the purification process. Therefore, neither a real yield nor a degree of polymerization could be obtained in these cases. On the other hand, the yield of the polymerization reaction was generally between 63 and 75 %, indicating that some amount of polymer was lost during the work-up process.

Table 3.2. Chemical reaction conditions (% of initiator and reaction time), achieved conversion, expected and obtained degrees of polymerization and molecular parameters of the synthesized family of PTOx.

Entry	EDP [a]	Initiator (mol %)	Time (h)	Monomer conversion [b] (%)	Yield [c] (%)	DP [d]	M_n [e] (kDa)	M_w [f] (kDa)	Đ [f]
11	20	5.0	30	96	64	23	23.4	9.6	1.25
14	30	3.3	42	94	63	32	32.6	14.0	1.26
15	40	2.5	47	93	75	39	39.7	6.6	1.16
16	50	2.0	50	95	66	49	49.9	13.1	1.33
17	60	1.7	84	93	75	59	60.0	12.5	1.35
18	80	1.3	120	75	-	-	-	-	-
19	90	1.1	144	72	-	-	-	-	-

[a] EDP: Expected degree of polymerization. [b] Estimated by ^{1}H NMR. [c] % of polymer isolated after purification. [d] DP: Degree of polymerization estimated by ^{1}H NMR. [e] Molecular weight estimated by ^{1}H NMR. [f] M_w and dispersity estimated by SEC.

Moreover, the molecular weights of this family of polymers were also estimated by SEC, although no correlation between M_w or M_n was found (**Figure 3.S2**). In our case, we used polystyrene patterns in SEC as a reference to calculate the molecular weight of these poly(2-oxazoline)s. Nevertheless, the hydrodynamic volume of this family of polymers is rather different from polystyrene, which is responsible of the lack of correlation between molecular weights estimated by ^{1}H NMR and SEC.

3.3.1. Chemical characterization

The chemical structure of PTOx was characterized by NMR and FT-IR spectroscopy.

As regards ^{1}H NMR, **Figure 3.1** shows the spectrum of PTOx40, which was performed using $CDCl_3$ as solvent. The first noticeable thing is that all ^{1}H NMR spectra are characterized by broad signals in three regions. We observe two broad peaks in the aromatic region between 6.25 and 7.34 ppm, which are the signals of the aromatic protons of the side chain dendron. When we move to lower frequencies, the first broad signal between 4.20 – 5.23 ppm is attributed to the benzylic methylenes of the dodecyloxybenzyloxy substituents. In the upfield region of the spectra, the peaks between 0.80 and 1.87 ppm are assigned to the aliphatic long chains of the dendron. These peaks are in agreement with the characterization of TAPOx monomer previously described by us [29]. The most interesting region is situated between 2.35 ppm and 4.03 ppm, since the peaks attributed to the protons of the polymer main

chain, the morpholine terminating agent and the initiator appear in this area. In fact, the broad peak centred at 3.75 ppm is assigned to both methylenes of the poly(2-oxazoline) main chain (indexed as f and g in **Figure 3.1**), the methylene contiguous to the oxygen of the long aliphatic side chains (1), the methylene of the initiator (s) and both methylenes contiguous to the oxygen of the morpholine terminating agent (y). In addition, the new broad peak centred at 2.35 ppm is attributed to both methylenes contiguous to the nitrogen of the terminating agent (x) in the final structure of the poly(2-oxazoline). This was confirmed by 2D NMR spectrum (COSY; **Figure 3.2**). Moreover, the lack of both characteristic signals of the oxazoline ring, which are expected to appear at 4.34 and 3.97 ppm respectively, confirms a complete monomer conversion [29].

CHAPTER 3

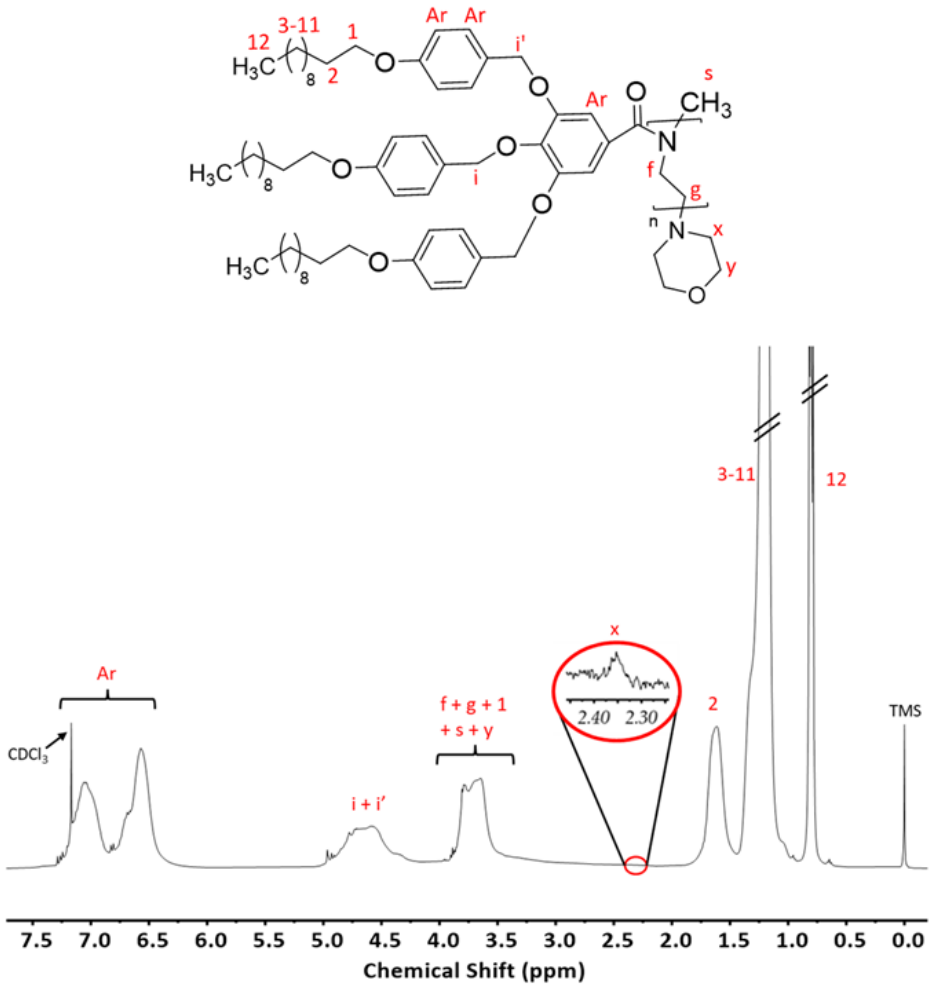

Figure 3.1. ^{1}H NMR spectrum of PTOx40 in $CDCl_3$.

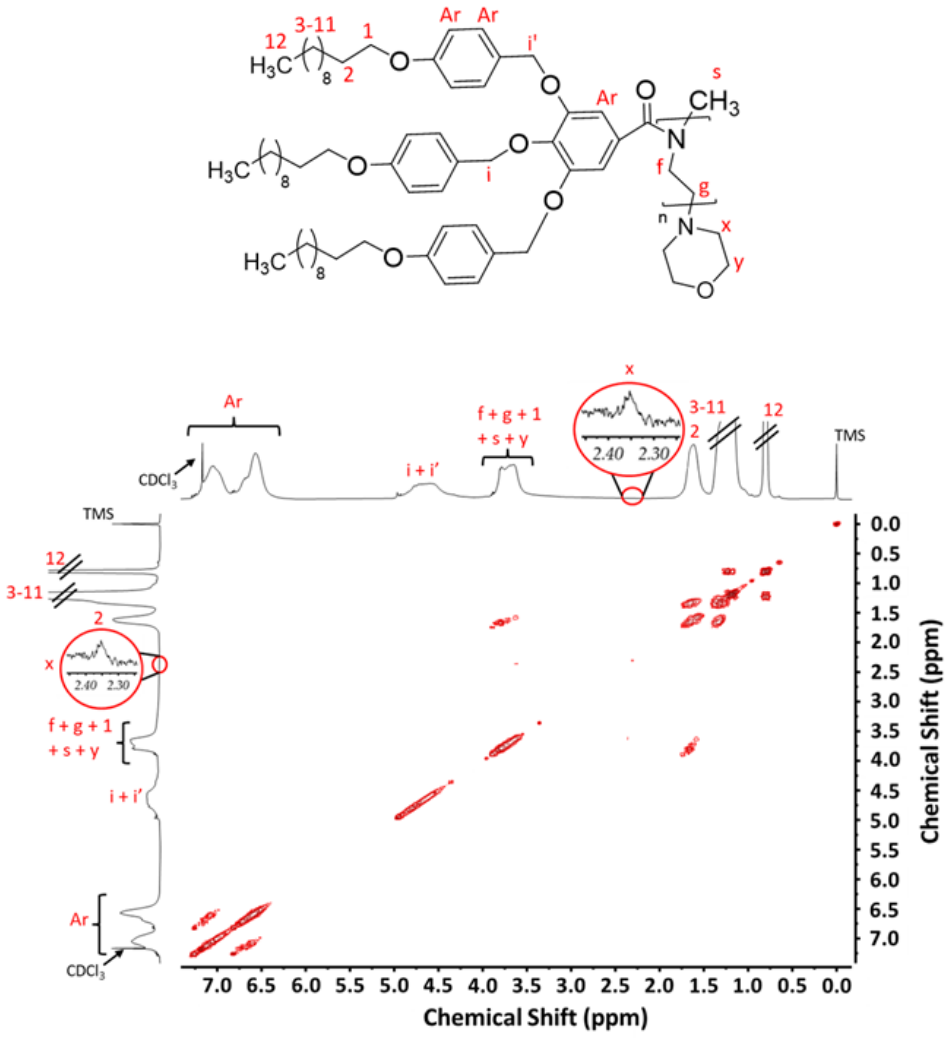

Figure 3.2. COSY NMR spectrum of PTOx40.

Figure 3.3 shows the ^{13}C NMR spectrum of PTOx40 with the corresponding assignments. First of all, the signal at 171.8 ppm is attributed to the carbonyl carbon of the amide of each side dendron (indexed with the letter q in **Figure 3.3**), whereas the signals between 106.7 and 158.9 ppm belong to the aromatic carbons of the dendronized side chain of the poly(2-oxazoline). In the

aliphatic region, two signals observed at 74.9 and 70.8 ppm are assigned to the carbons of the benzylic methylenes of the central and lateral dodecyloxybenzyloxy substituents of each dendron, respectively. Moving upfield in the spectrum, the peak at 68.2 ppm is attributed to the methylenic carbons contiguous to the oxygen of the long aliphatic side chains together with the methylenic carbons contiguous to the oxygen of the morpholine terminating agent. In addition, the small peak observed at 53.6 ppm belongs to both methylenic carbons contiguous to nitrogen of morpholine, thus confirming that the terminating agent was successfully incorporated in the final polymer structure. Besides, the small broad peak at 46.1 ppm is attributed to the carbons of the main chain of the acyl-substituted poly(ethyleneimine) (f and g). This peak, as well as the absence of the peaks assigned to the methylenic carbons of the oxazoline ring expected at 67.9 and 55.0 ppm respectively, corroborate that TAPOx monomer was completely consumed during the CROP [29]. Finally, all the peaks between 32.1 and 14.3 ppm are assigned to the carbons of the aliphatic side chain of the dendrons (2-12). This information agrees with the previously reported characterization of the TAPOx monomer [29].

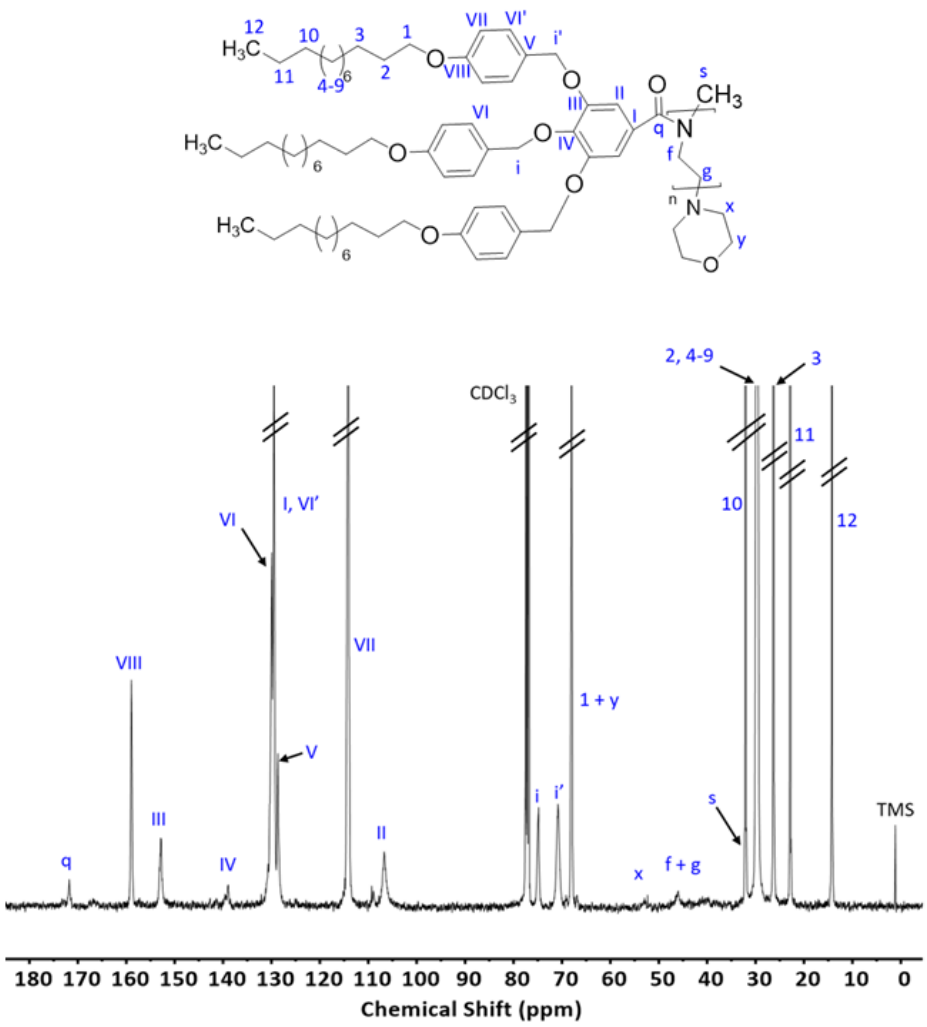

Figure 3.3. ^{13}C NMR spectrum of PTOx40 in $CDCl_3$.

Moreover, PTOx40 structure was also characterized by means of FT-IR spectroscopy (**Figure 3.S1**). Thus, the FT-IR spectrum of this poly(2-oxazoline) shows an intense band at 1613 cm^{-1}, which is attributed to the C=O stretching vibration of the amide carbonyl group. This band was also detected when we recorded the FT-IR of *N*-(2-hydroxyethyl)-3,4,5-tris(4-dodecyloxybenzyloxy) benzamide (TAPAm), the dendritic amide precursor synthesized in the

reported pathway to obtain TAPOx [29]. Furthermore, total monomer conversion was also certified by the complete disappearance of the stretching vibration band typical of 2-oxazolines (1643 cm^{-1} in FT-IR spectrum of TAPOx monomer, **Figure 3.S1**) [40].

3.3.2. Thermal and mesomorphic characterization

Thermal and mesomorphic characterization of the members of the PTOx family was performed by DSC, TGA, POM and XRD experiments. **Table 3.3** shows calorimetric data of the whole PTOx family.

Table 3.3. Calorimetric features of the PTOx family.

Sample	T_g (°C) [a]	T_c (°C) [a]	$T_{5\%}$ (°C)	ΔH (kJ/mol) [b]
PTOx20	-13	81	282	1.1
PTOx30	-15	-	288	-
PTOx40	-12	80 [c]	287	1.2 [c]
PTOx50	-14	-	290	-
PTOx60	-16	-	287	-

[a] Determined by DSC first heating scan. [b] Expressed per mol of tapered repeating unit. [c] Determined by DSC second heating scan.

As represented in **Figure 3.4**, DSC thermograms reveal the presence of a glass transition temperature between -16 and -12 °C for all side chain liquid

crystalline poly(2-oxazoline)s synthesized. Furthermore, a small endotherm centred at 81 and 80 °C was observed in the case of PTOx20 and PTOx40, respectively. Moreover, POM experiments put into evidence that this endotherm corresponds to the clearing temperatures (T_c) of the dendronized polymers, since an isotropic viscous liquid was observed above it. This endotherm could be only detected by DSC in the first heating for PTOx20 and PTOx40, while no exotherm was observed on cooling from the molten state of these polymers except for PTOx40 (T_c was also not detected by DSC second heating scan except for PTOx40). Nevertheless, it was possible to see by POM how different LC textures grew on cooling to RT after 24 h of annealing at 74 °C **(Figures 3.5a and c)**. Besides, a small shoulder just after the endotherm at 80 °C could be seen for some SCLC poly(2-oxazoline)s, which corresponds to an endothermic peak. As the XRD studies demonstrated, this endotherm was not attributed to a thermal transition between different LC mesophases Figure **3.S3**); suggesting that a hysteresis phenomenon occurs in this temperature range. Unlike the other members of the family, PTOx40 showed an exotherm at 64 °C on cooling, which was attributed to the anisotropization temperature (**Figure 3.S4**). Besides, a shoulder that appears overlapped with the endotherm associated to the T_c in the DSC first heating scan is not detected in the second heating scan, allowing to determine both the T_c and the associated enthalpy in a more accurate way. In this case, the LC mesophase was also observed by POM during both heating and cooling, confirming the thermal transitions previously detected by DSC. As observed in **Figure 3.5b**, a pseudo-focal conic fan-shaped texture typical of these mesogens was exhibited by PTOx40.

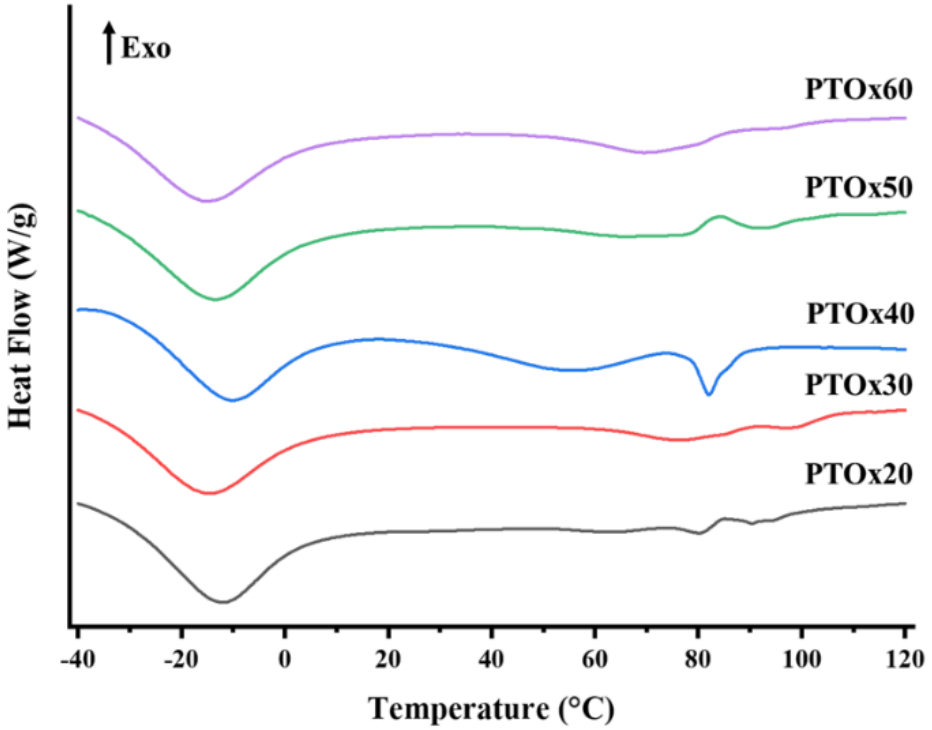

Figure 3.4. Calorimetric analysis of all synthesized PTOx; DSC first heating scan of: PTOx20, PTOx30, PTOx40, PTOx50 and PTOx60 (Scan rate: 10 °C/min).

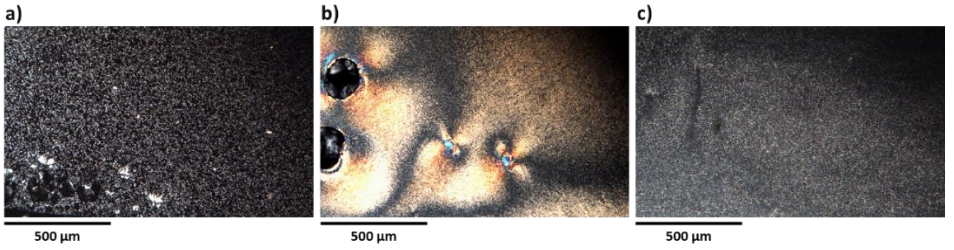

Figure 3.5. Optical micrographs between crossed polars of: (a) PTOx20, (b) PTOx40 and (c) PTOx60 recorded at RT (25 ± 5 °C) on cooling from isotropization. In the case of PTOx20 and PTOx60, pictures were taken after annealing at 74 °C during 24 h and then cooling the poly(2-oxazoline)s to RT.

The associated enthalpies to the clearing transitions of PTOx20 and PTOx40 (**Table 3.3**) roughly coincide with the already reported enthalpies for systems that self-assemble into hexagonal columnar (Col_h) lattices [26,41,42].

For the purpose to confirm calorimetric features and to assign the LC mesophases of the synthesized poly(2-oxazoline)s, X-ray diffraction analysis was carried out at different temperatures (**Figure 3.6** and **3.7**). As reported in **Table 3.4**, the investigated PTOx presented columnar mesophases (*Col*), as expected. Actually, Percec and co-workers established that the columnar self-assembly of this type of hemiphasmidic polymers is driven mainly by supramolecular interactions (π-π interactions) of the aromatic moieties present in tapered side chain dendrons. Thanks to these interactions, these dendritic side-groups can induce a helical arrangement of the polymer chain into columns [43,44].

Below the T_c, the X-ray diffractograms of PTOx show a sharp peak located in the ranges of 2θ angles 2.2 – 2.3° (corresponding to d-spacings between 38.6 and 39.3 Å), and a broad halo centred around 2θ = 19.2 – 19.5° (which corresponds to d-spacings between 4.5 and 4.6 Å). The higher spacing seen in the XRD pattern should correspond to the lateral distance between columns, while the lower spacing might be attributed to the planar distance between dendrons, as we have previously reported for SCLCPs that contain this dendritic side group and self-assemble into columnar structures [23,24,26,45,46].

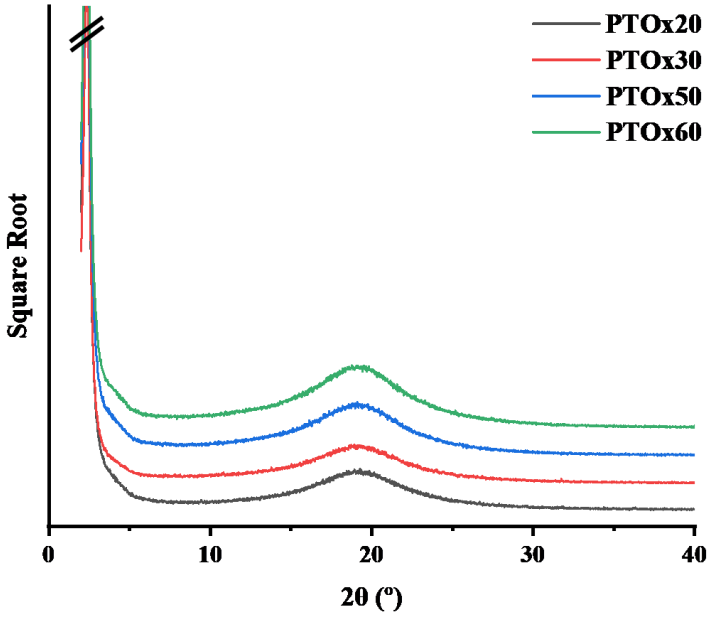

Figure 3.6. X-ray diffractograms of PTOx20, PTOx30, PTOx50 and PTOx60 recorded at 50 °C.

Regarding PTOx40, its XRD diffractogram presents three sharp reflections centred at 2θ = 2.3° (d = 38.6 Å), 3.9° (d = 22.3 Å) and 4.6° (d = 19.3 Å). The relationship between these d-spacings, which is equal to $1:1/\sqrt{3}:1/2$, together with the presence of the diffuse halo centered at 2θ = 19.3° (d = 4.6 Å) confirms the existence of a hexagonal columnar mesophase (Col_h). Thus, the sharp reflections are assigned to the lattice planes indexed as (100), (110) and (200), respectively, while the broad halo corresponds to the plane (001). In all cases, the columnar organization of these dendronized poly(2-oxazoline)s suggests that their main chains could arrange forming biomimetic ion channels.

Table 3.4. XRD diffraction data of PTOx family.

Sample	d_{100} (Å)	d_{110} (Å)	d_{200} (Å)	d_{001} (Å)	a (Å)	Mesophase [b]
PTOx20 [a]	39.3	-	-	4.6	-	*Col*
PTOx30 [a]	38.9	-	-	4.6	-	*Col*
PTOx40 [a]	38.6	22.3	19.3	4.6	44.6	Col_h
PTOx50 [a]	38.6	-	-	4.5	-	*Col*
PTOx60 [a]	38.9	-	-	4.5	-	*Col*

[a] X-ray diffractograms of PTOx20, PTOx30, PTOx50 and PTOx60 were recorded at 50 °C, while X-ray diffractogram of PTOx40 was recorded at 60 °C. [b] *Col*: columnar. Col_h: hexagonal columnar.

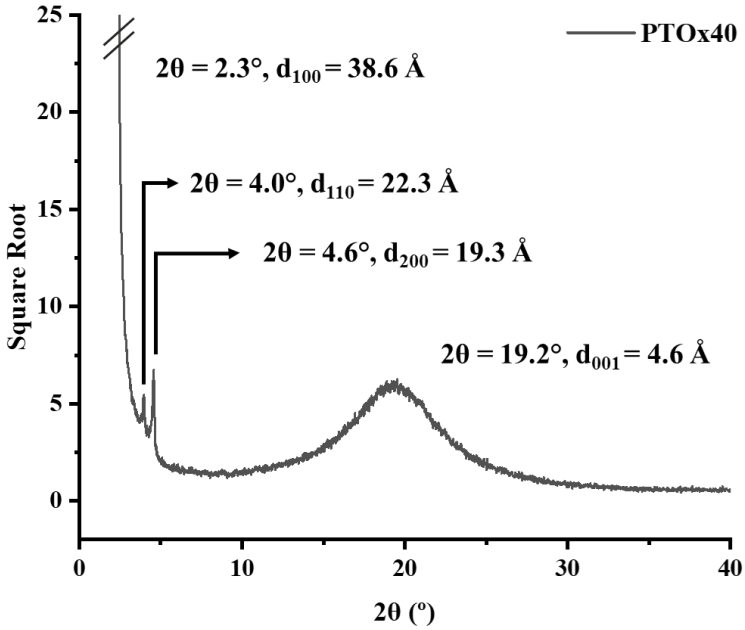

Figure 3.7. X-ray diffractogram of PTOx40 recorded at 60 °C.

Thermal stability of all the members of the PTOx family was studied by TGA. As can be seen in **Figure 3.8**, this family of dendronized poly(2-oxazoline)s presents the same thermal stability pattern. All these liquid crystalline polymers present an onset of thermal weight loss (determined as the temperature corresponding to 5 % mass loss) in the range between 282 and 290 °C (**Table 3.3**) and a remaining char yield between 15 and 17 % at 600 °C. Moreover, the DGTA curves of these dendronized poly(2-oxazoline)s evidenced that their thermal degradation occurs *via* two-step weight loss (**Figure 3.S5**). This data agrees with the information reported in literature during the last years for 2-phenyl-oxazoline based polymers, which exhibited complex decomposition mechanisms [47,48].

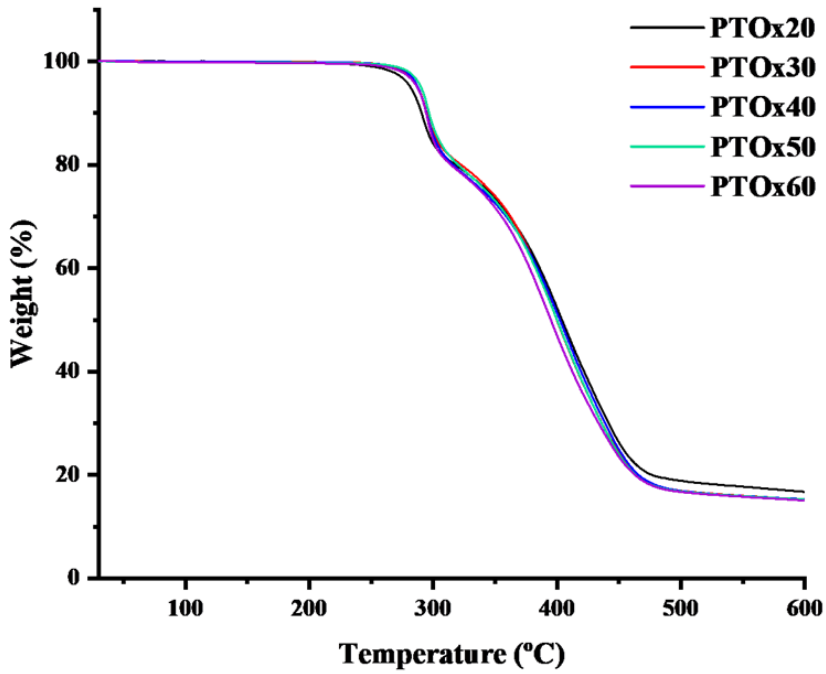

Figure 3.8. TGA thermogram of PTOx family recorded at a heating rate of 10 °C/min in nitrogen atmosphere.

3.4.Conclusions

A new family of poly(*N*-acylethyleneimine)s has been successfully synthetized by *living* CROP of dendronized TAPOx, obtaining poly(2-oxazoline)s within a range of molecular weights between 20 and 60 kDa. Early investigations suggest that several factors affect the polymerization reaction of TAPOx: temperature, type of initiator, monomer concentration, terminating agent and solvent. Concerning the reaction temperature, our studies showed that a compromise between time and temperature was necessary to avoid the cleavage of the benzylic positions of the side dendron. When the reactions were carried out above 105 °C, this cleavage occurred; on the other hand, working at lower temperatures determined too long reaction times. Therefore, the optimal temperature to perform this CROP is 105 °C. With respect to the initiator, methyl based initiators such as MeOTs and MeOTf allowed the obtention of dendronized poly(2-oxazoline)s, even though the polymerizations carried out with MeOTf showed shorter reaction times as expected. Therefore, these studies allowed tuning the optimal polymerization conditions, which resulted the following: reaction temperature equal to 105 °C, use of MeOTf as an initiator, chlorobenzene as a solvent, morpholine as a terminating agent, while the monomer concentration was fixed at 1.0 M.

The liquid crystalline character of these poly(*N*-acylethyleneimine)s was investigated. Calorimetric studies showed that the entire family of PTOx exhibited liquid crystalline behaviour. In fact, the liquid crystalline mesophases of these poly(2-oxazoline)s, which could be evidenced by DSC,

present a wide range of temperature (*ca* 90 °C), exhibiting the liquid crystalline mesophase already at RT (25 ± 5 °C). Nevertheless, this mesophase could be only observed by DSC on the first heating scan for all PTOx except for PTOx40, which showed a clear enantiotropic liquid crystalline mesophase. On the other hand, POM experiments proved that LC mesophases of PTOx20-30 and PTOx50-60 could be grown on cooling after annealing at 74 °C during 24 h. XRD analysis showed that the entire family of poly(2-oxazoline)s self-assembles into columnar mesophases, being able to detect a hexagonal columnar mesophase in the case of PTOx40. All these results evidenced that these novel family of SCLC acyl-substituted poly(ethyleneimine)s could be promising materials with the ability to transport diverse cations in the development of new biomimetic membranes.

3.5.References

[1] H. Zhang, P.K. Shen, Recent development of polymer electrolyte membranes for fuel cells, Chem. Rev. 112 (2012) 2780–2832. https://doi.org/10.1021/cr200035s.

[2] A.K. Sahu, G. Selvarani, S. Pitchumani, P. Sridhar, A.K. Shukla, A Sol-Gel Modified Alternative Nafion-Silica Composite Membrane for Polymer Electrolyte Fuel Cells, J. Electrochem. Soc. 154 (2007) B123-B132. https://doi.org/10.1149/1.2401031.

[3] G. Hernández-Flores, H.M. Poggi-Varaldo, O. Solorza-Feria, Comparison of alternative membranes to replace high cost Nafion ones in microbial fuel cells, Int. J. Hydrog. Energy. 41 (2016) 23354–23362. https://doi.org/10.1016/j.ijhydene.2016.08.206.

[4] M. Schadt, Photo alignment and patterning of liquid crystal polymer films and optical devices by side-chain photopolymers, Mol. Cryst. Liq. Cryst. 594 (2014) 11–20. https://doi.org/10.1080/15421406.2014.917456.

[5] J.R. Werber, C.O. Osuji, M. Elimelech, Materials for next-generation desalination and water purification membranes, Nat. Rev. Mater. 1 (2016) 1–15. https://doi.org/10.1038/natrevmats.2016.18.

[6] M. Zhou, P.R. Nemade, X. Lu, X. Zeng, E.S. Hatakeyama, R.D. Noble, D.L. Gin, New type of membrane material for water desalination based on a cross-linked bicontinuous cubic lyotropic liquid crystal assembly, J. Am. Chem. Soc. 129 (2007) 9574–9575. https://doi.org/10.1021/ja073067w.

[7] T. Kato, M. Yoshio, T. Ichikawa, B. Soberats, H. Ohno, M. Funahashi, Transport of ions and electrons in nanostructured liquid crystals, Nat. Rev. Mater. 2 (2017) 17001. https://doi.org/10.1038/natrevmats.2017.1.

[8] J. Sakuda, E. Hosono, M. Yoshio, T. Ichikawa, T. Matsumoto, H. Ohno, H. Zhou, T. Kato, Liquid-crystalline electrolytes for lithium-ion batteries: Ordered assemblies of a mesogen-containing carbonate and a lithium salt, Adv. Funct. Mater. 25 (2015) 1206–1212. https://doi.org/10.1002/adfm.201402509.

[9] W. Seeliger, E. Aufderhaar, W. Diepers, R. Feinauer, R. Nehring, W. Thier, H. Hellmann, Recent Syntheses and Reactions of Cyclic Imidic Esters,

Angew. Chem. Int. Ed. Engl. 5 (1966) 875–888. https://doi.org/10.1002/anie.196608751.

[10] D.A. Tomalia, D.P. Sheetz, Homopolymerization of 2-alkyl- and 2-aryl-2-oxazolines, J. Polym. Sci., Part A-1: Polym. Chem. 4 (1966) 2253–2265. https://doi.org/10.1002/pol.1966.150040919.

[11] T. Kagiya, S. Narisawa, T. Maeda, K. Fukui, Ring-opening polymerization of 2-substituted 2-oxazolines, J. Polym. Sci., Part B: Polym. Lett. 4 (1966) 441–445. https://doi.org/10.1002/pol.1966.110040701.

[12] T.G. Bassiri, A. Levy, M. Litt, Polymerization of cyclic imino ethers. I. Oxazolines, J. Polym. Sci., Part B: Polym. Lett. 5 (1967) 871–879. https://doi.org/10.1002/pol.1967.110050927.

[13] B. Guillerm, S. Monge, V. Lapinte, J.J. Robin, How to modulate the chemical structure of polyoxazolines by appropriate functionalization, Macromol. Rapid Commun. 33 (2012) 1600–1612. https://doi.org/10.1002/marc.201200266.

[14] V. Mazánková, P. Sťahel, P. Matoušková, A. Brablec, J. Čech, L. Prokeš, V. Buršíková, M. Stupavská, M. Lehocký, K. Ozaltin, P. Humpolíček, D. Trunec, Atmospheric pressure plasma polymerized 2-ethyl-2-oxazoline based thin films for biomedical purposes, Polymers (Basel). 12 (2020) 2679. https://doi.org/10.3390/polym12112679.

[15] M.N. Ramiasa, A.A. Cavallaro, A. Mierczynska, S.N. Christo, J.M. Gleadle, J.D. Hayball, K. Vasilev, Plasma polymerised polyoxazoline thin films for biomedical applications, Chem. Comm. 51 (2015) 4279–4282. https://doi.org/10.1039/c5cc00260e.

[16] X. Liu, J. Yuan, J. Zhang, R.M. Visalakshan, W. Wang, Y. Xiang, Y. He, Q. Feng, K. Vasilev, The introduction of nanotopography suppresses bacterial adhesion and enhances osteoinductive capacity of plasma deposited polyoxazoline surface, Mater. Lett. 309 (2022) 131452. https://doi.org/10.1016/j.matlet.2021.131452.

[17] M.J. Sánchez-Fernández, J. Rutjes, R.P. Félix Lanao, J.C.M.E. Bender, J.C.M. van Hest, S.C.G. Leeuwenburgh, Bone-Adhesive Hydrogels Based on Dual Crosslinked Poly(2-oxazoline)s, Macromol. Biosci. 21 (2021) 2100257. https://doi.org/10.1002/mabi.202100257.

[18] R. Konradi, C. Acikgoz, M. Textor, Polyoxazolines for nonfouling surface coatings - A direct comparison to the gold standard PEG, Macromol. Rapid Commun. 33 (2012) 1663–1676. https://doi.org/10.1002/marc.201200422.

[19] O. Sedlacek, O. Janouskova, B. Verbraeken, R. Hoogenboom, Straightforward Route to Superhydrophilic Poly(2-oxazoline)s via Acylation of Well-Defined Polyethylenimine, Biomacromolecules. 20 (2019) 222–230. https://doi.org/10.1021/acs.biomac.8b01366.

[20] J. Svoboda, O. Sedláček, T. Riedel, M. Hrubý, O. Pop-Georgievski, Poly(2-oxazoline)s One-Pot Polymerization and Surface Coating: From Synthesis to Antifouling Properties Out-Performing Poly(ethylene oxide), Biomacromolecules. 20 (2019) 3453–3463. https://doi.org/10.1021/acs.biomac.9b00751.

[21] J.M. Rodriguez-Parada, V. Percec, Synthesis and characterization of liquid crystalline poly(N-acylethyleneimine)s, J. Polym. Sci., Part A: Polym. Chem. 25 (1987) 2269–2279. https://doi.org/10.1002/pola.1987.080250823.

[22] V. Percec, M.N. Holerca, S. Uchida, D.J.P. Yeardley, G. Ungar, Poly(oxazoline)s with tapered minidendritic side groups as models for the design of synthetic macromolecules with tertiary structure. A demonstration of the limitations of living polymerization in the design of 3-D structures based on single polymer chains, Biomacromolecules. 2 (2001) 729–740. https://doi.org/10.1021/bm015559l.

[23] S.V. Bhosale, M.A. Rasool, J.A. Reina, M. Giamberini, New liquid crystalline columnar poly(epichlorohydrin-co-ethylene oxide) derivatives leading to biomimetic ion channels, Polym. Eng. Sci. 53 (2013) 159–167. https://doi.org/10.1002/pen.23240.

[24] X. Montané, S.V. Bhosale, J.A. Reina, M. Giamberini, Columnar liquid crystalline polyglycidol derivatives: A novel alternative for proton-conducting membranes, Polymer (Guildf). 66 (2015) 100–109. https://doi.org/10.1016/j.polymer.2015.03.071.

[25] A. Šakalyte, J.A. Reina, M. Giamberini, Liquid crystalline polyamines containing side dendrons: Toward the building of ion channels based on polyamines, Polymer (Guildf). 54 (2013) 5133–5140. https://doi.org/10.1016/j.polymer.2013.07.027.

[26] X. Montané, K.A. Bogdanowicz, G. Colace, J.A. Reina, P. Cerruti, A. Lederer, M. Giamberini, Advances in the design of self-supported ion-

conducting membranes-new family of columnar liquid crystalline polyamines. Part 1: Copolymer synthesis and membrane preparation, Polymer (Guildf). 105 (2016) 298–309. https://doi.org/10.1016/j.polymer.2016.10.047.

[27] X. Montané, K.A. Bogdanowicz, J. Prats-Reig, G. Colace, J.A. Reina, M. Giamberini, Advances in the design of self-supported ion-conducting membranes – New family of columnar liquid crystalline polyamines. Part 2: Ion transport characterisation and comparison to hybrid membranes, Polymer (Guildf). 105 (2016) 234–242. https://doi.org/10.1016/j.polymer.2016.10.046.

[28] D.D. Perrin, W.L.F. Armarego, Purification of laboratory chemicals, Pergamon Press, 2009.

[29] J. Guardià, A. Zare, J. Eleeza, M. Giamberini, J.A. Reina, X. Montané, Synthesis and characterization of dendritic compounds containing nitrogen: monomer precursors in the construction of biomimetic membranes, Sci. Rep. 12 (2022) 1725. https://doi.org/10.1038/s41598-022-05747-1.

[30] B. Verbraeken, B.D. Monnery, K. Lava, R. Hoogenboom, The chemistry of poly(2-oxazoline)s, Eur. Polym. J. 88 (2017) 451–469. https://doi.org/10.1016/j.eurpolymj.2016.11.016.

[31] M. Glassner, M. Vergaelen, R. Hoogenboom, Poly(2-oxazoline)s: A comprehensive overview of polymer structures and their physical properties, Polym. Int. 67 (2018) 32–45. https://doi.org/10.1002/pi.5457.

[32] N. Klikovits, L. Sinawehl, P. Knaack, T. Koch, J. Stampfl, C. Gorsche, R. Liska, UV-Induced Cationic Ring-Opening Polymerization of 2-Oxazolines for Hot Lithography, ACS Macro Lett. 9 (2020) 546–551. https://doi.org/10.1021/acsmacrolett.0c00055.

[33] R. Hoogenboom, M.W.M. Fijten, U.S. Schubert, The Effect of Temperature on the Living Cationic Polymerization of 2-Phenyl-2-oxazoline Explored Utilizing an Automated Synthesizer, Macromol. Rapid Commun. 25 (2004) 339–343. https://doi.org/10.1002/marc.200300233.

[34] M. Glassner, D.R. D'Hooge, J. Young Park, P.H.M. van Steenberge, B.D. Monnery, M.F. Reyniers, R. Hoogenboom, Systematic investigation of alkyl sulfonate initiators for the cationic ring-opening polymerization of 2-oxazolines revealing optimal combinations of monomers and initiators, Eur. Polym. J. 65 (2015) 298–304. https://doi.org/10.1016/j.eurpolymj.2015.01.019.

[35] B. Pásztói, T.M. Trötschler, Á. Szabó, B. Kerscher, H. Tenhu, R. Mülhaupt, B. Iván, Quasiliving cationic ring-opening polymerization of 2-ethyl-2-oxazoline in benzotrifluoride, as an alternative reaction medium, Polymer (Guildf). 212 (2021) 123165. https://doi.org/10.1016/j.polymer.2020.123165.

[36] V. Percec, M.N. Holerca, S.N. Magonov, D.J.P. Yeardley, G. Ungar, H. Duan, S.D. Hudson, Poly(oxazolines)s with tapered minidendritic side groups. The simplest cylindrical models to investigate the formation of two-dimensional and three-dimensional order by direct visualization, Biomacromolecules. 2 (2001) 706–728. https://doi.org/10.1021/bm015550j.

[37] R. Hoogenboom, R.M. Paulus, M.W.M. Fijten, U.S. Schubert, Concentration effects in the cationic ring-opening polymerization of 2-ethyl-2-oxazoline in N,N-dimethylacetamide, J. Polym. Sci., Part A: Polym. Chem. 43 (2005) 1487–1497. https://doi.org/10.1002/pola.20603.

[38] B.D. Monnery, S. Shaunak, M. Thanou, J.H.G. Steinke, Improved synthesis of linear poly(ethylenimine) via low-temperature polymerization of 2-isopropyl-2-oxazoline in chlorobenzene, Macromolecules. 48 (2015) 3197–3206. https://doi.org/10.1021/acs.macromol.5b00437.

[39] M. Vergaelen, B.D. Monnery, V.V. Jerca, R. Hoogenboom, Detailed Understanding of Solvent Effects for the Cationic Ring-Opening Polymerization of 2-Ethyl-2-oxazoline, Macromolecules. (2023). https://doi.org/10.1021/acs.macromol.2c01930.

[40] T. Kagiya, T. Matsuda, Selective Polymerization of 2-Isopropenyl-2-oxazoline and Cross-linking Reaction of the Polymers, Polym. J. 3 (1972) 307–314. https://doi.org/10.1295/polymj.3.307.

[41] V. Percec, C.-H. Ahn, W.-D. Cho, A.M. Jamieson, J. Kim, T. Leman, M. Schmidt, M. Gerle, M. Mo, S.A. Prokhorova, S.S. Sheiko, S.Z.D. Cheng, ǀ A Zhang, ǀ G Ungar, D.J.P. Yeardley, Visualizable Cylindrical Macromolecules with Controlled Stiffness from Backbones Containing Libraries of Self-Assembling Dendritic Side Groups, J. Am. Chem. Soc. 120 (1998) 8619–8631. https://doi.org/10.1021/ja981211v

[42] V. Percec, M.N. Holerca, S.N. Magonov, D.J.P. Yeardley, G. Ungar, H. Duan, S.D. Hudson, Poly(oxazolines)s with tapered minidendritic side groups. The simplest cylindrical models to investigate the formation of two-

dimensional and three-dimensional order by direct visualization, Biomacromolecules. 2 (2001) 706–728. https://doi.org/10.1021/bm015550j.

[43] V. Percec, M. Glodde, T.K. Bera, Y. Miura, I. Shiyanovskaya, K.D. Singer, V.S.K. Balagurusamy, P.A. Heiney, I. Schnell, A. Rapp, H.W. Spiess, S.D. Hudsonk, H. Duan, Self-organization of supramolecular helical dendrimers into complex electronic materials, Nature. 417 (2002) 384–387. https://doi.org/10.1038/nature01072.

[44] M. Peterca, D. Sahoo, M.R. Imam, Q. Xiao, V. Percec, Searching for the simplest self-assembling dendron to study helical self-organization and supramolecular polymerization, Giant. 12 (2022) 100118. https://doi.org/10.1016/j.giant.2022.100118.

[45] K.A. Bogdanowicz, G.A. Rapsilber, J.A. Reina, M. Giamberini, Liquid crystalline polymeric wires for selective proton transport, part 1: Wires preparation, Polymer (Guildf). 92 (2016) 50–57. https://doi.org/10.1016/j.polymer.2016.03.073.

[46] A. Zare, B. Pascual-Jose, S. de la Flor, A. Ribes-Greus, X. Montané, J.A. Reina, M. Giamberini, Membranes for cation transport based on dendronized poly(Epichlorohydrin-co-ethylene oxide). part 1: The effect of dendron amount and column orientation on copolymer mobility, Polymers (Basel). 13 (2021) 3532. https://doi.org/10.3390/polym13203532.

[47] T.B. Kohlan, A.E. Atespare, M. Yildiz, Y.Z. Menceloglu, S. Unal, B. Dizman, Synthesis and Structure-Property Relationship of Amphiphilic Poly(2-ethyl- co-2-(alkyl/aryl)-2-oxazoline) Copolymers, ACS Omega. 7 (2022) 40067–40077. https://doi.org/10.1021/acsomega.2c04809.

[48] M.E. Kourti, E. Fega, M. Pitsikalis, Block copolymers based on 2-methyl- and 2-phenyl-oxazoline by metallocene-mediated cationic ring-opening polymerization: Synthesis and characterization, Polym. Chem. 7 (2016) 2821–2835. https://doi.org/10.1039/c6py00405a.

3.6.Supporting Information

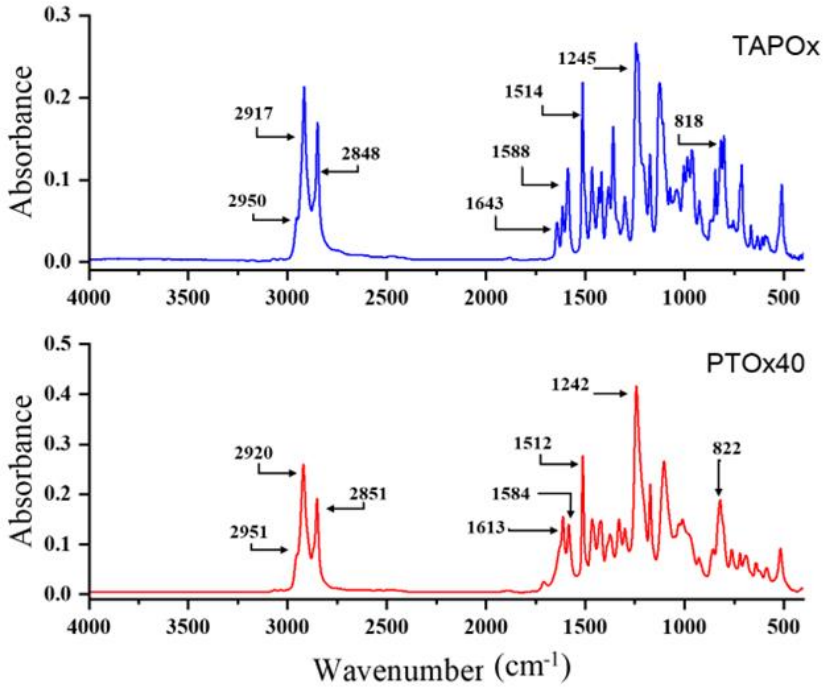

Figure 3.S1. FT-IR spectra of: TAPOx monomer and PTOx40 poly(2-oxazoline).

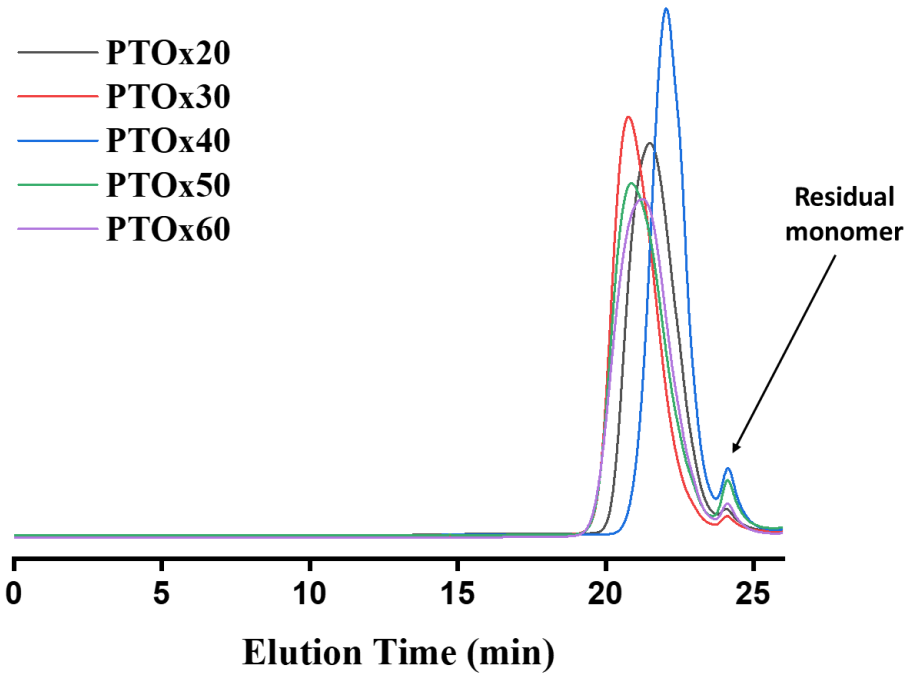

Figure 3.S2. SEC curves of PTOx family.

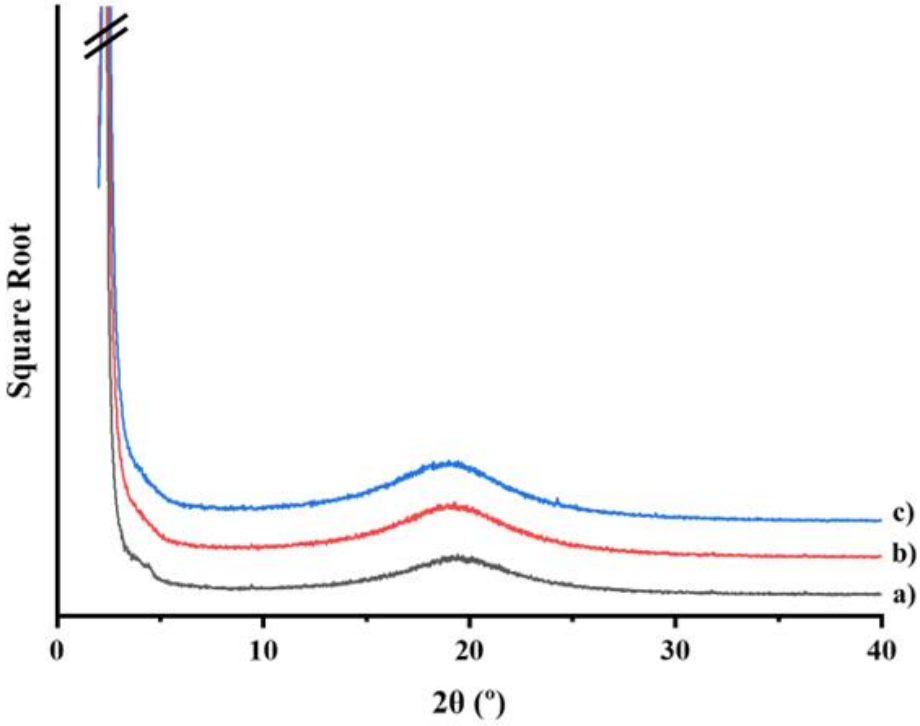

Figure 3.S3. X-ray diffractograms of PTOx20 recorded at: a) 50, b) 85 and c) 110 °C.

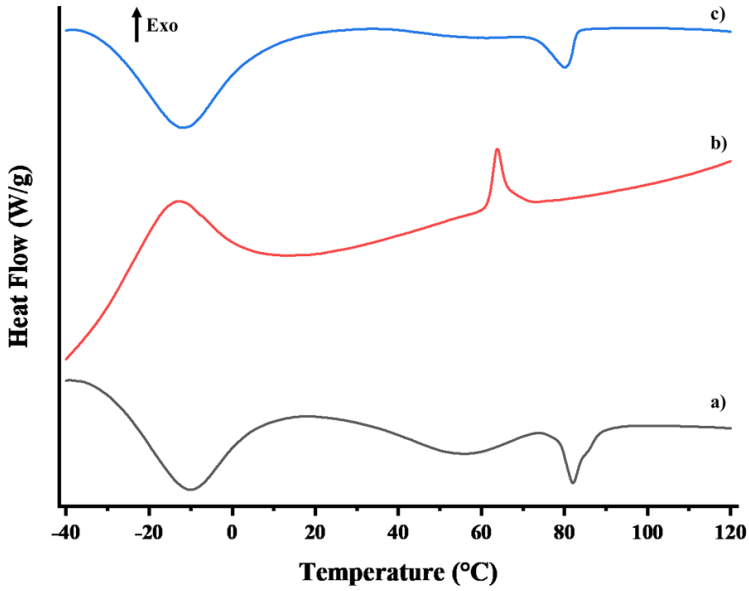

Figure 3.S4. Calorimetric analysis of PTOx40: a) first heating, b) first cooling and c) second heating (Scan rate: 10 °C/min).

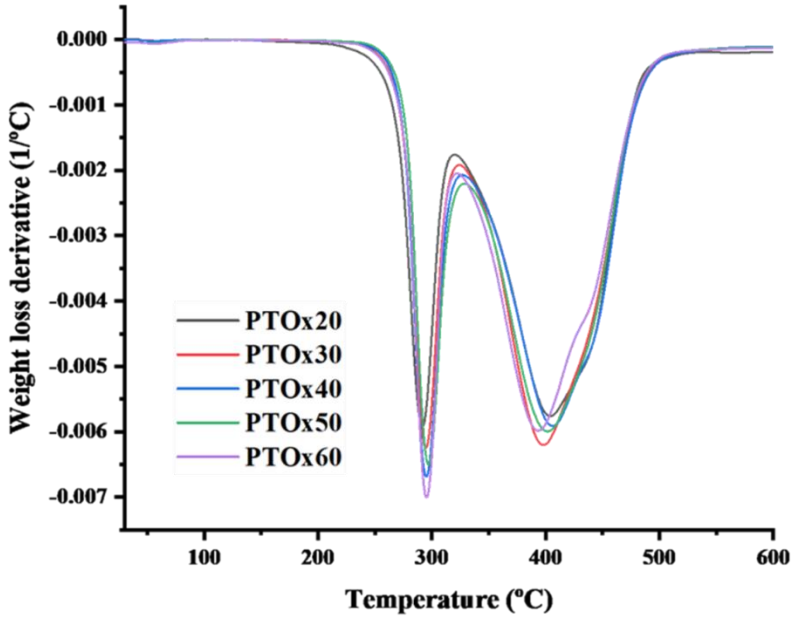

Figure 3.S5. DTGA curves of PTOx family recorded at a heating rate of 10 °C/min in nitrogen atmosphere.

UNIVERSITAT ROVIRA I VIRGILI
COLUMNAR LIQUID-CRYSTALLINE POLYMERS CONTAINING NITROGEN AT THE BACKBONE TO BE USED TO PREPARE ION-TRANSPORT MEMBRANES
Jordi Guardià Blanch

Chapter 4

Tapered hybrid poly(2-oxazoline) membranes for proton transport. New approach to PEM assembly

UNIVERSITAT ROVIRA I VIRGILI
COLUMNAR LIQUID-CRYSTALLINE POLYMERS CONTAINING NITROGEN AT THE BACKBONE TO BE USED TO PREPARE ION-TRANSPORT MEMBRANES
Jordi Guardià Blanch

CHAPTER 4

4.1.Introduction

Nowadays, climate change is a reality. An increasing amount of greenhouse gases (GHG) over the years has been released into the atmosphere for the last century, leading to an increase in the global temperature [1]. With this background, the scientific community has been focused on the development of alternatives to fossil fuels. One of these alternatives is the proton exchange fuel cells (PEMFC). These types of cells are assembled similarly to a sandwich. In the middle of the sandwich, there is the polymer electrolyte membrane (PEM), which is surrounded by two electrodes, one on each side [2]. In the last decades, PEMFC have aroused a great interest in power-generating devices for portable devices and automotive due to their low cost, lightweight, low emissions, and high-power density [3].

Nowadays, PEMFC membranes are based on perfluorosulfonic acid ionomer (PFSI). However, these types of membranes present some drawbacks such as poor chemical stability at high temperatures, methanol crossover (when operating on direct methanol fuel cells (DMFC)), and a huge dependency on water, limiting their range of operating temperature from 0 to 100 °C [4].

Despite PFSI-based membranes present advantages like excellent proton conductivity and electrochemical stability, other alternatives have been investigated in recent years. For instance, Wang and co-workers have proven the use of amino acid-modified chitosan nanofibers to build up nanocomposites for proton exchange membranes, obtaining good conductivity at 80 °C (0.192 S/cm) and lower methanol crossover than the typical PFSI-based membranes [5].

Looking for other alternatives, our group has focused over the last decades on providing an alternative to PFSI-based membranes. To do so, tapered side chain liquid crystal polymers (SCLCP)s have been investigated. Lately, liquid crystals and liquid crystal polymers have been investigated deeply due to their broad range of applications, from different optoelectronic devices [6], to sensors [7] or membranes [8–10].

For instance, Bogdanowicz and co-workers designed a family of modified SCLCPs for the anodized aluminium oxide hybrid membrane, based on a poly(aziridine) modified with the dendron 3,4,5-tris[4-(n-dodecan-1-yloxy)bezyloxy]benzoate (TAPER) that showed methanol crossover at the level of 10^{-8} cm^2 s^{-1}, two orders of magnitude lower than Nafion®117, high permselectivity towards proton in comparison to other monovalent cations [11]. In other work, Montané et al. and Zare et al. prepared a SCLC linear polyethers modified with the same dendron, for which columnar structure in self-supported membrane was obtained, with proton conductivity similar to low-hydrated Nafion®117 [12,13]. An advantage of the above-mentioned polymers is their ability to self-assemble into column-like structures due to π-π stacking of the side chain mesogen aromatic moieties in lateral position and not in the main chain [14]. In our previous studies [12,13,15] a full chemical modification polymer was not able to be prepared, instead a partially modified SCLCP was obtained. Despite the rather low modification degree in some cases, the presence of the mesogenic tapered unit confers the liquid crystal behaviour, obtaining columnar structures. The presence of columnar structures, using this dendron, was confirmed in previous studies by Percec and co-workers [16,17].

As aforementioned, SCLCPs were modified followed by the strategy of grafting the dendronized tapered mesogen 3,4,5-tris[4-(n-dodecan-1-yloxy)bezyloxy]benzoate to a polymeric chain (*i.e.,* polyepichloridine-co-ethylene oxide, polyglycidol and polyaziridine)[12,13,18]. Another explored strategy includes the synthesis of a SCLCP by directly polymerizing a mesogenic tapered monomer containing the same dendron as the one used for the chemical modifications in the first strategy, leading in both cases to columnar structure [19–21].

The formation of these columnar structures allows the design of ion-transporting channels. The aromatic moieties support this conformation thanks to the rigidity of the aromatic rings. Additionally, long aliphatic chains at the outer part of the dendron build an additional layer toward the surface of the columns. This flexible layer further stabilizes the formed columns. In this group of polymers, the presence of heteroatoms (oxygen or nitrogen) in the polymer backbone facilitates the transport of the cations across the columns, forming the permeation path. Dodecyl aliphatic chains additionally ensure a sufficient level of columns' mobility allowing thermally induced rearrangement and ideally homeotropical columns' orientation. The highly hydrophobic nature reduces the influence of the external environment reducing water cross-over [16].

Mechanical properties of the polymers described in the literature exhibit some differences according to the used backbones. On the one hand, polyepichloridine-co-ethylene oxide-based SCLCP present good mechanical properties despite their lack of sufficient proton permselectivity in comparison to other monovalent cations, such as Li^+, K^+ and Na^+ [22]. On the other hand, polyamines-based SCLCPs show good proton conductivity and

relatively good permselectivity towards proton despite their poor mechanical properties. In these cases, polyamines modified membranes were fragile and brittle and therefore needed a support material [11].

In this work, we present the preparation and characterization of tapered liquid crystal poly(2-oxazoline) membranes, based on poly(2-(3,4,5-tris(4-dodecyloxybenzyloxy)phenyl)-2-oxazoline) (PTOx). The idea of using this monomer to prepare a SCLCP resides in the 2-oxazoline moiety. It is well known that 2-oxazoline monomers polymerize in a *living* polymerization fashion. This allows us to synthesize mesogenic homopolymers with a well-defined degree of polymerization (DP) and, by extension, molecular weight. In addition, *living* polymerizations are characterized by a narrow molecular weight distribution.

A recently published work presenting in detail the synthesis and characterization of a family of PTOx, with DP from 20 to 60 is a starting point for this work [20]. For the following work, the PTOx with a degree of polymerization of 40 (PTOx40) was selected, since it is the only one that exhibited a clear hexagonal columnar mesophase with well-defined clearing and anisotropy temperatures observed after first heating. Ŝakalytė and co-workers, for instance, synthesized a family of modified polyaziridines (poly[2-(aziridin-1-yl)ethanol] (PAZE)) with the dendron 3,4,5-tris[4-(ndodecan-1-yloxy)benzyloxy]benzoate (TAPER) obtaining different degrees of modifications from 16 to 100%. In this work, the presence of crystalline domains was noticed for the modified PAZE with modification degrees between 16 and 48%, and 100%, which resulted in polymers with a brittle behaviour [23]. PTOx liquid crystal homopolymers family did not exhibit the presence of crystalline domains, as was seen according to differential scanning

calorimetry and X-ray diffraction, which should be an advantage in terms of the homopolymer performance [20]. The preparation of the membranes was made according to the literature [15,24,25]: initially, an attempt to prepare a self-supported PTOx membrane was made, however, after several iterations, a rupture of the membrane was observed. For this reason, a polyester fabric was chosen as support to prepare poly(2-oxazoline) hybrid membranes and studied in detail.

4.2.Experimental Section

4.2.1. Materials

Inorganic and organic compounds were purchased from Sigma Aldrich and Fischer Scientific and used as received. The used polyester fabric was Hollytex 22 g/cm^2. For membrane assembling and all experiments in which water was required, Milli-Q ultra-pure water was used.

4.2.2. Polymer synthesis

Poly(2-(3,4,5-tris(4-dodecyloxybenzyloxy)phenyl)-2-oxazoline) (PTOx) with a degree of polymerization of 40 was synthetized as described elsewhere [14]: a previously flame dried Schlenk tube was filled with 2-(3,4,5-tris(4-dodecyloxybenzyloxy)phenyl)-4,5-dihydro-1,3-oxazole) (TAPOx) (0.5 g, 0.5 mmol) and kept under vacuum for 30 min. After that, the tube was immersed

in a previously heated oil bath at 105 °C. When TAPOx was melted, the appropriate amount of dry chlorobenzene was added to reach 1.0 M concentration inside the Schlenk tube (considering the amount of chlorobenzene that was already added with the initiator). Then, the initiator (MeOTf) was added via syringe according to the desired DP (DP = 40) from a freshly prepared solution of the initiator in dry chlorobenzene ([MeOTf] = 0.135 M). The mixture was stirred until ^{1}H NMR spectrum indicated almost complete conversion of the monomer (≥93 %). Then, a large excess of morpholine (200 μL) was added to the reaction mixture, acting as a terminating agent. After 30 min, the crude mixture was precipitated twice in a cold KOH solution (0.1 M). Finally, the product was dried under vacuum at 50 °C until constant weight to obtain a beige solid.

4.2.3. Membrane Preparation

4.2.3.1. Surface type for membrane preparation

Fluorinated Ethylene Propylene Resin (FEPR) paper sheet base, with a thickness of 0.1 mm, was purchased from Saint-Gobain. The FEPR sheet was washed with acetone and air-dried before used.

Hydrophobic glass: the glass plates were immersed in a 10% (v/v) solution of clorotrimethylsilane overnight. After that, hydrophobic glass plates were washed several times with acetone and air-dried overnight.

4.2.3.2. Membrane preparation

A general overview of the hybrid membrane preparation, involving the immersion precipitation and the thermal treatment, is depicted in **Figure 4.1**.

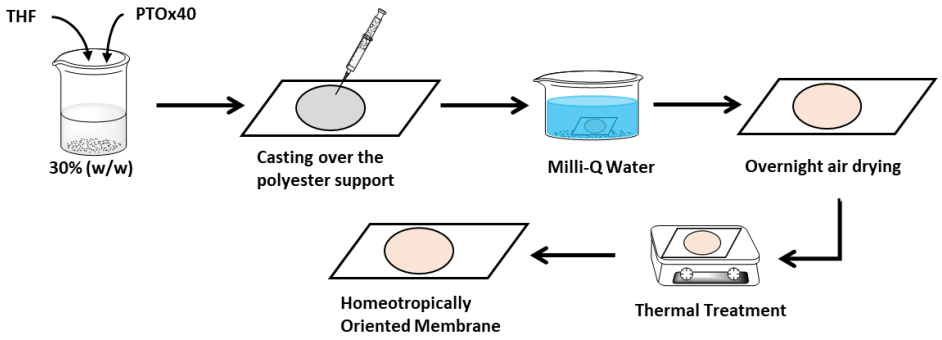

Figure 4.1. General overview of the hybrid membrane assembling.

The immersion precipitation process included: a 30% solution (w/w) of PTOx in THF was prepared and cast over the polyester fabric. The polyester fabric was placed over a hydrophobic base (treated glass or FEPR sheet) or over a hydrophilic glass plate. Later, the impregnated support was immersed in a bath of Milli-Q water for 15 minutes. Finally, the membrane was air-dried overnight.

The thermal treatment (baking process) consisted of the previously prepared hybrid membrane was placed on a Linkam TP92 hot stage, heated above the polymer clearing temperature and kept for 30 min. Next, it was slowly cooled (0.5 °C/min) to the selected annealing temperature (**Table 4.2**). Hybrid

membranes were annealed for 24 h. Finally, the hybrid membranes were cooled down to room temperature at 0.1 °C/min.

4.2.4. Characterization

Differential Scanning Calorimetry (DSC). Calorimetric analyses were carried out on a Mettler DSC-821 instruments calibrated using indium (156.6 °C) and zinc (419.6 °C) pearls. Samples were placed in an aluminium standard crucible of 40 μL with pierced lids (between 4 and 6 mg of the sample), which were analysed in N_2 atmosphere (gas flow rate of 50 cm^3/min).

Contact angle (CA). The static contact angles with water on a membrane surface were measured with an optical goniometer (Ossila LTd, Sheffield, UK) supported by dedicated software. For the tests, water drops of (7 μL) were deposited in the sample surface. The contact angle was calculated, immediately after placing the water drop, using the tangent to the surface at the point of contact of three phases, *i.e.*, solid, liquid and gas. For each test reported, at least three drops of water were used.

X-Ray diffraction (XRD). The XRD measurements were made using a Bruker-AXS D8-Discover diffractometer equipped with a parallel incident beam (Göbel mirror), vertical θ-θ goniometer, XYZ motorized stage and a GADDS (General Area Diffraction System). Samples were placed directly on the

Si(510) sample holder for reflection analysis. An X-ray collimator system close-to-the-sample allows to analyse areas of 500 μm. An X-ray diffractometer was operated at 40 kV and 40 mA to generate $Cu_{K\alpha}$ radiation. The GADDS detector was a VÅNTEC-500 (silicon strip technology) placed at 30 cm from the sample. We collected one *frame* (2D XRD pattern) that covered at such distance a range from 0.9 up to 11° 2θ and from 9.0° to 30.5° 2θ. The exposition time was 600s per *frame*.

Electrochemical Impedance Spectroscopy (EIS). Electrochemical Impedance Spectroscopy analysis was performed using PGStat Autolab M204 (Metrohm, Barendrecht, Netherland), coupled to a frequency response analyser (FRA) and two-point cell composed of two copper plates. We carried out the analysis in dried stat and after adding water drops. EIS analysis was performed through-plane and in-plane configuration. The measurements were performed at room temperature (24 ± 1 °C).

Permeability tests. Permeability tests were performed using a methacrylate test cell that consisted of two compartments, separated by the tested membrane, containing the feed and the stripping solutions, respectively. The feed and the stripping were 200 mL, and the effective area was 0.28 cm^2. For the proton transportation experiments, the initial feed solution was 0.1 M HCl aqueous solution and the stripping solution 0.1 M aqueous of: NaCl, LiCl or KCl. The pH of the stripping solution was measured every 10 s by a pH-Conductivity meter CPC-505 connected to a computer, which registered all results. All experiments were repeated three times.

Linear Sweep voltammetry (LSV): Linear sweep voltammetry was performed using Metrohm / Eco Chemie Autolab PGSTAT12 (Metrohm, Barendrecht, Netherland), in potentiostatic mode with current ranging (automatic) from 100 mA to 100 nA, potential range from 0 V to 5 V, step 0.01 V, and scan rate 0.01 V/s. The experimental setup is presented in **Figure 4.8**. The distance between the reference electrodes (Ag/AgCl) and the membrane was 1 cm. The solution volume in each compartment was 200 mL. The measurements were performed at RT (24 ± 1 °C). Samples for these experiments were placed in a Teflon sheet with a hole in the middle, giving a total membrane area equal to 0.28 cm^2. The hybrid membrane was placed between two Teflon sheets and sealed.

0.1 M hydrochloric acid was used to study the proton transport. Additionally, a series of measurements with chlorides (LiCl, KCl and NaCl) in 0.1 M solutions were performed to study the selectivity performance.

Solution uptake test. Weighted membranes were immersed in Milli-Q water at room temperature, and the measurements were taken every hour for the first 5 hours and then at 24h, to ensure complete water saturation of the membranes. The water on the surface was quickly removed with filter paper, and the mass was measured afterwards. The water uptake can be calculated as follows.

$$Water\ Uptake\ (\%) = \frac{(Wwet - Wdry)}{Wdry} * 100 \qquad (1)$$

Where W_{wet} and W_{dry} are the mass of wet and dry membrane samples, respectively.

The same procedure was used when calculating the methanol uptake. In these cases, solutions of 2M, 6M and 12M of methanol in water were used. Measurements were taken every hour for the first 5 hours, and then at 24 h, to ensure complete methanol saturation of the membranes.

Optical Microscopy Analysis. It was performed with a Keyence digital microscope VHX – 7000 series, with 4K high-resolution camera.

4.3.Results and discussion

4.3.1. Membrane preparation and characterization

As previously described, we have synthetized a family of columnar liquid crystal poly2-oxazolines based on the tapered monomer 2-(3,4,5-tris(4-dodecyloxybenzyloxy)phenyl)-4,5-dihydro-1,3-oxazole) [19]. This family contains 5 family members depending on the degree of polymerization (DP) from 20 to 60 [20]. The specific design of dendronized polymer structure allows the formation of columnar structures where the polymer backbone forms an inner channel. The channel is stabilized and protected by the tapered dendron. According to literature, this stabilization is possible due to the π-π stacking of the aryl moieties of the dendron [14,26]. The inner part of the columns contains nitrogen atoms, which thanks to their electron donor

character are expected to be responsible for the proton transport across the columns, without the need for water molecules [11,22,24].

Therefore, for this study, we choose a poly2-oxazoline (structure can be seen in **Figure 4.2**) with a DP of 40 (PTOx40), since it is the only one that presents a clear hexagonal columnar mesophase, as we could observe by XRD in previous studies (**Table 4.1**) [20]. During the membrane assembling, preliminary studies demonstrated the impossibility of preparing self-supported PTOx40 membranes, due to their brittleness. In order to solve this drawback, a support was used. A polyester fabric (Hollytex 22 g/cm^2) was used as the support for the preparation of hybrid PTOx membranes. Membrane preparation process involved two main steps: the first one was the preparation of a solution of PTOx40 in tetrahydrofuran (THF) 30% (w/w) followed by the impregnation of the polymeric solution over the polyester support, and the second step, was the precipitation of the polymer using a Milli-Q water bath, followed by overnight air drying at room temperature.

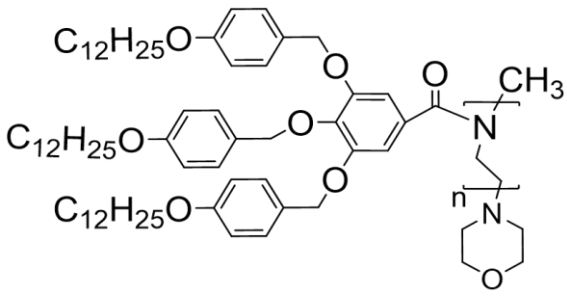

Figure 4.2. Poly(2-oxazoline) (PTOx40) chemical structure.

During the preparation of the hybrid membranes different surfaces were employed: normal glass (hydrophilic), silanized glass (hydrophobic) and a

Fluorinated Ethylene Propylene Resin (FEPR) sheet (hydrophobic). We used both hydrophobic and hydrophilic substrates to evaluate the influence of the hydrophobicity of the surface on the orientation and transport capability of the prepared membranes. The homeotropical orientation of the PTOx40 columns was induced according to the thermal treatment. The treatment can be summarized as follows: first, heating above the clearing temperature (T_c), followed by a slow cooling until the annealing temperature (see **Table 4.2**). At this moment, the membranes were kept at a constant temperature for 24 hours. Subsequently, hybrid membranes were cooled to room temperature, at the cooling rate of 0.1 °C/min. Additionally, for comparison's sake, a non-oriented hybrid membrane was prepared. Therefore, three membrane sets were prepared depending on the type of substrates; hydrophilic glass (PTOxM13), hydrophobic glass (PTOxM15), hydrophobic FEPR (PTOxM14), the non-oriented membrane supported on a hydrophilic glass (PTOxM12).

Table 4.1. Calorimetric features of PTOx40 obtained by DSC, and type of mesophase obtained from XRD results.

Polymer	**T_c (°C)** [a]	**Mesophase**
PTOx40	74	Col_h

[a] Clearing temperature obtained from second heating scan (scan rate: 10°C/min) (**Figure 4.S1**).

The hybrid membranes, prepared by the impregnation with a polymeric solution and the phase inversion precipitation, were analysed by XRD to establish polymer organization. From XRD analysis we observed a relatively sharp (full width at half maximum (FWHM) = 0.2) peak centred at $2\theta = 2.3°$ (d

= 38.6 Å) which indicates the presence of columnar structures (**Figure 4.3**). This peak was assigned to the lattice plane indexed (1 0 0). These results are in agreement with the dendronized polymers modified with TAPER described in the literature [12,13,15,18,20,25]. From the azimuthal scan we could confirm the proper orientation of the columns for the membranes PTOxM13, PTOxM14 and PTOxM15. In this analysis, we observed the presence of a relatively narrow (FWHM = 7.8 – 8.1) peak centred at approximately 270°, which indicates homeotropic orientation (**Figure 4.4**). XRD data is summarized in **Table 4.2**. As a comparison, the non-oriented membrane (PTOxM12) does not present a narrow peak at the azimuthal scan, which indicates no homeotropic orientation of the columns in the membrane. Meanwhile, a very flat and broad peak is presented, which could indicate the presence of a random orientation. The result of the lack of desired orientation could be explained by the use of the elevated annealing temperature, above the clearing temperature used during the preparation of the membrane. Since the temperature used to orient the polymer columns was close to the clearing temperature, the excess of the energy provided to the system may have exceeded the energy level required for the homeotropical orientation of the polymeric columns, and thus, the equilibrium at the annealing stage was not reached. Therefore, in the following step, the cooling process occurred in a disbalanced environment, reducing the possibility for homeotropic orientation of the columns. Evaluating the influence of the bottom surface from the azimuthal scan we can observe that when a hydrophobic substrate was used (PTOxM14 and PTOxM15), the obtained orientation was better than for the hybrid membrane PTOxM13, in which a hydrophilic substrate was used.

The morphology and the topographic analysis of the membrane surfaces were evaluated through optical microscopy. All membranes presented a pallid light brown colour with a low transparency (**Figure 4.4**). It was observed that the membrane PTOxM12 presented a slightly greater transparency than the oriented membranes, PTOxM13, PTOxM14 and PTOxM15. One could expect that the homeotropically oriented membranes should present an increased transparency in comparison to the non-oriented membrane, due to the transmission of light across the membrane. Nevertheless, it seems that this is not the case, and the transparency of these samples is not related to the orientation of the hybrid membranes. The images shown in **Figure 4.4** were recorded for the membranes attached to the substrates (glass, silanized glass and FEPR). In all oriented membranes air bubbles were observed. PTOxM14 was the membrane with bigger number of bubbles and bigger size. This can be explained due to the used substrate (FEPR)- the most flexible substrate for the series. After the immerse precipitation, during the overnight drying, the substrate adopted an undulated shape, hence the contraction of the polymeric material could promote the appearance of the increased number of bubbles, as well as their bigger size.

Table 4.2. XRD diffraction data of PTOx membranes and resulting full width at half maximum (FWHM) and angle of orientation.

Membrane	Annealing Temperature (°C)	Oriented	2θ (°)	d_{100} (Å)	Mesophase	FWHM (°)	Angle of Orientation (°)
PTOxM12	73	No	2.3	38.6	Col	-	-
PTOxM13	69	Yes	2.3	38.6	Col	7.8	90
PTOxM14	69	Yes	2.3	38.6	Col	8.1	90
PTOxM15	69	Yes	2.3	38.6	Col	7.8	90

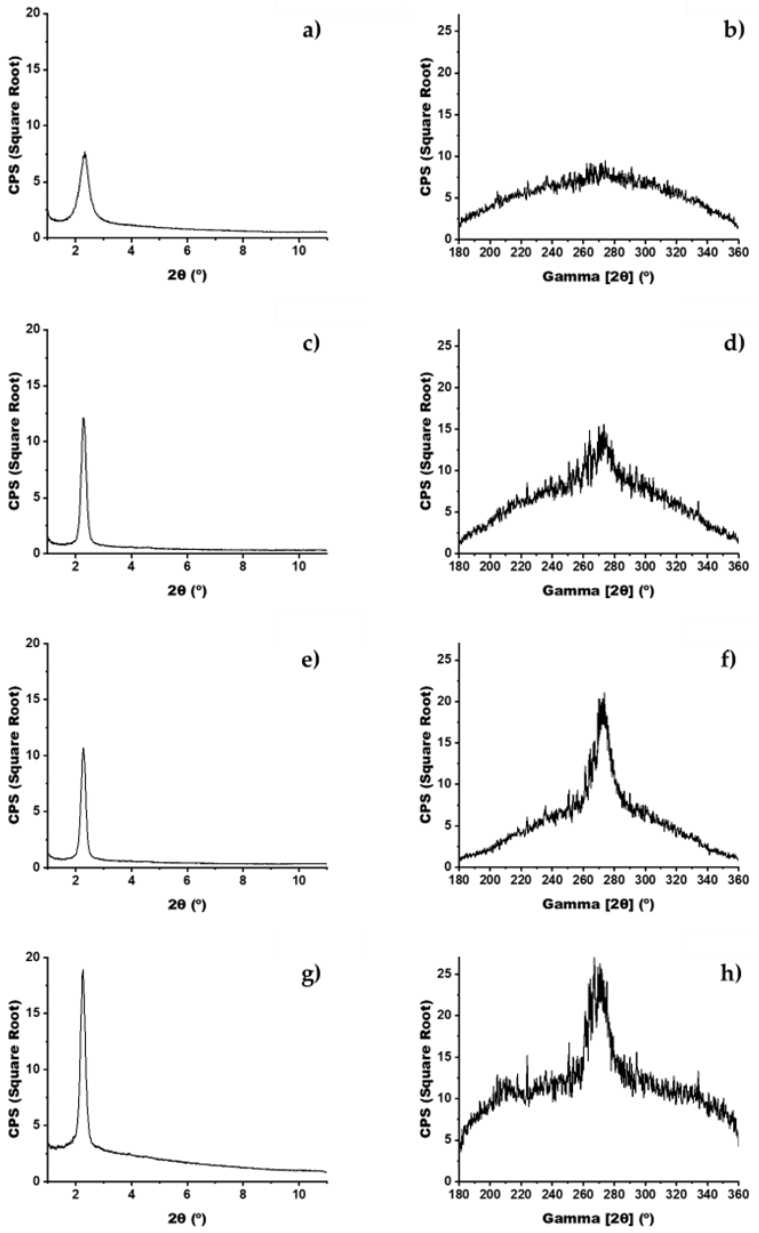

Figure 4.3. XRD diffractograms of the membranes a) PTOxM12, c) PTOxM13, e) PTOxM14 and g) PTOxM15, and the azimuthal scan of the hybrid membranes b) PTOxM12, d) PTOxM13, f) PTOxM14 and h) PTOxM15.

Bubbles can be segregated into three groups, in terms of diameter: small (80 – 300 μm), medium (300 – 800 μm) and large (800 – 1600 μm). Bubbles observed in the PTOxM13 and PTOxM15 were mainly small and medium (**Figure 4.4b** and **4.4d**) with few exceptions of single large bubbles (PTOxM13) (**Figure 4.4b**). On the other hand, the PTOxM14 presented a variety of bubbles (**Figure 4.4c**). An extended number of small bubbles could be seen across the whole membrane. Medium bubbles were located mainly close to the border of the membrane. The largest bubbles were found in this membrane. It was noteworthy that these bubbles were not observed during the preparation of the membranes, but after the immersion precipitation, probably as a consequence of the exchange of the solvent (THF) and the antisolvent (Milli-Q water). The PTOxM12 membrane, on the other hand, did not present any kind of bubbles of any size. This fact can be explained by several heating attempts performed on the same membrane in non-ideal conditions. The PTOxM12 was heated several times to achieve homeotropical orientation, however, this orientation was never obtained. Therefore, this membrane was used as a non-oriented membrane that underwent unsuccessful thermal treatment.

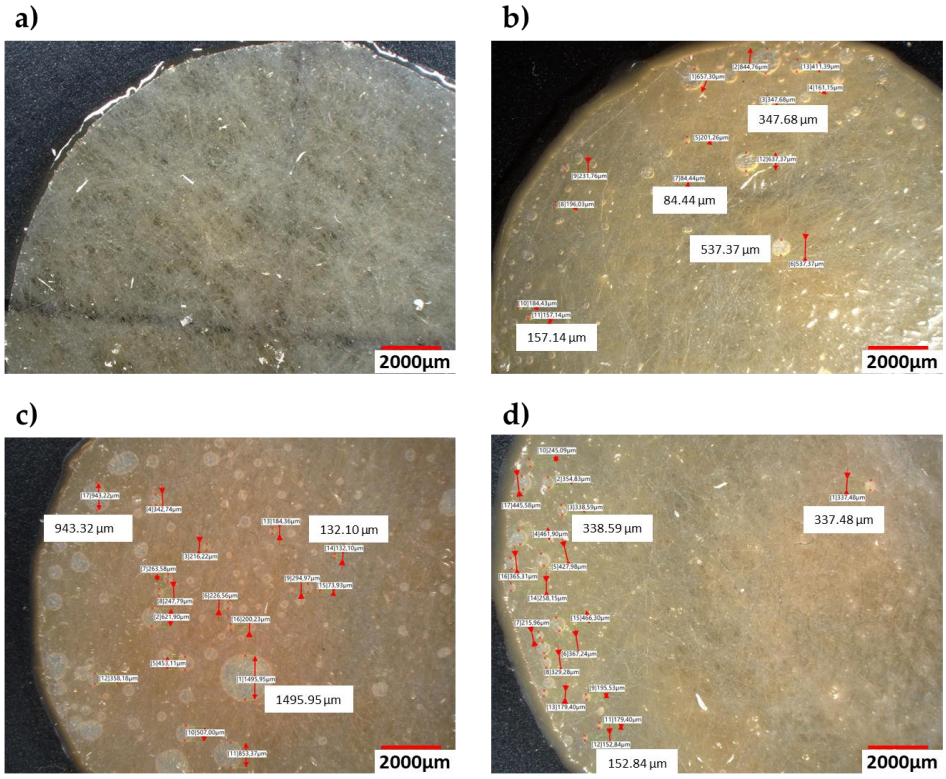

Figure 4.4. Optical microscopy images of a) PTOxM12, b) PTOxM13, c) PTOxM14 and d) PTOxM15 were recorded at RT (24 ± 1 °C).

To study the morphology of the membrane surface, a topographic analysis was carried out with the same optical microscope. This analysis allowed the characterization of both oriented and unoriented membranes with the purpose of identifying visible structural defects along with any discontinuity of the surface or cracks (**Figure 4.5**). Nevertheless, PTOxM12 seemed to present a more irregular surface. This membrane, as it was already commented, presented a bigger level of transparency than the other studied membranes, which did not allow the observation of any defects on the surface. Therefore, in this membrane, we were not observing any important

morphology characteristics of the surface, only the morphology beneath the upper surface. The areas with bubbles seemed to have a sunken surface, as can be seen in **Figure 4.S2**. According to the depth, bubbles could be located close to the surface of the air side, or dept at the bottom part close to the support. Regardless of the depth, they could present a thin film at the upper part of the entrapped bubble, thus increasing the transparency of this part (**Figure 4.S2b, 4.S2d** and **4.S2f**). As a consequence, in the topographic analysis, we could observe mainly the bottom part of the bubble and not the upper part. Another possibility is the presence of these bubbles at the bottom part of the membrane, and because of the transparency of the hybrid membrane, they seem to be close to the upper surface or in the middle of the membrane.

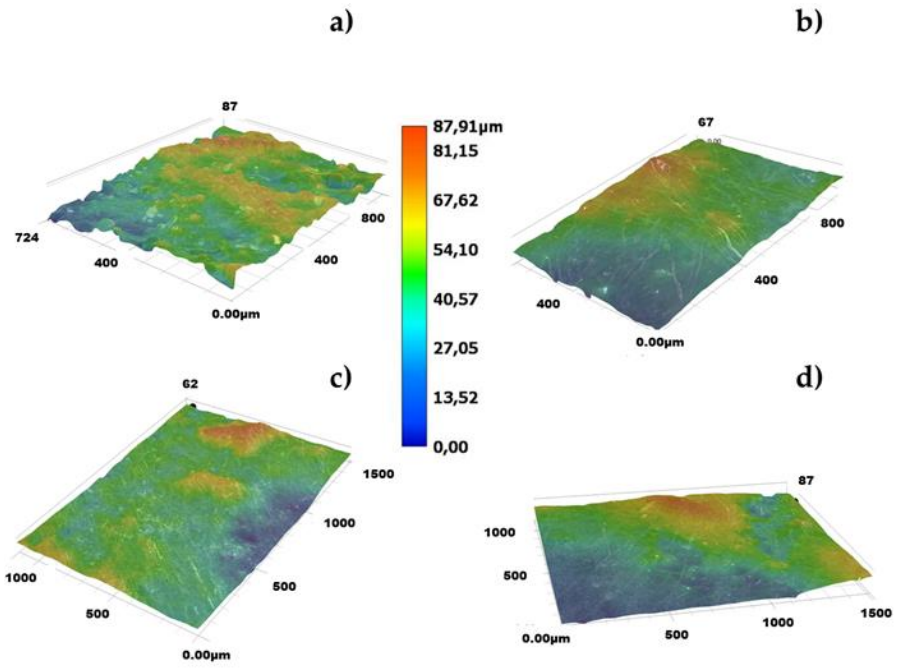

Figure 4.5. 3D images from hybrid membranes a) PTOxM12, b) PTOxM13, c) PTOxM14 and recorded with an optical microscope at RT (24 ± 1 °C).

Finally, we analysed utilizing the optical microscope the bottom surface of the membrane after detaching them from the substrates. We could observe how membranes PTOxM12, PTOxM13 and PTOxM15 demonstrate a more regular surface than the air side of the membranes. When detaching the hybrid membrane PTOxM14 from the substrate surface, we observed a small cracking of the excess of the polymer used, located in between the membrane and the surface. In this case, the membrane conserved its structure, and no rupture was observed. From the topographic analysis of the bottom side of the membranes, we could confirm that the observed bubbles were located mainly at the bottom side of the membrane and not at the upper and middle part. In **Figure 4.S3** we can observe the presence of the bubbles in this polymer in excess and not inside the membrane. From the topographic analysis, we can observe how the membrane surfaces are highly homogenous. The only phenomenon that disrupts this homogeneity are the bubbles, which denote a sunken zone. In these cases, we did not observe a thin film at the top of the bubble, which was always presented in the topographic analysis of the air side.

Polyester fabric fibres were also analysed through optical microscopy in order to compare the fibre thickness before and after the polymer impregnation. As can be seen in **Figure 4.S4**, there is no difference between the fibres before and after the preparation of the hybrid membranes. The thickness of the polyester fabric fibres was between 25 to 35 μm (**Figure 4.S4c**), meanwhile, the hybrid membrane fibres presented similar thickness (**Figure 4.S4a-b**). This could indicate that the polymer (PTOx40) was not swallowed by the fibres during the impregnation, instead it surrounded the fibres. For this study, we prepared a set of membranes based on PTOx40 and polyester support. The

preparation process of the membrane is shown in **Figure 4.1**. To induce the homeotropical orientation of the polymeric columns in the membrane, the samples underwent a thermal process. The list of samples is presented in **Table 4.2.**

4.3.2. Transport properties

One of the aims of this study was to determine the ion transport properties of the membrane, therefore in the first step, wettability tests were performed. The membrane wettability was studied employing water static contact angle (CA) measurements using an optical goniometer supported by dedicated software. In our previous studies, the CA values were analysed for different polyether and polyamine membranes bearing a tapered group as the side chain, with the ability to form polymeric columns [12,22,24]. The results of this analysis evidenced an increased hydrophobicity value for the homeotropically oriented membranes in comparison to the non-oriented membranes. Therefore, this increased hydrophobicity was explained as the result of exposure to the highly hydrophobic tapered group, due to the homeotropic orientation of polymeric columns. For instance, Zare and co-workers observed an increased hydrophobicity from 87 ± 2 ° to 104.5 ± 0.9 ° on the air side (top side of the membranes) [22]. Nevertheless, for the PTOx membranes such distinguished change in the CA values: for the unoriented membranes were equal 108 ± 1.1 ° for PTOxM12, whereas for the oriented membranes were equal 112.4 ± 1.2 °. All the results of the contact angle measurements are summarized in **Table 4.3**.

Oriented and non-oriented PTOx membranes exhibited similar contact angles with the difference of *c.a.* 4 ° for the air side (**Figure 4.S5**). The difference in the obtained results in comparison to the literature findings can be explained by two main factors: first, our membranes are supported by a polyester fabric with a hydrophobic character, as we can see in **Table 4.3**, this fabric is impregnated by the polymer, where the polymeric column rearranges to increase the interaction between outer hydrophilic sites. Second, the structure of the lateral chains differs. In our case, the tapered group was linked directly to the nitrogen placed in the polymer main chain, whereas in previous cases the TAPER was linked via an ethyl spacer. The formation of hybrid membranes using this fabric could favour the increased contact angle value of the non-oriented membrane; when the polymer was cast on the polyester support the interaction between the hydrophobic groups presented on the surface of the threads of the support predefines the orientation of the polymeric columns increasing the overall hydrophobicity – higher CA values, however, due to not well-defined structure of the support, columns are unable to full form the ideal homeotropic orientation.

Table 4.3. Water and methanol uptake, and water contact angles of oriented (PTOxM13, PTOxM14 and PTOxM15) and non-oriented (PTOxM12) PTOx membranes, as well as for the polyester fabric support.

Membrane	Water Contact Angle [a, b]	Water Uptake (%) [c]	2 M Methanol (%) [c]	6 M Methanol (%) [c]	12 M Methanol (%) [c]
PTOxM12	108.7 ± 1 [a] /111.3 ± 2 [b]	10 ± 1	4 ± 2	4 ± 2	5 ± 2
PTOxM13	113.0 ± 1 [a] /110.7 ± 2 [b]	11 ± 2	6 ± 1	5 ± 1	4 ± 1
PTOxM14	111.2 ± 2 [a] /116.8 ± 4 [b]	10 ± 1	8 ± 1	7 ± 2	4 ± 1
PTOxM15	112.4 ± 1 [a] /111.5 ± 2 [b]	10 ± 1	6 ± 1	4 ± 1	4 ± 1
PTOxVM [d]	104.7 ± 1	-	-	-	-
Polyester Support	114.2 ± 1	23 ± 2	25 ± 1	26 ± 1	24 ± 1

[a] Air side. [b] Substrate side. [c] Water and methanol uptake after 24 h. [d] PTOx virgin membrane (no support was used). No thermal treatment was employed.

As mentioned before, oriented membranes were assembled over different substrates, hydrophilic (PTOxM13) and hydrophobic (PTOxM14 and PTOxM15). As we can also observe in **Table 4.3** there was no difference between each hydrophilic/hydrophobic surface, indicating that the substrate's nature does not affect the wettability of both sides of the membrane. In addition, when analysing the bottom part of the membranes we did not observe any difference of the contact angles regarding the zones with bubbles in comparison with the zones without. Therefore, the observed variations were only driven by the PTOx40 between the fabric and the surfaces.

To assess the possible influence of the aqueous environment and the methanol an uptake test with water and methanol aqueous solutions was performed. The results for all membranes revealed almost identical behaviour, regardless the orientation, for both water and methanol solutions. Evaluation of the mass over time indicated full solution uptake within the first hour of the experiment for all solutions and concentrations. As can be seen in **Table 4.3**, water uptake values were roughly around 10 % for all tested membranes. The methanol uptake presented approximately 6 % of weight increase for the 2M solution, showing a decreasing tendency of uptake values upon increasing concentrations (6M and 12M) solutions.

For the ionic conductivity experiments, such as EIS, permeability test and linear sweep voltammetry, the membranes with a diameter of 0.8 cm were used. Each of these small membranes has been chosen to perform each of the different conductivity experiments. The ionic conductivity of both oriented and non-oriented hybrid membranes was studied firstly by electrochemical impedance spectroscopy (EIS). The experiment was carried out for dry membrane and after adding few water drops, to rule out the influence of

moisture on the conductivity behaviour. As we could observe from the contact angle experiments, all studied membranes are hydrophobic. Hence, the addition of water should not imply any changes in the conductivity results obtained from impedance spectroscopy. To describe the polymer conductivity behaviour of the hybrid membranes, we performed a simulation of the impedance data fitted to model electrical circuits. Depending on the impedance data the system can be simulated by different simple or complex equivalent circuits. Electrical circuits were labelled by using the "circuit description code" (CDC) [27] where, a circuit composed for example by a resistor (R) (**Figure 4.S6a**) and a capacitor (C) (**Figure 4.S6b**) can form different combinations. If a capacitor and a resistor are connected in series the circuit is denoted as RC (**Figure 4.S6c**), but if it is connected in parallel it is expressed enclosed in parentheses (RC) (**Figure 4.S6d**). As mentioned, other more complex circuits can be formed, *i.e.* a circuit in which a resistor and a capacitor are connected in parallel and connected to another resistor is denoted as R(RC) (**Figure 4.S6e**), among many other examples.

For a better understanding, we decided to perform EIS in-plane and through-plane measurements. Water drops were only added during the in-plane experiments. The results of these experiments are shown in **Figure 4.6** and **Figure 4.S7**, for dry membranes and after the addition of 10 drops of water, respectively.

As we can observe, in both graphics membranes do not display a significant difference between the dry membranes and the membranes after 10 drops of water. The hydrophobic behaviour of the membranes prevented the water from spreading across the hybrid membranes. Additionally, the added water

formed a uniform drop which did not spread over the membrane surface, as expected (**Figure 4.S8**).

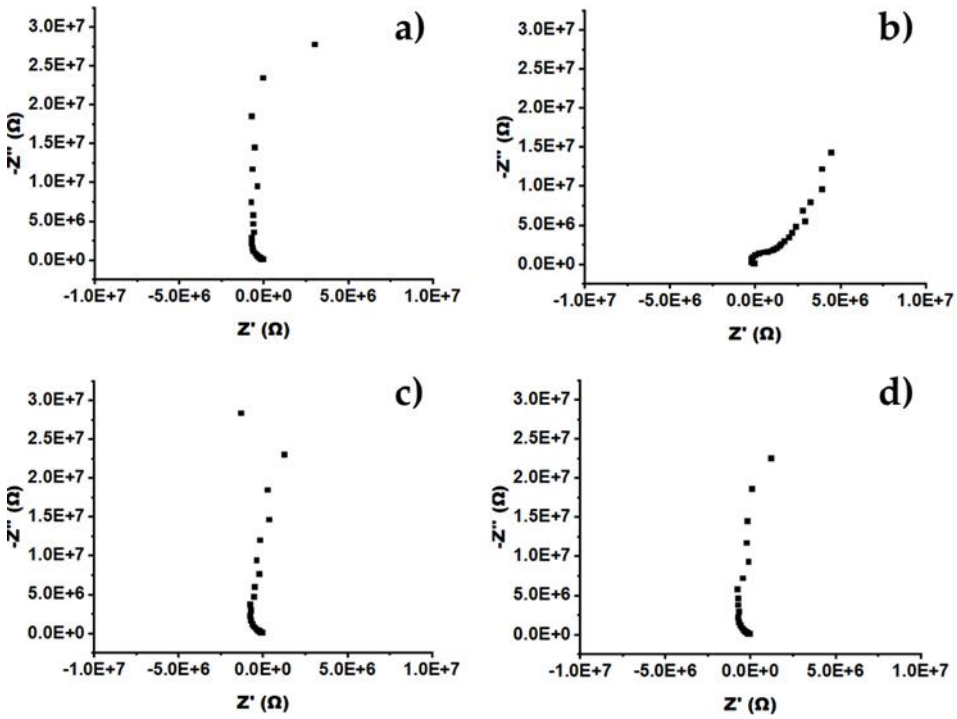

Figure 4.6. Nyquist plots of dried PTOx hybrid membranes. a) PTOxM12, b) PTOxM13, c) PTOxM14 and d) PTOxM15.

As mentioned above, we also performed the EIS impedance analysis through-plane without the addition of water. During the analysis we could not observe any significant differences between both in-plane and through-plane experiments (**Figure 4.6** and **Figure 4.7**, respectively).

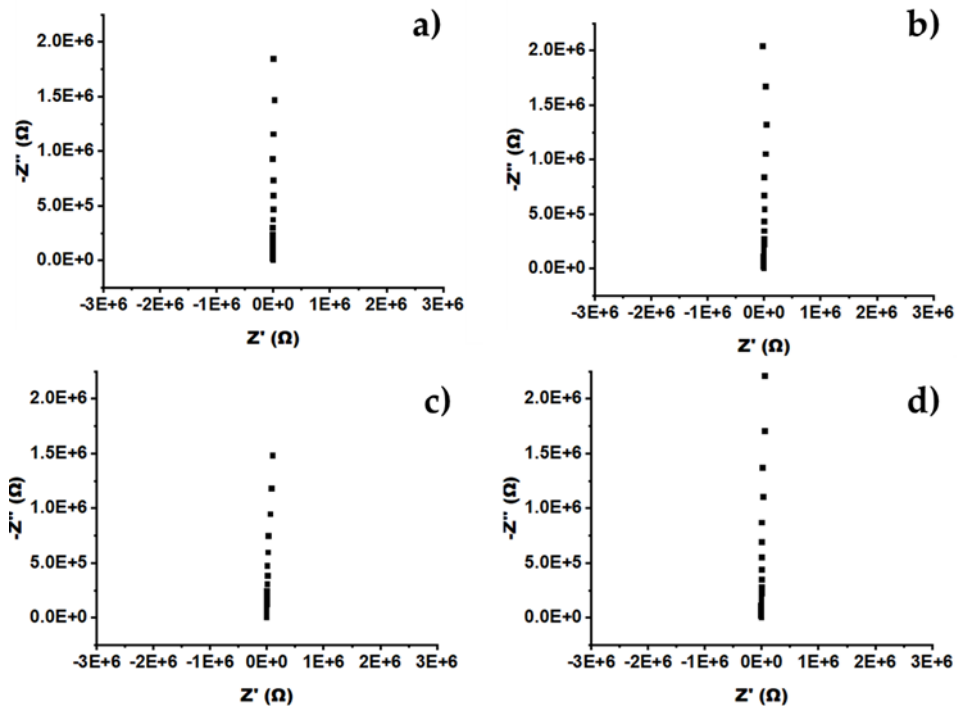

Figure 4.7. Through-plane impedance Nyquist plots of the hybrid membranes. a) PTOxM12, b) PTOxM13, c) PTOxM14 and d) PTOxM15.

Fitting results obtained from both horizontal and vertical impedance can be expressed by two different circuits (RC and R(RC)) (see **Figure 4.S6c** and **4.S6e**). **Table 4.S1** and **Table 4.S2** summarize the results obtained from the fitting, where **Table 4.S1** reveals the data obtained from in-plane EIS analysis of the dried membranes, and after 10 drops of water. **Table 4.S2** shows the data of the through-plane EIS analysis of the hybrid membranes.

Graphical representation of obtained EIS data suggests that the behaviour of hybrid membranes can be correlated with a both resistance-capacitance response. The value of the capacitance was observed with the order of magnitude 10^{-07} and 10^{-08}, or in other words almost negligible. Regarding the

resistance value, we obtained a resistance with the order of magnitude 10^{+11} and, in many cases, with an error bigger than 100 % or, in some cases, lower than 0 %, when compared to the simulated equivalent circuit. The power of the CPE (n) value used to be between 0 (when perfect resistor) and 1 (when perfect capacitor). PTOx40 hybrid membrane "n" values, in almost all cases, are bigger than 1, preventing the exact determination of their behaviour as a capacitor or a resistor. Therefore, the data obtained from the fitting models suggests that membranes are mostly insulating materials from an electronic point of view.

The behaviour distinguished for the hybrid membranes can be explained by the non-ionic nature of the poly(2-oxazoline) main chain. The presence of ionic elements inside the channels of membranes like Nafion®, for instance, sulfonic groups, are responsible for the ionic conductivity observed under AC, due to their easy polarizability [28–31]. The channels of studied hybrid membranes do not contain ionic groups. In a pristine state they present weakly polarized bonds and are not filled with ions. For this reason, the observed impedance values show significantly high resistance values. Thus, the actual conducting behaviour for ions cannot be directly established from the resistance values taken from EIS experiments, since the channels are not filled with ions. The low water uptake values obtained, together with the use of highly hydrophobic mesogenic groups do not allow the filling of the membrane's inner channel during the preconditioning phase. Therefore, EIS cannot be used for the determination of the conductivity of our hybrid membranes. For this reason, we have explored the use of other techniques to determine the ionic conductivity of hybrid membranes, such as permeability tests and linear sweep voltammetry. The construction of polymeric pathways

was designed to create a specific environment allowing "solvation" of cations by the main chain of the polymer and movement of cations along the conductive pathways thanks to external stimuli, such as concentration gradient or difference of potentials.

Cation antiport transport mechanism for liquid crystal membranes based on dendronized columnar copolymers was confirmed in the literature [22,32]. Confirmation of the cation transport for dendronized columnar copolymer was observed based on the increase of proton concentration in the stripping solution and, the simultaneous increase of the sodium concentration at the feed solution (when HCl 0.1M and NaCl 0.1M were used for feed and stripping solutions, respectively). As it was demonstrated, channel size affects the antiport transport mechanism, because the cation transport occurs simultaneously in both directions to maintain the charge balance in both compartments. In this study, the antiport transport mechanism was evaluated using different salts such as NaCl, LiCl and KCl. The best results were obtained when NaCl stripping solution was used, and worse results were observed for LiCl and KCl. From the three evaluated cations, it is known that the potassium cation is the one with the biggest ionic radius, therefore its size exclusion transport mechanism across the inner channel of the membrane was an important factor. On the other hand, the lithium cation, despite its small ionic radius, showed lower than sodium cation performance, which might be related to the fact of having the biggest hydrated radius from all tested cations. As a result, its transport across the membrane is also affected by its size.

Following the literature findings in the evaluation of the conductivity employing antiport transport first tests were performed using a NaCl solution

as the stripping compartment. In these experiments, we did not observe a decrease in the pH value after 4 days for all membranes. The same trend was observed when a solution of KCl and LiCl was employed. The results observed for the presented hybrid membranes were different from the previously reported for polyether copolymers with dendronized side chains. Nevertheless, even though in both cases the same type of dendron was presented and the membrane possessed a columnar structure, the structure of the conducting channel seems completely different. Polyether's structure described in the literature is based on a copolymer with lateral chains only partially dendronized, meanwhile, poly(2-oxazoline) is a homopolymer, which means that the dendron is present in 100 % of monomers. The lack of antiport transport may result from the low adaptability of polymeric columns of poly(2-oxazoline) to the moving along cation, which does not allow transport in both directions to balance the charge difference caused by moving transport. It is very likely, that the high degree of the backbone stiffness in the case of modified poly(2-oxazoline) in comparison to polyethers partially modified with the dendritic group prevents simultaneous transport of cations in both directions.

To characterize the ion transport, current-voltage measurements were performed using the setup described in **Figure 4.8**. From the current-voltage measurements obtained in the case of ion transport using LSV one can distinct three main regions; (i) at low currents exists a linear relationship between the observed current and the applied potential, showing an ohmic or quasi-ohmic behaviour, (ii) after, a limiting current can be observed, presenting a plateau or semi-plateau region – the maximum of the possible observable transfer across the membrane, indicating cation's permselectivity, which implies that

only the cation contributes to the charge transfer across the membrane, and (iii) an overlimiting region where an increment of the current is observed, which can be explained due to an electroconvection phenomenon or the dissociation of water. [33–35] The current–voltage (C–V) curves obtained with the studied membranes in 0.1M HCl evidence the three main characteristic regions: ohmic, limiting current and overlimiting, as presented in **Figure 4.9**.

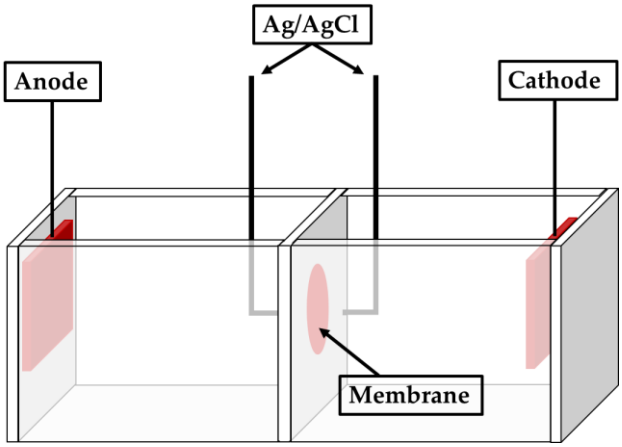

Figure 4.8. Experimental setup for linear sweep voltammetry measurements.

In addition to the proton conductivity, we also studied the conductivity of other monovalent cations. Alkaline cations, such as Na^+, K^+ and Li^+, were selected for this study. The results of these experiments can be found, along with the results obtained from proton conductivity, in **Table 4.4**. The value of the ohmic resistance (R_{ohm}) density of the hybrid membrane PTOxM13 was $0.082 \times 10^7\ \Omega \cdot cm^{-2}$ and the limiting current (I_{lim}) density value is 8.64×10^{-5} A $\cdot cm^{-2}$. For the membranes PTOxM14 and PTOxM15, the ohmic resistance density was $0.083 \times 10^7\ \Omega \cdot cm^{-2}$ and $0.084 \times 10^7\ \Omega \cdot cm^{-2}$, respectively, meanwhile the limiting current density is 1.82×10^{-5} A $\cdot cm^{-2}$ and 1.33×10^{-5} A

· cm^{-2}, respectively. On the other hand, PTOxM12 presented R_{ohm} values up to two orders of magnitude higher than the other membranes (1.11 x 10^7 Ω · cm^{-2}), with distinguishable limiting current regions, similarly to the general behaviour of hybrid membranes (limiting current density, 2.27 x 10^{-6} A · cm^{-2}).

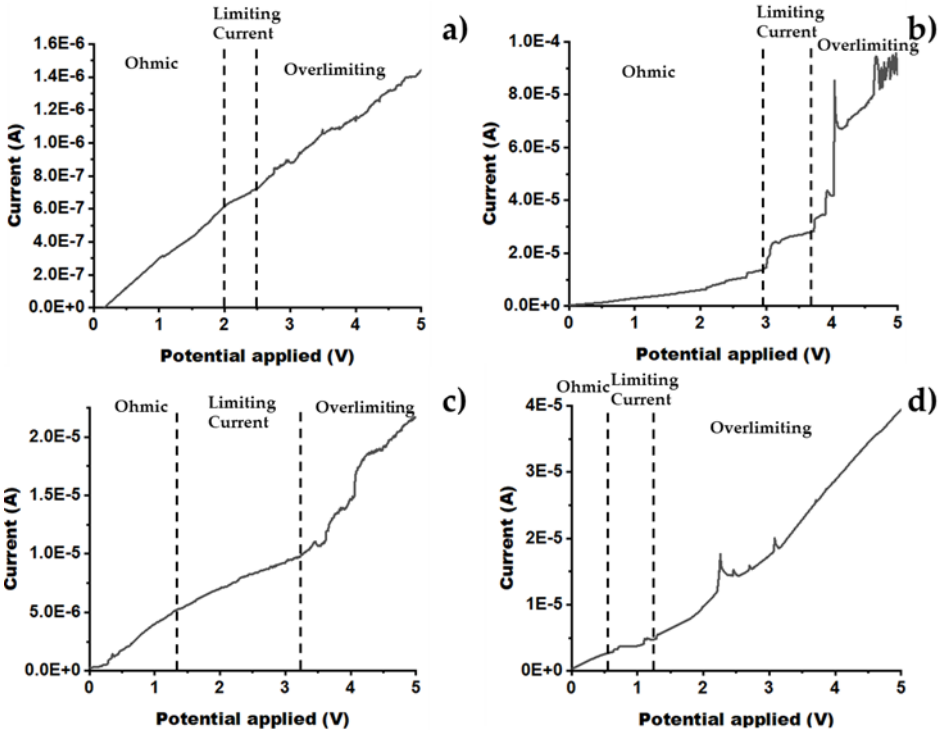

Figure 4.9. C–V curves of hybrid membranes. a) PTOxM12, b) PTOxM13, c) PTOxM14 and d) PTOxM15.

The difference between ohmic resistance densities between the membranes PTOxM13, PTOxM14 and PTOx15, and the membrane PTOxM12 can be explained by the orientation of the membranes. PTOxM12 was not oriented, therefore the membrane showed the highest resistance density value since the conducting paths were not properly aligned. In addition, the PTOxM12

hybrid membrane did not present the transport of potassium cations, therefore, it was impossible to establish an ohmic resistance density for this ion (**Table 4.4**). The lack of orientation in this membrane may prevented the transport of potassium cation through the membrane columns. If we compare the oriented membranes, PTOxM14 and PTOxM15 hybrid membranes were assembled over hydrophobic substrates, which led to a better column orientation (**Figure 4.3**). This fact has promoted a reduction of the ohmic resistance density observed for the membranes PTOxM14 and PTOxM15 compared to the membrane PTOxM13, which was assembled over a hydrophilic substrate.

Table 4.4. Ohmic resistance obtained from C – V curves for the different cations of the studied PTOx hybrid membranes.

Sample	**R_{ohm} x 10^7 [$\Omega \cdot cm^{-2}$]**			
	HCl	**LiCl**	**NaCl**	**KCl**
Nafion®117	0.003*	0.006*	0.019*	0.012*
PTOxM12	1.110	106.640	339.060	-
POTxM13	0.082	17.630	125.860	311.310
PTOxM14	0.083	7.290	55.710	41.220
PTOxM15	0.084	7.141	147.820	279.540

* Ohmic resistance expressed in R_{ohm} x 10^3 $\Omega \cdot cm^{-2}$. Data obtained from [11].

To express the membrane preferential selectivity of the proton over the studied monovalent cations, a ratio of conductance (reverse resistance) of alkali ion over proton (G_{ion}/G_{H+}) was calculated for each membrane (**Table 4.5**). As we can observe, all membranes seem to be highly selective, according

to the G_{ion}/G_{H+} ratio. PTOxM12 does not present selectivity values for the transport of potassium cations. As mentioned previously, PTOxM12 does not exhibit potassium cation transport. As we could observe in previous studies, lithium cation presents a lower selectivity if we compare it with the other two studied cations [11,22]. Similar trends are observed for sodium and potassium cations for PTOxM13 and PTOxM15 oriented membranes. As expected, lower selectivity values are observed for sodium, meanwhile potassium presents a higher selectivity.

Table 4.5. Selectivity (G_{ion}/G_{H+} ratio) values for alkaline monovalent cations.

Sample	G_{ion}/G_{H+} x 100 [%]		
	Li^+	Na^+	K^+
Nafion®117	47.3*	14.2*	22.8*
PTOxM12	1.00	0.30	-
PTOxM13	0.50	0.07	0.03
PTOxM14	1.10	0.15	0.20
PTOxM15	1.20	0.06	0.03

* Selectivity data obtained from [11].

The values of G_{ion}/G_{H+} expressed in **Table 4.5** put in evidence the importance of the distribution of the columns across the membrane together with their orientation, were the key factors for cation passage to occur. Our results present membranes with a high proton selectivity over monovalent cations, such as lithium, potassium, and sodium cations. Zare and co-workers studied the proton transport using linear sweep voltammetry of membranes based on polyether copolymers [22]. In their work, Zare and co-workers show

selectivity values in the order of 20 to 55 %, which are values far higher than those presented in this study. This can be explained by the fact that the polyether copolymers do not present a regular distribution of the tapered group across the main chain. Their membranes are based on a polymer where the tapered group was introduced as a post-polymerization procedure. Because of that, the distribution of the tapered group across the main chain of the polymer is random. The difference between both selectivity results put in evidence the importance of the homogeneous distribution of the tapered group. The large number of tapered groups in the PTOx likely elongates the polymer backbone, reducing its possibility to rearrange without changing the position of the linked aromatic ring, hence displaying lower resistance during the transport of small proton compared to the other monovalent cations. Similar behaviour was observed for modified poly(epichlorohydrin-co-ethyl oxide) using Raman spectroscopy coupled with chronoamperometry. It was evident that during the transport process, a smaller proton was able to move along the polymeric column using the main chain ether linkage together with the lateral ester groups, evidenced by Raman spectroscopy and bands at approx. 2870 cm^{-1} and 1250 cm^{-1}, respectively. For the same experiment only with a sodium cation, only one signal at approx. 2870 cm^{-1} was altered from the neat spectrum, confirming such a tendency [36].

4.4.Conclusions

Ion transport for novel hybrid membranes based on the homopolymer poly(2-oxazoline, obtained from the *living* polymerization of 2-(3,4,5-tris(4-dodecyloxybenzyloxy)phenyl)-4,5-dihydro-1,3-oxazole), supported on a

polyester fabric were studied. The effect of the substrate hydrophobicity was studied in terms of column orientation. According to X-ray diffraction no difference was observed during this analysis. Membrane wettability was studied by means of water, and methanol aqueous solution, uptake. Water uptake did not reveal any difference between oriented and non-oriented hybrid membranes. Methanol aqueous solution uptake revealed a decreasing methanol uptake upon increasing the methanol concentration in the solution. These results suggest that the hybrid membranes can be a suitable candidate for systems with methanol as a hydrogen supply. Bibliographic data of Nafion®117 membranes shows a water uptake of 21 % and reports a deformation of the membrane by swelling [37]. Static contact angle measurements were performed to study the hydrophobicity of the hybrid membranes. This analysis evidenced a hydrophobic behaviour of both oriented and non-oriented hybrid membranes, with a difference of *c. a.* 4 ° between them. However, when comparing the CA of the non-oriented PTOxVM (membrane without support) with the other hybrid membranes, a bigger difference can be observed. This difference can be attributed to the lack of the polyester fabric as support for the PTOxVM membrane, which is slightly hydrophobic.

Proton transport was studied by three different techniques, EIS, permeability test and LSV. Electrochemical impedance spectroscopy failed in the determination of the proton conductivity for the studied PTOx hybrid membranes. Due to the non-ionic nature of the membranes, it was impossible to observe the ionic conductivity under AC. As consequence, PTOx hybrid membranes behaves as insulating materials from an electronic point of view. Permeability tests and LSV were proposed as alternative to EIS for the

determination of the ionic conductivity. In order to study the effect of the concentration gradient, permeability tests were performed studying different monovalent cations, such as Na^+, K^+ and Li^+. Nevertheless, no cation transport was observed with these experiments, even after 4 days of experiment. The small space inside the column channel, promoted by the polymer chain homogeneity could prevent the transport of this cations due to its size. Whereby, current-voltage experiments were used for ion transport characterization. Homeotropical oriented membranes (PTOxM13, PTOxM14 and PTOxM15) showed lower resistance density values than the non-oriented membrane (PTOxM12) up to two orders of magnitude, denoting that the column orientation is a key factor for the proton transport. On the one hand, results obtained showed low proton conductivity when compared with Nafion® 117. On the other hand, PTOx hybrid membranes showed an excellent selectivity to proton in front of other monovalent cations. All these results indicate the potential use of this kind of hybrid membranes to be used in applications where a high proton selectivity is required, like artificial photosynthesis.

4.5.References

[1] D. Kweku, O. Bismark, A. Maxwell, K. Desmond, K. Danso, E. Oti-Mensah, A. Quachie, B. Adormaa, Greenhouse Effect: Greenhouse Gases and Their Impact on Global Warming, J Sci Res Rep 17 (2018) 1–9. https://doi.org/10.9734/jsrr/2017/39630.

[2] M. Tanaka, Y. Takeda, T. Wakiya, Y. Wakamoto, K. Harigaya, T. Ito, T. Tarao, H. Kawakami, Acid-doped polymer nanofiber framework: Three-dimensional proton conductive network for high-performance fuel cells, J Power Sources 342 (2017) 125–134. https://doi.org/10.1016/j.jpowsour.2016.12.018.

[3] M. Pan, C. Pan, C. Li, J. Zhao, A review of membranes in proton exchange membrane fuel cells: Transport phenomena, performance and durability, Renewable and Sustainable Energy Reviews 141 (2021). https://doi.org/10.1016/j.rser.2021.110771.

[4] H. Zhang, P.K. Shen, Recent development of polymer electrolyte membranes for fuel cells, Chem Rev 112 (2012) 2780–2832. https://doi.org/10.1021/cr200035s.

[5] S. Wang, L. Shi, S. Zhang, H. Wang, B. Cheng, X. Zhuang, Z. Li, Proton-conducting amino acid-modified chitosan nanofibers for nanocomposite proton exchange membranes, Eur Polym J 119 (2019) 327–334. https://doi.org/10.1016/j.eurpolymj.2019.07.041.

[6] B.R. Kaafarani, Discotic liquid crystals for opto-electronic applications, Chemistry of Materials 23 (2011) 378–396. https://doi.org/10.1021/cm102117c.

[7] R.J. Carlton, J.T. Hunter, D.S. Miller, R. Abbasi, P.C. Mushenheim, L.N. Tan, N.L. Abbott, Chemical and biological sensing using liquid crystals, Liq Cryst Rev 1 (2013) 29–51. https://doi.org/10.1080/21680396.2013.769310.

[8] M. Zhou, T.J. Kidd, R.D. Noble, D.L. Gin, Supported Lyotropic Liquid-Crystal Polymer Membranes: Promising Materials for Molecular-Size-Selective Aqueous Nanofiltration, Advanced Materials 17 (2005) 1850–1853. https://doi.org/10.1002/adma.200500444.

[9] T. Kato, M. Yoshio, T. Ichikawa, B. Soberats, H. Ohno, M. Funahashi, Transport of ions and electrons in nanostructured liquid crystals, Nat Rev Mater 2 (2017). https://doi.org/10.1038/natrevmats.2017.1.

[10] Z.Z. Nie, B. Zuo, L. Liu, M. Wang, S. Huang, X.M. Chen, H. Yang, Nanoporous Supramolecular Liquid Crystal Polymeric Material for Specific and Selective Uptake of Melamine, Macromolecules 53 (2020) 4204–4213. https://doi.org/10.1021/acs.macromol.0c00322.

[11] K.A. Bogdanowicz, P. Sistat, J.A. Reina, M. Giamberini, Liquid crystalline polymeric wires for selective proton transport, part 2: Ion transport in solid-state, Polymer (Guildf) 92 (2016) 58–65. https://doi.org/10.1016/j.polymer.2016.03.080.

[12] X. Montané, S.V. Bhosale, J.A. Reina, M. Giamberini, Columnar liquid crystalline polyglycidol derivatives: A novel alternative for proton-conducting membranes, Polymer (Guildf) 66 (2015) 100–109. https://doi.org/10.1016/j.polymer.2015.03.071.

[13] A. Zare, B. Pascual-Jose, S. De la Flor, A. Ribes-Greus, X. Montané, J.A. Reina, M. Giamberini, Membranes for cation transport based on dendronized poly(Epichlorohydrin-co-ethylene oxide). part 1: The effect of dendron amount and column orientation on copolymer mobility, Polymers (Basel) 13 (2021). https://doi.org/10.3390/polym13203532.

[14] V. Percec, M. Glodde, T.K. Bera, Y. Miura, I. Shiyanovskaya, K.D. Singer, V.S.K. Balagurusamy, P.A. Heiney, I. Schnell, A. Rapp, H.W. Spiess, S.D. Hudsonk, H. Duan, Self-organization of supramolecular helical dendrimers into complex electronic materials, Nature 417 (2002) 384–387. https://doi.org/10.1038/nature01072.

[15] K.A. Bogdanowicz, G.A. Rapsilber, J.A. Reina, M. Giamberini, Liquid crystalline polymeric wires for selective proton transport, part 1: Wires preparation, Polymer (Guildf) 92 (2016) 50–57. https://doi.org/10.1016/j.polymer.2016.03.073.

[16] A. Rapp, I. Schnell, D. Sebastiani, S.P. Brown, V. Percec, H.W. Spiess, Supramolecular Assembly of Dendritic Polymers Elucidated by 1 H and 13 C Solid-State MAS NMR Spectroscopy, J Am Chem Soc 125 (2003) 13284–13297. https://doi.org/10.1021/ja035127d.

[17] V. Percec, M.N. Holerca, S.N. Magonov, D.J.P. Yeardley, G. Ungar, H. Duan, S.D. Hudson, Poly(oxazolines)s with tapered minidendritic side

groups. The simplest cylindrical models to investigate the formation of two-dimensional and three-dimensional order by direct visualization, Biomacromolecules 2 (2001) 706–728. https://doi.org/10.1021/bm015550j.

[18] A. Šakalyte, J.A. Reina, M. Giamberini, Liquid crystalline polyamines containing side dendrons: Toward the building of ion channels based on polyamines, Polymer (Guildf) 54 (2013) 5133–5140. https://doi.org/10.1016/j.polymer.2013.07.027.

[19] J. Guardià, A. Zare, J. Eleeza, M. Giamberini, J.A. Reina, X. Montané, Synthesis and characterization of dendritic compounds containing nitrogen: monomer precursors in the construction of biomimetic membranes, Sci Rep 12 (2022). https://doi.org/10.1038/s41598-022-05747-1.

[20] J. Guardià, M. Giamberini, J.A. Reina, X. Montané, Synthesis and Characterization of Dendronized Side Chain Liquid Crystalline Poly(2-oxazoline)s towards Biomimetic Ion Channels, Eur Polym J (2023) 112273. https://doi.org/10.1016/j.eurpolymj.2023.112273.

[21] A. Šakalyte, M. Giamberini, J.A. Reina, Synthesis and characterisation of a monotropic dendritic liquid crystalline aziridine monomer, Liq Cryst 41 (2014) 153–162. https://doi.org/10.1080/02678292.2013.845309.

[22] A. Zare, X. Montané, J.A. Reina, M. Giamberini, Membranes for cation transport based on dendronized poly(Epichlorohydrin-co-ethylene oxide). part 2: Membrane characterization and transport properties, Polymers (Basel) 13 (2021). https://doi.org/10.3390/polym13223915.

[23] A. Šakalyte, J.A. Reina, M. Giamberini, Liquid crystalline polyamines containing side dendrons: Toward the building of ion channels based on polyamines, Polymer (Guildf) 54 (2013) 5133–5140. https://doi.org/10.1016/j.polymer.2013.07.027.

[24] X. Montané, K.A. Bogdanowicz, J. Prats-Reig, G. Colace, J.A. Reina, M. Giamberini, Advances in the design of self-supported ion-conducting membranes – New family of columnar liquid crystalline polyamines. Part 2: Ion transport characterisation and comparison to hybrid membranes, Polymer (Guildf) 105 (2016) 234–242. https://doi.org/10.1016/j.polymer.2016.10.046.

[25] X. Montané, K.A. Bogdanowicz, G. Colace, J.A. Reina, P. Cerruti, A. Lederer, M. Giamberini, Advances in the design of self-supported ion-conducting membranes-new family of columnar liquid crystalline

polyamines. Part 1: Copolymer synthesis and membrane preparation, Polymer (Guildf) 105 (2016) 298–309. https://doi.org/10.1016/j.polymer.2016.10.047.

[26] M. Peterca, D. Sahoo, M.R. Imam, Q. Xiao, V. Percec, Searching for the simplest self-assembling dendron to study helical self-organization and supramolecular polymerization, Giant 12 (2022). https://doi.org/10.1016/j.giant.2022.100118.

[27] A.C. Lazanas, M.I. Prodromidis, Electrochemical Impedance Spectroscopy—A Tutorial, ACS Measurement Science Au 3 (2023) 162–193. https://doi.org/10.1021/acsmeasuresciau.2c00070.

[28] M. Shabani, M.H. Entezari, Designing continuous proton-conductive channels for direct methanol fuel cell through the sulfonated poly(ether ether ketone)/carbon quantum dot/graphitic carbon nitride nanosheet, Eur Polym J 202 (2024). https://doi.org/10.1016/j.eurpolymj.2023.112641.

[29] J.H. Lim, J. Hou, W.Y. Kim, S. Wi, C.H. Lee, The relationship between chemical structure of perfluorinated sulfonic acid ionomers and their membrane properties for PEMEC application, Int J Hydrogen Energy 49 (2024) 794–804. https://doi.org/10.1016/j.ijhydene.2023.09.131.

[30] M. Díaz, A. Ortiz, I. Ortiz, Progress in the use of ionic liquids as electrolyte membranes in fuel cells, J Memb Sci 469 (2014) 379–396. https://doi.org/10.1016/j.memsci.2014.06.033.

[31] S. Tan, Y. Wu, T. Liang, X. Yang, Kinetic modeling of anhydrous proton conduction in side chain liquid crystal polyacrylates, Int J Hydrogen Energy 39 (2014) 17391–17397. https://doi.org/10.1016/j.ijhydene.2014.08.043.

[32] K.A. Bogdanowicz, S. V. Bhosale, Y. Li, I.F.J. Vankelecom, R. Garcia-Valls, J.A. Reina, M. Giamberini, Mimicking nature: Biomimetic ionic channels, J Memb Sci 509 (2016) 10–18. https://doi.org/10.1016/j.memsci.2016.02.038.

[33] E.H. Rotta, M.C. Martí-Calatayud, V. Pérez-Herranz, A.M. Bernardes, Evaluation by Means of Electrochemical Impedance Spectroscopy of the Transport of Phosphate Ions through a Heterogeneous Anion-Exchange Membrane at Different pH and Electrolyte Concentration, Water (Switzerland) 15 (2023). https://doi.org/10.3390/w15010009.

[34] J.H. Choi, J.S. Park, S.H. Moon, Direct measurement of concentration distribution within the boundary layer of an ion-exchange membrane, J Colloid Interface Sci 251 (2002) 311–317. https://doi.org/10.1006/jcis.2002.8407.

[35] J.H. Choi, H.J. Lee, S.H. Moon, Effects of electrolytes on the transport phenomena in a cation-exchange membrane, J Colloid Interface Sci 238 (2001) 188–195. https://doi.org/10.1006/jcis.2001.7510.

[36] K.A. Bogdanowicz, D. Pirone, J. Prats-Reig, V. Ambrogi, J.A. Reina, M. Giamberini, In situ raman spectroscopy as a tool for structural insight into cation non-ionomeric polymer interactions during ion transport, Polymers (Basel) 10 (2018). https://doi.org/10.3390/polym10040416.

[37] T.A. Zawodzinski, C. Derouin, S. Radzinski, R.J. Sherman, V.T. Smith, T.E. Springer, S. Gottesfeld, Water Uptake by and Transport Through Nafion® 117 Membranes, J Electrochem Soc 140 (1993) 1041–1047. https://doi.org/10.1149/1.2056194.

4.6.Supporting Information

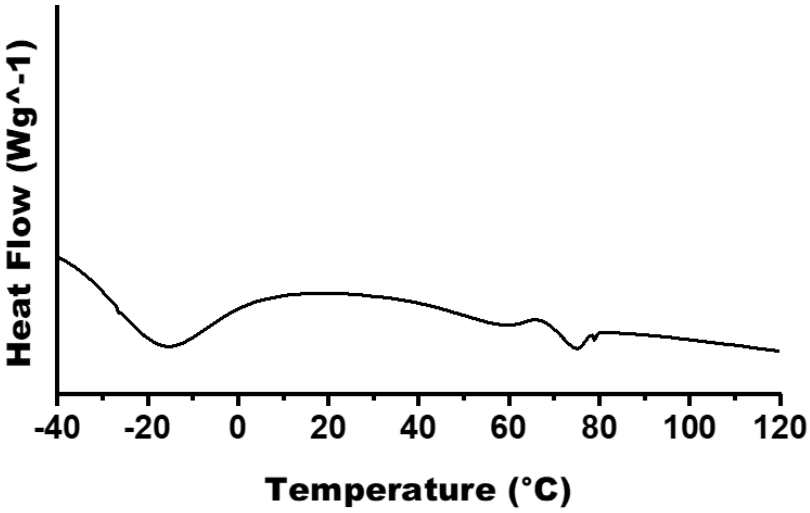

Figure 4.S1. Calorimetric analysis of PTOx40. DSC second heating scan. (Scan rate 10 °C/min).

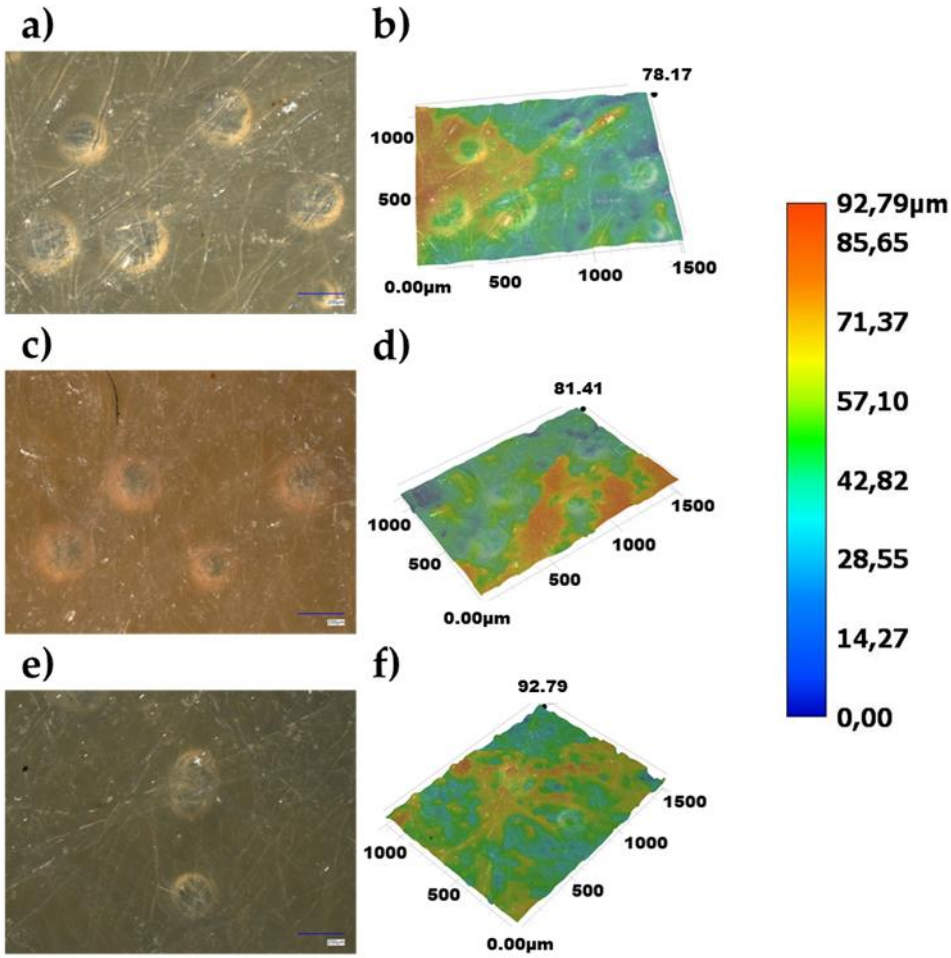

Figure 4.S2. 2D and 3D images of zones with bubbles from hybrid membranes (a – b) PTOxM13, (c – d) PTOxM14, (e – f) PTOxM15, respectively, recorded with an optical microscope at RT (25 ± 5 °C).

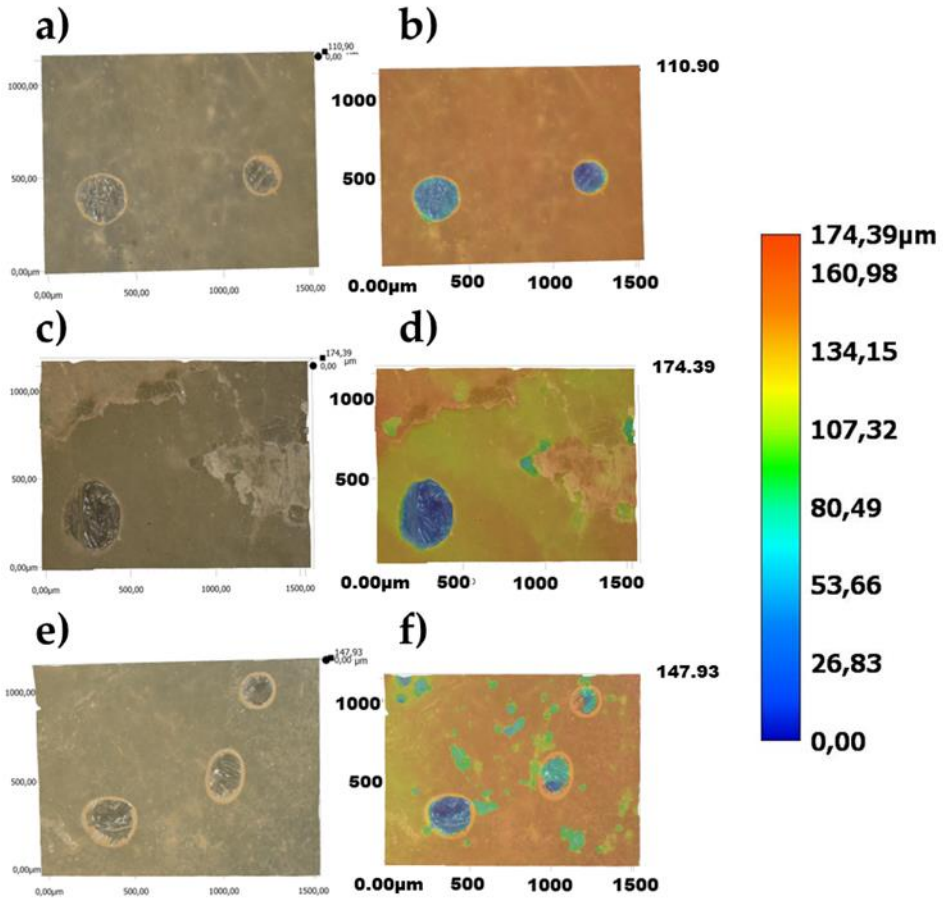

Figure 4.S3. 2D and 3D images of zones with bubbles from the bottom part of the hybrid membranes (a – b) PTOxM13, (c – d) PTOxM14, (e – f) PTOxM15, respectively, recorded with an optical microscope at RT (25 ± 5 °C).

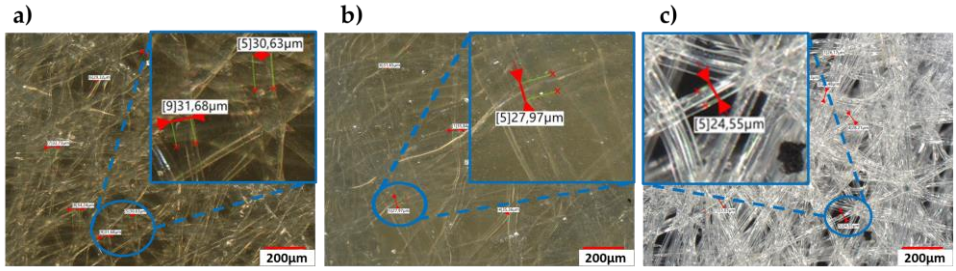

Figure 4.S4. Augmented optical microscopy images of the hybrid membranes a) PTOxM12 and b) PTOxM13, and c) polyester fabric recorded at RT (25 ± 5 °C).

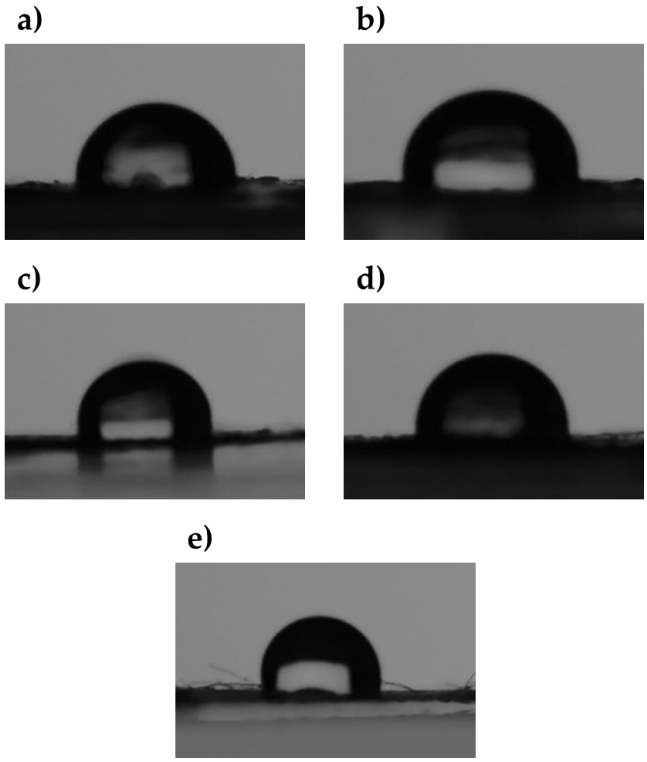

Figure 4.S5. Water contact angle images from oriented and non-oriented PTOx hybrid membranes a) PTOxM12, b) PTOxM13, c) PTOxM14 and d) PTOxM15, and e) polyester fabric.

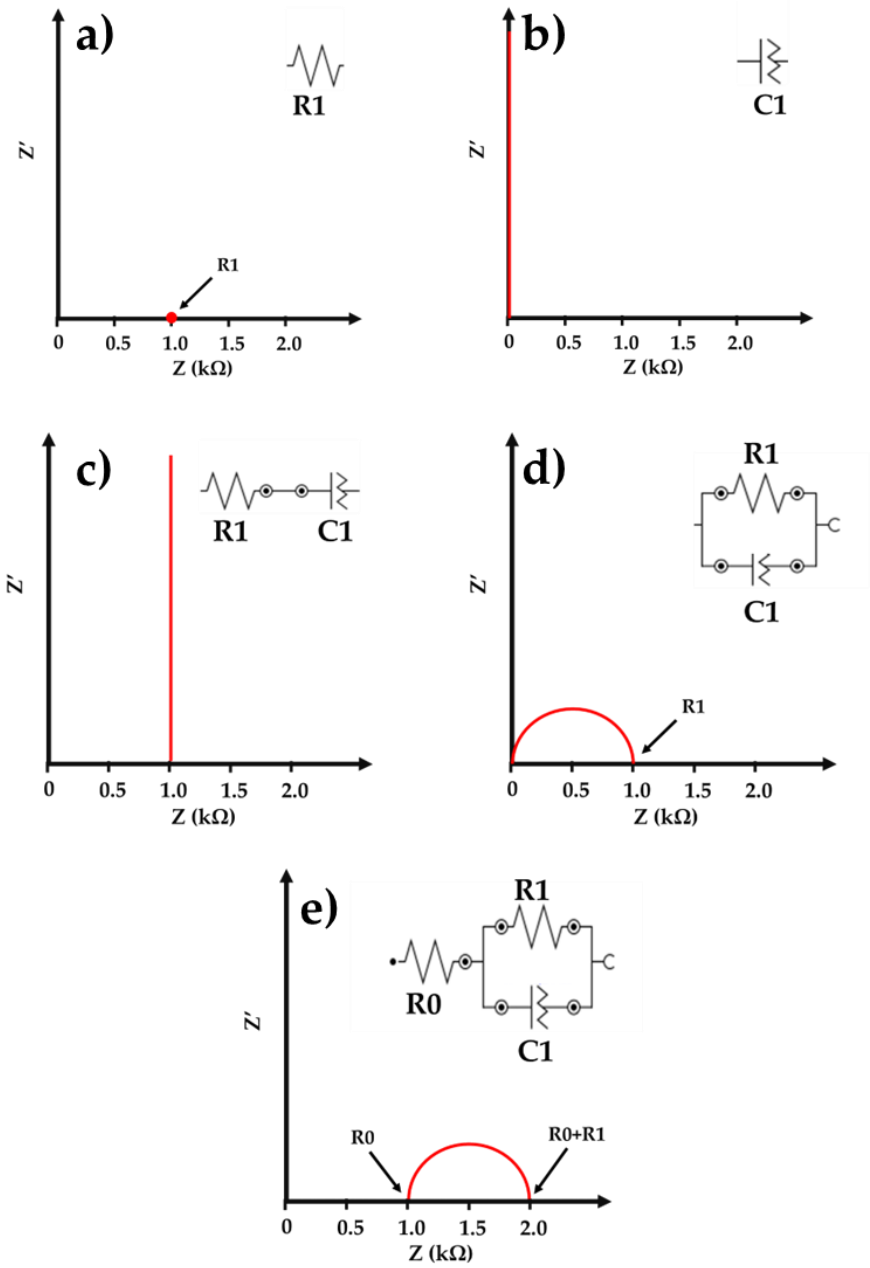

Figure 4.S6. Nyquist plots of exemplary model circuits. R0 = R1 = 1 kΩ.

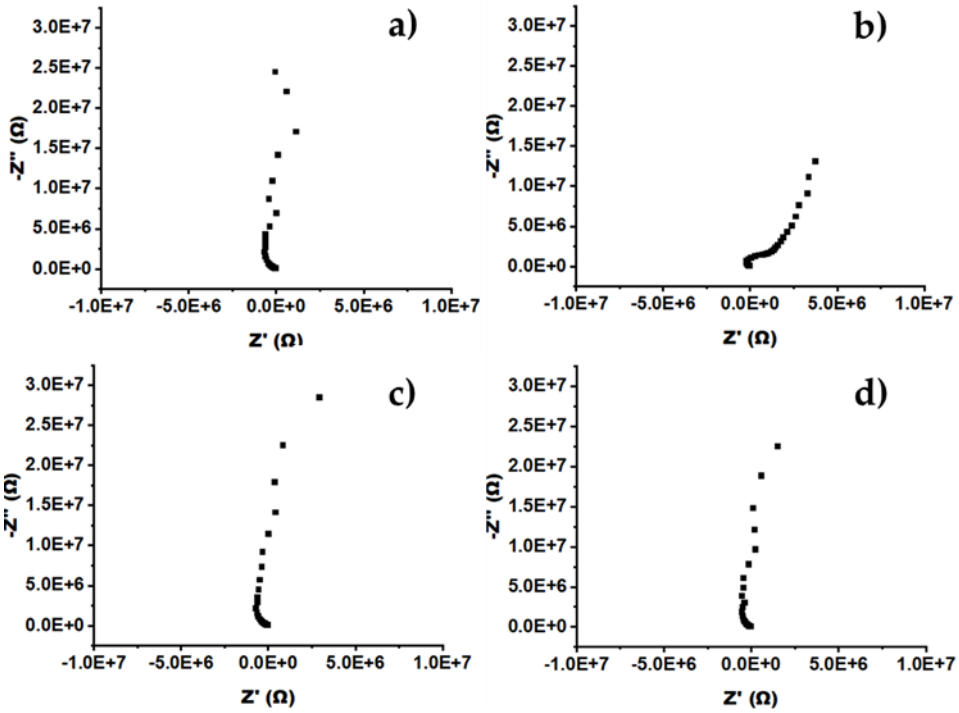

Figure 4.S7. Nyquist plots after 10 drops of water of PTOx hybrid membranes. a) PTOxM12, b) PTOxM13, c) PTOxM14 and d) PTOxM15.

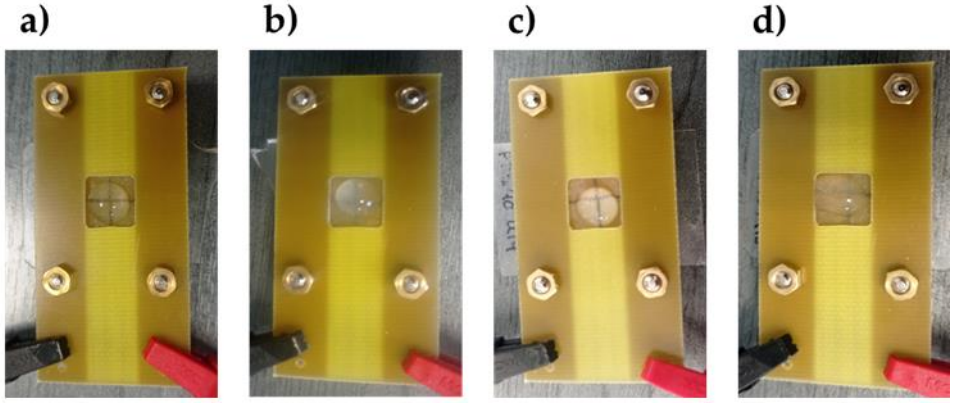

Figure 4.S8. Pictures of the hybrid membranes after the addition of 10 drops of water. a) PTOxM12, b) PTOxM13, c) PTOxM14 and d) PTOxM15.

Table 4.S1. Fitting data from in-plane EIS of PTOx dried hybrid membranes and after 10 drops of water.

M12Dry				**M1210Drop**			
Element	**Parameter**	**Value**	**Error (%) ***	**Element**	**Parameter**	**Value**	**Error (%) ***
Rs	R	-1287.2	-567.7	R1	R	-1396.1	-486.7
Rp	R	6.49E+11	371.6	Q1	Y0	1.40E-08	116.3
CPE	Y0	1.35E-08	124.4		N	1.1	7.2
	N	1.1	7.7		χ^2	87.145	
	χ^2	91.857					
M13Dry				**M1310Drop**			
Element	**Parameter**	**Value**	**Error (%) ***	**Element**	**Parameter**	**Value**	**Error (%) ***
Rs	R	-4705.2	-119.4	Rs	R	-5431.7	-103.8
Rp	R	1.88E+11	37.6	Rp	R	2.02E+11	42.9
CPE	Y0	5.79E-08	61.3	CPE	Y0	7.90E-09	60.6
	N	10.199	4.7		N	0.99975	4.8
	χ^2	87.264			χ^2	86.702	
M14Dry				**M1410Drop**			
Element	**Parameter**	**Value**	**Error (%) ***	**Element**	**Parameter**	**Value**	**Error (%) ***
R1	R	-1513.5	-477.9	Rs	R	-1119.7	-646.2
Q1	Y0	1.39E-08	127.9	Rp	R	5.68E+11	294.4
	N	1.1	7.9	CPE	Y0	1.29E-08	117.1
	χ^2	93.536			N	1.1	7.2
					χ^2	90.924	
M15Dry				**M1510Drop**			
Element	**Parameter**	**Value**	**Error (%) ***	**Element**	**Parameter**	**Value**	**Error (%) ***
Rs	R	-1280	-576.4	Rs	R	-1092.6	-569.9
Rp	R	5.97E+11	362.4	Rp	R	5.54E+11	255.2
CPE	Y0	1.35E-08	126.3	CPE	Y0	1.41E-08	100.9
	N	1.1	7.8		N	1.1	6.3
	χ^2	92.147			χ^2	75.552	

*Estimated Error.

Table 4.S2. Fitting data from through-plane EIS of PTOx dried hybrid membranes.

M12				**M13**			
Element	**Parameter**	**Value**	**Error (%) ***	**Element**	**Parameter**	**Value**	**Error (%) ***
R1	R	-93.35	-539.5	R1	R	-163.79	-199.0
Q1	Y0	1.12E-07	13.8	Q1	Y0	1.91E-07	10.9
	N	10.434	1.0		N	10.235	0.8
	χ^2	0,33581			χ^2	0.20774	
M14				**M15**			
Element	**Parameter**	**Value**	**Error (%) ***	**Element**	**Parameter**	**Value**	**Error (%) ***
R1	R	-136.26	-155.1	R1	R	-87.829	-373.5
Q1	Y0	3.17E-07	9.4	Q1	Y0	1.77E-07	11.0
	N	1.009	0.7		N	10.281	0.8
	χ^2	0.14674			χ^2	0.20832	

*Estimated Error.

UNIVERSITAT ROVIRA I VIRGILI
COLUMNAR LIQUID-CRYSTALLINE POLYMERS CONTAINING NITROGEN AT THE BACKBONE TO BE USED TO PREPARE ION-TRANSPORT MEMBRANES
Jordi Guardià Blanch

Chapter 5

Development of wood-based membranes for ion transport applications. Part 1: Support preparation and membrane assembly

UNIVERSITAT ROVIRA I VIRGILI
COLUMNAR LIQUID-CRYSTALLINE POLYMERS CONTAINING NITROGEN AT THE BACKBONE TO BE USED TO PREPARE ION-TRANSPORT MEMBRANES
Jordi Guardià Blanch

CHAPTER 5

5.1.Introduction

Wood has been used for generations in human civilization since ancient times. Its use as fuel, as construction material, as raw material for furniture and weaponry are only a few examples of its broad applications. The modification of wood structure has broadened the applications of this material. Nevertheless, this modification is not new. Examples of this process are, the production of paper, which is a well-known process for humankind during centuries [1] or the protection of exterior wood from weathering [2]. Due to the environmental emergency, the seek of new biobased, renewable and/or biodegradable products has gain a lot of interest to the scientific community, and the society itself. For this reason, the last decades the modification of wood through delignification has broadened even more the use of wood as natural scaffold for different applications [3,4]. For instance, Kumar and co-workers, reported in a review the last advances in wood delignification methodologies as well as the most predominant applications for delignified wood (DW) [4]. In this way, it has been reported the preparation of transparent wood [5–11], the formation of composites to be used in applications of industrial waste-water purification [12], the preparation of super thermally insulating nanowood [13], or the synthesis of functional cellulose-based beads for drug delivery [14]. However, the removal of lignin is not the only methodology to revalorize wood. The extraction of lignin from wood, or biomass, and its modification has allowed to prepare lignin composites for a broad range of applications [15,16].

To the best of our knowledge, however, the use of delignified wood as support for proton transport applications has not been explored yet. Wood presents a hierarchical well-defined structure and, therefore, exhibits a natural cellulose channel orientation. In this work, we present the use of delignified wood discs as supports for side chain liquid crystal polymers (SCLCP)s for proton transport applications. A side chain liquid crystal polymer is a type of compound with a mesogenic moiety grafted as side chain, which is the responsible of the liquid crystal behaviour. Our group has an extend experience in the synthesis of liquid crystal polymers. By polymer modification, we have prepared different liquid crystal polymers with main chains such as polyepichlorohydrin [17,18], polyepichlorohydrin-*co*-ethylene oxide [19,20], polyglycidol [21] and polyamines [22–24]. These main chains were grafted with the mesogenic group 3,4,5-tris[4-(n-dodecan-1-yloxy)benzyloxy]benzoate (TAPER). The use of this mesogenic group lies in its ability to build up columnar structures.

When the columns are formed, the main chain adopts a helical conformation, thus an inner channel is created. This inner channel, containing basic oxygen or nitrogen atoms, is the responsible of the proton transport. The membranes prepared with these polymers presents, when properly oriented, great proton conductivities; however, they present some drawbacks, like poor mechanical properties. In order to solve this drawback and to help with the column orientation, Bogdanowicz and co-workers developed hybrid membranes using an anodized aluminium oxide (AAO) discs as supports for the infiltration of poly [2-(aziridin-1-yl)ethanol] (PAZE) grafted with the dendron 3,4,5-tris[4-(n-dodecan-1-yloxy)benzyloxy] benzoate [22,25]. Therefore, employing delignified wood as supports for the preparation of hybrid

membranes for proton transport applications can be a helpful tool. We assumed that, since cellulose fibres present a natural orientation, they can help with the orientation of the SCLCPs columns, as AAO discs did before.

We present the preparation of SCLCP hybrid membranes, based on polyepichlorohydrin (PECH) modified with the dendron 3,4,5-tris[4-(n-dodecan-1-yloxy)benzyloxy] benzoate (TAPER) as side chain, using a highly hydrophobic delignified wood support. We assumed that, upon lignin removal during the delignification step, the environment inside the cellulose fibres is polar due to the presence of hydroxyl groups from cellulose and hemicellulose. The mesogenic group of this polymer confers a high hydrophobicity to the outer part of the columns, due to the presence of long aliphatic chains. Therefore, the polarity of the delignified wood pores would hinder the infiltration of the modified PECH inside the wood support, resulting in a bad distribution of the polymer inside the cellulose pores. To solve this problem, we functionalized the delignified wood support with lauroyl chloride, with the aim to introduce long aliphatic chains inside the cellulose fibres, thus reducing the polarity.

5.2.Experimental section

5.2.1. Materials

Commercial polyepichlorohydrin (PECH, average M_w: ~ 700.000, determined by gel permeation chromatography), glacial acetic acid (≥ 99.9%), sodium

chlorite ($NaClO_2$) (80%), pyridine (≥ 99.9%) and lauroyl chloride (98%) were purchased from Sigma Aldrich. Tetrabutylammonium bromide (TBAB) (≥ 98%) was purchased from Fluka. N,N-dimethylformamide (DMF), ethanol (96%) and tetrahydrofuran (THF) were purchased from VWR. Delignified solutions were prepared using 18.2 $M\Omega \cdot cm^{-1}$ double deionized water (Milli-Q water systems, Merck Millipore). All chemical compounds were used as received without any further purification except for THF and DMF which were dried prior to use according to literature [26]. Beech wood bars with a diameter of 15 mm were purchased from Leroy Merlin (Lezennes, France). Discs with a thickness of 1.5 mm were obtained by cutting the beech wood bars using a scroll saw purchased in Lidl Stiftung & Co. KG (Neckarsulm, Germany).

5.2.2. Synthesis of the copolymers

SCLC polyether was synthetized by chemical modification of commercial PECH with potassium 3,4,5-tris[4-(n-dodecan-1-yloxy)benzyloxy] benzoate (TAPER) following a reported procedure (**Scheme 5.S1**) [27]:

In a 125-mL Schlenk flask under argon, 1.01 g of PECH (10.92 mmol) were dissolved in 100 mL of anhydrous THF by stirring overnight at room temperature (RT = 25 ± 5 °C). Over the resulting viscous solution, 13.52 g of TAPER (13.10 mmol) and 4.22 g of TBAB (13.10 mmol) were added, in this other, with inert atmospheric techniques. The mixture was heated at 60 °C, and magnetically stirred for 8 days. Then, the reaction mixture was diluted

with THF to reach a total volume of 200 mL and precipitated into 1 L of warm water. The precipitated product was dissolved in hot THF and reprecipitated again in hot ethanol 96 % twice. Finally, the obtained white copolymer was collected and dried at 55 °C under vacuum for 48 h (7.52 g, 85 %). The modification degree was determined from the ^{1}H NMR spectrum of the copolymer. The obtained polyether, which presents a modification degree of 75 %, was named PECH75 from now on.

5.2.3. Wood delignification process

Wood delignification was carried out following a modification of a reported procedure [28]. Non-treated beech wood (NTW) was dried for 24 h at 103 °C before chemical extraction. In a round bottom flask a solution of $NaClO_2$ (2 wt %), glacial acetic acid (0.1 wt %) was prepared in ultrapure Milli-Q water. Then, the dried beech wood discs were added to the delignification solution. The solution was slowly stirred (40 rpm) and heated at the corresponding temperature for different times (3, 6 and 9 h) under reflux to prevent water evaporation. After that, delignified wood discs (DWD) were washed twice with deionized water under low stirring (40 rpm), for 2 hours. During the washing procedure, water was changed every hour. Finally, DWD were vacuum dried at 50 °C for 24 h.

5.2.4. Wood functionalization

A procedure reported by Kim and co-workers was adapted to carry out the functionalization of delignified beech wood discs (**Scheme 5.1**) [29]. Delignified wood discs were dried for 24h at 103 °C before chemical functionalization. In a round bottom flask, pyridine (1.58 g, 20.0 mmol) was dissolved in dry DMF (25 mL) under argon atmosphere. Subsequently, DWD were added, and the solution was heated at the corresponding temperature (50 or 90 °C). After that, lauroyl chloride (2.01 g, 9.2 mmol) was added. After 30 min, the functionalized beech wood discs (FDWD) were washed with methanol for 1h and then, they were kept in diethyl ether for 1h to remove residual chemicals. In both cases, methanol and diethyl ether, were changed by fresh solvent every 30 min. Finally, FDWD were vacuum dried at 50 °C for 24h.

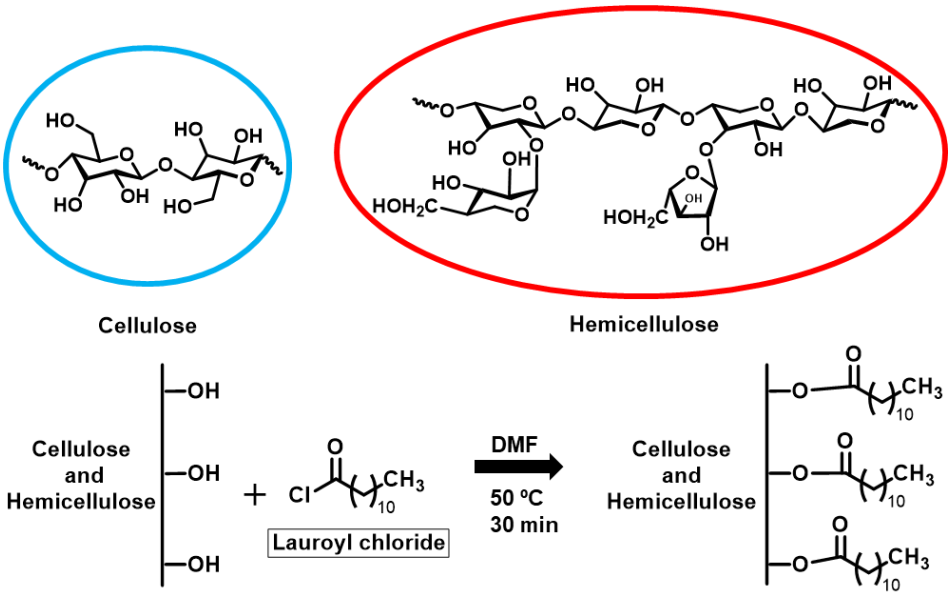

Scheme 5.1. General scheme of the functionalization reaction that takes place between delignified beech wood discs and lauroyl chloride.

5.2.5. Preparation of the membranes

The hybrid membranes derived from dendronized polymers were prepared by immersion precipitation process. This process consisted of the following steps: a homogeneous solution of dendronized PECH75 in tetrahydrofuran (THF, 15 wt%) was cast over the distinct beech wood discs: delignified and functionalized discs (**Figure 5.1)**. Vacuum was applied to help the polymer solution to penetrate and spread through the interior of the wooden support. Subsequently, the hybrid membranes were submerged in a bath of Milli-Q water for 15 min, to induce polymer precipitation and dried in air overnight at room temperature (RT = 25 ± 5 °C).

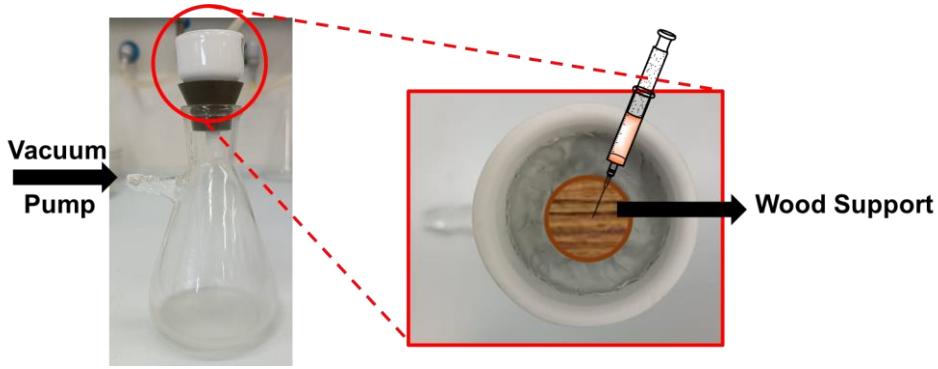

Figure 5.1. Setup used in the casting procedure of PECH75 solution onto the beech wood discs.

Homogeneous hybrid membranes were obtained by using a thermal treatment (baking process). The baking process consisted of the following steps: first of all, a previously prepared hybrid membrane was placed on a Linkam TP92 hot stage (Linkam Scientific Instruments, Tadworth, UK) and it was heated above the clearing temperature of PECH75 (170 °C) and kept for 30 min. Afterwards, it was slowly cooled down (0.1 °C/min) to 30 °C, obtaining a uniform hybrid membrane on both sides. Thermally treated membranes are labelled with the suffix: _T.

5.2.6. Characterization

Fourier transform infrared spectroscopy (FT-IR). FT-IR spectra were recorded on an FT/IR-6700 spectrophotometer from JASCO in the wavelength

range of 4000–400 cm−1 with a resolution of 4 cm−1 in the absorbance mode. This device was equipped with an attenuated total reflection accessory (ATR) with thermal control and a diamond crystal (Golden Gate heated single reflection diamond ATR from Specac-Teknokroma). The spectra were recorded at room temperature (RT = 25 ± 5 °C) from the solid-state pure compounds. Beech wood samples (NTW, DWD and FDWD) were dried at RT under vacuum before the analysis.

Environmental scanning electron microscopy (ESEM). A morphological analysis of both delignified wood discs (DWD) and functionalized delignified wood discs (FDWD) cross-section was carried out using a FEI ESEM Quanta 600 instrument (Hillsboro, OR, USA) in high vacuum mode, using electron detector and an accelerating voltage of 20 kV. Cross-sections were prepared by fracturing the membranes by hand. Dry samples were fixed to metal stubs with two-sided adhesive carbon tape.

Polarized optical microscopy (POM). LC mesophases were investigated by polarized optical microscopy (POM). The textures of the samples were observed with an Axiolab Zeiss optical microscope equipped with a Linkam TP92 hot stage and a Moticam S6 digital camera.

Differential scanning calorimetry (DSC). Calorimetric analyses were carried out on a Mettler DSC-821 instruments calibrated using indium (156.6 °C) and zinc (419.6 °C) pearls. Samples were placed in an aluminium standard crucible

of 40 μL with pierced lids (between 4 – 6 mg of sample), which were analysed in N_2 atmosphere (gas flow rate of 50 cm^3/min). Heating and cooling rate of 10 °C/min was always employed.

Thermogravimetric analysis (TGA). Thermal stability studies were carried out in ALUOXIDE crucibles of 70 μL (ME-24123) with a Mettler Toledo TGA2 thermobalance. All samples, weighing around 6–8 mg, were heated between 30 and 600 °C at a heating rate of 10 °C/min in N_2 atmosphere with a flow rate of 50 cm^3/min. The equipment was previously calibrated with indium (156.6 °C) and aluminium (660.3 °C) pearls. Beech wood samples (NTW, DWD and FDWD) were dried for 24h at 50 °C under vacuum before the analysis.

Contact angle (CA). The static contact angles with water on a membrane surface were measured with an optical goniometer (Ossila LTd, Sheffield, UK) supported by dedicated software. For the tests, water drops (7 μL) were deposited on the sample's surface. The contact angle was calculated, immediately after placing the water drop, using the tangent to the surface at the point of contact of three phases, *i.e.*, solid, liquid and gas. The measurements were repeated using different areas of the membrane or support. For each test reported, at least three drops of water were used.

5.3.Results and discussion

5.3.1. Wood delignification

The main objective of this research work was the preparation of homogeneous hybrid membranes based on columnar SCLCP inside a biobased support [30]. As described in a previous paper, our group reported the chemical modification of PECH with a dendritic group with a tapered shape (TAPER) [30]. Moreover, we used one of these SCLCPs to prepare membranes for proton transport applications [31]. However, they were brittle and, therefore not suitable for preparing self-supported membranes. [22–24] To overcome this drawback, we designed the preparation of homogeneous hybrid membranes based on a columnar SCLCP supported on beech wood as natural support. To achieve this objective, the removal of lignin from wood was carried out to obtain highly porous materials that allow the infiltration of the polymer inside the support [32]. Besides, it is known that delignification processes do not affect the hierarchical structure of the fibre cell walls, which means that the mechanical properties of the wood will be practically unaffected [33,34].

Prior to cut the beech wood bars, it is very important to consider the orientation of the lignocellulosic fibres in wood to obtain discs suitable for the desired applications. As observed in **Figure 5.2**, two different types of cutting can be done: radial (R) or longitudinal (L) cutting. In a radial cut, the lignocellulosic fibres are expected to be perpendicular to the surface of the thin discs (**Figure 5.2b**). Therefore, the resulting pores are short. On the other

hand, the same orientation of the lignocellulosic fibres is expected when a longitudinal cut is applied (**Figure 5.2c**). Nevertheless, the fibres are longer compared to the ones obtained by the application of a "R" cut and the available surface with pores is smaller. However, the rotation of this disc 90° to use the bigger surface cannot be done in this case because the lignocellulosic fibres are mainly oriented parallel to the surface of the disc (**Figure 5.2d**). Thus, beech wood bars were cut applying a radial cutting to get the highest number of regular pores in the wood support to be filled with the side chain liquid crystalline polymer.

For the delignification process applied to beech wood discs, different temperatures and reaction times were tested to optimize this process. To choose the best temperature, we took as reference previous research works that selected 80 °C as the temperature at which good delignification degrees of balsa wood were obtained (up to 1%) [28,35,36]. At this temperature, the delignification of wood was investigated at 3 different reaction times (3, 6 and 9 h). Furthermore, the same reaction was carried out at 70 and 90 °C. The wood delignification degree was determined by FT-IR spectroscopy by comparing the relative intensity of the band at 1506 cm^{-1} with the same band in the FT-IR spectrum of NTW. This band, together with the band at 1593 cm^{-1}, are attributed to aromatic skeleton vibrations from lignin, which are characteristics of aromatic compounds (phenolic hydroxy groups). **Figure 5.3** shows the FT-IR spectra of NTW and delignified wood samples obtained when delignification was performed during 3 h. From the experiments performed, the highest delignification degrees were obtained at 90 °C (**Figure 5.S2**). It is noteworthy that the characteristic bands of cellulose and

hemicellulose that appear at 3320 cm^{-1} (ν(O-H), 1375 cm^{-1} (δ(C-H)) and 1032 cm^{-1} (ν(C-O-C)) were not affected by delignification [37].

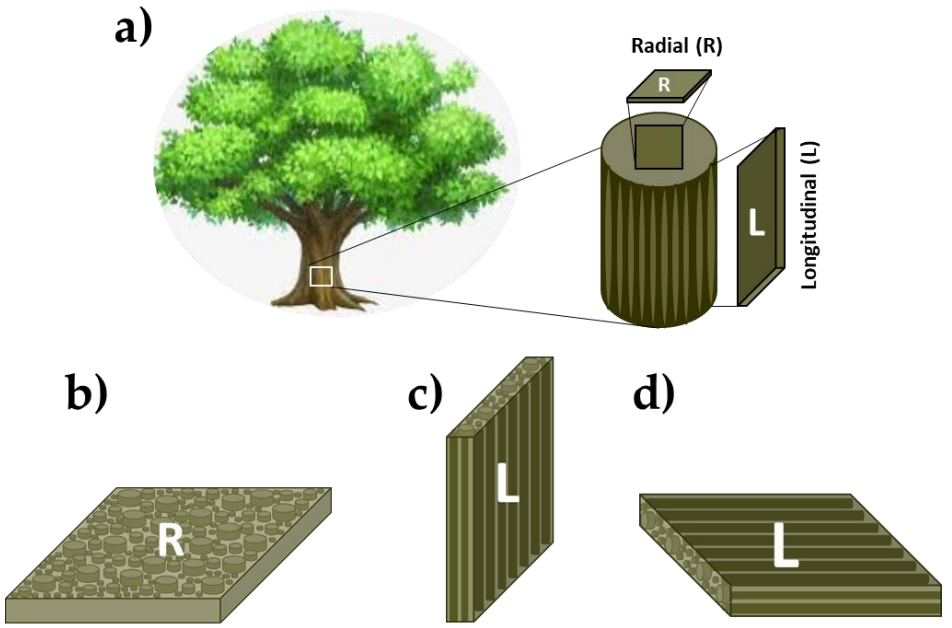

Figure 5.2. a) Schematic illustration of two types of wood discs that can be obtained depending on the cutting direction from a tree log. Radial cut is named "R", while longitudinal cut is named "L"; b) "R" cut wood disc, in which it is expected that the lignocellulosic fibres are oriented perpendicular to the surface of the disc; c) "L" wood cut wood disc, in which the lignocellulosic fibres are expected to be oriented perpendicular to the surface of the disc. d) Representation of the "L" cut wood disc rotated 90°.

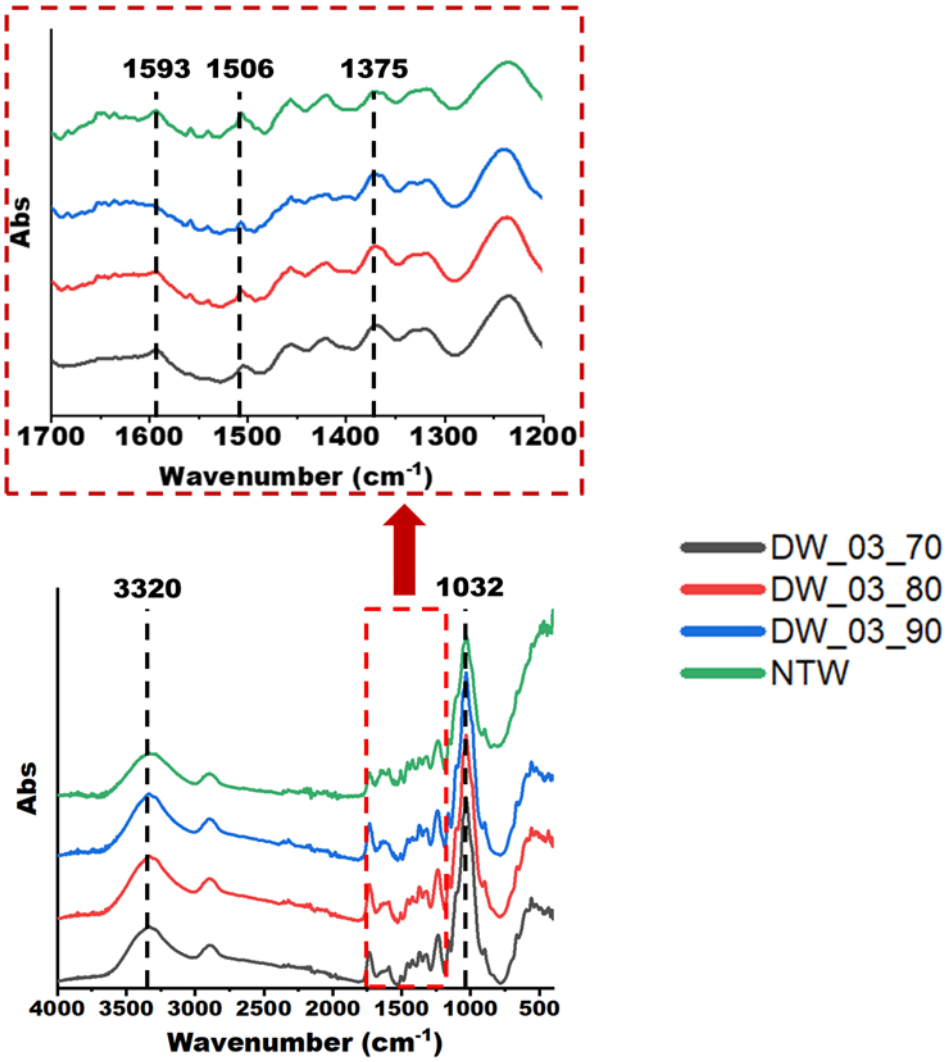

Figure 5.3. FT-IR spectra of non-treated beech wood (NTW) and delignified beech wood discs obtained when delignification was performed during 3h.

When the process was performed at 70 or 80 °C, long reaction times were required to achieve a delignification degree higher than 90 % (**Table 5.1**). In addition, the rupture of the discs was observed when the delignification was

carried out at 90 °C during 6 and 9 h. However, the fracture of the discs was not observed when the reaction was carried out at this temperature for 3h (**Figure 5.S2**). Considering these results, we chose 90 °C and 3 h as the best conditions to carry out the delignification of beech wood discs.

Table 5.1. Chemical reaction conditions and degrees of delignification obtained in the optimization of the delignification process of beech wood discs.

Sample	Reaction time (h)	Reaction temperature (°C)	Delignification degree (%) [a]
DWD_3_70	3	70	57
DWD_6_70	6	70	70
DWD_9_70	9	70	92
DWD_3_80	3	80	58
DWD_6_80	6	80	84
DWD_9_80	9	80	92
DWD_3_90	3	90	90
DWD_6_90	6	90	91
DWD_9_90	9	90	91

[a] Calculated from the intensity of the band at 1506 cm^{-1} in FT-IR spectra.

To further characterize the structural changes that could occur during the delignification reaction, delignified wood samples cross-sections were analysed by means of environmental scanning electron microscopy (ESEM).

Images of these analyses are shown in **Figure 5.4**. We could observe how, despite the different reaction times and temperatures, cellulose fibres were practically unaffected by the delignification process. Moreover, changes in the temperature reaction and/or reaction times did not affect the size of these fibres as can be seen in the measurements taken from the different samples (**Figure 5.4b**). Thereby, the width of the fibres was measured, observing that they had a diameter between 39.34 and 48.34 μm in NTW, which are very similar to the diameters of the fibres of the delignified samples (between 38.86 and 51.28 μm (**Figure 5.4ii-iv**). From ESEM analysis, it can also be observed that not all the cellulose fibres are aligned perpendicular to the surface of the wood discs (there are areas in which they are oriented parallel to the surface as shown in the circles highlighted in red from **Figures 5.4a – i, iii** and **iv**) parallel to each other.

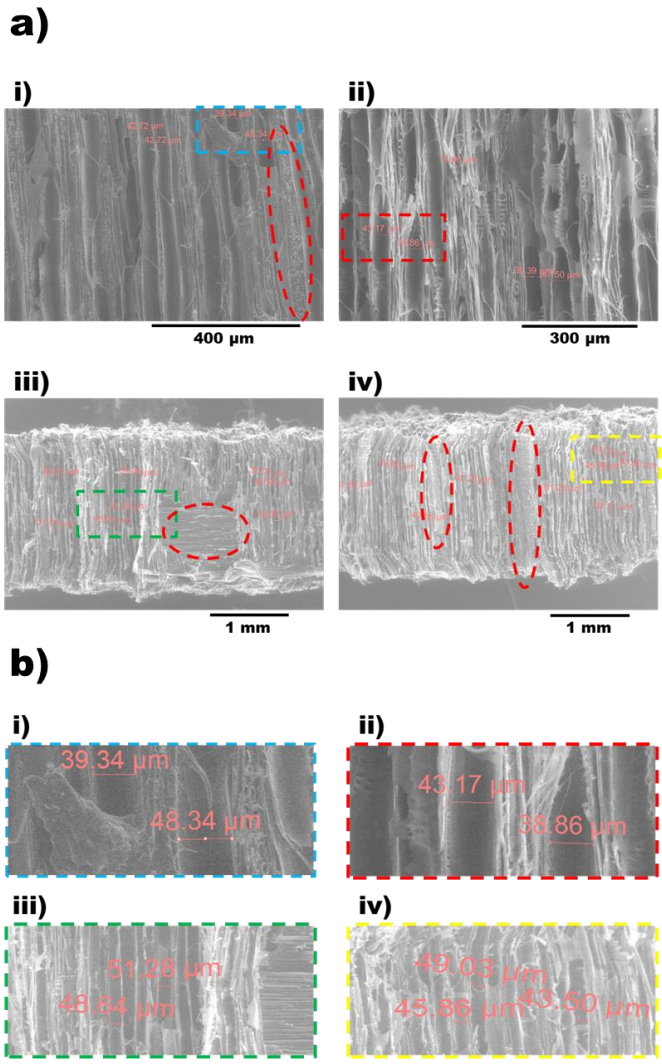

Figure 5.4. a) Cross-section ESEM images of: i) NTW (magnification x240), ii) sample DWD_3_70 (magnification x250), iii) sample DWD_3_90 (magnification x50) and iv) sample DWD_6_90 (magnification x50). b) Zoom of the cross-section ESEM images of: i) NTW (magnification x780) ii) sample DWD_3_70 (magnification x750), iii) sample DWD_3_90 (magnification x140) and iv) sample DWD_6_90 (magnification x170). The selected areas correspond to the coloured regions of the images shown in **Figure 5.4a**.

5.3.2. Functionalization of delignified wood

At this point, an easy functionalization of delignified wood with lauroyl chloride was performed to reduce the amount of pendant hydroxyl groups of cellulose and hemicellulose (band centred at 3320 cm^{-1}, ν(O-H), **Figure 5.3**) since we believed that the hydrophilic character of the wood fibres would not allow an adequate distribution of the SCLC polyether in the pores of the support. Furthermore, the long aliphatic chains introduced could interact via non-covalent interactions with the side chain dendrons once the SCLCP was introduced into the pores of the wood support, helping its self-assembly process.

Thus, different reaction conditions were investigated to achieve the highest yield in this nucleophilic acyl substitution. As we had previously done with the delignification process, the functionalization of wood was monitored by FT-IR comparing the relative intensity of the band centred between 3400 – 3300 cm^{-1} (ν(O-H)) with the same band in the spectra of DWD_3_90 (**Figure 5.5**). Following a procedure reported by Takahito and co-workers, several trials were carried out at 90 °C using different reaction times [38]. As observed in **Table 5.2**, a wood functionalization estimation higher than 82 % was reached after 30 min. When the reaction time increased, the functionalization of wood also increased achieving a complete functionalization when the reaction was kept during 24 h. Besides, the observation of a band attributed to the formed carbonyl group of the ester (ν(C=O) at 1746 cm^{-1}) confirmed that the functionalization of wood discs had taken place (**Figure 5.5**). It can also be observed that this band presents a greater intensity when a higher

functionalization yield is achieved. The dodecanoyl chains grafted to cellulose and hemicellulose also produce an increase of the two bands attributed to the ν(C–H) in $–CH_3$ (asymmetric) that appear at 2918 cm^{-1} and $–CH_3$ (symmetric) and $–CH_2–$ (asymmetric and symmetric), which appear between 2918 and 2852 cm^{-1}, respectively.

Table 5.2. Chemical reaction conditions and yields of nucleophilic acyl substitution obtained in the optimization of the functionalization of delignified beech wood discs.

Sample	Reaction time (h)	Reaction temperature (°C)	Functionalization degree (%) [a]
FDWD_0.5_90	0.5	90	82
FDWD_0.75_90	0.75	90	90
FDWD_1_90	1	90	90
FDWD_3_90	3	90	90
FDWD_5_90	5	90	90
FDWD_24_90	24	90	100
FDWD_0.5_50	0.5	50	71

[a] Calculated from the intensity of the band centred between 3400 – 3300 cm^{-1} in FT-IR spectra.

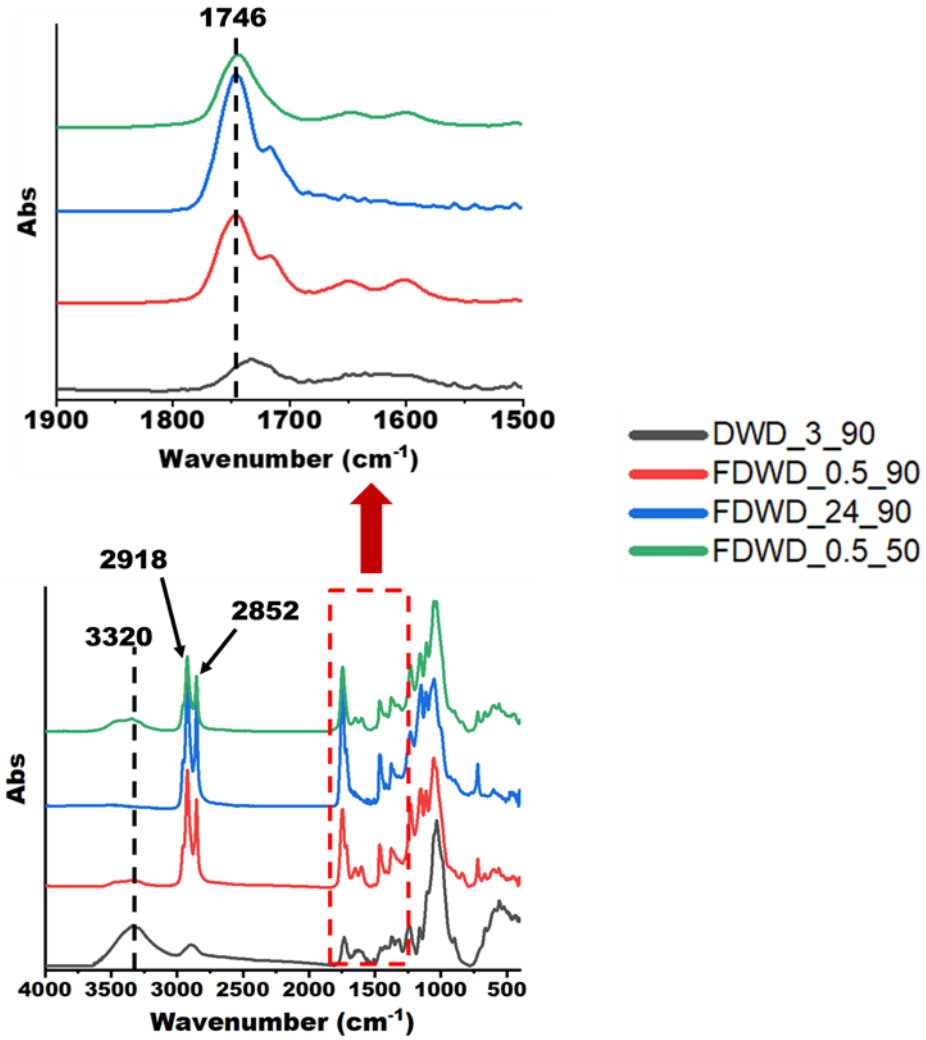

Figure 5.5. FT-IR spectra of DWD_3_90 and the following functionalized samples: FDWD_0.5_50, FDWD_0.5_90 and FDWD_24_90.

Unfortunately, in these experiments we always isolated broken discs (**Figure 5.S4**). To avoid this fact, we performed the functionalization of wood supports at a lower temperature (50 °C) during 30 min. In this experiment, a

functionalization yield of 71 % was obtained. Moreover, we did not observe the rupture of the discs in this case. In view of these results, these last conditions were used to carry out the functionalization of delignified beech wood discs.

The morphology of the sample FDWD_0.5_50 was characterized by means of ESEM. The cross-section of the functionalized discs is shown in **Figure 5.6**, in which channels with the same diameter that the ones observed in the DWD samples were detected (**Figure 5.6b**). As we had previously seen with the NTW, some fibres parallel to the surface of the discs were also observed (regions highlighted in red of **Figure 5.6**).

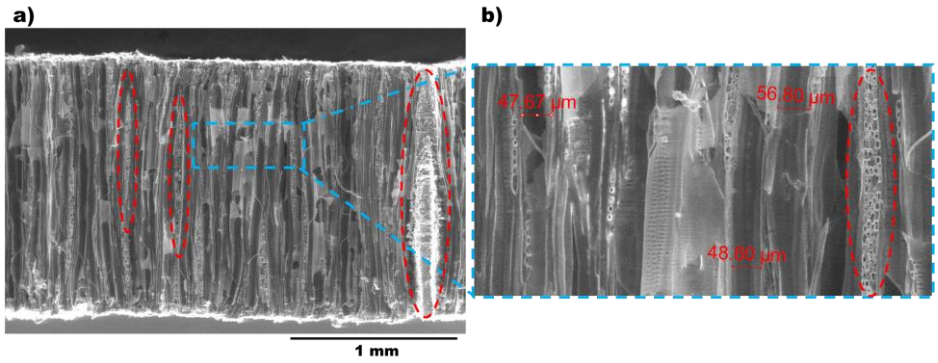

Figure 5.6. Cross-section ESEM images of: a) sample FDWD_0.5_50 (magnification x75), and b) zoom of the region highlighted in blue (magnification x250). The measurements of the diameter of the cellulose fibres are also shown.

5.3.3. Thermal and mesomorphic characterization

Thermal characterization of PECH75 was performed by DSC, TGA and POM experiments (**Table 5.3**). As observed in the DSC thermogram, PECH75 has a glass transition temperature of -13 °C. Besides, the endotherm centred at 127 °C corresponds to the clearing temperature (T_c) of the SCLCP (**Figure 5.S5**). POM observation of PECH75 evidenced the growth of a broken fan-shaped liquid crystalline texture on heating around 120 °C after 24h (**Figure 5.7**). Furthermore, thermal stability of dendronized PECH, NTW, DWD and FDWD was evaluated by TGA (**Table 5.3**, **Figure 5.S6**). In the case of PECH75, it presented an onset of thermal weight loss (determined as the temperature corresponding to the 5 % mass loss) equal to 290 °C and a remaining char yield of 15 % at 600 °C. These values are almost identical to those reported for the chemically modified PECH with a degree of modification with TAPER equal to 80% [27]. Furthermore, the great similarity between these calorimetric data with the results published in literature for other polymers containing TAPER side groups, evidenced the strong influence of the dendron in the thermal properties of these polymers [39,40].

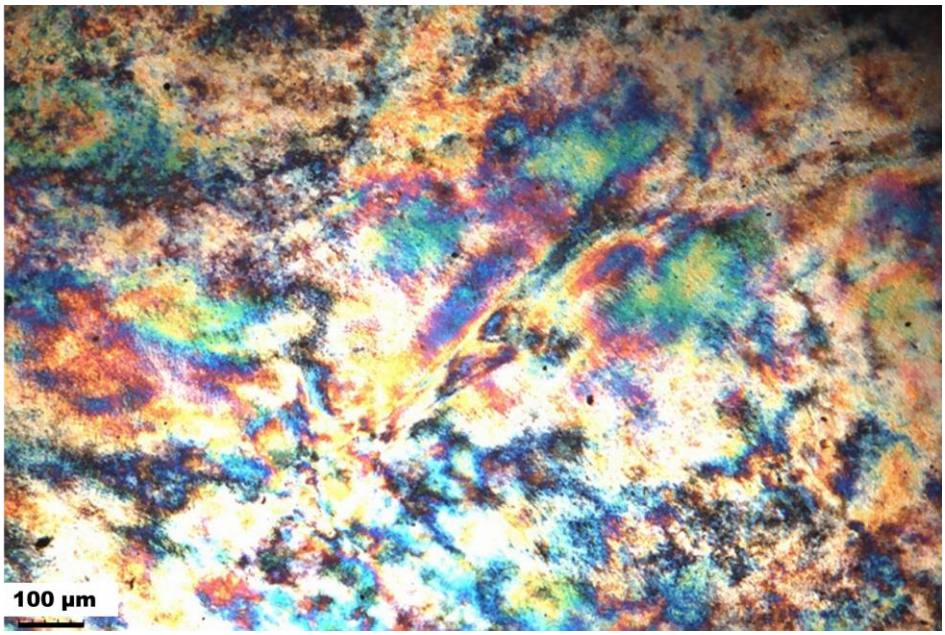

Figure 5.7. Optical micrograph between crossed polars of PECH75 recorded during the first heating at 120 °C.

Concerning the wood samples, DGTA curves (**Figure 5.S7**) evidenced that the thermal degradation of the NTW and DWD samples showed mainly a three-step weight loss. The first mass loss is associated to the evaporation of moisture, intrinsic water loss and elimination of low molecular weight components (2 %) and occurs between 30 and 110 °C. The second mass loss step corresponds to the degradation of hemicellulose (200-300 °C), meanwhile the third one is associated to the degradation of cellulose (above 300 °C). [41,42] On the other hand, FDWD samples presented only a two-step weight loss. As observed in NTW and DWD samples, the first one corresponds to the loss of water, moisture and volatile compounds. The second one is attributed to the degradation of cellulose and hemicellulose, maybe due to the

incorporation of lauroyl chloride into the wood structure by chemical modification. The incorporation of these moieties into the support structure is responsible for the highest hydrophobic character of FDWD discs and may explain that these discs contain a smaller amount of water molecules in its structure compared to NTW and DWD samples.

Table 5.3. Calorimetric features of PECH75 and wood samples (NTW, DWD_3_90 and FDWD_0.5_50).

Sample	T_g (°C) [a]	T_c (°C) [a]	$T_{5\%}$ (°C)	Char yield (%) [b]
PECH_75	-13	127	290	15
NTW	-	-	270	20
DWD_3_90	-	-	238	26
FDWD_0.5_50	-	-	265	12

[a] Determined by DSC second heating scan. [b] Char yield obtained at 600 °C.

5.3.4. Preparation and characterization of hybrid membranes

As previously described, self-supported membranes using SCLCPs derived from PECH with modification degrees between 39 and 58 % were prepared by our research group. [18,31] Previous investigations revealed that the resulting membranes exhibited poor mechanical properties, limiting their possible future applications. Thus, the samples DWD_3_90 and

FDWD_0.5_50 were used as a support with the purpose of improving the performance of the new hybrid membranes prepared by the immersion precipitation method. In the first trials, the high viscosity of the dendronized polymer in THF made the complete impregnation of the wood discs with the dendronized polymer solution very difficult. To solve this, the concentration of the polymer solution was decreased to 15 wt%. Additionally, a vacuum pump was used to help the solution to penetrate the pores of the wood support (**Figure 5.1**). ESEM analyses were carried out to confirm the infiltration of PECH75 in both DWD_3_90 and FDWD_0.5_50 wood discs. The obtained results (samples DWD_PECH75 and FDWD_PECH75) are shown in **Figure 5.8**.

The micrographs of the cross-section and upper surface of the sample DWD_PECH75 evidenced that this sample does not present a homogeneous distribution of PECH75 inside the cellulose fibres of the support since many holes can be observed on the surface of the membrane (**Figure 5.8b**). This could be ascribed to the distinct hydrophilic character of the delignified wood discs and PECH_75. In the case of delignified wood discs, the presence of a large number of polar hydroxyl groups in the chemical structure of cellulose and hemicellulose could repel the hydrophobic dendronized polymer, interfering with its penetration into the delignified wood support as well as its subsequent distribution within it. In the case of sample FDWD_PECH75 (**Figures 5.8c** and **5.8d**), it revealed the presence of a thin layer of PECH75 on both sides of the wood discs. Besides, it could be seen that not all the cellulose fibres were filled with the dendronized polyether, which may be attributed to the breaking process necessary to observe the cross-sections of the hybrid material. The other possibility is that the incorporated PECH75 could remain

on the other side of the cross-section. **Figure 5.8d** confirmed that PECH75 was homogeneously distributed on the surface of the sample FDWD_0.5_50. Thus, the functionalization of delignified wood helps the polymer penetrate the support.

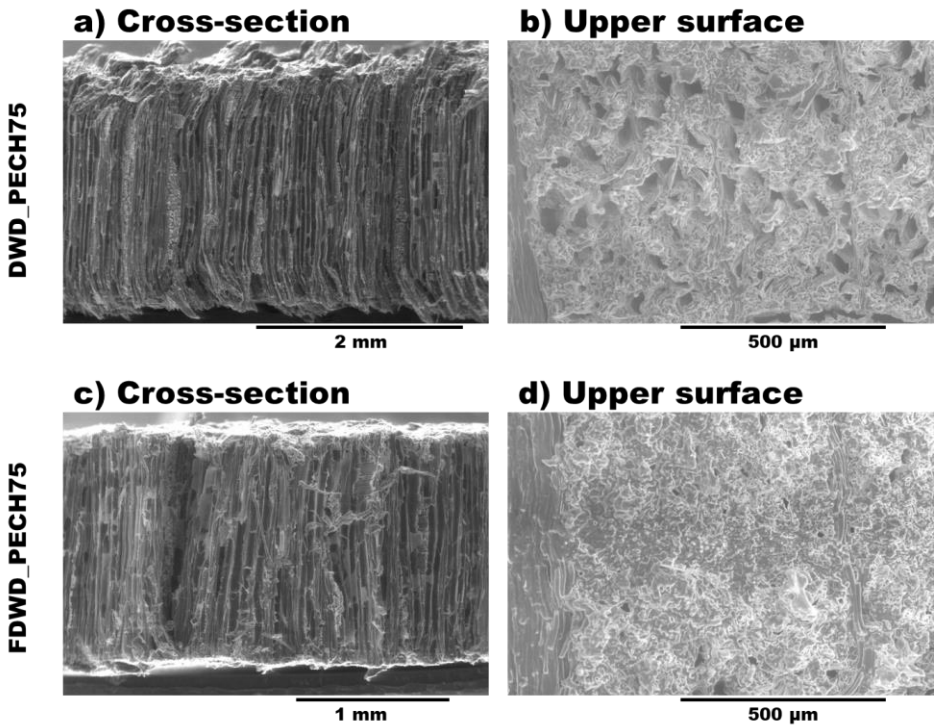

Figure 5.8. ESEM images of the samples DWD_PECH75 and FDWD_PECH75 showing their cross-sections (a) and c), respectively. magnification x50) and their upper surfaces (b) and d), respectively. magnification x200).

Despite this, a thermal treatment was used to achieve a homogeneous distribution of PECH75 inside the pores of the wood support. To evaluate the

effect of the thermal treatment in the morphology of the hybrid membranes as well as the distribution of PECH75 inside the wood supports, thermally treated membranes (DWD_PECH75_T and FDWD_PECH75_T) and membranes not subjected to thermal treatment (DWD_PECH75 and FDWD_PECH75) were evaluated by means of static water contact angle. Moreover, samples DWD_3_90 and FDWD_0.5_90 were also investigated to determine their hydrophilic/hydrophobic character. The values of water contact angles on both sides of the wood membranes are reported in **Table 5.4**.

Table 5.4. Water contact angles of samples DWD_3_90, FDWD_0.5_90 and hybrid membranes DWD_PECH75 and FDWD_PECH75, before and after applying the thermal treatment.

Sample	**Water contact angle (°)**	
	Membrane air side	**Membrane bottom side**
DWD_3_90	120 ± 2	125 ± 1
FDWD_0.5_90	134 ± 1	131 ± 2
DWD_PECH_75	130 ± 1	114 ± 3
DWD_PECH_75_T	135 ± 1	138 ± 1
FDWD_PECH_75	129 ± 2	126 ± 1
FDWD_PECH_75_T	134 ± 1	135 ± 2

All the tested membranes exhibited a hydrophobic character in both sides (air and bottom sides). As expected, the functionalization of wood produces an

increase in its hydrophobic character. Furthermore, no significant differences between contact angle values of both sides of the same membrane were found except for DWD_PECH75. For this sample, the bottom side is clearly less hydrophobic due to the smaller contact angle value compared to the air side. This can be attributed to the nonuniform distribution of tapered groups (hydrophobic part of the dendronized polymer) grafted to PECH75 in each side of the hybrid membrane. This effect was also reported by Montané and co-workers. [21] Related to this, the less hydrophobic character of delignified wood hinders the diffusion of the side chain liquid crystalline polyether through the pores of the support. When delignified wood discs were functionalized, the hydrophobicity of the new support was more similar to PECH75, facilitating its dissemination within the wood support. After the application of the thermal treatment, we could observe that the contact angles of both sides of DWD_PECH75 were very similar which evidenced that a homogeneous distribution of PECH75 inside DWD was achieved.

Another tendency is that the contact angle values increased slightly for both samples when they were subjected to thermal treatment. As observed in **Table 5.4**, contact angle values between 134 and 138° were obtained for both thermally treated membranes (DWD_PECH75 and FDWD_PECH75, respectively), which also proved that good homogenization of PECH75 was achieved within the delignified and the functionalized wood discs.

These polymer columns could be homeotropically oriented, which would present enormous potential in applications related to sustainable energy applications (fuel cells, artificial photosynthesis, etc.).

5.4.Conclusions

The preparation of new hybrid membranes based on dendronized polyepichlorohydrin inside the wood pores of biobased supports was achieved through the delignification and subsequent chemical modification of wood, thus preparing two type of hybrid membranes, using a delignified wood (DWD) or a functionalized delignified wood (FDWD) supports. Wood delignification was achieved successfully, obtaining discs with more than 90 % of delignification degree, without compromising the structure of the wooden discs, as we could see from the ESEM analysis.

Subsequent chemical functionalization of the delignified wood discs was performed successfully using lauroyl chloride. The aim of this modification was to promote the affinity of the SCLC polyepichlorohidryn inside the pores of the wood support. Functionalization degrees higher than 70 % were obtained, although the process had to be carried out at 50 °C to avoid breaking of the wooden discs. Same as we observed before, the chemical functionalization of wood did not affect the channel width and their structure, as it was observed by means of ESEM analysis. FT-IR revealed an increasing band at 1746 cm^{-1}, related to the recently formed carbonyl, and a decrease in the band centred at 3300 cm^{-1}, related to the hydroxyl groups of the cellulose and hemicellulose moieties.

During the membrane assembly with the two prepared supports, substantial differences between both systems were found. On the one hand, membrane prepared with delignified wood discs resulted to be unsuccessfully filled, as it was evidenced during the ESEM analysis. On the contrary, functionalized

delignified wood discs presented a homogeneous distribution of the polymer, thus showing a successful pore filling as was denoted by ESEM analysis. Contact angle measurements, resulted in different CA values in both sides of DWD based hybrid membranes, revealing that the SCLC polyepichlorohidryn was not distributed correctly across the support. FDWD based hybrid membranes, on the other hand, did not show such observation, thus revealing similar CA on both sides of the membrane. Nevertheless, thermal treatment proved to be helpful to distribute the SCLCP more homogeneously inside the wood support.

These polymer columns could be homeotropically oriented, which would present enormous potential in applications related to sustainable energy applications (fuel cells, artificial photosynthesis, etc.). Furthermore, the evaluation of the polymer orientation inside the wood support, studies on ionic transport across hybrid membranes and membrane wettability will be the subject of extensive studies presented in the following chapter.

5.5.References

[1] D. Mboowa, A review of the traditional pulping methods and the recent improvements in the pulping processes, Biomass Convers Biorefin (2021). https://doi.org/10.1007/s13399-020-01243-6.

[2] Y.S. Kim, Current researches on the protection of exterior wood from weathering, Journal of the Korean Wood Science and Technology 46 (2018) 449–470. https://doi.org/10.5658/WOOD.2018.46.5.449.

[3] S.L. Zelinka, M. Altgen, L. Emmerich, N. Guigo, T. Keplinger, M. Kymäläinen, E.E. Thybring, L.G. Thygesen, Review of Wood Modification and Wood Functionalization Technologies, Forests 13 (2022). https://doi.org/10.3390/f13071004.

[4] A. Kumar, T. Jyske, M. Petrič, Delignified Wood from Understanding the Hierarchically Aligned Cellulosic Structures to Creating Novel Functional Materials: A Review, Adv Sustain Syst 5 (2021). https://doi.org/10.1002/adsu.202000251.

[5] A. Mariani, G. Malucelli, Transparent Wood-Based Materials: Current State-of-the-Art and Future Perspectives, Materials 15 (2022). https://doi.org/10.3390/ma15249069.

[6] C. Montanari, Y. Li, H. Chen, M. Yan, L.A. Berglund, Transparent Wood for Thermal Energy Storage and Reversible Optical Transmittance, ACS Appl Mater Interfaces 11 (2019) 20465–20472. https://doi.org/10.1021/acsami.9b05525.

[7] J. Qin, X. Li, Y. Shao, K. Shi, X. Zhao, T. Feng, Y. Hu, Optimization of delignification process for efficient preparation of transparent wood with high strength and high transmittance, Vacuum 158 (2018) 158–165. https://doi.org/10.1016/j.vacuum.2018.09.058.

[8] M. Zhu, J. Song, T. Li, A. Gong, Y. Wang, J. Dai, Y. Yao, W. Luo, D. Henderson, L. Hu, Highly Anisotropic, Highly Transparent Wood Composites, Advanced Materials 28 (2016) 5181–5187. https://doi.org/10.1002/adma.201600427.

[9] L. Ding, X. Han, L. Chen, S. Jiang, Preparation and properties of hydrophobic and transparent wood, Journal of Bioresources and Bioproducts 7 (2022) 295–305. https://doi.org/10.1016/j.jobab.2022.02.001.

[10] Y. Li, Q. Fu, R. Rojas, M. Yan, M. Lawoko, L. Berglund, Lignin-Retaining Transparent Wood, ChemSusChem 10 (2017) 3445–3451. https://doi.org/10.1002/cssc.201701089.

[11] Y. Li, Q. Lu, J. Yang, W. He, Delignified wood for thermal energy storage with high efficient photo-thermal conversion efficiency, J Energy Storage 80 (2024). https://doi.org/10.1016/j.est.2023.110235.

[12] D. Song, D. Zheng, Z. Li, C. Wang, J. Li, M. Zhang, Research Advances in Wood Composites in Applications of Industrial Wastewater Purification and Solar-Driven Seawater Desalination, Polymers (Basel) 15 (2023). https://doi.org/10.3390/polym15244712.

[13] T. Li, J. Song, X. Zhao, Z. Yang, G. Pastel, S. Xu, C. Jia, J. Dai, C. Chen, A. Gong, F. Jiang, Y. Yao, T. Fan, B. Yang, L. Wågberg, R. Yang, L. Hu, Anisotropic, lightweight, strong, and super thermally insulating nanowood with naturally aligned nanocellulose, 2018. https://www.science.org.

[14] B. El Allaoui, H. Benzeid, N. Zari, A. el kacem Qaiss, R. Bouhfid, Functional cellulose-based beads for drug delivery: Preparation, functionalization, and applications, J Drug Deliv Sci Technol 88 (2023). https://doi.org/10.1016/j.jddst.2023.104899.

[15] M.A. Taher, X. Wang, K.M. Faridul Hasan, M.R. Miah, J. Zhu, J. Chen, Lignin Modification for Enhanced Performance of Polymer Composites, ACS Appl Bio Mater (2023). https://doi.org/10.1021/acsabm.3c00783.

[16] A. Moreno, J. Delgado-Lijarcio, J.C. Ronda, V. Cádiz, M. Galià, M.H. Sipponen, G. Lligadas, Breathable Lignin Nanoparticles as Reversible Gas Swellable Nanoreactors, Small 19 (2023). https://doi.org/10.1002/smll.202205672.

[17] M. Giamberini, J.C. Ronda, J.A. Reina, Poly(epichlorohydrin) modified with 3,4,5-tris(dodecyloxy)benzoate: The structure and dynamics of the aliphatic side chains in the columnar mesophase, J Polym Sci A Polym Chem 43 (2005) 2099–2111. https://doi.org/10.1002/pola.20680.

[18] J.C. Ronda, J.A. Reina, M. Giamberini, Self-organized liquid-crystalline polyethers obtained by grafting tapered mesogenic groups onto

poly(epichlorohydrin): Toward biomimetic ion channels 2, J Polym Sci A Polym Chem 42 (2004) 326–340. https://doi.org/10.1002/pola.11016.

[19] K.A. Bogdanowicz, S. V. Bhosale, Y. Li, I.F.J. Vankelecom, R. Garcia-Valls, J.A. Reina, M. Giamberini, Mimicking nature: Biomimetic ionic channels, J Memb Sci 509 (2016) 10–18. https://doi.org/10.1016/j.memsci.2016.02.038.

[20] A. Zare, B. Pascual-Jose, S. De la Flor, A. Ribes-Greus, X. Montané, J.A. Reina, M. Giamberini, Membranes for cation transport based on dendronized poly(Epichlorohydrin-co-ethylene oxide). part 1: The effect of dendron amount and column orientation on copolymer mobility, Polymers (Basel) 13 (2021). https://doi.org/10.3390/polym13203532.

[21] X. Montané, S.V. Bhosale, J.A. Reina, M. Giamberini, Columnar liquid crystalline polyglycidol derivatives: A novel alternative for proton-conducting membranes, Polymer (Guildf) 66 (2015) 100–109. https://doi.org/10.1016/j.polymer.2015.03.071.

[22] K.A. Bogdanowicz, G.A. Rapsilber, J.A. Reina, M. Giamberini, Liquid crystalline polymeric wires for selective proton transport, part 1: Wires preparation, Polymer (Guildf) 92 (2016) 50–57. https://doi.org/10.1016/j.polymer.2016.03.073.

[23] A. Šakalyte, J.A. Reina, M. Giamberini, Liquid crystalline polyamines containing side dendrons: Toward the building of ion channels based on polyamines, Polymer (Guildf) 54 (2013) 5133–5140. https://doi.org/10.1016/j.polymer.2013.07.027.

[24] X. Montané, K.A. Bogdanowicz, G. Colace, J.A. Reina, P. Cerruti, A. Lederer, M. Giamberini, Advances in the design of self-supported ion-conducting membranes-new family of columnar liquid crystalline polyamines. Part 1: Copolymer synthesis and membrane preparation, Polymer (Guildf) 105 (2016) 298–309. https://doi.org/10.1016/j.polymer.2016.10.047.

[25] K.A. Bogdanowicz, P. Sistat, J.A. Reina, M. Giamberini, Liquid crystalline polymeric wires for selective proton transport, part 2: Ion transport in solid-state, Polymer (Guildf) 92 (2016) 58–65. https://doi.org/10.1016/j.polymer.2016.03.080.

[26] W.L.F. Armarego, C.L.Lin. Chai, Purification of laboratory chemicals, Elsevier/BH, 2009.

[27] S. V. Bhosale, Proton-exchange biomimetic membranes based on columnar side-chain liquid-crystalline polyethers, PhD Thesis, Universitat Rovira i Virgili, 2013

[28] J. Wu, Y. Wu, F. Yang, C. Tang, Q. Huang, J. Zhang, Impact of delignification on morphological, optical and mechanical properties of transparent wood, Compos Part A Appl Sci Manuf 117 (2019) 324–331. https://doi.org/10.1016/j.compositesa.2018.12.004.

[29] J.-K. Kim, R. Bandi, R. Dadigala, L. Van Hai, S.-Y. Han, G.-J. Kwon, S.-W. Cho, S.-Y. Ma, S.-H. Lee, Esterification of nanofibrillated cellulose using lauroyl chloride and its composite films with polybutylene succinate, Bioresources 18 (2023) 7143–7153. https://doi.org/10.15376/biores.18.4.7143-7153.

[30] J.C. Ronda, J.A. Reina, M. Giamberini, Self-organized liquid-crystalline polyethers obtained by grafting tapered mesogenic groups onto poly(epichlorohydrin): Toward biomimetic ion channels 2, J Polym Sci A Polym Chem 42 (2004) 326–340. https://doi.org/10.1002/pola.11016.

[31] B. Tylkowski, N. Castelao, M. Giamberini, R. Garcia-Valls, J.A. Reina, T. Gumí, The importance of orientation in proton transport of a polymer film based on an oriented self-organized columnar liquid-crystalline polyether, Materials Science and Engineering C 32 (2012) 105–111. https://doi.org/10.1016/j.msec.2011.10.003.

[32] J. Li, C. Chen, J.Y. Zhu, A.J. Ragauskas, L. Hu, In Situ Wood Delignification toward Sustainable Applications, Acc Mater Res 2 (2021) 606–620. https://doi.org/10.1021/accountsmr.1c00075.

[33] L.H. Thomas, A. Martel, I. Grillo, M.C. Jarvis, Hemicellulose binding and the spacing of cellulose microfibrils in spruce wood, Cellulose 27 (2020) 4249–4254. https://doi.org/10.1007/s10570-020-03091-z.

[34] S.-Y. Zhang, C.-G. Wang, B.-H. Fei, Y. Yu, H.-T. Cheng, G.-L. Tian, Mechanical Function of Lignin and Hemicelluloses in Wood Cell Wall Revealed with Microtension of Single Wood Fiber, Bioresources 8 (2013) 2376–2385. https://doi.org/10.15376/biores.8.2.2376-2385.

[35] A. Kumar, T. Jyske, M. Petrič, Delignified Wood from Understanding the Hierarchically Aligned Cellulosic Structures to Creating Novel Functional Materials: A Review, Adv Sustain Syst 5 (2021). https://doi.org/10.1002/adsu.202000251.

[36] M. Zhu, J. Song, T. Li, A. Gong, Y. Wang, J. Dai, Y. Yao, W. Luo, D. Henderson, L. Hu, Highly Anisotropic, Highly Transparent Wood Composites, Advanced Materials 28 (2016) 5181–5187. https://doi.org/10.1002/adma.201600427.

[37] S.Y. Oh, D. Il Yoo, Y. Shin, G. Seo, FTIR analysis of cellulose treated with sodium hydroxide and carbon dioxide, Carbohydr Res 340 (2005) 417–428. https://doi.org/10.1016/j.carres.2004.11.027.

[38] K. Takahito, Y. Kazuhiro, I. Shiro, Sugar fatty acid ester and oil getting agent, Patent JP2019089719A, June 13, 2019.

[39] J. Guardià, M. Giamberini, J.A. Reina, X. Montané, Synthesis and Characterization of Dendronized Side Chain Liquid Crystalline Poly(2-oxazoline)s towards Biomimetic Ion Channels, Eur Polym J (2023) 112273. https://doi.org/10.1016/j.eurpolymj.2023.112273.

[40] X. Montané, K.A. Bogdanowicz, G. Colace, J.A. Reina, P. Cerruti, A. Lederer, M. Giamberini, Advances in the design of self-supported ion-conducting membranes-new family of columnar liquid crystalline polyamines. Part 1: Copolymer synthesis and membrane preparation, Polymer (Guildf) 105 (2016) 298–309. https://doi.org/10.1016/j.polymer.2016.10.047.

[41] H. Yang, R. Yan, H. Chen, C. Zheng, D.H. Lee, D.T. Liang, In-depth investigation of biomass pyrolysis based on three major components: Hemicellulose, cellulose and lignin, Energy and Fuels 20 (2006) 388–393. https://doi.org/10.1021/ef0580117.

[42] M. Poletto, A.J. Zattera, R.M.C. Santana, Thermal decomposition of wood: Kinetics and degradation mechanisms, in: Bioresour Technol, Elsevier Ltd, 2012: pp. 7–12. https://doi.org/10.1016/j.biortech.2012.08.133.

5.6.Supporting Information

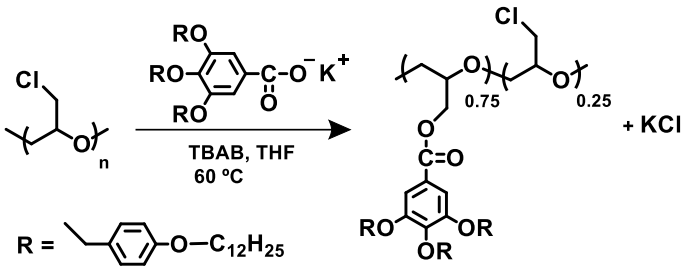

Scheme 5.S1. Synthetic procedure for the obtention of PECH75.

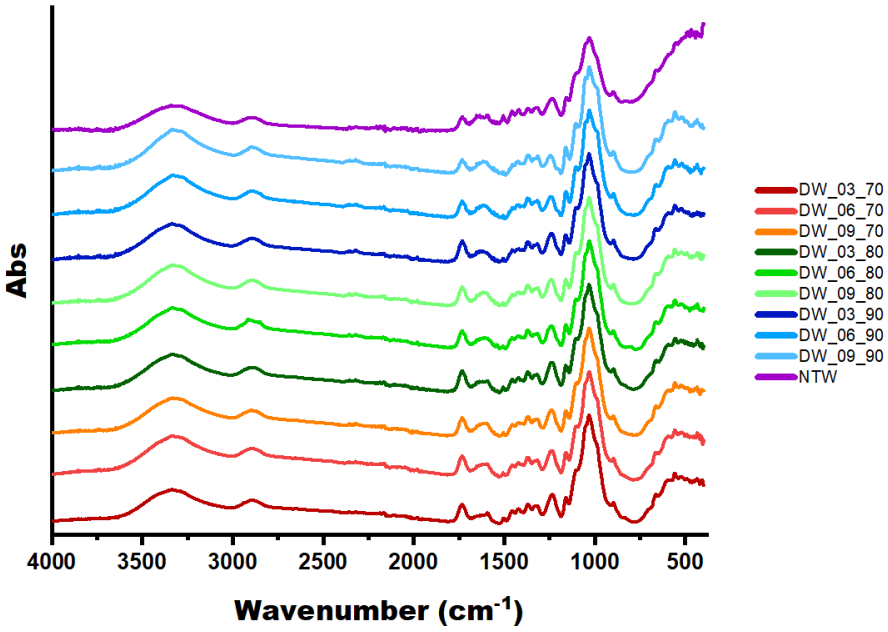

Figure 5.S1. FT-IR of non-treated beech wood (NTW) and all delignified beech wood discs performed at different temperatures and time.

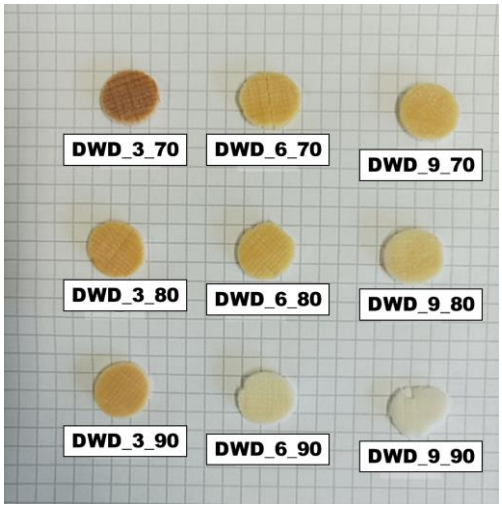

Figure 5.S2. Pictures of the beech wood discs obtained after delignification process using different reaction conditions.

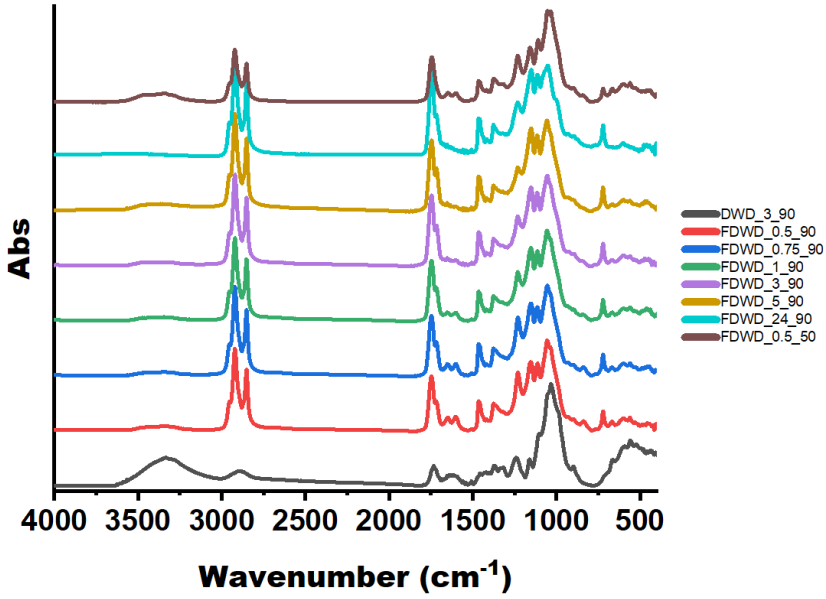

Figure 5.S3. FT-IR of DWD_3_90 and all functionalized delignified beech wood discs performed at different temperatures and time.

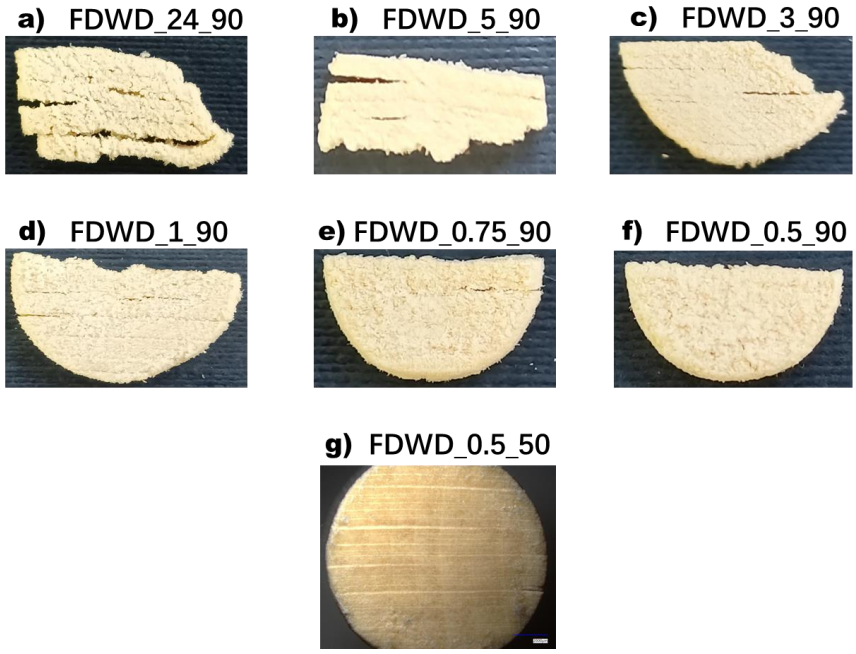

Figure 5.S4. Photographs of the functionalized delignified wood discs (FDWD) obtained using different reaction conditions.

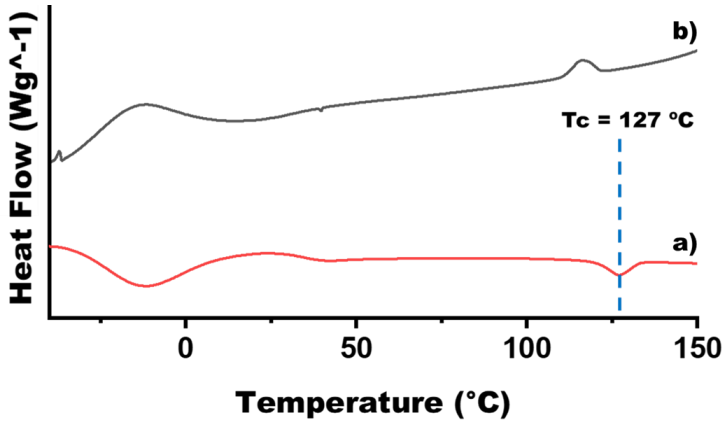

Figure 5.S5. DSC thermogram of: a) second heating scan of PECH_75; and b) second cooling scan of PECH_75. (Scan rate: 10 °C/min).

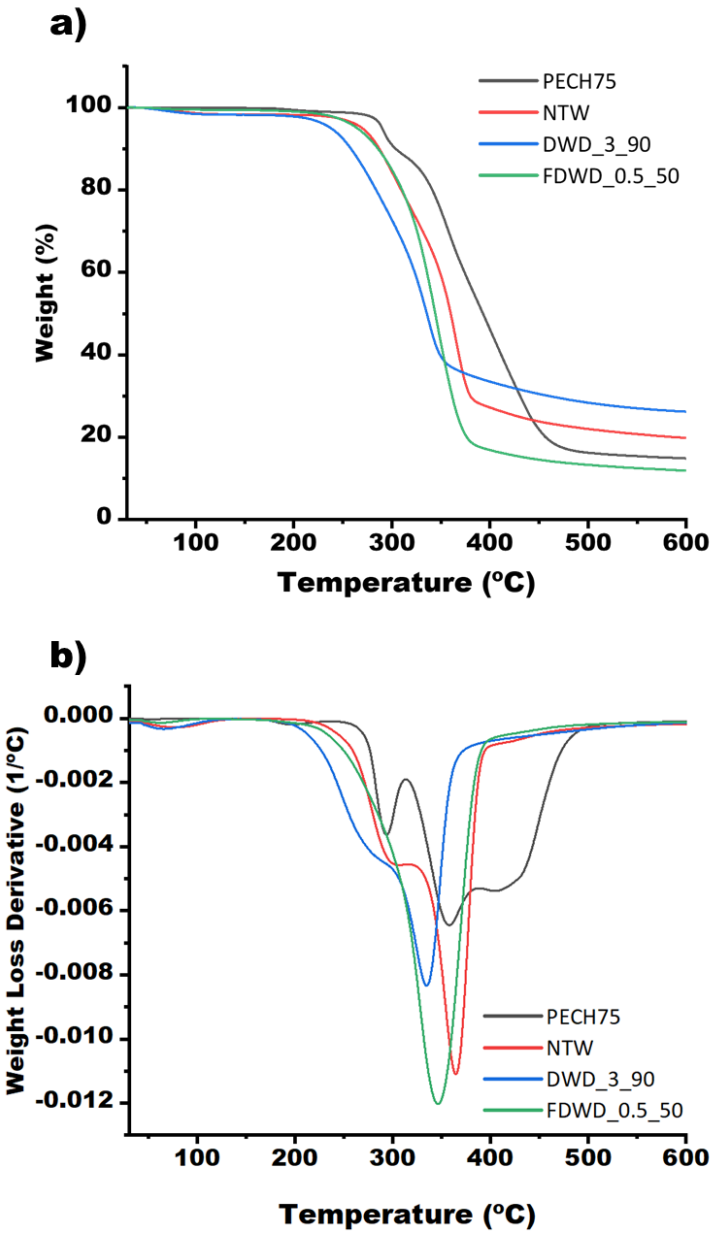

Figure 5.S6. a) TGA thermograms of: PECH75, NTW, DWD_3_90 and FDWD_0.5_50. b) DTGA curves of: PECH75, NTW, DWD_3_90 and FDWD_0.5_50. Thermogravimetric analyses were carried out using a heating rate 10 °C/min in nitrogen atmosphere.

UNIVERSITAT ROVIRA I VIRGILI
COLUMNAR LIQUID-CRYSTALLINE POLYMERS CONTAINING NITROGEN AT THE BACKBONE TO BE USED TO PREPARE ION-TRANSPORT MEMBRANES
Jordi Guardià Blanch

Chapter 6

Development of wood-based membranes for ion transport applications. Part 2: Membrane characterization and evaluation of ionic transport

UNIVERSITAT ROVIRA I VIRGILI
COLUMNAR LIQUID-CRYSTALLINE POLYMERS CONTAINING NITROGEN AT THE BACKBONE TO BE USED TO PREPARE ION-TRANSPORT MEMBRANES
Jordi Guardià Blanch

CHAPTER 6

6.1.Introduction

Since life was formed in Earth's oceans, membranes have been part of all living beings for millennia. Nowadays, the presence of a membrane in the cell wall is undoubtedly affirmed and confirmed. However, this was not the case some centuries ago. The cell wall theory was first formulated in the 19th century, nonetheless it was not until 1970s when the fluid mosaic model prevails [1]. In the cell wall, the presence of proteins allows the transport of different compounds from the outside of the cell to inside the cell and vice versa [1]. This transport occurs with high selectivity and efficiency. However, biological membranes are not the only interesting membranes. In fact, synthetic membranes have been used successfully in large-scale industrial applications since 1960s [2].

During the last decades, membrane technology has been proved to be very useful for several applications, such as water purification [3–7], gas separation [3,7,8], CO2 capture [9], polyelectrolytes [8,10,11], hydrogen production [12] or sensors [13–15], among other applications. The environmental emergency, promoted by the intensive use of fossil fuels and the greenhouse gas emissions, has driven the use of alternative technologies to produce clean energy. One of these technologies are the proton-exchange membrane fuel cells (PEMFC), which use polymer membranes as solid polyelectrolytes to transport protons across the membrane. The most used membranes for this application are perfluorosulfonic acid (PFSA) ionomer-based membranes . Nafion® (a registered trademark of DuPont) is the benchmark membrane for this purpose thanks to its high proton conductivity, good mechanical

strength, and chemical stability [16]. Despite this, Nafion® is difficult to recycle at the end-of-life, and its performance presents a huge water dependency, since the transport mechanism is based on the Grotthus mechanism and electroosmotic drag [17]. Therefore, it presents a decrease on the transport properties at high temperatures caused by water evaporation [18], together with a loss of mechanical properties. Moreover, it shows low selectivity against proton. Consequently, the design of new membranes has aroused a great interest during the last decades.

Trying to mimic the transport phenomenon through biological membranes, different families based on side-chain liquid crystal polymers (SCLCP)s have been explored as an alternative to Nafion® and thus try to solve its drawbacks [19–26]. SCLCPs consist of two distinct parts: first the main chain that is formed by carbon scaffold plus the presence of basic heteroatoms (nitrogen or oxygen); and second a dendron with a tapered shape that is grafted as side chain The supramolecular interactions between the mesogenic groups, which in our research works is the dendron 3,4,5-tris[4-(n-dodecan-1-yloxy)benzyloxy]benzoate (TAPER), grafted to the polymer main chain favours a self-assembly process of the side-chain dendrons leading to the polymer main chain to adopt a helical conformation; and resulting in a columnar structure which presents an inner channel [27,28]. In this way, these polymers can be used to prepare membranes for proton transport applications since the inner channel is expected to be the responsible of the ionic transport across the polymer columns. Our research group has synthetized different families of SCLCPs such as polyethers [22,24,25,29–31] and polyamines [19,23,26] using TAPER as a mesogen. Proton transport membranes based on these polymers exhibit remarkable proton transport properties and

selectivity. Nevertheless, some of them also present poor mechanical properties and brittleness.

In order to solve these drawbacks, the use of an external support has been explored. As reported in the first part of this article, we have used beech wood discs as supports for the infiltration of a dendronized polyepichlorohydrin (PECH) with TAPER groups (PECH75, **Figure 6.1**) [32]. In that work, two types of discs were prepared: delignified wood discs (DWD) and functionalized delignified wood discs (FDWD). After delignification and subsequent functionalization of wood the discs, hybrid membranes were assembled by infiltration of a polymer solution on both wood discs. Environmental scanning electron microscopy (ESEM) revealed that cellulose fibres in DWD supports were not fully filled with the dendronized PECH. On the contrary, FDWD supports presented an adequate channel filling.

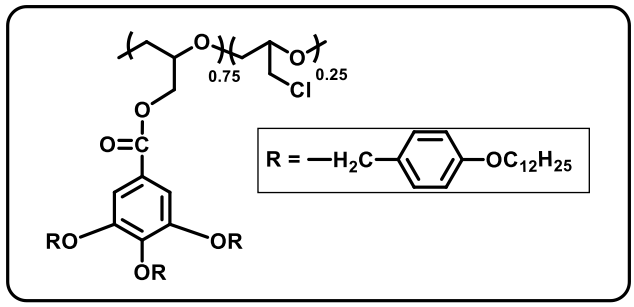

Figure 6.1. Chemical structure of PECH75.

The aim of this work is to characterize the hybrid membranes synthesized in Part 1 of this article in terms of column orientation, membrane wettability, and

surface morphology . In addition, the evaluation of ion transport properties through biomimetic channels will be also investigated by means of electrochemical impedance spectroscopy (EIS), permeability tests and linear sweep voltammetry (LSV). The results obtained using LSV revealed that these hybrid membranes exhibited remarkable proton selectivity compared to other biomimetic membranes presented by our group.

6.2.Experimental Part

6.2.1. Materials

Commercial polyepichlorohydrin (PECH, average M_w: ~ 700.000, determined by gel permeation chromatography), glacial acetic acid (≥99.9 %), sodium chlorite ($NaClO_2$, 80 %), pyridine (≥99.9 %) and lauroyl chloride (98 %) were purchased from Sigma Aldrich. *N,N*-dimethylformamide (DMF) and tetrahydrofuran (THF) were purchased from VWR. Delignified solutions were prepared using 18.2 MΩ·cm^{-1} double deionized water (Milli-Q water systems, Merck Millipore). All chemical compounds were used as received without any further purification except DMF which was dried prior to use according to literature [33] Beech wood bars with a diameter of 15 mm were purchased from Leroy Merlin (Lezennes, France). Discs with a thickness of 1.5 mm were obtained by cutting the beech wood bars using a scroll saw purchased in Lidl Stiftung & Co. KG (Neckarsulm, Germany).

6.2.2. Synthesis of copolymers

The copolymers were obtained by grafting the dendron potassium 3,4,5-tris[4-(n-dodecan-1-yloxy)benzyloxy]benzoate (TAPER) to commercial PECH according to the procedure described in Chapter 5 [32].

6.2.3. Preparation of the membranes

Hybrid membranes were prepared using both delignified wood disks (DWD) and functionalized delignified wood disks (FDWD) as reported in Chapter 5 [32].

Oriented membranes were obtained by using a thermal treatment (baking process). The baking process consists of the following steps: first, the hybrid membrane was placed on a Linkam TP92 hot stage (Linkam Scientific Instruments, Tadworth, UK), it was heated above the clearing temperature of PECH (170 °C) and kept for 30 min at this temperature. Afterwards, it was slowly cooled down (0.1 °C/min) to 30 °C, obtaining a uniform hybrid membrane. Oriented membranes were labelled with the prefix: O-, while non-oriented membranes were labelled with the prefix: NO-. In the case of virgin wood discs (discs that do not contain PECH75), they were labelled by adding the prefix: V-.

6.2.4. Characterization

Environmental scanning electron microscopy (ESEM). A morphological analysis of both DWD and FDWD cross-sections was carried out using a FEI ESEM Quanta 600 instrument (Hillsboro, OR, USA) in high vacuum mode, using electron detector and an accelerating voltage of 20 kV. Cross-sections were prepared by fracturing the membranes by hand. Dry samples were fixed to metal stubs with two-sided adhesive carbon taper.

Contact angle (CA). The static contact angles with water on a membrane surface were measured with an optical goniometer (Ossila LTd, Sheffield, UK) supported by dedicated software. For the tests, water drops of (7 μL) were deposited on the sample's surface. The contact angle was calculated, immediately after placing the water drop, using the tangent to the surface at the point of contact of three phases, *i.e.*, solid, liquid and gas. The measurements were repeated using different areas of the membrane surfaces. For each test reported, at least three drops of water were used.

X-Ray diffraction (XRD). XRD measurements were performed using a Bruker-AXS D8-Discover diffractometer equipped with parallel incident beam (Göbel mirror), vertical θ-θ goniometer, XYZ motorized stage and with a GADDS (General Area Diffraction System). Samples were placed directly on the Si(510) sample holder for reflection analysis. An X-ray collimator system close-to-the-sample allows to analyse areas of 500 μm. An X-ray

diffractometer was operated at 40 kV and 40 mA to generate $Cu_{K\alpha}$ radiation. The GADDS detector was a VÅNTEC-500 (silicon strip technology) placed at 30 cm from the sample. The collected frame (2D XRD pattern) covers a 2θ range from 0.9 up to 11° and from 9.0 to 30.5°. The exposition time was 600 s per frame. The resulting frames were both gamma integrated to obtain a 2θ diffractogram and 2θ integrated to obtain an azimuthal intensity plot. XRD experiments were performed on both sides of the membranes and no differences could be detected.

Electrochemical Impedance Spectroscopy (EIS). Electrochemical Impedance Spectroscopy analysis was performed using PGStat Autolab M204 (Metrohm Nederland, Barendrecht, The Netherlands), coupled to a frequency response analyser (FRA) and two-point cell composed of two copper plates. The analyses were carried out in the dry state on both sides of the hybrid membranes. EIS analysis was performed through-plane and in-plane configuration. The measurements were performed at room temperature (RT = 24 ± 1 °C).

Permeability tests. Transport experiments were performed using a methacrylate test cell that consisted of two compartments, separated by the tested membrane, containing the feed and the stripping solutions, respectively. The volumes of the feed and the stripping solutions were 200 mL, and the effective membrane area was 0.28 cm^2. For the proton transport experiments, the initial feed solution was 0.1 M HCl aqueous solution, and the stripping solution was 0.1 M aqueous solution of: NaCl, LiCl or KCl. The pH

of the stripping solution was measured every 10 s by a pH-Conductivity meter CPC-505 connected to a computer, which registered all results. All experiments were repeated three times.

Linear Sweep voltammetry. Linear sweep voltammetry was performed using Autolab PGSTAT204 (Metrohm Nederland, Barendrecht, The Netherlands), in potentiostatic mode with current ranging from 100 mA to 100 nA, potential range from 0 V to 5 V, step 0.01 V, and scan rate 0.01 V/s. The experimental set-up is presented in **Figure 2**. The distance between the reference electrodes (Ag/AgCl) and membrane was 1 cm. The solution volume in each compartment was 200 mL. The measurements were performed at RT (24 ± 1 °C). Samples for these experiments were placed in a Teflon sheet with a hole in the middle, giving a total membrane area equal to 0.5 cm^2. The membranes were placed between to Teflon sheets and sealed.

0.1 M HCl aqueous solution was used to study the proton transport. Additionally, a series of measurements with chlorides salts (LiCl, KCl and NaCl) using 0.1 M aqueous solutions were performed in order to study the selectivity of the membranes.

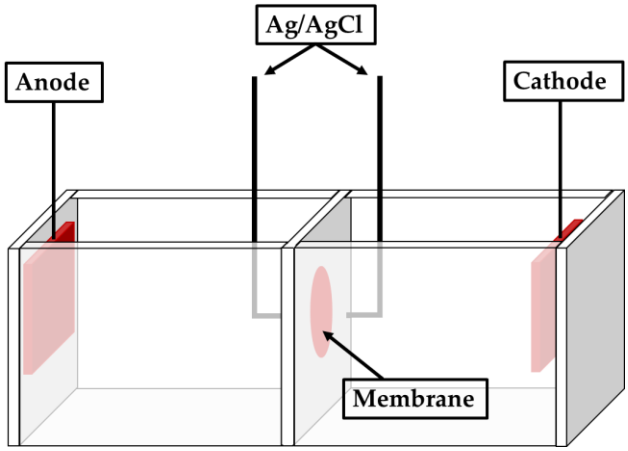

Figure 6.1. Experimental set-up for lineal sweep voltammetry measurements.

Solution Uptake Test. Weighted membranes were immersed in Milli-Q water at RT (24 ± 1 °C). Wet membranes were weighted every hour during the first 5 hours, and after 24 and 48 h to ensure complete water saturation of the membranes. The water on the surface of the wet membranes was quickly removed with filter paper, and the mass was measured later. All experiments were made by triplicate. The mass of the dry membranes was obtained by weighting the membranes after drying them at 50 C during 24 h. The water uptake can be calculated as follows:

$$Water\ Uptake\ (\%) = \frac{(Wwet - Wdry)}{Wdry} \cdot 100 \qquad (1)$$

Where W_{wet} and W_{dry} are the mass of wet and dry membrane samples, respectively.

Optical Microscopy. The surface morphology of the membranes was studied by means of Keyence digital microscope VHX – 7000 series, with a 4K high-resolution digital camera.

6.3.Results and discussion

This work has been divided into two parts. The first part entails the preparation of the hybrid membranes using delignified and functionalized delignified wood discs as supports. The application of the reported methodology allowed the obtention of highly hydrophobic wood supports. Finally, DWD and FDWD membranes were assembled by the infiltration of PECH75 inside the pores of wood support in order to obtain hybrid membranes that could be promising candidates for ion transport applications. In this part of the research work, the characterization of these hybrid membranes in terms of orientation, wettability, and morphology was carried out. Furthermore, an exhaustive study of the ion transport properties of these wood-based membranes was also performed.

6.3.1. Structural and morphological characterization

The morphology of the non-thermally treated membranes (NO-DWD and NO-FDWD), the thermally treated ones (O-DWD and O-FDWD) and the wood discs that did not contain the polymer inside its pores (V-DWD and V-FDWD) have been analysed by optical microscopy. Images of the top side

view of the membranes are shown in **Figure 6.3.** Optical microscopy analysis revealed a change in the colour of thermally treated membranes in comparison with the non-thermally treated ones. Thermally treated membranes showed a brownish surface meanwhile the non-thermally treated membranes presented a lighter brown surface. The presence of some lines across the support surfaces was observed during this analysis. Besides, ESEM analysis revealed that these lines correspond to small cellulose fibres stacked perpendicular to the direction of the vast majority of cellulose fibres (highlighted areas in red from **Figure 6.S1**. The presence of large fibres stacks (> 100 μm), medium channel stacks (50 – 100 μm), and small channel stacks (<50 μm) has been observed.

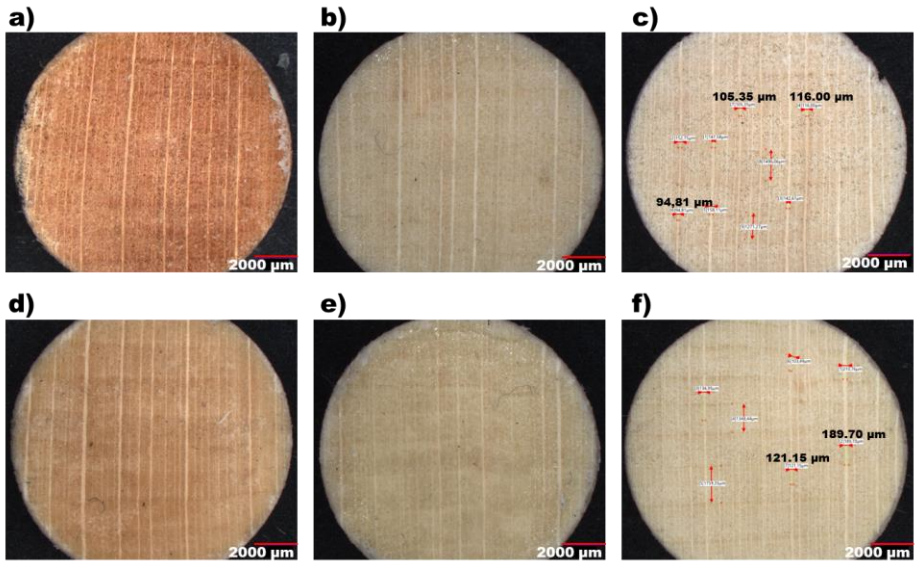

Figure 6.2. Microscopy images from the hybrid membranes; a) O-DWDM, b) NO-DWDM, d) O-FDWDM and e) NO-FDWDM, and the virgin supports, c) V-DWD and f) V-FDWD.

The surface morphology of the supports was analysed by optical microscopy obtaining 3D topographic pictures (**Figure 6.4**). In NO-DWD and O-DWD samples, we could observe the presence of unfilled channels on the membrane surface. Comparing the surface of DWD (**Figures 6.4a and b**) with the surface of FDWD (**Figures 6.4c and d**), we can observe some differences regarding their morphology. On the one hand, FDWD membranes present a more regular surface than DWD membranes, either thermally treated or not. This phenomenon was also observed in the bottom surface of both DWD and FDWD membranes.

The most irregular surface of DWD membranes could be explained by the lower affinity of PECH75 (hydrophobic polymer) with the internal composition of DWD membranes (hydrophilic character), meaning that fewer pores of the membrane had been filled [32]. In the case of FDWD membranes, many of these hydroxyl groups have been functionalized with lauroyl chloride, thus replacing them by long aliphatic chains. In this way, long aliphatic chains are able to interact by supramolecular forces with the side chains of the dendronized PECH75. Therefore, the polarity of the inner channels has been changed from hydrophilic to hydrophobic character.

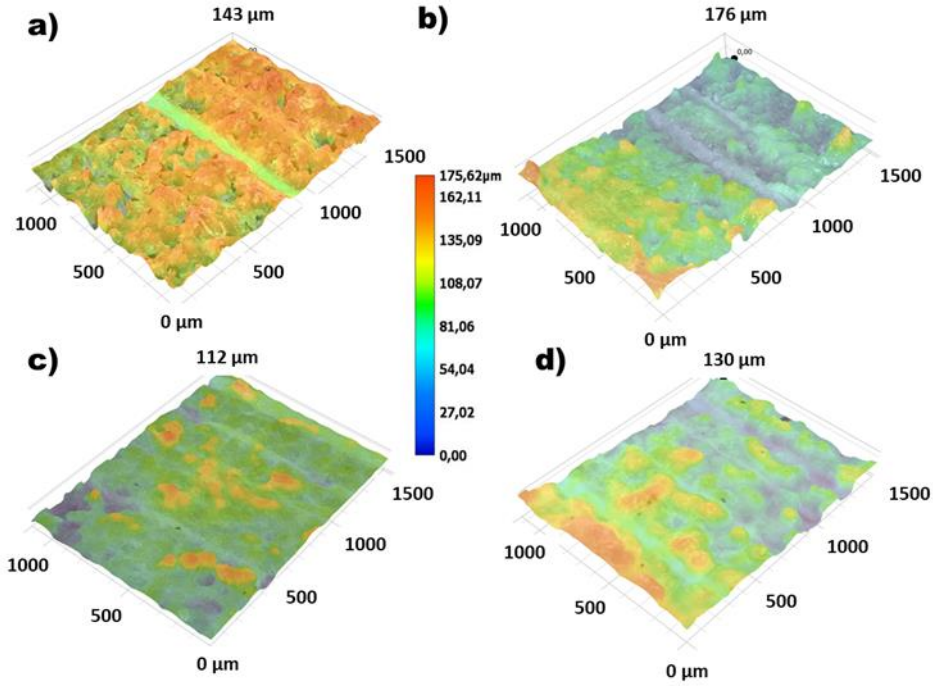

Figure 6.4. Topographic 3D images obtained by optical microscopy of: a) O-DWDM, b) NO-DWDM, c) O-FDWDM and d) NO-FDWDM.

After the application of the thermal treatment membranes were analysed by means of XRD in order to stablish the orientation of the polymer columns inside the pores of the support. Data obtained from XRD analysis and azimuthal analysis are shown in **Table 6.1**.

Table 6.1. XRD diffraction data of hybrid membranes (O-DWD, NO-DWD, O-FDWD and NO-FDWD) and data obtained from azimuthal scan at RT (24 ± 1 °C).

Membrane	Mesophase	2θ (°)	d_{100} (Å)	Angle of orientation (°)	Full Width at Half Maximum (FWHM) (°)
O-DWD	Col	42.5	2.1	93	49
NO-DWD	Col	42.5	2.1	-	-
O-FDWD	Col	42.4	2.1	90	59
NO-FDWD	Col	42.4	2.1	-	-

From XRD analysis we observed a peak centred at 2θ = 2.1° (d = 42.4 – 42.5 Å) which indicates that the side chain liquid crystalline polyether chains were organized in columnar mesophases (**Figure 6.5**). This peak has been related to the lattice plane indexed as (1 0 0). These results are in agreement with the mesophases exhibited by the liquid crystalline polymers previously synthetized by our research group [19,21,23–26,29–31,34–36]

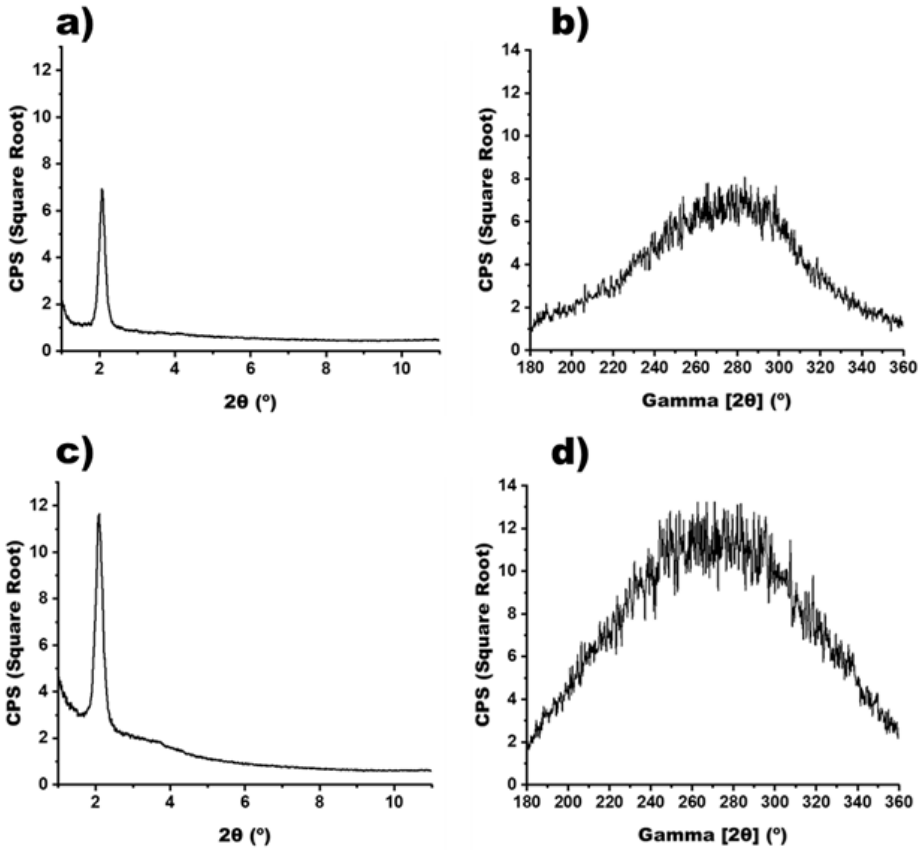

Figure 6.5. a) XRD diffractogram of the thermally treated: O-DWD and b) the azimuthal scan of O-DWD; c) XRD diffractogram of the thermally treated O-FDWD and d) the azimuthal scan of O-FDWD.

From azimuthal scan we could observe the trend of the polymer columns to achieve a homeotropical orientation **Figure 6.5**. Nevertheless, the observed peak was a broad peak. This shape can be attributable to two reasons: first the polymer columns tend to orient homeotropically although not all of them achieved this orientation. Secondly, the non-flat surface of these hybrid membranes observed in the topographic analysis affects the determination of the column orientation by XRD. These irregularities make that the exact determination of the column orientation by XRD were not completely possible.

Membrane wettability was studied by means of static contact angle (**Table 6.2**). In previous works, we could find a direct relationship between the CA values and the column orientation in the membranes [20,36]. Homeotropically orientation of polymer columns was evidenced by an increase in the hydrophobic character of the oriented membranes due to the presence of the hydrophobic moieties of the polymer stacked in the external part of the columns. For instance, Zare and co-workers observed an increased hydrophobicity on the air side of the membranes (top side) from 87 ± 2° before the application of the thermal treatment to 104.5 ± 0.9° after having applied the thermal treatment [20].

Table 6.2. Contact Angle data from the hybrid membranes DWDM and FDWDM samples, with and without thermal treatment.

Samples		Contact Angle (°)		Water Uptake (%) [a]
		Air Side	Bottom Side	
DWD	V-DWD	120 ±2	125 ± 1	120 ± 1
	O-DWD	135 ± 1	138 ± 1	96 ± 1
	NO-DWD	130 ± 1	114 ± 3	117 ± 1
FDWD	V-FDWD	134 ± 1	131 ± 2	68 ± 3
	O-FDWD	134 ± 1	135 ± 2	29 ± 1
	NO-DWD	129 ± 2	126 ± 1	39 ± 1

[a] Water uptake after 48h.

This behaviour was also observed in these hybrid membranes. Non-oriented membranes (NO-DWD and NO-FDWD) show lower CA values than oriented membranes (O-DWDM and O-FDWD), denoting an increasing of the CA values after the application of the thermal treatment. These data support the actual orientation of the polymer columns suggested by XRD.

Water uptake values are presented in **Table 6.2**. For all the membranes, the saturation point was reached after 24 h of immersion time. Water uptake tests evidenced the higher hydrophobic character of V-FDWD supports. Upon lignin removal, V-DWD supports exhibited a higher hydrophilicity due to the presence of a large number of hydroxyl groups from cellulose and hemicellulose in its scaffold, which resulted in the obtention of a water uptake of 120 %. On the other hand, V-FDWD supports showed lower water uptake (68 %) since the functionalization of the hydroxyl groups of cellulose and hemicellulose with lauroyl chloride produces an increase of the hydrophobic character of the support. Furthermore, a more significant reduction of the water uptake values was observed for NO-FDWD and O-FDWD filled with PECH75 compared to NO-DWD and O-DWD respect to the virgin discs. This trend revealed that the infiltration of the dendronized polyether inside the wood pores was more effective when wood discs were also functionalized.

6.3.2. Transport properties

The ionic conductivity of all hybrid membranes was studied by electrochemical impedance spectroscopy (EIS). As we could observe during

the CA experiments, all membrane surfaces present a hydrophobic character. Hence, EIS analysis in dry state were performed because the addition of water should not imply any changes in the conductivity values obtained from electrochemical impedance. To describe the polymer conductivity behaviour, we performed a simulation of the impedance data fitted to model electrical circuits (**Figure 6.S2**). Depending on the results obtained from the impedance data, a system can be simulated by different complex or simple equivalent circuits, which are labelled by using the "circuit description code" (CDC). [37] Using these equivalences, a circuit composed by a resistor (R) (**Figure 6.S2a**) and a capacitor (C) (**Figure 6.S2b**) can be combined to form different simple or complex circuits. For instance, if a capacitor and resistor are connected in series, it is expressed as RC (**Figure 6.S2c**), but if they are connected in parallel it is written enclosed in parentheses (RC) (**Figure 6.S2d**). Moreover, more complex circuits can be formed from all these combinations, for example, we can obtain a circuit where a resistor and a capacitor are connected in parallel, and connected to another resistor, this complex circuit is denoted as R(RC) (**Figure 6.S2e**).

EIS measurements were performed in-plane, thus locating the electrodes at the same surface of the membrane, and through-plane, where the electrodes were located on both sides of the membrane. In-plane experiments were carried out on both sides of the membrane. The results obtained from the experiments of the air side of the membranes are shown in **Figure 6.6**, meanwhile the results obtained from the bottom side of the membranes are shown in **Figure 6.S3**. As we could observe there is no significative difference when comparing both sides of the hybrid membranes. **Figure 6.7** shows the results obtained from the through-plane experiments. Data obtained from

these measurements did not denote any difference when comparing both in-plane and through-plane experiments.

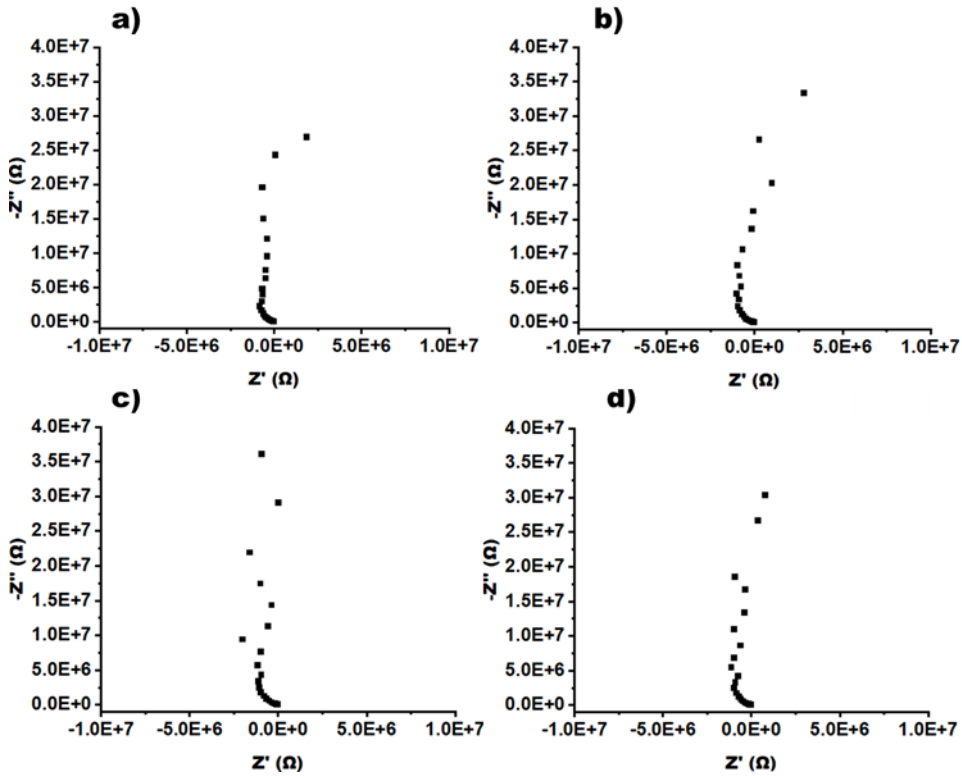

Figure 6.6. In-plane air side Nyquist plots of hybrid membranes. a) O-DWD, b) NO-DWD, c) O-FDWD and d) NO-FDWD.

According to the results obtained from the fitting data, impedance of hybrid membranes can be adjusted to two different circuits (RC and R(RC)) (see **Figure 6.S2c** and **S2e**). **Table 6.S1** shows the data obtained from in-plane EIS

experiments and **Table 6.S2** displays the results obtained from through-plane EIS measurements.

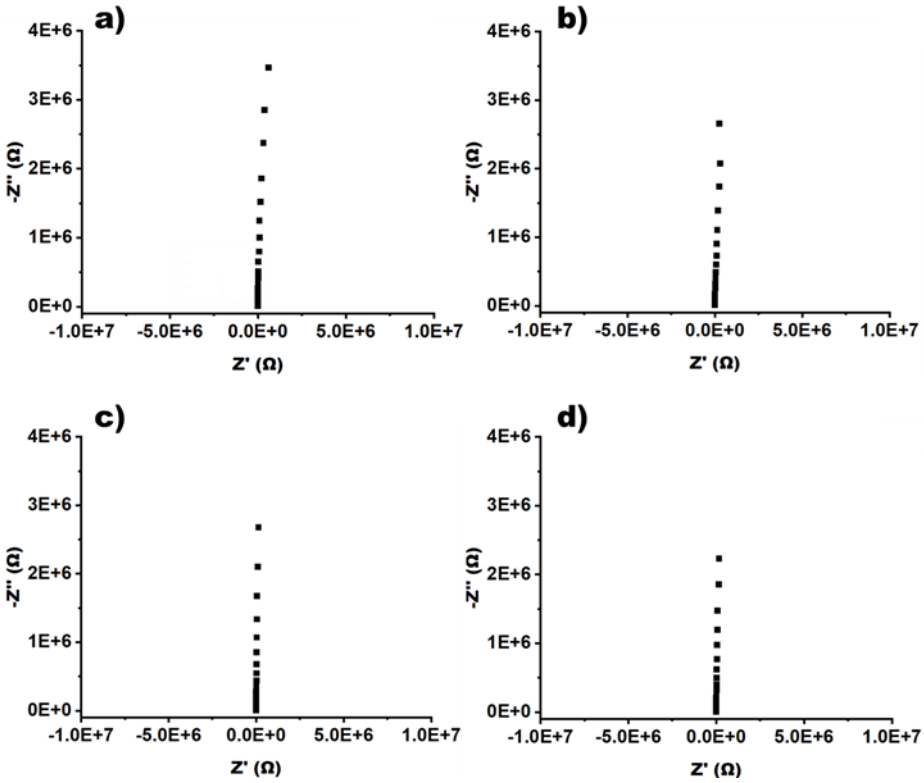

Figure 6.7. Through-plane impedance Nyquist plots of hybrid membranes: a) O-DWD, b) NO-DWD, c) O-FDWD and d) NO-FDWD.

Graphical representation of the obtained EIS, for both in-plane and through-plane experiments, suggests that these membranes can be correlated with both resistance-capacitance response. From the values presented in the tables, the capacitance detected in these experiments resulted to be almost negligible

(order of magnitude between 10^{-07} and 10^{-09}), meanwhile they presented high resistance values (order of magnitude equal to 10^{+11}).

On the other hand, the power of the Constant Phase Element (CPE, expressed as "n" in both tables) used to be between 0 (when the system acts as a perfect resistor) and 1 (when it works as a perfect capacitor). For these hybrid membranes, CPE presented "n" values higher than 1 in almost all cases, which prevented us from accurately determining the real behaviour of these membranes, whether capacitor or resistor. Therefore, the data obtained from the fitting models suggest that these hybrid membranes behave as insulating materials from an electronic point of view.

The insulating behaviour of these hybrid membranes can be reasonably explained by the internal structure they have. As aforementioned, the polymer columns formed inside these membranes contain an inner channel formed by basic heteroatoms (oxygen), which should be the responsible of the transport across them. The non-ionic nature of the polyepichlorohydrin main chain results in a significantly high resistance values observed in the impedance analysis. In membranes that present another structure, such as Nafion®, the presence of ionic sulfonic groups in their internal structure are responsible for the ionic conductivity observed in Alternate Current (AC), due to their easy polarizability [38–41] As a consequence, the conductivity properties cannot be directly established from the resistance values obtained from EIS. Therefore, it could be stated that EIS was not the best technique to determine the ionic conductivity of this group of membranes.

For this reason, we have explored the use of other techniques as alternatives to EIS such as linear sweep voltammetry (LSV) and permeability tests. Using

these last two techniques, cations can be transported across the polymeric channels thanks to an external stimulus such as concentration gradient or by difference of potentials.

Linear sweep voltammetry was used to study the cation transport across the membrane by current-voltage measurements. The set-up used to carry out these experiments is described in **Figure 6.2**. In a typical current-voltage (C–V) curve, one can distinguish three main regions : region I or also called ohmic region, where the observed current after applying a potential is governed by the Ohm's law and exhibits a linear trend. As the current density increases, a plateau or semi-plateau region is observed in the C–V curves (region II). This second region corresponds to the limiting current density region, which is related with the cation permselectivity of the membrane. The limiting current density (I_{lim}) is the necessary current to transfer all the available cations across the membrane. Finally, an overlimiting region where an increase of the current is observed can be explained by the electroconvection theory or water's dissociation [42–44]

In this study, we evaluated the conductivity of the oriented and non-oriented hybrid membranes. **Figure 6.8** shows the current-voltage curves of O-FDWD and NO-FDWD using HCl 0.1 M. In the current-voltage curve of the membrane O-FDWD, the three characteristic regions: ohmic, limiting current and overlimiting can be observed (**Figure 6.8a**). On the other hand, NO-FDWD only presents the ohmic and the overlimiting regions (**Figure 6.8b**).

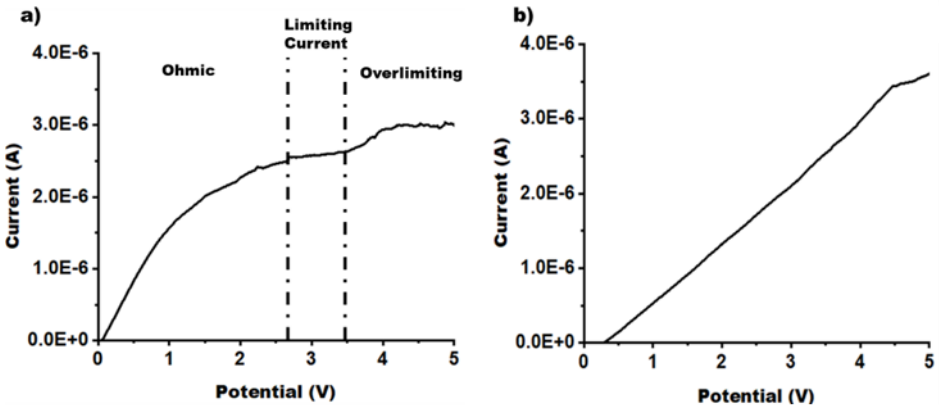

Figure 6.8. C–V curves of the hybrid membranes. a) O-FDWDM and b) NO-FDWDM

Apart from evaluating the proton conductivity, we also studied the conductivity of other monovalent cations, such as alkaline cations Na^+, K^+ and Li^+. The proton conductivities as well as the conductivities associated to the other tested alkaline cations are shown in **Table 6.3**. As commented before, the current-voltage curve of NO-FDWD did not show the limiting current region and therefore it was only possible to determine the ohmic resistance density (R_{ohm}), which was 0.25 x 10^7 $\Omega \cdot cm^{-2}$. On the other hand, the current-voltage curve of O-FDWD showed the three main regions and in this case the limiting current density (I_{lim} = 4.35 x 10^{-6} $A \cdot cm^{-2}$) and the ohmic resistance density (R_{ohm} = 0.11 $\Omega \cdot cm^{-2}$) could be calculated. It can be noted that ohmic resistance density values of the non-oriented membranes are approximately double that of oriented hybrid membranes. The difference between both types of membranes can be associated to the orientation of dendronized PECH75 columns. Comparing the non-oriented membranes with each other, NO-

FDWD showed higher ohmic resistance density since the conductive paths in this membrane do not exhibit a homeotropic alignment.

Table 6.3. Ohmic resistance densities obtained from C – V curves of the FDWD membranes.

Sample	R_{ohm} x 10^7 ($\Omega \cdot cm^{-2}$)			
	HCl	**LiCl**	**NaCl**	**KCl**
Nafion®117	0.003*	0.006*	0.019*	0.012*
O-FDWDM	0.110	5.430	2.520	16.430
NO-FDWDM	0.250	2.100	7.010	6.270

[a] Ohmic resistance of Nafion®117 expressed in R_{ohm} x 10^3 $\Omega \cdot cm^{-2}$. These data were reported by Bogdanowic *et al.* [45].

To express the membrane selectivity of proton over other monovalent cations, a conductance ratio (reverse resistance) is expressed as the G_{ion}/G_{H+} ratio for each hybrid membrane. Selectivity results are shown in **Table 6.4**. As can be observed in the table, oriented membranes present a higher proton selectivity for lithium and potassium cations, meanwhile sodium's selectivity seems to be similar in both membranes, whether oriented or not. Although the small difference between ohmic resistance densities (R_{ohm}) of both hybrid membranes, oriented membranes present a higher selectivity. Furthermore, the potassium selectivity rates of these membranes are up to two orders of magnitude lower than those rates observed for Nafion®, meanwhile the other cation selectivity rates are up to one order of magnitude higher, as can be seen in **Table 6.4**.

Table 6.4. Selectivity (G_{ion}/G_{H+} ratio) values for alkaline monovalent cations.

Sample	G_{ion}/G_{H+} x 100 (%)		
	Li^+	Na^+	K^+
Nafion®117	47.3*	14.2*	22.8*
O-FDWDM	2.1	4.5	0.7
NO-FDWDM	11.6	3.5	3.9

[a] Cation selectivity data of Nafion®117 was reported by Bogdanowic *et al.* [45].

The improvements of these selectivity ratios are similar to the ones observed in previous studies reported by Bogdanowicz and co-workers, in which they investigated the proton conductivity of a liquid crystalline poly[2-(aziridine-1-yl)ethanol] (PAZE) modified with the same dendron [45] However, another side chain liquid crystalline polyether copolymer (poly(epichlorohydrin-*co*-ethylene oxide) synthesized by Zare and co-workers showed a lower selectivity with respect to those obtained with our systems [20] Conductivity measurements with DWD were unsuccessful since when filling the compartments of the LSV set-up with the solution under study we could observe that this membrane was leaking. These group of membranes, presented unfilled or partially filled cellulose (and hemicellulose) pores as we could see during ESEM analysis, which can explain the free cationic transport across DWD-based membranes detected during the performance of LSV experiments.

We also studied the effect of membrane conditioning. With this purpose, we immersed the hybrid membranes in the solution under study for 30 min prior to LSV analysis. Afterwards, we evaluated the membrane conductivity as we

did before. In these experiments, there was no evidence of the three regions on a typical C–V curve and a straight line was observed. Ohmic resistance density values of these experiments are shown in **Table 6.5**.

Table 6.5. Ohmic resistance densities obtained from C – V curves of the FDWD membranes after conditioning them.

Sample	R_{ohm} x 10^7 Ω · cm^{-2}			
	HCl	**LiCl**	**NaCl**	**KCl**
Nafion®117	0.003*	0.006*	0.019*	0.012*
O-FDWDMA	0.014	0.032	0.42	0.25
NO-FDWDMA	0.53	0.48	1.32	0.030

[a] Ohmic resistance of Nafion®177 expressed in R_{ohm} x 10^3 Ω · cm^{-2}. These data were reported by Bogdanowic *et al.* [45].

After membrane conditioning, it can be noted that the resistance densities obtained are lower than the resistance density obtained without conditioning for all tested cations. Regarding the oriented membranes, we could observe an increase of the ohmic resistance densities when increasing the ionic radius of the cations except potassium. On the other hand, non-oriented membranes do not seem to follow the same tendency observed in the case of oriented membranes. The first notable difference is that the transport of K^+ seems to be favoured over the rest of the evaluated cations. A possible explanation of this behaviour could be the relatively elevated water uptake value (39 %) of NO-FDWD membranes. The polymeric chains inside the wood pores could be rearranged during membrane conditioning in such a way that the conducting

paths of NO-FDWD membranes presented a straightforward path for large cations like potassium, and a winding path for smaller cations (H^+, Li^+ and Na^+). As a result, higher resistance density values were detected when smaller cations were tested.

Permeability tests were carried out with O-FDWD and NO-FDWD membranes using aqueous solutions of different monovalent salts (NaCl, LiCl and KCl) as stripping solution. In all the cases, we did not observe any change in the pH of the stripping solution even after 4 days. These results differ from the ones reported by Zare and co-workers, who studied the antiport transport mechanism of membranes based on dendronized poly(epichlorohydrin-*co*-ethylene oxide) (PECH-co-EO) [20,25]. Despite the similarities between the main chain of PECH75 and dendronized PECH-co-EO, it seems that the high modification degree with the side chain dendron of PECH75 could restrict the simultaneously passage of the different cations in both directions. [20,25]

6.4.Conclusions

Ion conductive novel hybrid membranes based on liquid crystalline modified poly(epicholorhydrin) supported on chemically modified wood discs have been successfully characterized in terms of surface morphology and wettability.

Optical microscopy supported the ESEM findings reported in Part 1, where unfilled pores were observed for DWD membranes. The irregularities presented at the surface in both DWD and FDWD membranes avoid the exact

determination of the columnar orientation. However, the increase of the CA values after thermal treatment supports the orientation denoted during the XRD analysis. In this sense NO-DWD membranes reported a contact angle value of 114 ± 3°, while O-DWD membranes exhibited a contact angle value of 138 ± 1° for the same side of the membrane. Membrane wettability revealed a greater water uptake (from 96 to 120 %) for DWD membranes and supports, meanwhile FDWD membranes evidenced lower uptake values between 30 and 40 %. These results agreed with our hypothesis formulated for the preparation of these hybrid membranes.

Further transport studies were carried out through electrochemical impedance spectroscopy, permeability tests and linear sweep voltammetry. According to electrochemical impedance spectroscopy, hybrid membranes behave as electrical insulators. A reasonable explanation to these observations lies in the non-ionic nature of the membranes which makes impossible the obtention of conductivity values under AC. Permeability tests were carried out as alternative to EIS for the determination of the transport properties. Nevertheless, we did not observe a change in the pH in the stripping solution even after 4 days of experimentation.

Current-voltage curves of the FDWD membranes revealed two behaviours depending on the orientation of the membrane when evaluating the proton transport. The limiting current region was observed for the O-FDWD membrane, meanwhile it was not denoted for the NO-FDWD membrane. Thus, indicating proton permselectivity. FDWD hybrid membranes showed an excellent selectivity of the proton in front of the other monovalent cations. This selectivity values (expressed as the percentage ratio of reverse conductance) are up to two orders of magnitude better than those expressed

by Nafion®117. These results indicate the potential use of this modified wood support as suitable support for the preparation of ion conductive membranes.

6.5.References

[1] J. Lombard, Once upon a time the cell membranes: 175 years of cell boundary research, Biol Direct 9 (2014). https://doi.org/10.1186/s13062-014-0032-7.

[2] I. Pinnau, B.D. Freeman, Formation and Modification of Polymeric Membranes: Overview, in: 1999: pp. 1–22. https://doi.org/10.1021/bk-2000-0744.ch001.

[3] A. Naeem, B. Saeed, H. AlMohamadi, M. Lee, M.A. Gilani, R. Nawaz, A.L. Khan, M. Yasin, Sustainable and green membranes for chemical separations: A review, Sep Purif Technol 336 (2024). https://doi.org/10.1016/j.seppur.2024.126271.

[4] Y. Wen, J. Wang, F. Wang, H. Wu, J. Zhou, Z. Dai, H. Guo, Recent advances in membranes modified with plant polyphenols in wastewater treatment: A review, Sep Purif Technol 334 (2024). https://doi.org/10.1016/j.seppur.2023.125861.

[5] W. Yu, L. Xiong, J. Teng, C. Chen, B. Li, L. Zhao, H. Lin, L. Shen, Advances in synthesis and application of amphoteric polymer-based water treatment agents, Desalination 574 (2024). https://doi.org/10.1016/j.desal.2023.117280.

[6] M. Zubair, M. Yasir, D. Ponnamma, H. Mazhar, V. Sedlarik, A.H. Hawari, M.A. Al-Harthi, M. Al-Ejji, Recent advances in nanocellulose-based two-dimensional nanostructured membranes for sustainable water purification: A review, Carbohydr Polym 329 (2024). https://doi.org/10.1016/j.carbpol.2024.121775.

[7] S. Karki, G. Hazarika, D. Yadav, P.G. Ingole, Polymeric membranes for industrial applications: Recent progress, challenges and perspectives, Desalination 573 (2024). https://doi.org/10.1016/j.desal.2023.117200.

[8] Y. Sun, J. Wu, X. Zhu, Poly(ionic liquids) membranes preparation and its application, J Mol Struct 1304 (2024). https://doi.org/10.1016/j.molstruc.2024.137683.

[9] Z. Dai, L. Deng, Membranes for CO2 capture and separation: Progress in research and development for industrial applications, Sep Purif Technol (2023) 126022. https://doi.org/10.1016/j.seppur.2023.126022.

[10] Y. Deng, A. Hussain, W. Raza, X. Cai, D. Liu, J. Shen, Review on current development of polybenzimidazole membrane for lithium battery, Journal of Energy Chemistry 91 (2024) 579–608. https://doi.org/10.1016/j.jechem.2023.12.044.

[11] J. Kang, N. Deng, B. Cheng, W. Kang, Progress in the application of polymer fibers in solid electrolytes for lithium metal batteries, Journal of Energy Chemistry 92 (2024) 26–42. https://doi.org/10.1016/j.jechem.2023.12.035.

[12] A. Mishra, H. Park, F. El-Mellouhi, D. Suk Han, Seawater electrolysis for hydrogen production: Technological advancements and future perspectives, Fuel 361 (2024) 130636. https://doi.org/10.1016/j.fuel.2023.130636.

[13] X. Wei, V.S. Reddy, S. Gao, X. Zhai, Z. Li, J. Shi, L. Niu, D. Zhang, S. Ramakrishna, X. Zou, Recent advances in electrochemical cell-based biosensors for food analysis: Strategies for sensor construction, Biosens Bioelectron 248 (2024). https://doi.org/10.1016/j.bios.2023.115947.

[14] M. Borràs-Brull, P. Blondeau, J. Riu, Characterization and Validation of a Platinum Paper-based Potentiometric Sensor for Glucose Detection in Saliva, Electroanalysis 33 (2021) 181–187. https://doi.org/10.1002/elan.202060221.

[15] R. Cánovas, M. Parrilla, P. Blondeau, F.J. Andrade, A novel wireless paper-based potentiometric platform for monitoring glucose in blood, Lab Chip 17 (2017) 2500–2507. https://doi.org/10.1039/c7lc00339k.

[16] E.Y. Safronova, A.A. Lysova, D.Y. Voropaeva, A.B. Yaroslavtsev, Approaches to the Modification of Perfluorosulfonic Acid Membranes, Membranes (Basel) 13 (2023). https://doi.org/10.3390/membranes13080721.

[17] K.-D. Kreuer, A. Rabenau, W. Weppner, Vehicle Mechanim, A New Model for the Interpretation of the Conductivity of Fas Proton Conductors, 1982.

[18] C. Yang, P. Costamagna, S. Srinivasan, J. Benziger, A.B. Bocarsly, Approaches and technical challenges to high temperature operation of proton exchange membrane fuel cells, n.d.

[19] A. Šakalyte, J.A. Reina, M. Giamberini, Liquid crystalline polyamines containing side dendrons: Toward the building of ion channels based on polyamines, Polymer (Guildf) 54 (2013) 5133–5140. https://doi.org/10.1016/j.polymer.2013.07.027.

[20] A. Zare, X. Montané, J.A. Reina, M. Giamberini, Membranes for cation transport based on dendronized poly(Epichlorohydrin-co-ethylene oxide). part 2: Membrane characterization and transport properties, Polymers (Basel) 13 (2021). https://doi.org/10.3390/polym13223915.

[21] J. Guardià, M. Giamberini, J.A. Reina, X. Montané, Synthesis and Characterization of Dendronized Side Chain Liquid Crystalline Poly(2-oxazoline)s towards Biomimetic Ion Channels, Eur Polym J (2023) 112273. https://doi.org/10.1016/j.eurpolymj.2023.112273.

[22] X. Montané, S.V. Bhosale, J.A. Reina, M. Giamberini, Columnar liquid crystalline polyglycidol derivatives: A novel alternative for proton-conducting membranes, Polymer (Guildf) 66 (2015) 100–109. https://doi.org/10.1016/j.polymer.2015.03.071.

[23] K.A. Bogdanowicz, G.A. Rapsilber, J.A. Reina, M. Giamberini, Liquid crystalline polymeric wires for selective proton transport, part 1: Wires preparation, Polymer (Guildf) 92 (2016) 50–57. https://doi.org/10.1016/j.polymer.2016.03.073.

[24] S.V. Bhosale, M.A. Rasool, J.A. Reina, M. Giamberini, New liquid crystalline columnar poly(epichlorohydrin-co-ethylene oxide) derivatives leading to biomimetic ion channels, Polym Eng Sci 53 (2013) 159–167. https://doi.org/10.1002/pen.23240.

[25] K.A. Bogdanowicz, S. V. Bhosale, Y. Li, I.F.J. Vankelecom, R. Garcia-Valls, J.A. Reina, M. Giamberini, Mimicking nature: Biomimetic ionic channels, J Memb Sci 509 (2016) 10–18. https://doi.org/10.1016/j.memsci.2016.02.038.

[26] X. Montané, K.A. Bogdanowicz, G. Colace, J.A. Reina, P. Cerruti, A. Lederer, M. Giamberini, Advances in the design of self-supported ion-conducting membranes-new family of columnar liquid crystalline polyamines. Part 1: Copolymer synthesis and membrane preparation,

Polymer (Guildf) 105 (2016) 298–309. https://doi.org/10.1016/j.polymer.2016.10.047.

[27] V. Percec, M. Glodde, T.K. Bera, Y. Miura, I. Shiyanovskaya, K.D. Singer, V.S.K. Balagurusamy, P.A. Heiney, I. Schnell, A. Rapp, H.W. Spiess, S.D. Hudsonk, H. Duan, Self-organization of supramolecular helical dendrimers into complex electronic materials, Nature 417 (2002) 384–387. https://doi.org/10.1038/nature01072.

[28] M. Peterca, D. Sahoo, M.R. Imam, Q. Xiao, V. Percec, Searching for the simplest self-assembling dendron to study helical self-organization and supramolecular polymerization, Giant 12 (2022). https://doi.org/10.1016/j.giant.2022.100118.

[29] B. Tylkowski, N. Castelao, M. Giamberini, R. Garcia-Valls, J.A. Reina, T. Gumí, The importance of orientation in proton transport of a polymer film based on an oriented self-organized columnar liquid-crystalline polyether, Materials Science and Engineering C 32 (2012) 105–111. https://doi.org/10.1016/j.msec.2011.10.003.

[30] M. Giamberini, J.C. Ronda, J.A. Reina, Poly(epichlorohydrin) modified with 3,4,5-tris(dodecyloxy)benzoate: The structure and dynamics of the aliphatic side chains in the columnar mesophase, J Polym Sci A Polym Chem 43 (2005) 2099–2111. https://doi.org/10.1002/pola.20680.

[31] A. Zare, B. Pascual-Jose, S. De la Flor, A. Ribes-Greus, X. Montané, J.A. Reina, M. Giamberini, Membranes for cation transport based on dendronized poly(Epichlorohydrin-co-ethylene oxide). part 1: The effect of dendron amount and column orientation on copolymer mobility, Polymers (Basel) 13 (2021). https://doi.org/10.3390/polym13203532.

[32] J. Guardià, M.H. Wolf, S. De la Flor, M. Giamberini, J.A. Reina, A. Ribes-Greus, S. Bidale, A. Mariani, X. Montané, Development of wood-based membraens for ion transport applications. Part 1: Support preparation and membrane assembly, In Preparation.

[33] W.L.F. Armarego, C.L.Lin. Chai, Purification of laboratory chemicals, Elsevier/BH, 2009.

[34] A. Šakalyte, M. Giamberini, J.A. Reina, Synthesis and characterisation of a monotropic dendritic liquid crystalline aziridine monomer, Liq Cryst 41 (2014) 153–162. https://doi.org/10.1080/02678292.2013.845309.

[35] J. Guardià, A. Zare, J. Eleeza, M. Giamberini, J.A. Reina, X. Montané, Synthesis and characterization of dendritic compounds containing nitrogen: monomer precursors in the construction of biomimetic membranes, Sci Rep 12 (2022). https://doi.org/10.1038/s41598-022-05747-1.

[36] X. Montané, S.V. Bhosale, J.A. Reina, M. Giamberini, Columnar liquid crystalline polyglycidol derivatives: A novel alternative for proton-conducting membranes, Polymer (Guildf) 66 (2015) 100–109. https://doi.org/10.1016/j.polymer.2015.03.071.

[37] A.C. Lazanas, M.I. Prodromidis, Electrochemical Impedance Spectroscopy—A Tutorial, ACS Measurement Science Au 3 (2023) 162–193. https://doi.org/10.1021/acsmeasuresciau.2c00070.

[38] J.H. Lim, J. Hou, W.Y. Kim, S. Wi, C.H. Lee, The relationship between chemical structure of perfluorinated sulfonic acid ionomers and their membrane properties for PEMEC application, Int J Hydrogen Energy 49 (2024) 794–804. https://doi.org/10.1016/j.ijhydene.2023.09.131.

[39] M. Díaz, A. Ortiz, I. Ortiz, Progress in the use of ionic liquids as electrolyte membranes in fuel cells, J Memb Sci 469 (2014) 379–396. https://doi.org/10.1016/j.memsci.2014.06.033.

[40] S. Tan, Y. Wu, T. Liang, X. Yang, Kinetic modeling of anhydrous proton conduction in side chain liquid crystal polyacrylates, Int J Hydrogen Energy 39 (2014) 17391–17397. https://doi.org/10.1016/j.ijhydene.2014.08.043.

[41] M. Shabani, M.H. Entezari, Designing continuous proton-conductive channels for direct methanol fuel cell through the sulfonated poly(ether ether ketone)/carbon quantum dot/graphitic carbon nitride nanosheet, Eur Polym J 202 (2024). https://doi.org/10.1016/j.eurpolymj.2023.112641.

[42] G. Chamoulaud, D. Bélanger, Modification of ion-exchange membrane used for separation of protons and metallic cations and characterization of the membrane by current-voltage curves, J Colloid Interface Sci 281 (2005) 179–187. https://doi.org/10.1016/j.jcis.2004.08.081.

[43] J.H. Choi, H.J. Lee, S.H. Moon, Effects of electrolytes on the transport phenomena in a cation-exchange membrane, J Colloid Interface Sci 238 (2001) 188–195. https://doi.org/10.1006/jcis.2001.7510.

[44] J.H. Choi, J.S. Park, S.H. Moon, Direct measurement of concentration distribution within the boundary layer of an ion-exchange membrane, J Colloid Interface Sci 251 (2002) 311–317. https://doi.org/10.1006/jcis.2002.8407.

[45] K.A. Bogdanowicz, P. Sistat, J.A. Reina, M. Giamberini, Liquid crystalline polymeric wires for selective proton transport, part 2: Ion transport in solid-state, Polymer (Guildf) 92 (2016) 58–65. https://doi.org/10.1016/j.polymer.2016.03.080.

6.6.Supporting Information

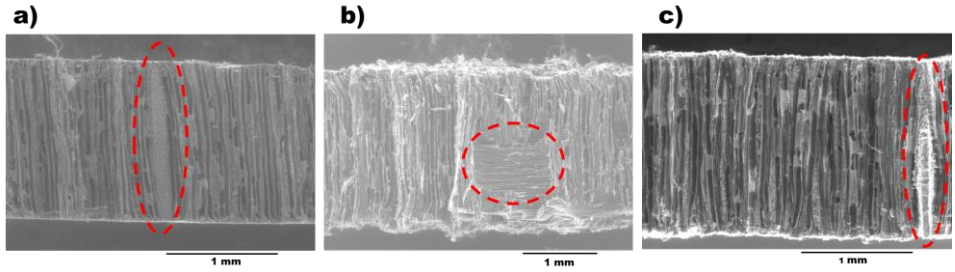

Figure 6.S1. ESEM cross-section images of: a) Non-treated beech wood (NTW), b) DWD and c) FDWD.

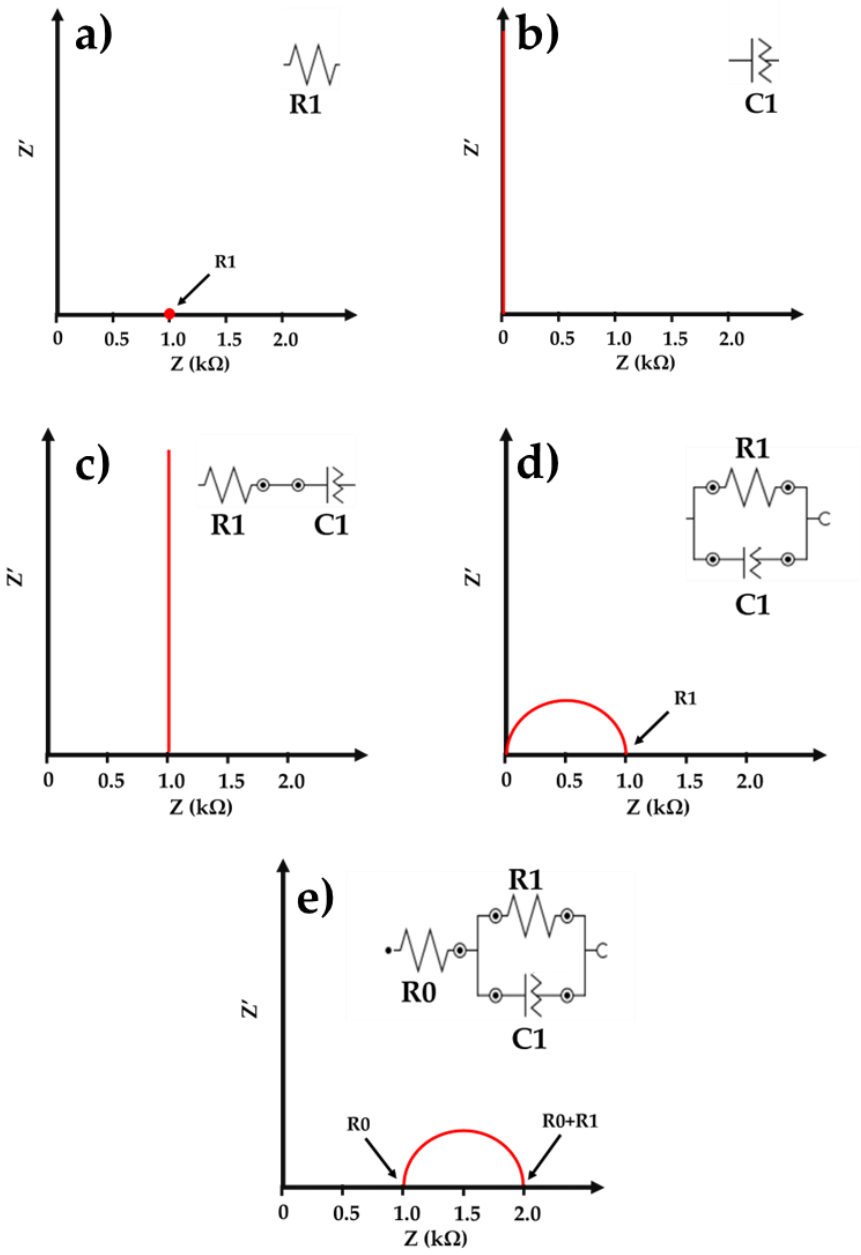

Figure 6.S2. Nyquist plots of exemplary model circuits. R0 = R1 = 1kΩ

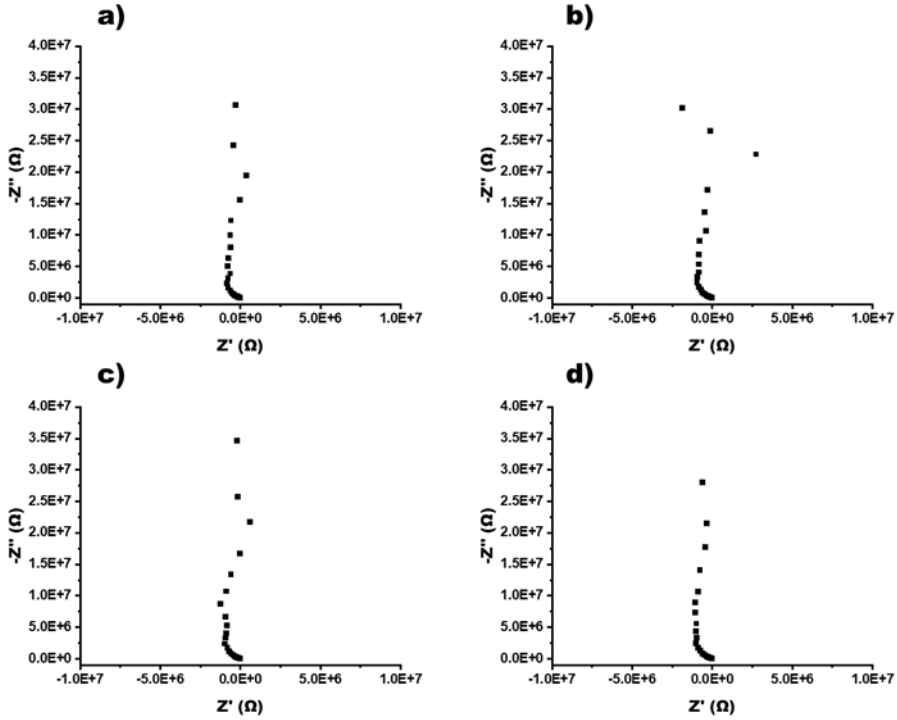

Figure 6.S3. In-plane bottom side Nyquist plots of: hybrid membranes. a) O-DWD, b) NO-DWD, c) O-FDWD and d) NO-FDWD.

Table 6.S1. Fitting data from, both air side and bottom side, in-plane EIS of hybrid PECH75 membranes.

O-DWDM Air side				**O-DWDM Bottom side**			
Element	**Parameter**	**Value**	**Error (%) ***	**Element**	**Parameter**	**Value**	**Error (%) ***
Rs	R	-1358.7	-557.2	R1	R	-1509.6	-499.6
Rp	R	6.75E+11	385.5	Q1	Y0	1.39E-08	136.3
CPE	Y0	1.34E-09	128.0				
	N	1.1	7.9		N	1.1	8.4
	χ^2	94.433			χ^2	97.591	
NO-DWDM Air side				**NO-DWDM Bottom side**			
Element	**Parameter**	**Value**	**Error (%) ***	**Element**	**Parameter**	**Value**	**Error (%) ***
Rs	R	-1265.2	-641.7	Rs	R	-528.22	-573.1
Rp	R	6.47E+11	397.1	Rp	R	6.17E+11	461.2
CPE	Y0	1.26E-08	137.2	CPE	Y0	8.73E-09	139.7
	N	1.1	8.4		N	1.1	8.6
	χ^2	10.258			χ^2	15.503	
O-FDWDM Air side				**O-FDWDM Bottom side**			
Element	**Parameter**	**Value**	**Error (%) ***	**Element**	**Parameter**	**Value**	**Error (%) ***
R1	R	-1763.3	-473.8	R1	R	-1612.9	-493.6
Q1	Y0	1.37E-08	158.9	Q1	Y0	1.37E-08	146.8
	N	1.1	9.7		N	1.1	9.0
	χ^2	10.818			χ^2	10.216	
NO-FDWDM Air side				**NO-FDWDM Air side**			
Element	**Parameter**	**Value**	**Error (%) ***	**Element**	**Parameter**	**Value**	**Error (%) ***
R1	R	-1613.9	-488.6	R1	R	-1472.9	-563.4
Q1	Y0	1.38E-08	143.9	Q1	Y0	1.27E-08	145.6
	N	1.1	8.8		N	1.1	8.9
	χ^2	10.194			χ^2	10.724	

*Estimated Error.

Table 6.S2. Fitting data from through-plane EIS of hybrid PECH75 membranes.

O-DWDM				**NO-DWDM**			
Element	**Parameter**	**Value**	**Error (%) ***	**Element**	**Parameter**	**Value**	**Error (%) ***
Rs	R	-321.21	-282.9	R1	R	-819.82	-101.9
Rp	R	1.15E+11	28.4	Q1	Y0	1.90E-07	19.8
CPE	Y0	7.76E-08	20.1				
	N	10.486	1.5		N	0.99664	1.5
	χ^2	0.6219			χ^2	0.6715	
O-FDWDM				**NO-FDWDM**			
Element	**Parameter**	**Value**	**Error (%) ***	**Element**	**Parameter**	**Value**	**Error (%) ***
R1	R	-215.49	-230.9	Rs	R	-244.11	-187.2
Q1	Y0	1.42E-07	13.9	Rp	R	1.46E+11	40.8
				CPE	Y0	1.69E-07	13.9
	N	10.289	1.0		N	1.021	1.1
	χ^2	0.33295			χ^2	0.28425	

*Estimated Error.

UNIVERSITAT ROVIRA I VIRGILI
COLUMNAR LIQUID-CRYSTALLINE POLYMERS CONTAINING NITROGEN AT THE BACKBONE TO BE USED TO PREPARE ION-TRANSPORT MEMBRANES
Jordi Guardià Blanch

Chapter 7

General Conclusions

UNIVERSITAT ROVIRA I VIRGILI
COLUMNAR LIQUID-CRYSTALLINE POLYMERS CONTAINING NITROGEN AT THE BACKBONE TO BE USED TO PREPARE ION-TRANSPORT MEMBRANES
Jordi Guardià Blanch

Conclusions

The main conclusions of this work are extracted from the different sections according to the specific objectives reported in Chapter 1.

1) The synthesis of the monomer TAPOx was successfully performed in two steps: the obtention of the intermediate TAPAm, followed by its dehydrative cyclisation, achieving high yields (92 and 85 %, respectively). An enantiotropic behaviour was observed for TAPAm according to DSC and X-ray analysis. Meanwhile, TAPOx did not present a liquid crystal behaviour.

2) Polymerization of TAPOx was successfully carried out by *living* cationic ring opening polymerization (CROP),thus preparing a family of poly(2-oxazoline)s with molecular weights up to 60 KDa. The poly(2-oxazolines)s prepared presented columnar mesophases in a broad range of temperatures. In particular, PTOx40, denoted the formation of a hexagonal columnar mesophase.

3) The formation of self-sustained membranes based on PTOx40 was not possible due to membrane brittleness. A polyester fabric was used as a support to improve the mechanical properties. The presence of bubbles with different size was observed for some membranes due to possible interactions between the wet membrane and the antisolvent. Nonetheless, they were present in the space between the polyester fabric and the substrate.

4) As expected, EIS analysis reported an insulating behaviour of the membranes, since they present weakly polarizable groups. LSV results of the homeotropically oriented hybrid membranes showed an outstanding proton selectivity, probably due to the low adaptability of the homopolymer chain to bigger cations, while presenting low conductivities.

5) The obtention of biobased wood supports was achieved by a two-step process using beech wood bars. Both delignification and functionalization processes did not alter the wood pore structure as was evidenced by ESEM analysis. During the preparation of the hybrid membranes, it was observed that a thermal treatment helps with the distribution of PECH75, thus making the contact angle on both sides of the membrane similar to each other.

6) ESEM analysis reported the presence of holes on both sides of the DWD hybrid membrane, thus suggesting our initial hypothesis. Homeotropical orientation of the polymer columns was poorly observed by XRD, due to membrane's irregular surface, but later corroborated by the increased contact angle after thermal process.

7) As expected, the presence of holes on DWD hybrid membranes caused membrane leaking, avoiding its transport study. Due to orientation, FDWD oriented membranes reported membrane permselectivity since the limiting current region was observed, according to LSV. Both oriented and non-oriented membranes

presented excellent proton selectivity compared to commercial Nafion®N117.

UNIVERSITAT ROVIRA I VIRGILI
COLUMNAR LIQUID-CRYSTALLINE POLYMERS CONTAINING NITROGEN AT THE BACKBONE TO BE USED TO PREPARE ION-TRANSPORT MEMBRANES
Jordi Guardià Blanch

Appendices

UNIVERSITAT ROVIRA I VIRGILI
COLUMNAR LIQUID-CRYSTALLINE POLYMERS CONTAINING NITROGEN AT THE BACKBONE TO BE USED TO PREPARE ION-TRANSPORT MEMBRANES
Jordi Guardià Blanch

List of figures

Chapter 1

Figure 1.1. General classification of liquid crystals and liquid crystal polymers 8

Figure 1.2. General template for thermotropic liquid crystals based on their shape 12

Figure 1.3. Example of self-assembly and self-organization of discotic liquid crystal molecules in columnar mesophases 17

Figure 1.4. Schematic illustration of a) MCLCPs, b) SCLCPs and, c) MCSCLCPs. From the side-chain LCPs, b1) SCLCPs with longitudinally attached rod-like mesogen and b2) SCLCPs with laterally attached rod-like mesogen. The blue cylinder is a mesogenic representative unit 23

Figure 1.5. Schematic representation of a liquid crystal network 24

Figure 1.6. General structure of the tobacco mosaic virus 28

Figure 1.7. Chemical structure of SCLCPs modified with the dendron 3,4,5-tris[4-(n-dodecan-1-yloxy)benzyloxy]benzoate. According to the backbone: a) PECH, b) PECH-co-EO and c) PAZE 35

Figure 1.8. Experimental set-up of a) permeability tests and b) linear sweep voltammetry 36

Chapter 2

Figure 2.1. Chemical structure of: Methyl 3,4,5-tris[*p*-(n-dodecan-1-yloxy) benzyloxy] benzoate (TAPEs) and 3,4,5-tris[*p*-(n-dodecan-1-yloxy) benzyloxy] benzoic acid (TAPAc) 72

Figure 2.2. Synthesis of *N*-(2-hydroxyethyl)-3,4,5–tris(4-dodecyloxy benzyloxy)benzamide (TAPAm) 76

Figure 2.3. ^{1}H NMR spectrum in $CDCl_3$ of TAPAm 79

Figure 2.4. ^{13}C NMR spectrum in $CDCl_3$ of TAPAm 81

Figure 2.5. Synthesis of 2-(3,4,5-tris(4-dodecyloxybenzyloxy)phenyl)-2-oxazoline(TAPOx) 82

Figure 2.6. ^{1}H NMR spectrum in $CDCl_3$ of TAPOx 83

Figure 2.7. ^{13}C NMR spectrum in $CDCl_3$ of TAPOx 84

Figure 2.8. General scheme of the synthetic routes addressed in the synthesis of dendronized TAPOx monomer 88

Figure 2.9. Calorimetric analysis of TAPAm; (blue) first heating, (orange) second heating, and (grey) cooling. Scan rate: 10 °C/min 89

Figure 2.10. XRD patterns of TAPAm recorded on heating at: (a) 70 °C, (b) 90 °C and (c) 110 °C on first heating; and (d) 80 °C and (e) 110 °C on second heating 91

Figure 2.11. Optical micrographs between crossed polars of TAPAm recorded during the first heating at 90 °C 92

Figure 2.12. Calorimetric analysis of TAPOx; (blue) first heating, (orange) second heating, and (grey) cooling. Scan rate: 10 °C/min 94

Figure 2.13. TGA thermogram of (a) TAPAm, (b) TAPOx and (c) TAPEs recorded at a heating rate of 10 °C/min in nitrogen atmosphere 95

Figure 2.14. Zooms of the NMR spectra of the polyoxazoline derived from TAPOx: a) ^{1}H NMR spectrum between 2.5 - 5.5 ppm (signals labelled in red); and b) ^{13}C NMR spectrum between 50-80 ppm (signals labelled in blue) 97

Figure 2.S1. Amidation of TAPAc with ethanolamine 111

Figure 2.S2. COSY NMR spectra of TAPAm 111

Figure 2.S3. HSQC spectra of TAPAm. In the spectra, the blue signals correspond to -CH- and -CH_3 signals, while the red ones correspond to -CH_2- signals 112

Figure 2.S4. COSY spectra of TAPOx 113

Figure 2.S5. HSQC spectra of TAPOx. In the spectra, the blue signals correspond to -CH- and -CH_3 signals, while the red ones correspond to -CH_2- signals 114

Figure 2.S6. HMBC spectra of TAPOx 115

Figure 2.S7. XRD patterns of TAPOx recorded on heating at: (a) 70 °C and (b) 100 °C on first heating; and (c) 70 °C on second heating 116

Figure 2.S8. DTGA curves of (a) TAPAm, (b) TAPOx and (c) TAPEs recorded at a heating rate of 10 °C/min in nitrogen atmosphere 117

Chapter 3

Figure 3.1. ^{1}H NMR spectrum of PTOx40 in $CDCl_3$ 140

Figure 3.2. COSY NMR spectrum of PTOx40 141

Figure 3.3. ^{13}C NMR spectrum of PTOx40 in $CDCl_3$ 143

Figure 3.4. Calorimetric analysis of all synthesized PTOx; DSC first heating scan of: PTOx20, PTOx30, PTOx40, PTOx50 and PTOx60 (Scan rate: 10 °C/min) 146

Figure 3.5. Optical micrographs between crossed polars of: (a) PTOx20, (b) PTOx40 and (c) PTOx60 recorded at RT (25 ± 5 °C) on cooling from isotropization. In the case of PTOx20 and PTOx60, pictures were taken after annealing at 74 °C during 24 h and then cooling the poly(2-oxazoline)s to RT 146

Figure 3.6. X-ray diffractograms of PTOx20, PTOx30, PTOx50 and PTOx60 recorded at 50 °C 148

Figure 3.7. X-ray diffractogram of PTOx40 recorded at 60 °C 149

Figure 3.8. TGA thermogram of PTOx family recorded at a heating rate of 10 °C/min in nitrogen atmosphere 150

Figure 3.S1. FT-IR spectra of: TAPOx monomer and PTOx40 poly(2-oxazoline) 159

Figure 3.S2. SEC curves of PTOx family 160

Figure 3.S3. X-ray diffractograms of PTOx20 recorded at: a) 50, b) 85 and c) 110 °C 161

Figure 3.S4. Calorimetric analysis of PTOx40: a) first heating, b) first cooling and c) second heating (Scan rate: 10 °C/min) 162

Figure 3.S5. DTGA curves of PTOx family recorded at a heating rate of 10 °C/min in nitrogen atmosphere 163

Chapter 4

Figure 4.1. General overview of the hybrid membrane assembling 173

Figure 4.2. Poly2-oxazoline (PTOx40) chemical structure 178

Figure 4.3. XRD diffractograms of the membranes a) PTOxM12, c) PTOxM13, e) PTOxM14 and g) PTOxM15, and the azimuthal scan of the hybrid membranes b) PTOxM12, d) PTOxM13, f) PTOxM14 and h) PTOxM15 183

Figure 4.4. Optical microscopy images of a) PTOxM12, b) PTOxM13, c) PTOxM14 and d) PTOxM15 were recorded at RT (25 ± 5 °C) 185

Figure 4.5. 3D images from hybrid membranes a) PTOxM12, b) PTOxM13, c) PTOxM14 and recorded with an optical microscope at RT (25 ± 5 °C) 186

Figure 4.6. Nyquist plots of dried PTOx hybrid membranes. a) PTOxM12, b) PTOxM13, c) PTOxM14 and d) PTOxM15 193

Figure 4.7. Through-plane impedance Nyquist plots of the hybrid membranes. a) PTOxM12, b) PTOxM13, c) PTOxM14 and d) PTOxM15 194

Figure 4.8. Experimental setup for linear sweep voltammetry measurements 198

Figure 4.9. C–V curves of hybrid membranes. a) PTOxM12, b) PTOxM13,) PTOxM14 and d) PTOxM15 199

Figure 4.S1. Calorimetric analysis of PTOx40. DSC second heating scan. (Scan rate 10 °C/min) 210

Figure 4.S2. 2D and 3D images of zones with bubbles from hybrid membranes (a – b) PTOxM13, (c – d) PTOxM14, (e – f) PTOxM15, respectively, recorded with an optical microscope at RT (25 ± 5 °C 211

Figure 4.S3. 2D and 3D images of zones with bubbles from the bottom part of the hybrid membranes (a – b) PTOxM13, (c – d) PTOxM14, (e – f) PTOxM15, respectively, recorded with an optical microscope at RT (25 ± 5 °C) 212

Figure 4.S4. Augmented optical microscopy images of the hybrid membranes a) PTOxM12 and b) PTOxM13, and c) polyester fabric recorded at RT (25 ± 5 °C) 213

Figure 4.S5. Water contact angle images from oriented and non-oriented PTOx hybrid membranes a) PTOxM12, b) PTOxM13, c) PTOxM14 and d) PTOxM15, and e) polyester fabric 213

Figure 4.S6. Nyquist plots of exemplary model circuits. R0 = R1 = 1 kΩ 214

Figure 4.S7. Nyquist plots after 10 drops of water of PTOx hybrid membranes. a) PTOxM12, b) PTOxM13, c) PTOxM14 and d) PTOxM15 215

Figure 4.S8. Pictures of the hybrid membranes after the addition of 10 drops of water. a) PTOxM12, b) PTOxM13, c) PTOxM14 and d) PTOxM15 215

Chapter 5

Figure 5.1. Setup used in the casting procedure of PECH75 solution onto the beech wood discs 228

Figure 5.2. a) Schematic illustration of two types of wood discs that can be obtained depending on the cutting direction from a tree log. Radial cut is named “R”, while longitudinal cut is named “L”; b) “R” cut wood disc, in which it is expected that the lignocellulosic fibres are oriented perpendicular to the surface of the disc; c) “L” wood cut wood disc, in which the lignocellulosic fibres are expected to be oriented perpendicular to the surface of the disc. d) Representation of the “L” cut wood disc rotated 90° 233

Figure 5.3. FT-IR spectra of non-treated beech wood (NTW) and delignified beech wood discs obtained when delignification was performed during 3h 234

Figure 5.4. a) Cross-section ESEM images of: i) NTW (magnification x240), ii) sample DWD_3_70 (magnification x250), iii) sample DWD_3_90 (magnification x50) and iv) sample DWD_6_90 (magnification x50). b) Zoom of the cross-section ESEM images of: i) NTW (magnification x780) ii) sample DWD_3_70 (magnification x750), iii) sample DWD_3_90 (magnification x140) and iv) sample DWD_6_90 (magnification x170). The selected areas correspond to the coloured regions of the images shown in **Figure 5.4a** 237

Figure 5.5. FT-IR spectra of DWD_3_90 and the following functionalized samples: FDWD_0.5_50, FDWD_0.5_90 and FDWD_24_90 240

Figure 5.6. Cross-section ESEM images of: a) sample FDWD_0.5_50 (magnification x75), and b) zoom of the region highlighted in blue (magnification x250). The measurements of the diameter of the cellulose fibres are also shown 241

Figure 5.7. Optical micrograph between crossed polars of PECH75 recorded during the first heating at 120 °C 243

Figure 5.8. ESEM images of the samples DWD_PECH75 and FDWD_PECH75 showing their cross-sections (a) and c), respectively. magnification x50) and their upper surfaces (b) and d), respectively. magnification x200 246

Figure 5.S1. FT-IR of non-treated beech wood (NTW) and all delignified beech wood discs performed at different temperatures and time 256

Figure 5.S2. Pictures of the beech wood discs obtained after delignification process using different reaction conditions 257

Figure 5.S3. FT-IR of DWD_3_90 and all functionalized delignified beech wood discs performed at different temperatures and time 257

Figure 5.S4. Photographs of the functionalized delignified wood discs (FDWD) obtained using different reaction conditions 258

Figure 5.S5. DSC thermogram of: a) second heating scan of PECH_75; and b) second cooling scan of PECH_75. (Scan rate: 10 °C/min) 258

Figure 5.S6. a) TGA thermograms of: PECH75, NTW, DWD_3_90 and FDWD_0.5_50. b) DTGA curves of: PECH75, NTW, DWD_3_90 and FDWD_0.5_50. Thermogravimetric analyses were carried out using a heating rate 10 °C/min in nitrogen atmosphere 259

Chapter 6

Figure 6.1. Chemical structure of PECH75 265

Figure 6.2. Experimental set-up for lineal sweep voltammetry measurements 271

Figure 6.3. Microscopy images from the hybrid membranes; a) O-DWDM, b) NO-DWDM, d) O-FDWDM and e) NO-FDWDM, and the virgin supports, c) V-DWD and f) V-FDWD 273

Figure 6.4. Topographic 3D images obtained with an optical microscope of a) O-DWDM, b) NO-DWDM, c) O-FDWDM and d) NO-FDWDM 275

Figure 6.5. a) XRD diffractogram of the thermally treated: O-DWD and b) the azimuthal scan of O-DWD; c) XRD diffractogram of the thermally treated O-FDWD and d) the azimuthal scan of O-FDWD 277

Figure 6.6. In-plane air side Nyquist plots of hybrid membranes. a) O-DWD, b) NO-DWD, c) O-FDWD and d) NO-FDWD 282

Figure 6.7. Through-plane impedance Nyquist plots of hybrid membranes: a) O-DWD, b) NO-DWD, c) O-FDWD and d) NO-FDWD 284

Figure 6.8. C–V curves of hybrid membranes. a) O-FDWDM and b) NO-FDWDM 287

Figure 6.S1. ESEM cross-section images of: a) Non-treated beech wood (NTW), b) DWD and c) FDWD 299

Figure 6.S2. Nyquist plots of exemplary model circuits. R0 = R1 = 1kΩ 302

Figure 6.S3. In-plane bottom side Nyquist plots of PECH75 hybrid membranes. a) O-DWD, b) NO-DWD, c) O-FDWD and d) NO-FDWD 303

List of tables

Chapter 2

Table 2.1. Starting materials, solvent, reaction conditions and results of the distinct chemical reactions carried out to obtain TAPAm 77

Table 2.2. Starting materials, solvent, reaction conditions and results obtained in the chemical reactions performed in the synthesis of TAPOx 87

Table 2.3. Enthalpies of phase transitions detected in the case of TAPAm 90

Table 2.4. Polymerization reaction conditions of TAPOx monomer (initiator, terminating agent, solvent, and reaction conditions) and the obtained results 98

Chapter 3

Table 3.1. Chemical reaction conditions and degrees of polymerization in the optimisation of the polymerization reaction of PTOx 134

Table 3.2. Chemical reaction conditions (% of initiator and reaction time), achieved conversion, expected and obtained degrees of polymerization and molecular parameters of the synthesized family of PTOx 137

Table 3.3. Calorimetric features of the PTOx family 144

Table 3.4. XRD diffraction data of PTOx family 149

Chapter 4

Table 4.1. Calorimetric features of PTOx40 obtained by DSC, and type of mesophase obtained from XRD results 179

Table 4.2. . XRD diffraction data of PTOx membranes and resulting peak width at half height (WHH) and angle of orientation 182

Table 4.3. Water and methanol uptake after 24h, and water contact angles of oriented (PTOxM13, PTOxM14 and PTOxM15) and non-oriented (PTOxM12) PTOx membranes, as well as for the polyester fabric support 190

Table 4.4. Ohmic resistance obtained from C – V curves for the different cations of the studied PTOx hybrid membranes 200

Table 4.5. Selectivity (G_{ion}/ G_{H+} ratio) values for alkaline monovalent cations 201

Table 4.S1. Fitting data from in-plane EIS of PTOx dried hybrid membranes and after 10 drops of water 216

Table 4.S2. Fitting data from through-plane EIS of PTOx dried hybrid membranes 217

Chapter 5

Table 5.1. Chemical reaction conditions and degrees of delignification obtained in the optimization of the delignification process of beech wood discs 235

Table 5.2. Chemical reaction conditions and yields of nucleophilic acyl substitution obtained in the optimization of the functionalization of delignified beech wood discs 239

Table 5.3. Calorimetric features of PECH75 and wood samples (NTW, DWD_3_90 and FDWD_0.5_50) 244

Table 5.4. Water contact angles of samples DWD_3_90, FDWD_0.5_90 and hybrid membranes DWD_PECH75 and FDWD_PECH75, before and after applying the thermal treatment 247

Chapter 6

Table 6.1. XRD diffraction data of FDWDM and DWDM hybrid membranes, resulting peak width at half height (WHH) and angle of orientation 276

Table 6.2. Contact Angle data from the hybrid membranes DWDM and FDWDM samples, with and without thermal treatment 279

Table 6.3. Ohmic resistance obtained from C – V curves for the different studied cations of the FDWDM hybrid membranes 287

Table 6.4. Selectivity (G_{ion}/G_{H+} ratio) values for alkaline monovalent cations 288

Table 6.5. Ohmic resistance obtained from C – V curves for the different studied cations of the FDWDM hybrid membranes after conditioning 289

Table 6.S1. Fitting data from, both air side and bottom side, in-plane EIS of hybrid PECH75 membranes 302

Table 6.S2. Fitting data from through-plane EIS of hybrid PECH75 membranes 303

Scientific contributions

1. J. Guardià, A. Zare, J. Eleeza, M. Giamberini, J.A. Reina, X. Montané, Synthesis and characterization of dendritic compounds containing nitrogen: monomer precursors in the construction of biomimetic membranes, Sci. Rep. 12 (2022).

2. J. Guardià, M. Giamberini, J.A. Reina, X. Montané, Synthesis and Characterization of Dendronized Side Chain Liquid Crystalline Poly(2-oxazoline)s towards Biomimetic Ion Channels, Eur. Polym. J. (2023) 112273.

3. J. Guardià, X. Montané, J.A. Reina, M. Giamberini, A. Iwan, K.A. Bogdanowicz, Tapered hybrid poly(2-oxazoline) membranes for proton transport. New approach to PEM assembly. (Under preparation).

4. J. Guardià, M.K. Wolf, S. De la Flor, M. Giamberini, J.A. Reina, A. Ribes-Greus, S. Bidali, A. Mariani, X. Montané, Development of wood-based membranes for ion transport applications. Part 1: Support preparation and membrane assembly. (Under preparation).

5. J. Guardià, K.A. Bogdanowicz, J.A. Reina, M. Giamberini, A. Iwan, X. Montané, Development of wood-based membranes for ion transport applications. Part 2: Membrane characterization and evaluation of ionic transport. (Under preparation).

Contributions to scientific conferences

1. **GEP2022: XVI Reunión del Grupo Especializado de Polímeros (GEP) de la Real Sociedad Española de Química y la Real Sociedad Española de Física. SLAP2022: XVII Simposio Latinoamericano de Polímeros.** Poster presentation. J. Guardià, A. Zare, M. Giamberini, J.A. Reina, X. Montané. Synthesis and characterization of novel dendronized poly(2-oxazoline)s: precursors in the construction of biomimetic membranes. Spain, May 2022.

2. **VI PhD Day.** Poster presentation. J. Guardià, M. Giamberini, J.A. Reina, X. Montané. Synthesis and characterization of novel dendronized poly(2-oxazoline)s: precursors in the construction of biomimetic membranes. Spain, October 2022.

3. **Advanced Polymers via Macromolecular Engineering 2023 (APME'23).** Oral presentation. X. Montané, J. Guardià, M. Giamberini, J.A. Reina. Novel columnar liquid crystalline poly(2-oxazoline)s containing side dendrons: advances in the design of biomimetic membranes. France, April 2023.

4. **I International Workshop in Organic Chemistry and Functional Materials.** Poster presentation. X. Montané, J. Guardià, M. Giamberini, J.A. Reina. Columnar liquid crystalline poly(2-oxazoline)s containing side dendrons: advances in the design of proton-conducting membranes. Spain, September 2023.

5. **XI Congreso de jóvenes investigadores en polímeros (JIP).** Oral Presentation. J. Guardià, M. Giamberini, J.A. Reina, X. Montané. Columnar liquid crystalline poly(2-oxazoline)s containing side dendrons: advances in the design of proton-conducting membranes. Spain, October 2023.

6. **VII PhD Day.** Poster presentation. J. Guardià, J.A. Reina, X. Montané, M. Giamberini. Development of wood-based membranes for proton transport applications. Spain, October 2023.

7. **13ª Trobada de Joves Investigadors dels Països Catalans.** Oral presentation. X. Montané, J. Guardià, M. Giamberini, J.A. Reina. Preparació i caracterització de noves membranes conductores de ions derivades de poli(2-oxazoline)s amb propietats cristall-líquid. Spain, January 2024.

8. **13ª Trobada de Joves Investigadors dels Països Catalans.** Oral presentation. J. Guardià, X. Montané, M. Giamberini, J.A. Reina. Membranes híbrides amb suports de fusta. Nova aproximació en el desenvolupament de membranes per al transport de protons. Spain, January 2024.

9. **Polychar 2024.** Flash and poster presentation. J. Guardià, X. Montané, J.A. Reina, M. Giamberini**.** Delignified wood: A new approach on the development of proton conducting membranes. Spain, May 2024

10. **Polychar 2024.** Oral presentation. X. Montané, J. Guardià, J.A. Reina, M. Giamberini. Preparation and characterization of new ion-conducting membranes derived from liquid crystalline poly(2-oxazoline)s Spain, May 2024.

UNIVERSITAT ROVIRA I VIRGILI
COLUMNAR LIQUID-CRYSTALLINE POLYMERS CONTAINING NITROGEN AT THE BACKBONE TO BE USED TO PREPARE ION-TRANSPORT MEMBRANES
Jordi Guardià Blanch

UNIVERSITAT ROVIRA I VIRGILI
COLUMNAR LIQUID-CRYSTALLINE POLYMERS CONTAINING NITROGEN AT THE BACKBONE TO BE USED TO PREPARE ION-TRANSPORT MEMBRANES
Jordi Guardià Blanch

UNIVERSITAT ROVIRA I VIRGILI
COLUMNAR LIQUID-CRYSTALLINE POLYMERS CONTAINING NITROGEN AT THE BACKBONE TO BE USED TO PREPARE ION-TRANSPORT MEMBRANES
Jordi Guardià Blanch

UNIVERSITAT ROVIRA I VIRGILI
COLUMNAR LIQUID-CRYSTALLINE POLYMERS CONTAINING NITROGEN AT THE BACKBONE TO BE USED TO PREPARE ION-TRANSPORT MEMBRANES
Jordi Guardià Blanch